An Experimental and Numerical Study on the Heat Transfer Driven Dynamics and Control of Transient Variations in a Solar Reactor

A THESIS SUBMITTED TO THE FACULTY OF THE GRADUATE SCHOOL OF THE UNIVERSITY OF MINNESOTA

BY

Mostafa M. Abuseada

IN PARTIAL FULFILLMENT OF THE REQUIREMENTS FOR THE DEGREE OF MASTER OF SCIENCE

Prof. Nesrin Ozalp, Thesis Advisor

July 2019

Acknowledgements

I would like to use this opportunity to express my gratitude to the following people, whose contribution to this research work was much appreciated:

- Prof. Nesrin Ozalp, thesis advisor, for her continuous guidance and great support.
- Prof. Richard Davis, thesis defense committee, for his assistance and helpful discussions.
- Mr. Michael Swanson, facilities management engineer, for his great assistance in the materialization of High Flux Gas Dynamics Laboratory and setup.
- Mr. Samuel Lucas and Mr. Eric Osten, undergraduate students, for their assistance in designing and/or constructing the experimental setup.
- Dr. Hamed Abedini Najafabadi and Mr. Cedric Ophoff, research team colleagues, for their research collaborations, stimulating discussions, and/or helpful feedbacks.
- University of Minnesota Duluth and Mechanical and Industrial Engineering Department for their fellowship and funding.
- Any others who contributed to this research work who were left unnamed.

Finally, I would also like to thank my family for their continuous guidance, encouragement, care, and support.

Abstract

One of the main challenges in concentrating solar power (CSP) applications is to provide better control systems that are capable of absorbing fluctuations in the sun's direct normal irradiance (DNI). In this work, a heat exchanger coupled variable aperture mechanism is designed and tested in a laboratory. To perform indoor testing, a new 10 kW_e xenon arc high flux solar simulator (HFSS) was fully characterized, providing maximum peak flux density and total power of 6.99 MWm^{-2} and 3.49 kW at the focal plane. Characterization was performed through an indirect heat flux mapping technique that used a single Lambertian target, as opposed to the use of two in literature. This saves cost and time and eliminates misalignment errors that can lead to a decrease in the peak flux density by around 6.8% or more. Additionally, a new method suitable for wider flux distributions was presented, demonstrating promising results. Then, the HFSS was numerically modeled in-house using two approaches: Monte Carlo ray tracing (MCRT) and inverse ray tracing methods. The MCRT method provided results with high accuracy, showing that the xenon arc can be properly modeled using a composite shape of a hemisphere attached to a cylinder. For the inverse ray tracing, it was shown that an intensity first-order interpolation unnecessary complicates the problem and that a zeroth-order interpolation significantly reduces the computational time and error values. Additionally, a new approach of eliminating intensity values that cannot be traced back to the reflector was proposed, which provided promising results. Following that, the setup of a cavity-type solar receiver was presented and numerically modeled using the validated MCRT model. Upon experimentally validating the model, it was shown that around 60% of the input power was lost through radiation from the receiver's cavity, which led to the introduction of the optimum aperture size at which the receiver's temperature would peak. It was shown that this optimum size depends on the HFSS's power level, meaning that the receiver can be continuously optimized at varying sun's DNI levels to obtain maximum temperatures if necessary, which might be possible to achieve using a variable aperture. Then, the design of the variable aperture mechanism to be coupled to the receiver was presented. The mechanism consisted of eight blades that moved in a translational type of motion to approximate a circular variable aperture, where only four of these blades were water-cooled by coupling them to a heat exchanger. It was experimentally demonstrated that with this arrangement, an average of 54% of the intercepted energy can be captured. Additionally, it was shown that intercepted radiation by the aperture mechanism was completely lost from the receiver's system. Hence, the behavior of obtaining peak temperatures by varying the aperture size was not observed by using the aperture mechanism. Therefore, if it is desired to maximize the temperature

inside a receiver rather than just regulate it, the aperture mechanism should be integrated more effectively into the receiver's design. Finally, the variable aperture mechanism was used to regulate the temperature within the solar receiver, which was successfully implemented using a model predictive control (MPC) and PID controllers. Both controllers performed satisfactory, keeping the average temperature overshoots and values within ± 3 °C of desired set points. However, the MPC system's response was slightly superior than that of the PID, where its temperature overshoots and values remained within a tighter tolerance. Furthermore, it was shown that the variable aperture can mitigate the effect of severe passing clouds or decrease the heating up time by fully closing. Additionally, experimental simulations based on real sun's DNI data demonstrated the aperture mechanism's superior capabilities in compensating for fluctuating DNI levels and maintaining the desired average temperature. To conclude, the variable aperture mechanism provided a simpler, easier, more accurate, and more energy efficient method of temperature control when compared to other methods in literature.

Table of Contents

List of Figures

List of Tables

Nomenclature

Latin Variables

A	Area (m^2) or model polynomial
$\mathbf{A}$	Linear operator
Amp	Input current (A)
a, b	Model parameters for polynomials A and B
B	Model polynomial
C	Constant or model polynomial
c_p	Specific heat capacity (J/kg.K)
D	Distribution factor
DNI	Direct Normal Irradiance (W/m^2)
d	Diameter (m)
e	Error
$\acute{e}$	White noise
F	Frequency function
f	Focal length (m)
GS	Grayscale value
h	Convection heat transfer coefficient ($W/m^2.K$)
I	Intensity – radiation ($W/m^2.sr$)
J	Cost function
K	Gain
k	Thermal conductivity (W/m.K)
L	Length (m)
$\mathbf{L}$	Roughening matrix
m	Mass (kg)
$\dot{m}$	Mass flow rate (kg/s)
N	Number or counter
na, nb	Polynomial orders for A and B
$\hat{\mathbf{n}}$	Normal unit vector
$\widehat{\mathbf{OP}}$	Starting position
P	Cumulative probability density function or covariance of estimation errors
$\hat{\mathbf{P}}$	Path of ray
p	Probability density function
$\dot{Q}$	Power (W)

$\mathbf{Q}$	Matrix of known parameters
q''	Heat flux density (W/m^2)
q^{-1}	Backward shift operator
$\Re$	Random number
$RMSE$	Root mean square error (%)
RNU	Radial non-uniformity (%)
r	Radius (m)
S	Surface equation
s	Length parameter
T	Temperature (K)
$\mathbf{TF}$	Transformation matrix
TI	Temporal instability (%)
t	Time (s) or thickness (m)
$\hat{\mathbf{t}}$	Tangential vector
u	Control signal or input
$\hat{\mathbf{u}}$	Direction unit vector
V	Volume (m^3)
$\dot{V}$	Volumetric flow rate (m^3/s)
W	Weighing factor – intensity
w	Future reference trajectory (°C)
y	System output (°C)
$\hat{y}$	Predicted/estimated system output (°C)

Greek Variables

α	Absorptivity or regularization parameter
β	Polar angle (rad)
Δ	Increment
ε	Emissivity
η	Efficiency
γ	Random variable
λ	Forgetting factor
ω	Weighing factor
ϕ	Azimuth angle (rad)
φ	Past input and output values
ρ	Density (kg/m^3)

ϱ	Reflectivity
σ	Stefan-Boltzmann constant ($W/m^2.K^4$)
τ	Transmissivity or time constant (s)
θ	Zenith/Polar angle (rad)
$\hat{\theta}$	Model parameters estimation
$\| \|_2$	Euclidean norm

Subscripts and Superscripts

ap	Aperture
avg	Average
arc	Xenon arc
b	Back
bp	Back plate
c	Cavity or center
cap	Captured
$cond$	Conduction
$conv$	Convection
d	Dead
$emit$	Emitted
eq	Equality
f	Front
ff	Front flange
in	Inner / Incident
ins	Insulations
i, j, k, n	Indices
m	Middle or index
out	Outer
P, I, D	PID controller respective parameters
p	Regularized parameter or prediction
$prim$	Primary
qp	Quartz plate
r	Reflection
rad	Radiation
ray	Ray – Monte Carlo method
rec	Recovered

sc	Shell cover
se	Specular error
sec	Secondary
T	Tikhonov regularization's order
tol	Tolerance
tr	Truncated
u	Control
w	Window
0	Focal plane, origin, or zeroth order
∞	Ambient
$'$	Modified or spatially transformed

Acronyms

ANSI	American National Standard Institute
ANU	Australian National University
ARMAX	Autoregressive Moving Average with Exogenous Inputs
ARX	Autoregressive with Exogenous inputs
ASME	American Society of Mechanical Engineers
ASTM	American Society of Testing and Materials
CCD	Charged Coupled Device
CGLS	Conjugate Gradient Least Squares
CIEMAT	Centro de Investigaciones Energéticas, Medioambientales y Tecnológicas
CIO	Centro de Investigaciones en Óptica
CMOS	Complementary Metal Oxide Semiconductor
cRIO	CompactRIO
CSP	Concentrating Solar Power
DLR	German Aerospace Center
DNI	Direct Normal Irradiance
EPFL	École Polytechnique Fédérale de Lausanne
ETH	Eidgenössische Technische Hochschule Zürich
GIT	Georgia Institute of Technology
GPC	Generalized Predictive Control
HFSS	High Flux Solar Simulator
HFG	Heat Flux Gauge
HFGL	High Flux Gas Dynamics Laboratory

IEC	International Electrotechnical Commission
IMDEA	Instituto Madrileño De Estudios Avanzados
KTH	KTH Royal Institute of Technology
MC	Monte Carlo
MCRT	Monte Carlo Ray Tracing
MISO	Multi-Input Single-Output
MPC	Model Predictive Control
NI	National Instruments
NNLS	Non-Negative Least Squares
NREL	National Renewable Energy Laboratory
PDF	Probability Density Function
PID	Proportional-Integral-Derivative
PSI	Paul Scherrer Institute
PV	Photovoltaic
RLS	Recursive Least Squares
RMSE	Root Mean Square Error
RNE	Radiosity Net Exchange
RNU	Radial Non-Uniformity
SoE	System of Equations
SVD	Singular Value Decomposition
TI	Temporal Instability
TSVD	Truncated Singular Value Decomposition
w.r.t.	with respect to

Chapter 1

Introduction

1.1. Background Information

Current energy conversion methods on Earth adversely affect the environment and lead to global warming. In the United States only, an average of 426 million metric tons of carbon dioxide (CO_2) was emitted per month during the year of 2017. This emission was primarily from nonrenewable energy sources including petroleum, coal, and natural gas, where these sources were 78.8% of the primary energy conversion processes [1]. If this issue is left unresolved, the atmospheric concentration of CO_2 can cause a significant impact on the climate and economy. Therefore, there is an increasing interest in incorporating the use of clean and renewable energy sources in energy conversion processes, such as solar, hydro-electric, bio-fuels, wind, and geo-thermal sources of energy. The focus on renewable energy, especially solar energy with particular research on fuel and commodity production, started to increase within the past decade.

In addition to reducing emissions of greenhouse gases, another major pressing need is to meet the expanding global energy demand. This is not only due to an increase in the population size, but is also due to an increase in the energy usage per capita [2]. Although solar energy is very promising to meet considerable amount of this demand, it is very intermittent and diffuse. Approximately 75,000 Terawatts of solar power from the sun reaches the Earth's surface [3]. Therefore, it is essential to develop new technologies to efficiently capture and store intermitted solar energy to achieve self-sustained energy economy. An example of a successful technology to capture solar energy is the implementation of photovoltaic (PV) panels for the direct generation of electricity. However, a large portion of the world's energy demand, especially at the industrial level, requires direct use of thermal energy. This is in addition to the efficiency challenges and high costs that can increase due to relatively long-term storage of electricity. Therefore, alternative uses of solar energy via concentrating solar power (CSP) applications and technologies offer promising pathways for industrial use of solar energy in processes in addition to power generation [4].

A large portion of the solar energy sector consists of CSP plants, where solar thermal energy is used for power generation. These plants implement the use of reflecting mirrors (curved/flat) or heliostats that are coupled with sun tracking systems in order to focus the solar radiation from the sun onto a point or line. Thus, the solar energy is no longer diffuse. There are four main types of CSP technologies: linear Fresnel, parabolic trough, parabolic dish, and central receiver systems,

with the parabolic trough being the most commonly used technology on the commercial level. Central receivers and parabolic dishes stand out with their capability to reach very high temperatures and accommodate solar thermochemical production of fuels and commodities, which would not be possible by other solar energy conversion systems that are limited to electricity generation. Three of the four main types of CSP technologies are illustrated in Figure 1-1. The capability of central receiver systems in achieving relatively higher operating temperatures results in higher thermodynamics efficiencies [3], and better efficiencies at elevated temperatures, which also allows for their implementation in thermochemical processes in addition to direct electricity generation [5]. Therefore, the main focus of this research work revolves around the applications of central receivers.

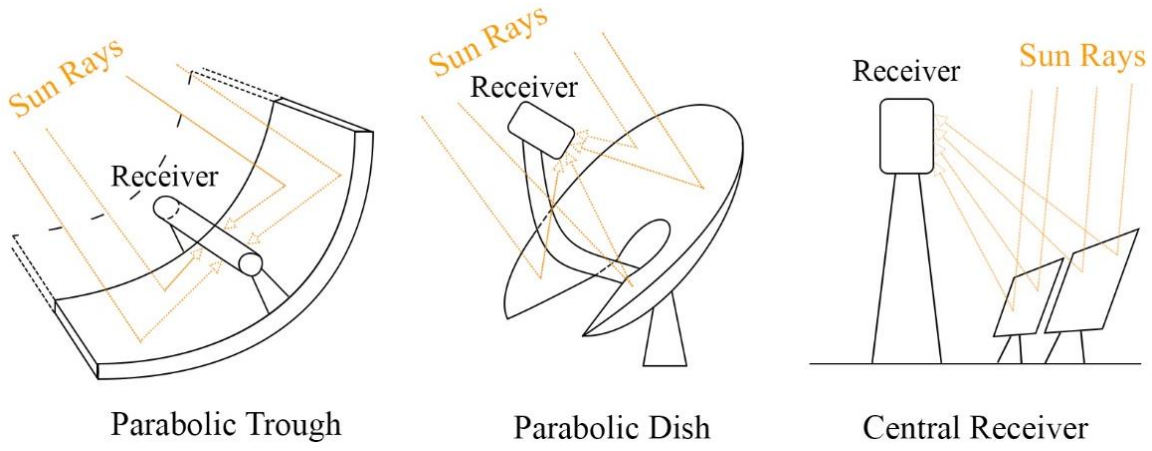

Figure 1-1: Schematic illustration of three main types of CSP technologies: parabolic trough, parabolic dish, and central receiver

CSP applications, namely point receivers (parabolic dish and central receiver), can be further subcategorized into two main systems: solar thermal and solar thermochemical [6]. In a solar thermal system, a working fluid is used to absorb the concentrated direct normal irradiance (DNI) from the sun for thermal utilization and/or storage. Therefore, there are no chemical processes taking place inside the receiver. Flow rate of the working fluid can be easily manipulated to obtain a specific operating/outlet temperature within a solar receiver. However, in a solar thermochemical system, where chemical processes take place, the manipulation of the feedstock flow rate would change the flow dynamics and residence time, which might yield undesired effects on the chemical conversion and process dynamics. Such changes might result in low yields that would require more complicated separation and recycling methods [6]. Having said that, the focus of this thesis is to offer an alternative approach to flow rate manipulation for solar thermochemical processes.

CSP central receiver facilities can be either in the form of a solar plant, as depicted in Figure 1-1, or in the form of a solar furnace. A solar furnace consists of three main components, namely being a collector system tracking the sun – heliostat(s), a Venetian-blind shutter, and a static parabolic reflector to focus the concentrated power to the reflector's focal point where the receiver is placed. The shutter is used as a mean of controlling the amount of solar radiation that actually passes to the parabolic reflector and thus the receiver. This type of facilities is mainly used for technology and design testing in addition to material treatment applications. In all facilities, the most common type of solar central receivers is a cavity-type receiver, which is a receiver with an aperture that aims for maximizing irradiation captured, while minimizing re-radiation lost within its cavity [7]. Therefore, the compromise between the captured solar energy and the radiation emission losses leads to an optimum aperture size and an optimum use of available incident flux.

Production of fuels (usually referred to as solar fuels) through solar energy has always been a promising field of study, where the solar fuels form long-term storable and transportable energy carriers [8,9]. These processes usually work by producing solar fuels and chemical commodities that are traditionally obtained through the combustion of fossil fuels to provide the required high temperature process heat. Example fuel and commodity productions from these processes include the production of hydrogen (H_2), syngas, and/or carbon [10–15], zinc (Zn) [16–18], and other products, such as lime [19]. Through the use of solar thermochemical processes, the carbon footprint is greatly reduced, where the solar alternatives involve relatively mild temperatures that have potential solar to fuel efficiencies exceeding 50% [20]. One of the application examples is the production of Zn from zinc oxide (ZnO) to be used as an energy source or commodity, where the Zn can be later oxidized to provide electricity or H_2 whenever necessary [18]. This provides a way of chemically storing the intercepted solar energy. However, most of the research interests are being targeted towards more sustainable and efficient hydrogen production methods. Currently, steam reforming of methane (CH_4) to produce H_2 is used, however at the expense of burning some of the CH_4 to provide the sufficient thermal energy for the endothermic process, which in return produces CO_2. A very promising alternative is the solar thermal decomposition (cracking) of CH_4, where both hydrogen and carbon particles are produced without any CO_2 emissions. A review of solar thermochemical processes for the production of hydrogen and syngas can be found in [21].

One of the main challenges in CSP applications, as discussed in [21], is to provide better control systems that are capable of absorbing changes and fluctuations in weather conditions. These changes mainly include fluctuations in the sun's DNI due to passing clouds or seasonal changes, in

addition to variations in the surrounding temperature and wind speed, which create difficulties in the regulation of a solar receiver's temperature. This in addition to the limitation on flow rate control for solar thermochemical applications is the driving force for developing more innovative and practical control systems and methodologies that would better help in mitigating the effects of weather conditions.

In order to tackle the fluctuation of the sun's DNI level, control systems should convert the sun's DNI level into an ideal one, as depicted in Figure 1-2. The DNI plots for an ideal day in addition to sunny and slightly cloudy days based on DNI data obtained from NREL [22] on December 15th and 12th, respectively, are shown in Figure 1-2. This shows the severity of the unideal conditions under which solar receivers operate, making it a challenge to accommodate for such variations.

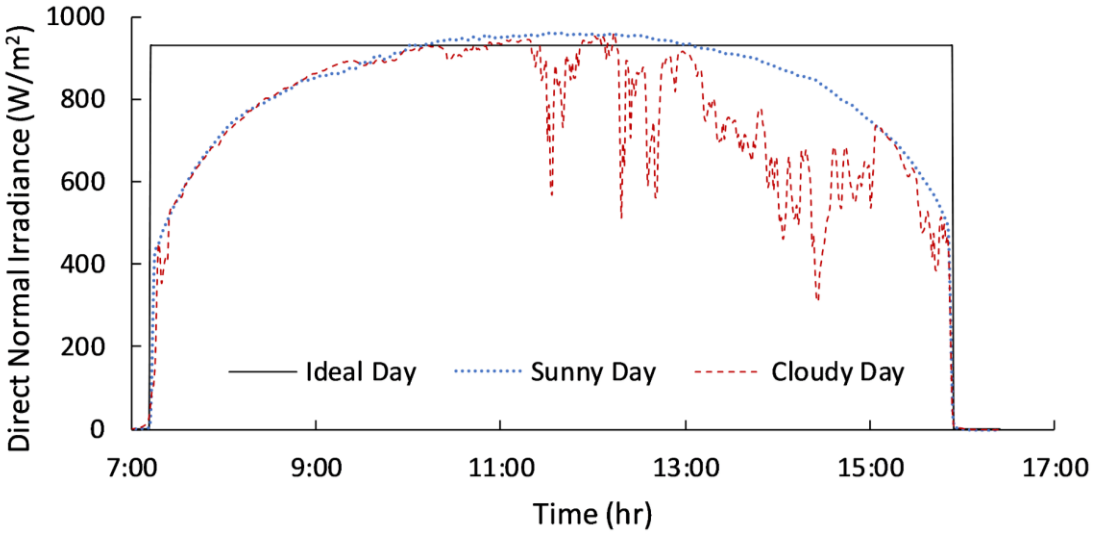

Figure 1-2: Direct normal irradiance plots for an ideal day, sunny day, and cloudy day

Unlike solar thermal applications which can relatively better accommodate for an increase or decrease in incident solar radiation, solar thermochemical applications usually need to be maintained at a specific operating temperature per Gibbs. Based on the nature of the process, there usually exists an optimum temperature at which the system and/or conversion efficiencies peak, or sometimes a compromise between two competing phenomena is made. Therefore, illustrating the need to closely monitor and regulate the operating temperature of a solar receiver around its desired temperature. In the upcoming section of this thesis, different solar thermochemical applications will be reviewed to elaborate this technical issue.

The first application to be discussed is the two-step splitting thermochemical cycles for CO_2 and water (H_2O) through the use of ceria as a dense membrane, as studied in [23]. Through their work of maximizing the energy conversion efficiency, it was shown in [23] that the energy efficiency of the system increases with temperature up to a certain peak point, where it then starts to decrease with temperature as a result of the increasing radiation losses. For example, in one of the system configurations they studied, the observed efficiency at 1600 K was approximately 26%, which then peaked to 43.8% at 1800 K, and then started to decrease to approximately 37% at 2100 K. In another similar study in [24] for a two-step redox cycle with heat recovery, an optimum operating temperature is also identified for the reduction of metal oxide based on two behaviors that compete as the temperature increases. These two phenomena are the increasing radiation losses from the receiver's cavity and the decreasing heat loss as a result of imperfect solid phase heat recovery [24].

One of the growing fields of applications in solar energy is syngas production through CH_4 reforming with CO_2, since it has a syngas production theoretical ratio of one [14]. Syngas can be used for several applications, such as to produce electricity. It can also be used as a commodity in industrial applications, converted to liquid fuels, or upgraded to gasoline [24]. The dry reforming of CH_4 over $SmCoO_3$ perovskite catalyst was studied in [14]. It was shown that the conversion efficiency of CH_4 and CO_2 peak or start to level off at a temperature of 850 °C, after which further increase in temperature causes no improvements in the reaction kinetics. Therefore, from an efficient utilization of energy point of view, an increase in operating temperature beyond this point is not desirable. Finally, in a different study on CH_4 decarbonisation, a temperature of approximately 1000 °C is observed at which the H_2 production no longer increases with increasing temperature [25].

Another application example is the non-catalytic cracking of ethane, as studied in [26]. It was shown that the operating temperature can have a significant effect on the performance of the system. As the temperature increases, the conversion efficiency and yield also increase while the selectivity of ethylene decreases. Thus, the optimum operating temperature is chosen based on a tradeoff between the yield and selectivity.

The final application to be discussed is a two-step solar thermochemical 100 kW pilot plant that was presented in [27] for water splitting in a solar tower. The plant consists of a two-chamber reactor that allows for the process to run in a quasi-continuous mode, by alternating the temperatures of the two chambers and maintaining them at 800 °C (for the water splitting step) and

1200 °C (for the regeneration step). Through this alternation and at the higher temperature cycle, the temperature of the redox material must not exceed 1250 °C to avoid its degradation or deactivation. Therefore, accurate control methods should be implemented to avoid the failure of the system.

As discussed previously, the operation and performance of a solar thermochemical receiver can be highly affected by changes in its operating temperature due to the amount of the sun's DNI level and its intermittent behavior. These changes usually decrease the processes' efficiencies and create several complications in the operation of solar reactors, such as unnecessary shutdowns or difficulties downstream of the reactor in the purification and separation processes. In addition, temperature regulation is also required to avoid the deterioration of receivers due to excessive thermal stresses and gradients [3]. Therefore, great focus should be dedicated towards creating better and more reliable control systems and methods.

1.2. Research Scope

The main objective of this research work is to develop and experimentally test a control system that is capable of regulating the operating temperature of a solar receiver. The control system should be simpler to control, easier to implement, and more energy efficient than current available control systems found in literature. In addition, the control system should be able to withstand relatively long times of operation and high thermal stresses with smooth operation and minimal maintenance. Since the control system is targeted for solar thermochemical applications, the control system should not solely depend on the manipulation of the feedstock flow rate or any similar control approach that will significantly change the flow characteristics. Having said that, the best approach to regulate the operating temperature of a solar receiver will be through the direct control of the incoming solar radiation. This method of control can be obtained using a variable aperture mechanism, where its performance will be evaluated through this thesis.

To be able to perform experimental testing in a laboratory scale setup, generally a high flux solar simulator (HFSS) is used. A HFSS allows mimicking the distribution of the sun's concentrated solar radiation that is normally obtained in CSP applications. Through the manipulation of the current supplied to the HFSS, it can also be used to experimentally simulate any variations in the sun's DNI. Hence, allowing for the experimental testing of the proposed control system under real-life scenarios. In order to effectively design the control system, understand any of the system's behaviors or responses, and propose any design changes, numerical models are created, validated, and used throughout this research work.

1.3. Thesis Outline

This research work is divided up into five main chapters. Each chapter covers a single main idea that aids in obtaining the final objective. Through the work performed in different chapters, some changes and recommendations are proposed to the current methodologies entailed in each. Since every chapter revolves around significantly different fundamentals, an introduction section is accompanied with each chapter to provide the necessary background information and relevant literature survey. With that being said, the thesis outline is as listed below.

- **Chapter 2:** In this chapter, the description and experimental setup of the HFSS is thoroughly presented. To be able to quantify the output power of the HFSS and identify its radiative capability, it has been experimentally characterized using an indirect flux mapping technique. With such a technique, all the relevant characteristics of the HFSS are easily obtained, where such information can be used in the evaluation of this research work and any future ones.
- **Chapter 3:** In this chapter, the only two known methods of numerically characterizing and modeling a HFSS are presented. One is a well-established forward method, while the other one is an inverse method undergoing further research improvements in the field. Both methods are used to numerically model the HFSS, where the two models have been rigorously validated. The output of the models provides an indicator of the HFSS's performance and input parameters for energy balance equations and efficiency calculations throughout this research work.
- **Chapter 4:** In this chapter, a cavity-type solar receiver system is thoroughly presented, which is specifically designed for this research work. The results from Chapter 3 are used to numerically model the system, where the model has been validated using experimentally obtained results. With the use of the numerical model, several phenomena are tested, such as the optimum aperture size, which leads to proposing a variable aperture mechanism.
- **Chapter 5:** In this chapter, the design of a variable aperture mechanism is presented and discussed in details. The aperture mechanism has been coupled with a heat exchanger to allow for its smooth operation under high thermal flux levels and to also recover some of the solar power it blocks as the aperture varies. The results from Chapter 4 are used to numerically model the variable aperture coupled system, where once again the model has been validated using experimentally obtained results.

- **Chapter 6:** In this chapter, the variable aperture mechanism is used to control the average temperature within the solar receiver. Using the validated numerical model from Chapter 5, two control methods are developed and optimized for the aperture control. Experimental implementation and testing of the two control methods are performed, where results are shown for tracking and maintaining a required set point in addition to rejecting disturbances due to variations in the sun's DNI based on actual DNI data. In addition, two other control strategies that comprise the manipulation of the feedstock flow rate are also investigated.

Chapter 2[1]

Experimental Characterization of Solar Simulator

In Chapter 2, HFSS configurations, utilizations, and their methods of characterization will be reviewed. The new HFSS setup at HFGL is presented along with the setup developed to characterize the solar simulator. The characterization was done by implementing an indirect heat flux mapping technique and a single Lambertian target, as opposed to the use of two Lambertian targets in literature. A methodology section is included to illustrate and describe how raw data to characterize the HFSS is captured and converted into meaningful results. A new promising approach, the *merging method*, is also presented for the characterization of HFSSs that have relatively wide heat flux distributions at the focal plane. Finally, results obtained from characterizing the HFSS setup at HFGL are presented and discussed, where Chapter 2 then ends with conclusions.

2.1. Introduction

2.1.1. High Flux Solar Simulators

Experimental testing of solar receivers or reactors for thermal and thermochemical applications requires a controllable source of high flux radiation mimicking the intensity of solar spectrum at different wavelengths. High flux radiation simulators comprise one or more lamps, each equipped with a truncated ellipsoidal reflector, to focus the rays to a common focal point where the radiation flux is concentrated [28,29]. Xenon arc is the most commonly used lamp type in high flux simulators, followed by both metal halide and argon lamps [30,31]. Xenon and metal halide lamps exhibit radiation peaks in the wavelength range of 800-1000 nm, while argon lamps have peaks in the 700-1000 nm range. These peaks represent the most notable deviation of each lamp from the sun's direct normal irradiance spectrum [28]. In addition, argon lamps have low energy emission in the visible light range, which is why argon lamps are considered to be the worst lamp type of the aforementioned types in mimicking the sun's DNI spectrum [28].

HFSS are characterized based on the type of lamp and the electrical power input versus the peak flux delivered. Literature shows that the highest power consuming single-source solar

[1] A large portion of this chapter created the paper by M. Abuseada, C. Ophoff, and N. Ozalp, titled "Characterization of a new 10 kWe high flux solar simulator via indirect radiation mapping technique", published in ASME J. Sol. Energy Eng. 141 (2019) 1-14.

simulator is a single argon lamp of 200 kW_e, which is capable of delivering lower to moderate power densities of around 5 MWm^{-2} [30]. On the other hand, metal halide lamps deliver the lowest power densities with less than 2 MWm^{-2} at power consumptions of less than 50 kW_e. As for the xenon lamps, there is a broad range of power requirements and densities with the possibility of reaching the highest peak fluxes of more than 15 MWm^{-2} [30]. An overview of several different HFSS types is shown in Table 2-1.

Table 2-1: Comparison of high flux solar simulators, their performance metrics, and flux characterization methods

Institute	**Lamp Type**	**No. of Lamps**	**Peak Flux** (kWm^{-2})	**Electric/Radiative Power** (kW_e/kW)	**Characterization Technique**
ETH [32]	15 kW_e Xenon	10	11,000	150 / 50	CCD + Kendall radiometer
Bucknell University [33]	2.5 kW_e Metal Halide	4	1140	10 / 3.5	Camera + calorimeter
KTH [34]	7 kW_e Xenon	12	6360	84 / 20.3	Thermopile flux sensor
GIT [35]	6 kW_e Xenon	7	6834	42 / 6.1	CCD + calorimeter
ANU/EPFL [36]	2.5 kW_e Xenon	18	21,700	45 / 7.5	CCD + Vatell TG1000-0 flux transducer
CIO [37]	2.5 kW_e Xenon	7	194/lamp	17.5 / -	CCD + Gardon-Schmidt-Boelter heat flux sensor
KU Leuven [38]	7 kW_e Xenon	1	3158	7 / 0.9	CMOS + Vatell TG1000-0 flux transducer
Berkeley [39]	20 kW_e Xenon	1	16,000	20 / 3	Model 1000-0 Thermogage
IMDEA [40]	6 kW_e Xenon	7	3600	42 / 14	CCD + Vatell TG1000-0 flux transducer
DLR [41]	7 kW_e Xenon	149	> 11,000	1043 / 280 or 2x220	-

Although most HFSSs use several lamps to achieve radiation concentrations and temperatures that are of most interest to researchers, there has been some work on smaller scale reactors using single-lamp setups that provide up to 10 kW_e input power. For example, a single-lamp setup can be created from an off-the-shelf cinema projector as described in [38] and [42], where a 7 kW_e xenon arc lamp in a projector was tested, just similar to that done in [43]. Single-lamp simulators can be used with solar reactors to characterize several applications, such as the kinetics of metal oxides reduction [44] and thermochemical water-splitting using ferrite [45]. There are also single-

lamp simulators with considerably higher input powers. For example, a single xenon arc solar simulator at Berkeley laboratory was using a 20 or 30 kW_e lamp [39].

There are many multi-lamp simulator designs operating in the 40-50 kW_e range, which is an optimal size for laboratory-scale reactors [36,43–45]. For example, an array of seven xenon arc lamps is used in both [40] and [46], and very similar HFSSs rated approximately 40 kW_e were also developed at Georgia Institute of Technology (GIT) [35], University of Florida [47], Swinburne University [31], and Instituto Madrileño De Estudios Avanzados (IMDEA) [40], whereas 18 lamps are used in [36] and ten 15 kW_e are used at the Swiss Federal Institute of Technology Zurich (Eidgenössische Technische Hochschule Zürich – ETH) [32]. The German Aerospace Center (DLR) recently created "the world's largest artificial sun" called Synlight, which consists of 149 xenon arc lamps [41]. The system is capable of producing 280 kW or two 220 kW for processes using two simultaneously heated chambers in three separate radiation chambers.

In some solar thermal applications, it may be of interest to create a uniform flux as opposed to a highly focused flux. For example, flat plate solar collectors, such as PV panels, should be tested under uniform flux resembling the natural solar irradiance because a concentrating unit is not necessarily used for flat plate collectors. As an example, a recent design used a virtual imaging approach to create a very uniform radiation flux [48], where four halogen lamps were used along with an internally reflective container to translate the point source of light from the lamps into a uniform flux. It was evaluated by a two-dimensional (2D) array of thermocouples placed on the surface of the prototype solar collector. However, it should be noted that there are several differences between solar simulators used for solar thermal applications and solar simulators used for photovoltaic research. Solar simulators used in photovoltaic research do not mimic the sun's concentrated radiation spectrum. Furthermore, because the performance of a PV panel is affected by the sun's angle relative to the normal angle of the panel and the change in air mass between the solar source and the panel throughout the day, PV solar simulators must be able to simulate these effects [49]. These assist to accurately characterize the expected performance of different cells for different parts of the world and for different types of installation, such as tracking, non-tracking, and rooftop installations [50]. The American Society of Testing and Materials (ASTM) as well as the International Electrotechnical Commission (IEC) classify solar simulators according to three criteria: spectral match, spatial non-uniformity of irradiance, and temporal stability [49].

2.1.2. Experimental Characterization of HFSS

With the use of any HFSS, it is vital to accurately map and characterize the radiative flux from the simulator at the focal plane. It does not only provide an indicator of the performance of the HFSS, but it also provides the input parameters for the energy balance equations and basis for efficiency calculations [51]. Therefore, an accurate flux mapping system is required. The current methods to flux mapping can be categorized into two main types: direct and indirect methods. Direct methods implement the use of a heat flux sensor to directly measure and map the flux distribution at the focal plane, such as the direct use of a thermogage in [39] or a thermopile flux sensor in [34]. Although direct methods are slightly more accurate than indirect methods, they are much more time consuming and less efficient. Hence, the preferred flux mapping methods in literature are the indirect ones due to their ability to quickly measure the flux distribution at an acceptable accuracy, which allows for efficiently aligning and optimizing HFSSs. Indirect flux mapping techniques incorporate the use of a grayscale camera, Lambertian (diffusely reflecting) target, and heat flux gauge (HFG) for the calibration of the grayscale values [32,33,35–37]. Most previous flux characterizations use two Lambertian targets: the HFG is embedded in one target, while the second is used for image capturing [42,52]. A new flux mapping system described in [53] also implements the use of two targets, where a smaller Lambertian target would move in front of the HFG to allow for capturing grayscale values at that location. However, the use of two targets might give rise to an additional error, which can be of a significant value depending on the amount of misalignment occurring when using two targets. Therefore, the use of a single target will eliminate this error, and hence deem the characterization to be of a higher accuracy.

In this chapter, heat flux characterization of a new 10 kW_e single-source HFSS is performed using an indirect radiation mapping method. The CMOS camera is first calibrated using a HFG, where the correlation obtained is presented and used to align and optimize the HFSS. The power of the source is varied by changing the current supplied to the simulator to determine the heat flux maps at several power levels, which can be used to mimic the sun's DNI throughout a full day. A sensitivity analysis is performed to inspect the impact of number of captured images on the accuracy and consistency of the experimental results. In addition to the quantification of the HFSS's transient response upon startup, temporal instability, and radial non-uniformity, a new method is proposed to identify flux distributions on larger areas within the focal plane.

2.2. Methodology

The first step in characterizing a solar simulator is to have a method that can accurately measure the radiant heat flux output. A HFG can be used to measure the flux distribution directly using a direct mapping technique or will allow the correlation of grayscale values from a camera to characterize the simulator using an indirect mapping method. HFGs provide a voltage output in the scale of millivolts which needs to be calibrated to obtain flux density values in kWm^{-2}. Calibration of a HFG can be either performed in-house as explained in [50] and [54], or the calibration provided by the manufacturer can be used. An important consideration is the relative size of the HFG sensor to the spot size of the measured flux density distribution. In this study the active gauge area has a diameter of 1.016 mm, which is an order of magnitude smaller than the observed spot size and can therefore be considered suitable for this experimental measurement campaign.

For an indirect mapping method, the heat flux density values obtained using a HFG should be correlated to grayscale values obtained from a Charged Coupled Device (CCD) camera or Complementary Metal Oxide Semiconductor (CMOS) camera. A Lambertian target is placed at the plane of interest to capture the flux density distribution using the grayscale values of the camera. An accurate positioning of the target is required to get the most precise focal point and flux density distribution. When the camera is placed coaxially with the target as in [36], the images can be captured and processed with no additional post-processing. However, most experimental setups do not allow coaxial image capturing due to direct exposure to the light beam. Hence, the camera is often placed with an angle to the target, i.e. *observer's angle*, which requires post-processing via a geometric transformation to get the undistorted image of the target as shown in Figure 2-1. This is performed through rectifying and scaling the image using a projective transformation method, where images in raw format are recommended and the image should not be saturated. Through this spatial transformation method, straight lines and quadrilaterals keep their geometries. The method of transforming from point $P'(x', y')$ to point $P(x, y)$ is defined through Eqns. (2-1) to (2-3), and visualized in Figure 2-1, where the transformation matrix $\mathbf{TF}$ is also defined.

$$x = \frac{C_{11}x' + C_{21}y' + C_{31}}{C_{13}x' + C_{23}y' + C_{33}} \tag{2-1}$$

$$y = \frac{C_{12}x' + C_{22}y' + C_{32}}{C_{13}x' + C_{23}y' + C_{33}} \tag{2-2}$$

$$\mathbf{TF} = \begin{bmatrix} C_{11} & C_{12} & C_{13} \\ C_{21} & C_{22} & C_{23} \\ C_{31} & C_{32} & C_{33} \end{bmatrix} \tag{2-3}$$

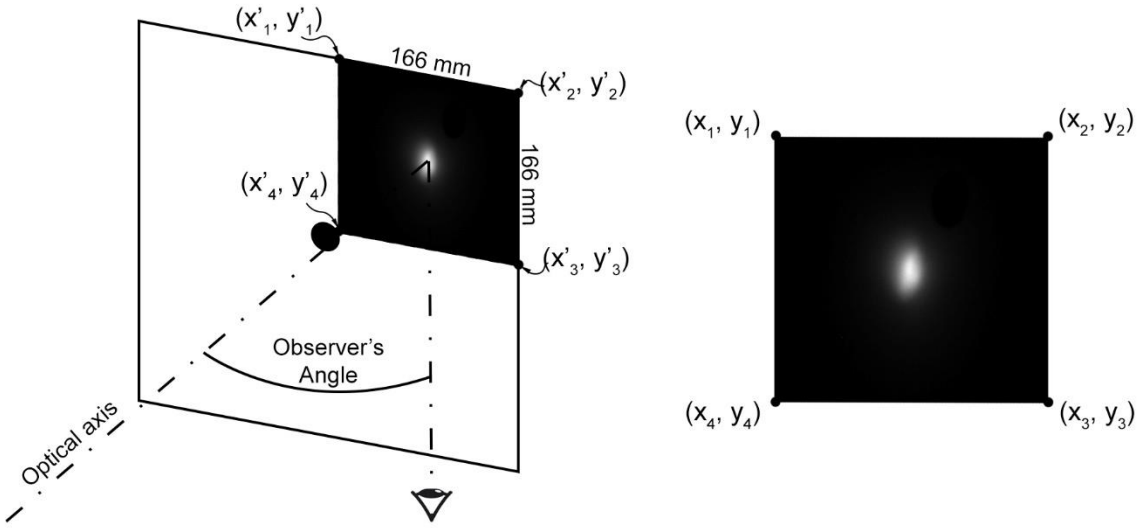

Figure 2-1: Rectification of the transformed grayscale captured image for indirect characterization

The transformation matrix shown in Eqn. (2-3) has nine coefficients that need to be solved to successfully complete the projective transformation. Although **TF** has nine coefficients, it only has 8 degrees of freedom since C_{33} is an arbitrary scale coefficient and it can be set to one. Hence, there are only eight coefficients to solve for using four sets of points. The coefficients in **TF** depends on the exact position of the camera, and therefore it can significantly differ from one experimental setup to the other. Transformation matrix given in Eqn. (2-4) is being used throughout the characterization of the HFSS in this chapter.

$$\mathbf{TF} = \begin{bmatrix} 0.4991 & -0.0138 & -6.8904 \times 10^{-5} \\ -0.0265 & 0.7841 & -3.0045 \times 10^{-6} \\ 459 & 144 & 1 \end{bmatrix} \tag{2-4}$$

To determine the optimum number of images to be captured by the camera, a statistical measure based on the root mean square error (RMSE) is implemented. The parameters tested are the total power on a 10 x 10 cm^2 target and maximum deviation at any point from the allegedly real value based on a total of 300 captured images.

Concentrated solar radiation especially from a single reflector is very uniform and symmetric in its distribution. To be able to mimic the behavior of concentrated solar radiation, it is crucial to define an index that expresses the level of symmetry in the distribution obtained from the solar simulator. Therefore, a radial non-uniformity (RNU) index has been implemented here, which is very similar to the spatial uniformity index, but is taken across annular areas centered at the focal point. This expresses the percentage deviation of the obtained flux density from a symmetrical circular distribution. The RNU is defined as shown in Eqn. (2-5), where q''_{max} and q''_{min} are the

maximum and minimum values of heat flux density at a given time and radius from the target's center.

$$RNU(r) = \frac{q''_{max}(r,t) - q''_{min}(r,t)}{q''_{max}(r,t) + q''_{min}(r,t)} \times 100 \quad (2\text{-}5)$$

The temporal instability is a characteristic for classification of solar simulators and it quantifies the relative change of irradiance over time for a specified time period. According to ASTM E927 and IEC 60904-9, solar simulators can be classified into three classes based on their temporal instability values: class A for values up to 2%, class B for 5%, and class C for 10% [55,56]. The temporal instability is calculated analogously to the RNU as shown in Eqn. (2-6), where q''_{max} and q''_{min} are the maximum and minimum values of heat flux density at a given position throughout a time period.

$$TI(r) = \frac{q''_{max}(r) - q''_{min}(r)}{q''_{max}(r) + q''_{min}(r)} \times 100 \quad (2\text{-}6)$$

While most of the previous flux characterization studies implemented the use of two Lambertian targets, where the HFG would be embedded in one while the second target would serve for image capturing [42,52], the present study demonstrates characterization of the solar simulator using one target. This eliminates misalignment errors that would otherwise occur when interchanging targets. The single target used in the present work covers a square area of 35 x 35 cm^2 and comprises a hole at the center to house the heat flux gauge as illustrated in Figure 2-1. As a result, the continuous reflective area on the target only allows to map the heat flux density on a maximum target size of 16.6 x 16.6 cm^2.

Extension of the current work led to a new method to increase the focal area size on which the flux density can be measured, referred to as the *merging method*. The target was displaced 3 cm from its center in both vertical and horizontal directions within the focal plane, as illustrated in Figure 2-2. This yields flux maps for five different target positions: *center*, *upper right*, *upper left*, *lower left*, and *lower right*. The flux data obtained was merged through post-processing into one larger data matrix. Flux density values of overlapping areas were averaged while values inside the heat gauge area, shown as dashed circles in Figure 2-2, were omitted using logical operations. The maximum dimensions of the final flux map are determined by the displacements of the target. In this study, the dimensions were set to 35 x 35 cm^2.

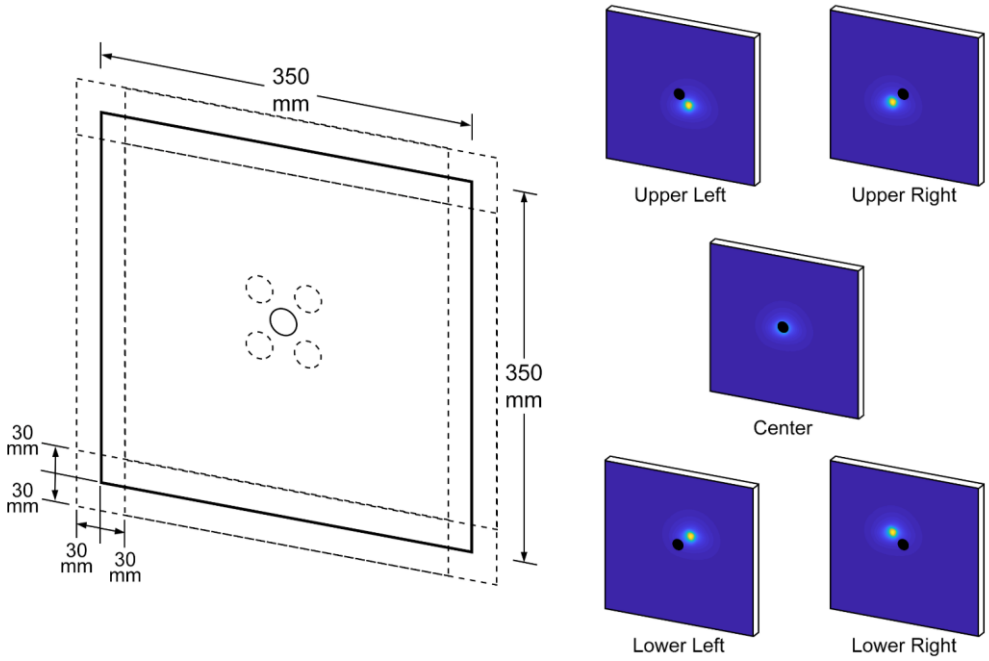

Figure 2-2: Configuration of the Lambertian target and individual flux maps for the merging method for indirect characterization

2.3. Experimental Setup and Components

The experimental setup consists of a lamp house with an installed 10 kW_e xenon arc, a heat flux gauge, 35 x 35 cm^2 Lambertian target, CMOS camera with optical filters, XYZ slider assembly with a motion controller, and a data acquisition system. The setup is depicted in Figure 2-3 (a), whereas a photo of the experimental setup is shown in Figure 2-3 (b).

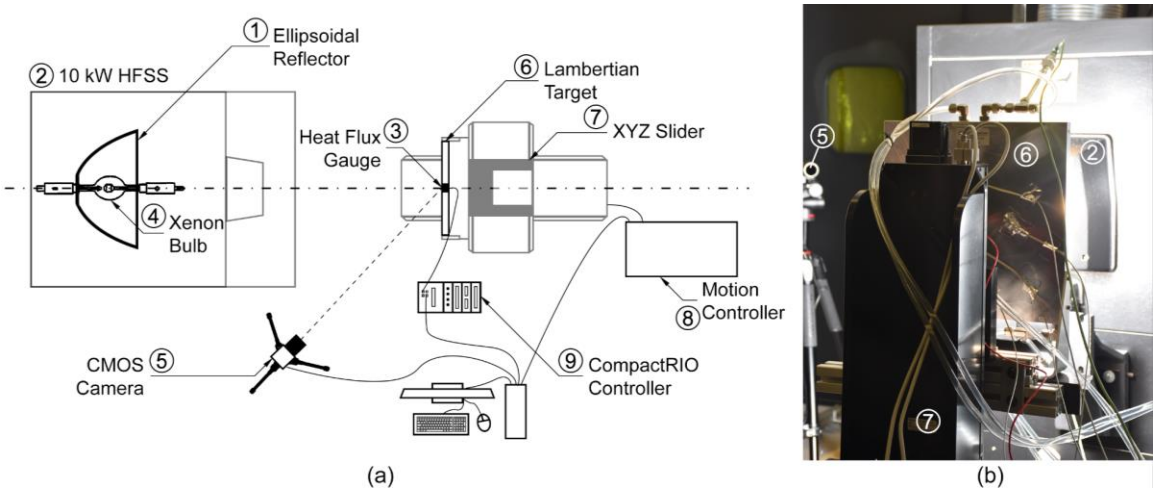

Figure 2-3: (a) Schematic illustration of the overall experimental setup, and (b) photo of the experimental setup

2.3.1. High Flux Solar Simulator

The solar simulator is manufactured by Strong Lighting (La Vista, NE) and is shown in Figure 2-4. It consists of an ellipsoidal reflector with truncated diameters of 9.1 cm and 39 cm in addition to two focal points at 7.5 cm and 82.5 cm from the vertex. The simulator comes equipped with intake blowers and an exhaust fan to ventilate the lamp house's interior and prevent the bulb from overheating. A power switch is used to control the power supplied to the lamp by controlling the current supplied within the range of 80 to 200 A. Since the nominal current for the 10 kW_e xenon bulb provided by Superior Quartz (Bethlehem, PA) is 200 A, the preferred range of controlling the bulb is within 160 to 200 A or as low as 80% of the nominal current to avoid instabilities within the arc and to preserve the condition of the bulb [57]. However, the supply current can be adjusted as low as 50% given that it does not continuously run at low current values. Therefore, the current supplied to the xenon bulb for its experimental characterization is varied from 120 to 200 A with increments of 5 A.

Figure 2-4: Overview of the high flux solar simulator and its components

2.3.2. Heat Flux Mapping Setup

The HFG used in experiments is provided by Vatell (Christiansburg, VA) model number TG1000-0, which can measure flux densities that are up to approximately 7.5 MWm^{-2} without

damaging the sensor or losing its calibration. The gauge has a sensor coated with colloidal graphite that has an emissivity of 0.82. The output voltage of the HFG lies within the range of 0 to 15 mV with an accuracy of ± 3%. The gauge was calibrated by the company, where it had a linear relationship with a sensor scale factor for absorbed radiant heat flux of 492.59 kWm^{-2}/mV for the aforementioned voltage output range. Exceeding this range will produce a non-linear output and therefore, the calibration will no longer be valid. It should be noted that the calibration done by the manufacturer may lead to overestimating the flux density values by up to 30% of the real values due to a mismatch between the radiation spectrum used for calibration and that used in solar applications [52]. In [52], the use of a third order polynomial relating the output voltage to heat flux density was recommended, whereas other researchers have used linear relationships through in-house calibrations, or verified the use of the calibration provided by Vatell [36,54,58,59]. A comparison of the calibration provided by Vatell and of that performed in-house by CIEMAT shows that both values agree with an error of 3.6%, which lies within the uncertainties of both calibration coefficients making the sensor scale factor provided by Vatell accurate enough to claim reliable [54].

A 35 x 35 cm^2 water-cooled Lambertian target provided by Haueter Engineering GmbH (Rombach, Switzerland) was used to diffusely reflect the incident flux from the simulator at any plane of interest. The target has an aluminum body coated with alumina at the front side, a 2.54 cm opening in the center to house the heat gauge, two water inlets at the top, and two water outlets at the bottom as shown in Figure 2-5. In order to control the position of the target accurately to determine the focal point and to precisely measure the flux density distribution, the assembly was mounted onto an XYZ slider configuration provided by Newmark Systems (Rancho Santa Margarita, CA). The XYZ slider is driven through a motion controller with a very high resolution of 0.08 microns that is capable of up to a maximum linear travel of 0.2 m, 0.3 m, and 0.5 m for the x, y, and z axes. With such a high resolution, the movement of the target assembly is very accurate and it enables high repeatability of measurements, granting precise testing of some parameters such as the inverse ray tracing of the radiative flux from the bulb, which will be covered in Chapter 3. To ensure consistency of measurements, the temperature of the inlet water, outlet water, and across the target's body was monitored using type-K thermocouple probes for the inlet and outlets in addition to four bolt-on thermocouples mounted at the back of the target via an arrangement shown in Figure 2-5.

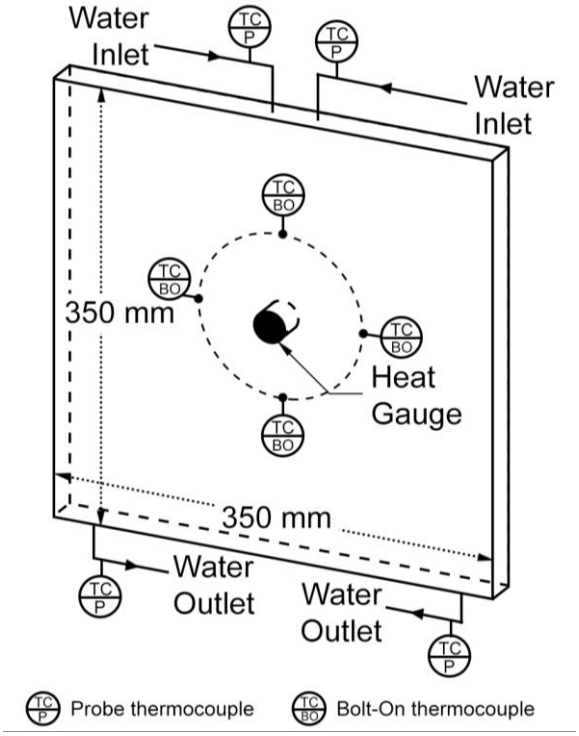

Figure 2-5: Configuration of the Lambertian target with K-type thermocouples to monitor its cooling

Once the Lambertian target is placed at the theoretical focal point, i.e. 82.5 cm from the reflector vertex, the next step is to calibrate the CMOS camera. The camera used in present study is model BlueCOUGAR X104fg provided by Matrix Vision (Oppenweiler, Germany) which has resolution of 1936 x 1216 pixels and pixel size of 5.86 µm x 5.86 µm. The camera is equipped with a lens that has two neutral density filters of absorptive 1% transmission and absorptive 0.01% transmission in order to protect the camera's sensors from damage due to exposure to high flux and also ensure the image is not saturated. The choice of equipped neutral density filters was based on obtaining the most stable grayscale measurements while ensuring that the image is not saturated, where combinations of filters of absorptive 6.25%, 1%, and 0.01% transmission were evaluated. Use of neutral density filters significantly reduces the possibility of white "hot pixels" formation due to damages resulting in an increased leakage of current, which could cause major distortions to the captured grayscale images [60].

Once the camera is set, the HFG is used to measure the heat flux at the focal point and at uniaxial distances across the focal plane along the positive and negative horizontal and vertical directions. The CMOS camera is then used to capture the raw grayscale images of the heat flux density distribution on the target, where the gain and exposure time of the camera needs to be

adjusted. This in turn affects the amplification of the analog-to-digital conversion of signals to ensure that the peak grayscale value is approximately 75% of the full-scale value of 255. This is done to achieve maximum accuracy for the measurements while avoiding the saturation of captured images. Once images are captured, they are processed to obtain grayscale values with respect to position across the focal plane. Grayscale values can then be correlated to heat flux density values, using a linear fit based on the least squares method. A linear fit is chosen for the correlation of the grayscale values based on the experimental results obtained, linear response of the CMOS camera with respect to light intensity, surface properties of the Lambertian target, and finally the previous work of other researchers in the field [36,40,42], where it is clear that there is a linear relationship between the grayscale and heat flux density values.

A data acquisition system using LabVIEW and hardware from National Instruments (NI) was implemented to have real-time data monitor and collection. The system consisted of cRIO 9030 to connect up to four modules in addition to NI-9214 temperature input module which can connect up to 16 sensors and has a minimum voltage increment of 9.3 μV. The temperature input module has resolution of 24 bits, and voltage measurement range of ± 78.125 mV. This makes it much superior for heat flux measurements than the analog input module NI-9215 which has resolution of 16 bits and voltage measurement range of ± 10 V. Initially, the data acquisition system was used to achieve two main purposes: to monitor temperatures within the Lambertian target to ensure uniform cooling, and to measure heat flux density values using the HFG. For all experimental runs, the solar simulator was operated for 15 to 30 minutes at start-up before acquiring measurements due to the transient nature of the xenon arc and solar simulators. As shown in [52], and shown later in the results section of this chapter, solar simulators exhibit a well-defined “long-term temporal behavior”, where the heat flux density distribution from the lamp increases upon ignition as time progresses. In [52], the initial irradiance obtained right after ignition was around 750 kWm^{-2}, which increased to around 925 kWm^{-2} within an hour approximately, exhibiting a nonlinear behavior that levels off in about 15 minutes. Moreover, the transient behavior of the lamp in [36] was also determined to reach a steady state, where intensity variations were less than 5%, after 10 minutes of data collection.

The bulb was optically aligned in order to identify the highest peak flux density, power, and uniformity by adjusting its position in three axes. Using the correlation between grayscale and irradiance values already established, it was straightforward to observe and quantify the effect of any changes made during alignment. This is an advantage of indirect heat flux mapping methods

over direct heat flux mapping methods, where it would take much longer to completely quantify such effects and properly align the bulb.

2.4. Results and Discussion

2.4.1. Calibration of Grayscale Values

The HFG was used to measure the heat flux density distribution at the focal plane starting from the origin at zero and reaching to a maximum radius of 65 mm. This was performed for the positive and negative horizontal and vertical axes along the focal plane, where the HFG was moved in a uniaxial manner to get the distribution along both axes. Starting from the origin, the HFG was moved up to 15 mm with increments of 0.5 mm, then from 15-30 mm with increments of 1 mm, and finally from 30-65 mm with increments of 5 mm. This ensured that the heat flux data collected covers the entire range of the distribution emitted by the bulb. The CMOS camera was then used to capture raw grayscale images that were then processed and correlated to heat flux values at the same location.

The correlation of the measured heat flux density and corresponding grayscale values is shown in Figure 2-6. The calibration equation was determined to be $q'' = 31.562\ GS \pm 66$ kWm^{-2}, not taking into account the calibration standard's uncertainty (HFG) of 3% and at a 95% confidence interval, where q'' is the flux density in kWm^{-2} and GS is the grayscale value. This correlation was obtained after optimizing the alignment of the bulb towards higher peak flux densities. Correlations prior to the alignment of the bulb would result in the CMOS camera reaching its saturation point, i.e. the increasing heat flux values would result in pixels reaching their saturation level yielding a full white color. The final correlation, as shown in Figure 2-6, should be valid for values approximately up to 8 MWm^{-2}, and therefore, the peak flux density obtained and stated later in this section is about 88% of the saturation point. Upon completion of the calibration, measurements taken using the HFG were plotted with those measured using the CMOS camera at different radial positions, which can be seen in Figure 2-7. The average percentage error of this verification was found to be 2.9% with a standard deviation of 3.2%, where the deviation between both plots decreased as the flux density values increased, since the effect of the camera's grayscale resolution became much lower. This shows a strong agreement between the values obtained using both methods.

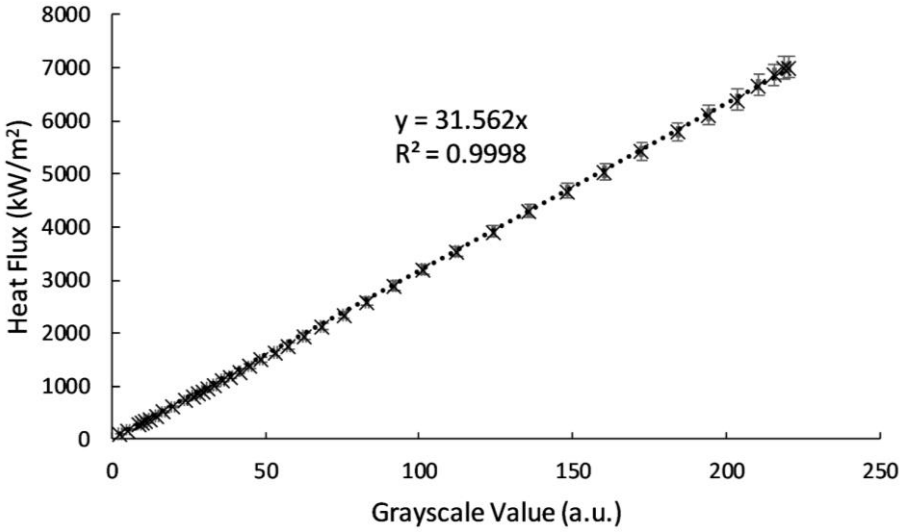

Figure 2-6: Correlation of measured heat flux density and corresponding grayscale values with error bars presenting uncertainty of each measurement

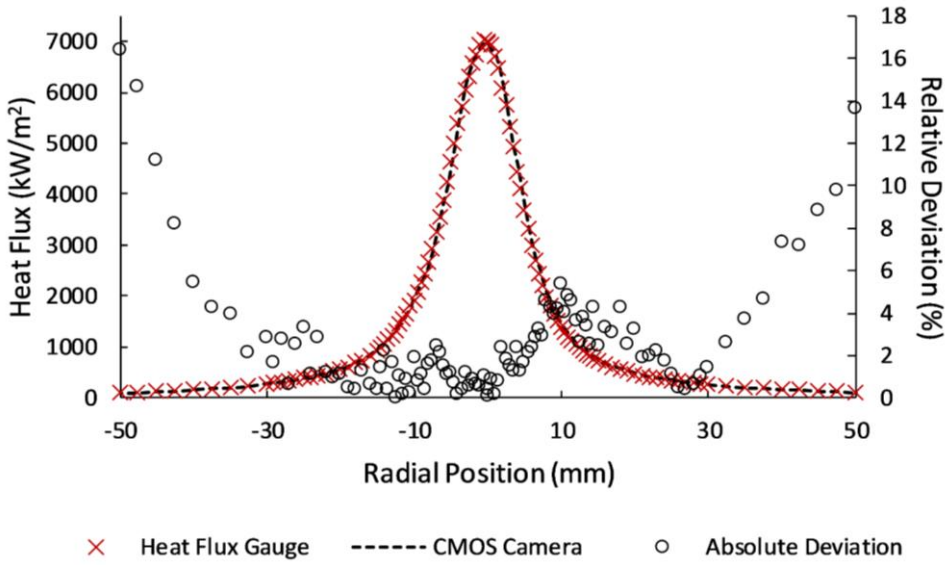

Figure 2-7: Verification of the grayscale calibration of the CMOS camera for indirect characterization

2.4.2. Optical Alignment of bulb

Optical alignment of the bulb was done in several steps, starting the optimization from an initial peak flux density of approximately 3.60 MWm^{-2}. One of these steps included adjusting the optical position of the bulb along the focal axis. Asymmetry was not studied here and therefore radial displacement of the bulb was not considered. The focal positioning was adjusted by turning a focal threaded knob that moves the bulb closer to or further away from the reflector vertex. Each full rotation (360°) of this knob provides a focal displacement of approximately 1.6 mm (sixteenth of

an inch). The zero reference (0 mm) is the position of the bulb after initial placement inside the simulator and based on the manual alignment guidelines of the solar simulator's manufacturer. Focal position of the bulb was adjusted in increments of 45° or 90°. Alignment of the bulb can be optimized with respect to maximum power or maximum flux at the focal plane. In this study, maximum achievable flux value is aimed for, to provide an optimum flux distribution for the applications undergone in this research (i.e. solar cavity receiver). Once an optimum adjustment was chosen, the optical alignment of the bulb proceeded to a different step by adjusting another parameter. Figure 2-8 shows one of the intermediate steps for adjusting the focal position of the bulb. The trends in this plot are comparable with the observations made in [61], especially the trend for total power agrees very well with those observations. Although it has not been shown in this study, it is assumed that displacement of the bulb in the opposite direction would yield the same bell shape as in [61]. The optimum adjustment was determined to be a focal displacement of 1.8 mm based on the highest obtained peak flux density. The peak flux density increased from a value of approximately 3.85 MWm^{-2} to 4.20 MWm^{-2}. Upon the final optimization, the peak flux density increased to 6.99 MWm^{-2} while the total power increased to 3.49 kW.

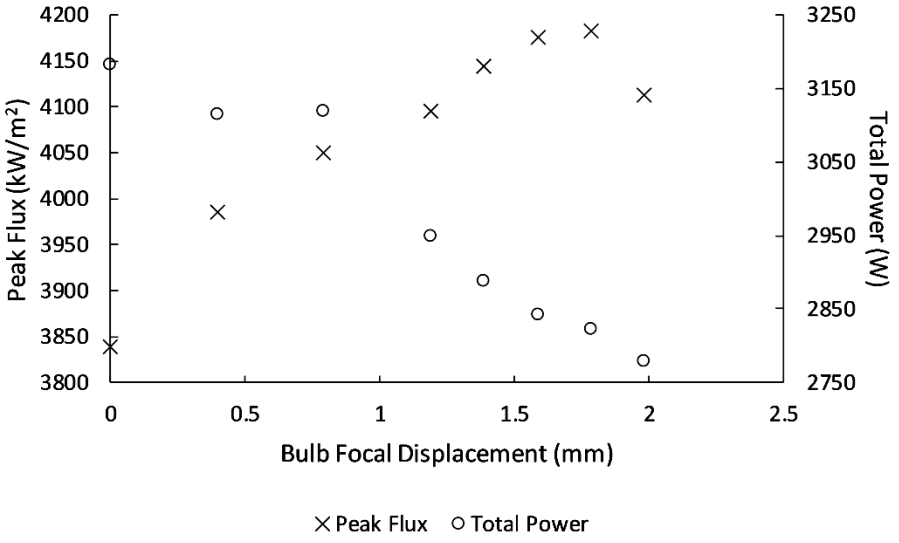

Figure 2-8: Variation of the measured peak flux density and total power for different focal alignments of the bulb

2.4.3. Heat Flux Distribution

The heat flux distribution of the solar simulator was first performed for the maximum supply current of 200 A. A two-dimensional color map on a 10 x 10 cm^2 target is shown in Figure 2-9, which represents the heat flux distribution on the area of interest to this research project that extends to a radial distance of approximately 5 cm from the center. The flux distribution can closely be

described by a Lorentzian distribution having a peak flux density of 6.99 ± 0.22 MWm^{-2} (95%) and a total power on a 10 x 10 cm^2 target of 3.49 ± 0.11 kW. Thus, the solar simulator has an electrical-to-radiative power efficiency of 35% based on the intercepted power on a 10 x 10 cm^2 target. The half width defines the radial distance from the center of the flux distribution at which the irradiance drops to half its peak value and was determined to be 6.25 mm. The half power defines the radial distance at which half of the power is contained and was determined to be 18 mm. Variation of the local flux density, average flux density, and the cumulative power with respect to the radial distance is shown in Figure 2-10. The average irradiance on a circular target with a radius of 5 cm was determined as 422 kWm^{-2}, which results in maximum blackbody stagnation temperature of around 1650 K.

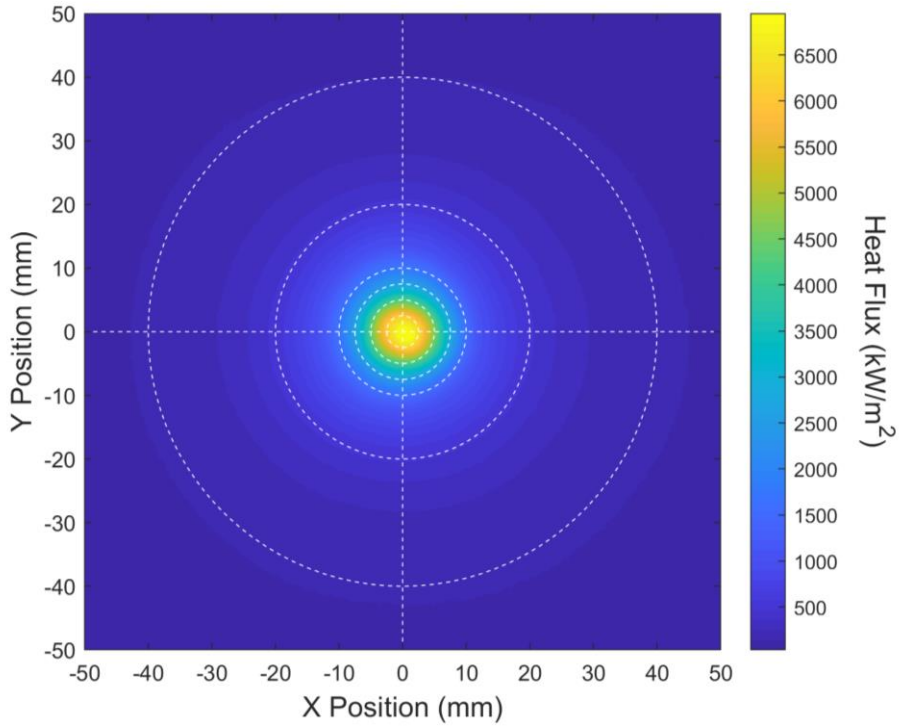

Figure 2-9: Two-dimensional view of the measured flux map on a 10 x 10 cm2 target area, and at a HFSS input current of 200 A, where centered concentric circles are shown having radii of 0.25, 0.5, 0.75, 1, 2, and 4 cm

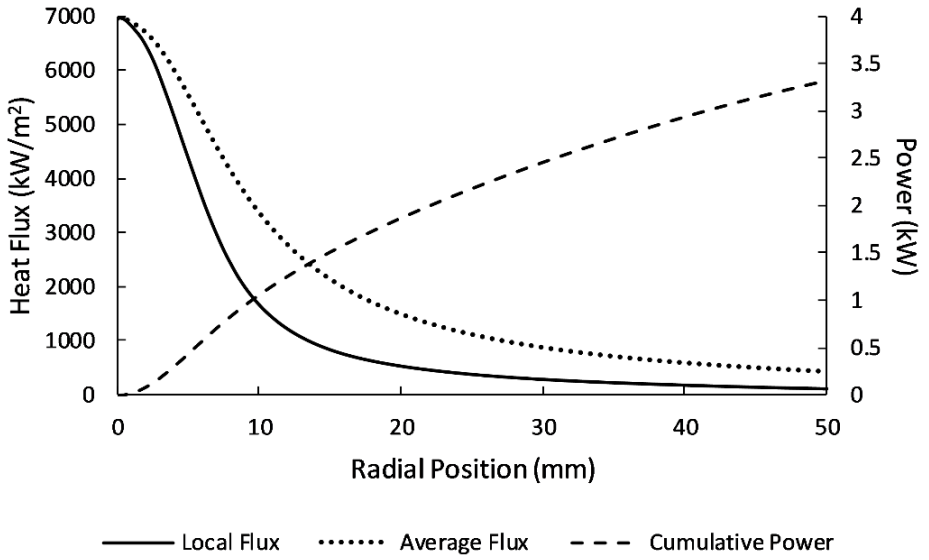

Figure 2-10: Local flux density, average flux density, and cumulative power as a function of radial distance from the target center at a HFSS input current of 200 A

2.4.4. Time Response of High Flux Solar Simulator

Temporal measurements were made to assess the output time response of the solar simulator. From the data, conclusions can be drawn on the warm-up time that would be required to reach steady operating conditions. The time response is quantified through observation of the flux density and total power on a 10 x 10 cm^2 target area. Flux density is measured at two different locations: one being the center of the distribution while the other one being at 5 mm below this center point. For these measurements, the results are taken from the correlated images obtained by the CMOS camera. Thus, this eliminates the temporal behavior of the heat gauge sensor. All three parameters are normalized with respect to their steady values 60 minutes after startup. The measurements are shown in Figure 2-11 and depict comparable results reported in [52]. The critical time period is during the first five minutes after startup where all three values reach approximately 95% of their final values. More steady behavior is observed after 10 minutes, where the normalized values fluctuate between 96 - 98% of their steady-state values. From this, it can be concluded that a warm-up time of 10 – 15 minutes is sufficient to reach steady operating conditions.

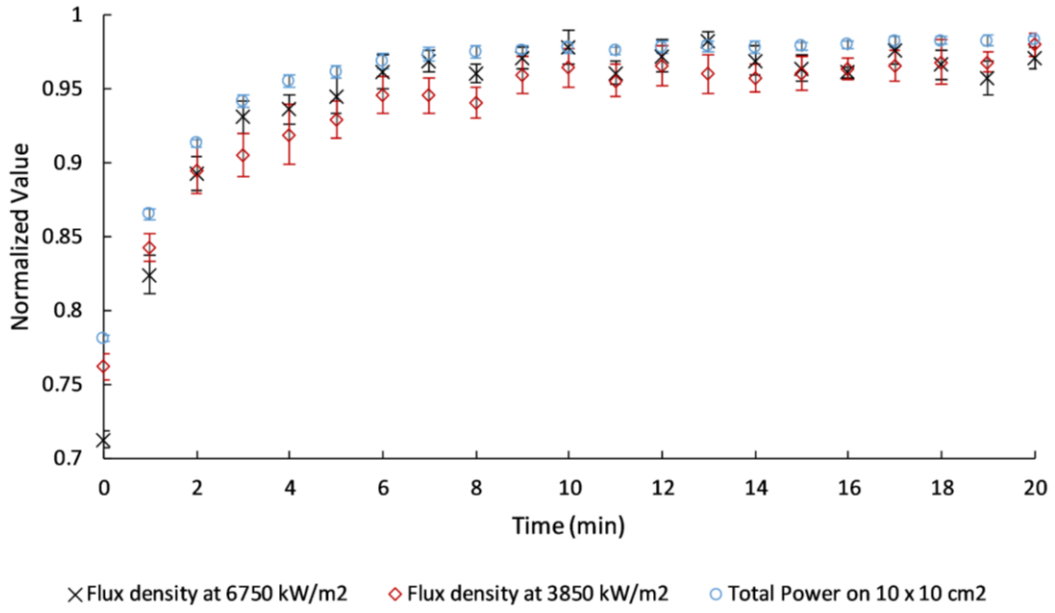

Figure 2-11: Startup time response of the HFSS at an input current of 200 A showing three parameters normalized with respect to their values 60 minutes after startup with error bars presenting standard deviation of each data point

2.4.5. Adjustment of Current and Power

The current supplied to the xenon arc bulb was varied in the range of 120 to 200 A, with increments of 5 A, to characterize the solar simulator at different power levels. Through the control of current supplied, the power received on a target or test object of interest can be varied as desired, which should enable mimicking the sun's DNI throughout the day. The peak flux and total power on a 10 x 10 cm^2 target with respect to the supplied current are shown in Figure 2-12 (a). Linear regressions were then performed for each variable with their respective equations and R^2 values shown, to provide a method of modeling these two parameters and adjusting the current supplied as necessary. In addition, Figure 2-12 (b) shows the relationship between the peak flux density and power, where almost a perfectly linear relationship exists between these two values based on its R^2 value. This, in addition to analyzing the obtained flux distributions at different currents, as shown in Figure 2-13 as a function of radial position, demonstrates that varying the current supplied to the bulb does not affect the overall heat flux distribution. It rather influences the distribution in a linear and uniform manner.

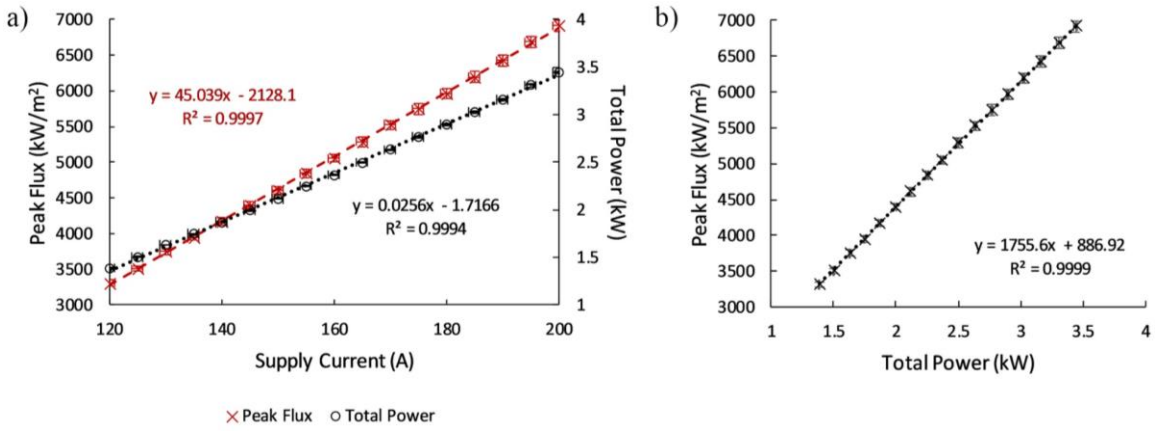

Figure 2-12: (a) Peak flux density and total power as a function of electrical input current to the HFSS with error bars presenting standard deviation on y-axes and uncertainty on x-axis, and (b) Linear correlation between measured peak flux density and total power with error bars presenting standard deviation

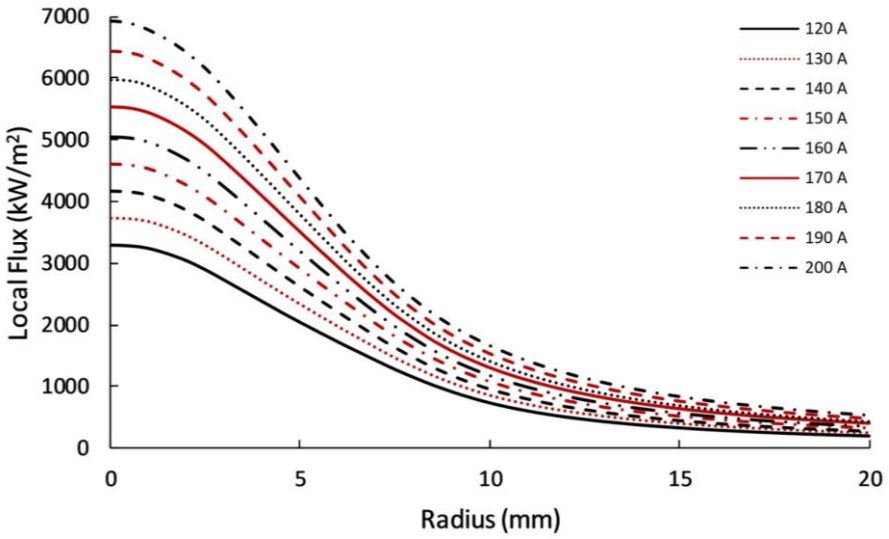

Figure 2-13: Two-dimensional plot of the heat flux distributions obtained at supply current values ranging from 120-200 A with increments of 10 A

2.4.6. Effect of the Number of Images Captured

The number of images captured by the CMOS can affect the results of the experimental determination of heat flux distribution. To determine a minimum threshold for the number of images to be captured, a sensitivity analysis was performed by comparing the RMSE values of the total power, peak flux, and maximum deviation at any point with respect to the number of images captured. This sensitivity analysis was performed for two different currents of 120 and 200 A to determine whether the threshold for the captured images is affected by instabilities in the arc due to lower current values. Both of the analyses performed are shown in Figure 2-14, where the peak flux results were omitted to better visualize the results since they had a similar trend as that shown

by the maximum deviation. As can be seen in Figure 2-14, the RMSE values for the two different parameters exhibit an inversely proportional behavior, which levels off as the number of images increases. Based on that, it can be concluded that the threshold for the number of images captured is around the 30 images mark for a current value of 200 A and 25 for a current of 120 A, where the reduction in the RMSE becomes insignificant thereafter. This threshold mark is slightly lower than the values of images captured in literature, where the number of images captured is around 30-40 images [36,42]. However, as expected, when the number of captured images increases, the RMSE values become slightly lower. Therefore, 100 images were captured and processed for characterizing the heat flux distribution, since time constraint was not a factor to overcome the additional capturing and processing time, which takes approximately three extra minutes.

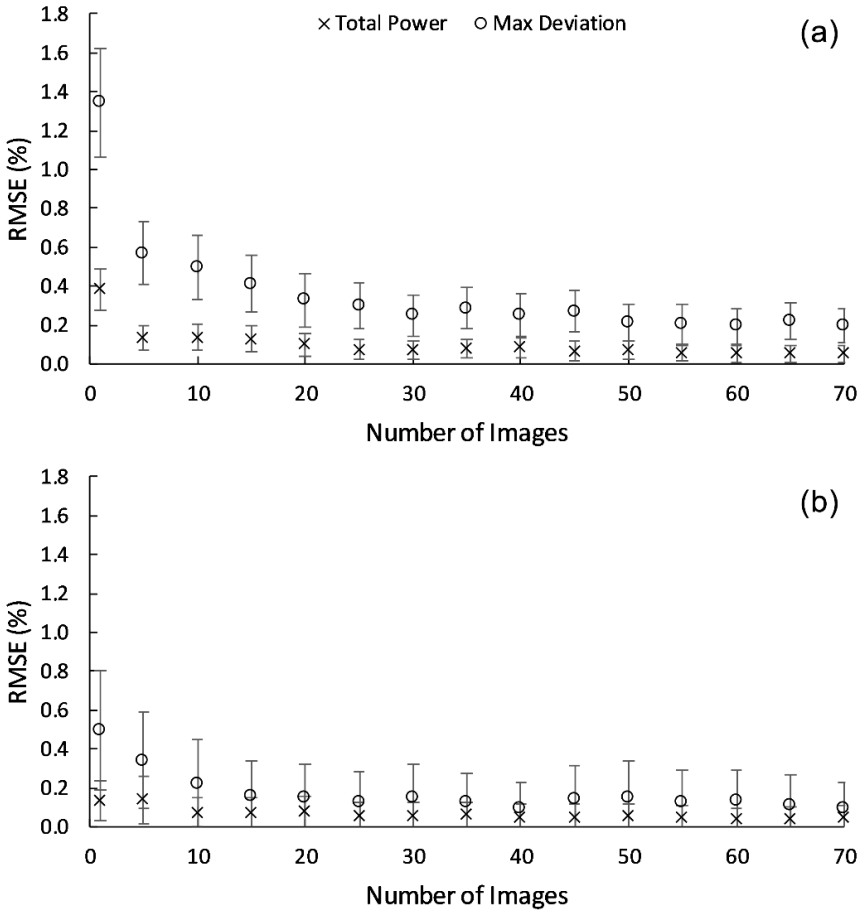

Figure 2-14: Sensitivity analysis on the number of captured images based on RMSE values at (a) 200 A, and (b) 120 A with error bars presenting standard deviation

As the current supplied to the bulb decreases from 200 A to 120 A, the xenon arc is expected to become more unstable especially below the 80% level of the nominal current of the bulb [62].

In efforts to numerically examine any effects due to the expected instabilities within the arc at lower supply current values, the RMSE values are compared for the two different current values. The RMSE values at a single captured image for total power and maximum deviation were 0.38 and 1.35% for 200 A as compared to 0.13 and 0.50% for 120 A. Based on the RMSE values at the two different current values, no direct effect was noticed due to the instabilities of the xenon arc on the parameters investigated, but rather it was noticed that the HFSS's output seemed to be more stable at lower current values. This observation also seems to agree with the results shown in Figure 2-12 (a), where the standard deviation of the values seen were significantly lower at lower current values. This could potentially mean that the xenon arc shows no instabilities at current values as low as 60% of its nominal value.

2.4.7. Determination of the Temporal Instability

The temporal instability of the heat flux obtained at the focal plane was then calculated using Eqn. (2-6) throughout a time span of 6 minutes. Temporal instability values were averaged out with respect to radial distance from the target's center to smooth out the relationship between the temporal instability and radial position. This relationship is plotted and shown in Figure 2-15. It can also be noticed that the temporal instability in addition to the measurement uncertainty would certainly deem the HFSS to be considered as running at steady operating conditions after 10 minutes based on the results shown in Figure 2-11. The temporal instability seemed to increase at distances further away from the center within the heat flux distribution obtained. Since the temporal instability values were all below 2% for circular areas with radii up to 50 mm, the solar simulator can be classified as class A for photovoltaic testing as identified by ASTM and IEC.

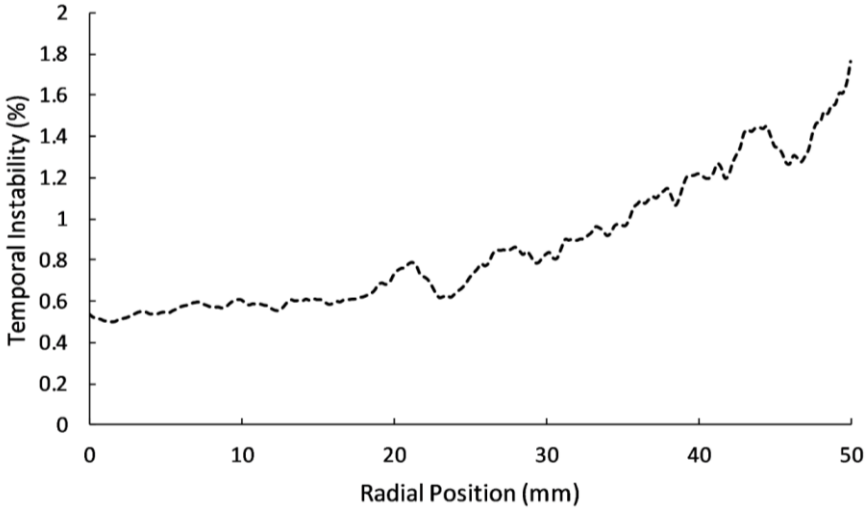

Figure 2-15: Averaged temporal instability of the HFSS for given radial positions at an input current of 200 A

2.4.8. Determination of the Radial Non-Uniformity

The RNU was calculated in a similar manner to the temporal instability using Eqn. (2-5) to represent the relationship between the non-uniformity and radial distance from the center. This is shown in Figure 2-16, where it can be seen that the RNU increases with an increasing radial distance up to approximately 8 mm since the flux density distribution's gradient is highest at those locations. Therefore, any slight misalignment in the HFSS will show amplified RNU values. As the radial distance continues to increase, measurement uncertainties and the resolution of the camera have a much more significant effect on fluctuating the results, which in return causes an increasing trend in RNU. Based on the values obtained across the total area of 10 x 10 cm^2 target, the radial uniformity of the flux distribution is satisfactory within the first 40 mm approximately, where RNU values lie within 10%, but becomes significantly less uniform further away from the center.

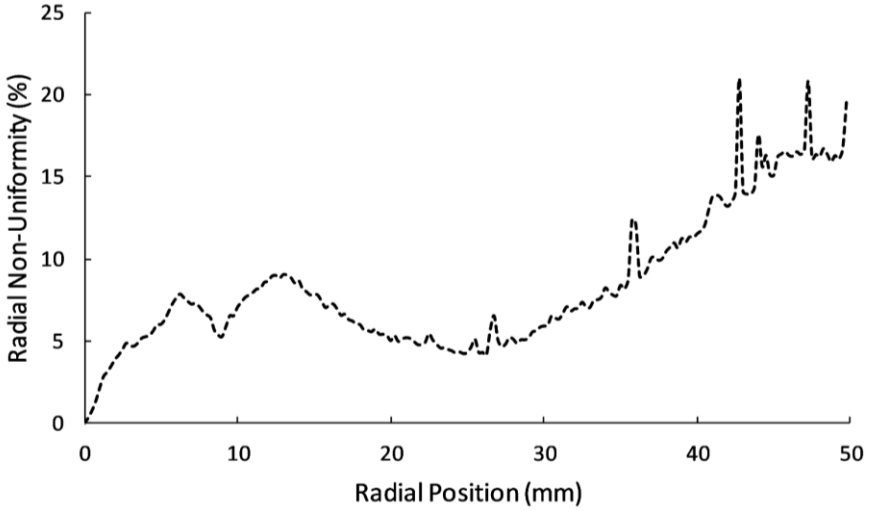

Figure 2-16: Radial non-uniformity of the HFSS as a function of radial position and at an input current of 200 A

The RNU can be attributed to manufacturing imperfections within critical components, mainly the ellipsoidal reflector. These imperfections are usually to be expected in most solar simulators. However, for this simulator, the adjustment mechanism of the bulb also played a significant role in the increased RNU. The mechanism for the bulb's horizontal and vertical positions did not allow for a precise motion of the bulb since it was manually moved by hand and held in place by two thumb screws. In addition, the mechanism did not allow motion in explicitly one axis, which made the optimization of the simulator, and hence the observation of a more radial uniform distribution much harder.

2.4.9. Uncertainty of the Measurements

There are several experimental sources of error that were examined to ensure that the data is reliable and any conclusions stated based on the experimental results are valid. The first source of error can be attributed to the equipment used in measuring the heat flux values directly in order to correlate the grayscale to heat flux density values. The HFG has an accuracy of ± 3%, which creates a maximum uncertainty of ± 210 kWm^{-2} for the peak flux density. Another source of error is the resolution of the CMOS camera, which has a grayscale range up to 255. Based on this grayscale range and the flux correlation factor, the uncertainty from the CMOS camera is ± 15.78 kWm^{-2}. In addition, the data acquisition system used has an uncertainty of ± 4.7 µV, which corresponds to an uncertainty of ± 2.315 kWm^{-2}. These uncertainty values were used to calculate a single weighted uncertainty value for the linear regression of the grayscale values that was used for acquiring experimental results. Using the aforementioned uncertainty values, in addition to any uncertainty that arises due to the process unsteadiness, the uncertainty of all measurements can be calculated using the method defined by the American National Standard Institute (ANSI) [63]. In accordance to this, the uncertainty in the determined peak flux is ± 220 kWm^{-2} with 95% confidence.

2.4.10. Image Merging Process

The resulting full flux map obtained by merging five overlapping flux measurements through the *merging method* is shown in Figure 2-17 (a), while a contour map on a 10 x 10 cm^2 target is shown in Figure 2-17(b). The peak flux density of the obtained distribution was found to be 6.95 MWm^{-2}. This differs by approximately 0.6% from the heat flux density obtained with the regular mapping method. Similarly, the total power incident on a 10 x 10 cm^2 area was determined as 3.73 kW which corresponds to a deviation of 6.5%. Per this method, the CMOS camera was re-positioned in order to fit the whole Lambertian target area inside the image frame rather than just a quarter (Figure 2-1). The observed deviation between the two methods is due to additional uncertainties that occur when considering a larger target size, where the resolution of the grayscale images is significantly affected. The resolution was computed by quantifying the amount of pixels representing the observed area in mm^2 in the untransformed image. The resolution was calculated as 8 px/mm^2 for the captured images of the *merging method*. For the regular mapping method, the resolution was calculated as 36 px/mm^2. This clearly indicates superior accuracy of the regular method and explains the slightly higher deviation on the total flux between both methods. However, this is to be expected when indirectly characterizing a larger target area.

It can be seen in Figure 2-17 (a) that the flux density was quantified up to a radius of 10 cm. Beyond this radius, processing of the grayscale images did not yield any flux density values. The reason for this is that the calibration of the grayscale values and the corresponding heat flux as depicted in Figure 2-6 is constrained by the 8-bit grayscale integer value. In other words, the range of obtainable flux density values up to approximately 8000 kWm^{-2} correlates to the range of 256 grayscale values. As aforementioned for the calibration, the applied correlation should account for saturation once higher flux values would be observed. This then leads to unclear distinction of the grayscale values close to 0 (black) in the tail of the flux distribution where values fluctuate between 0 and 1.

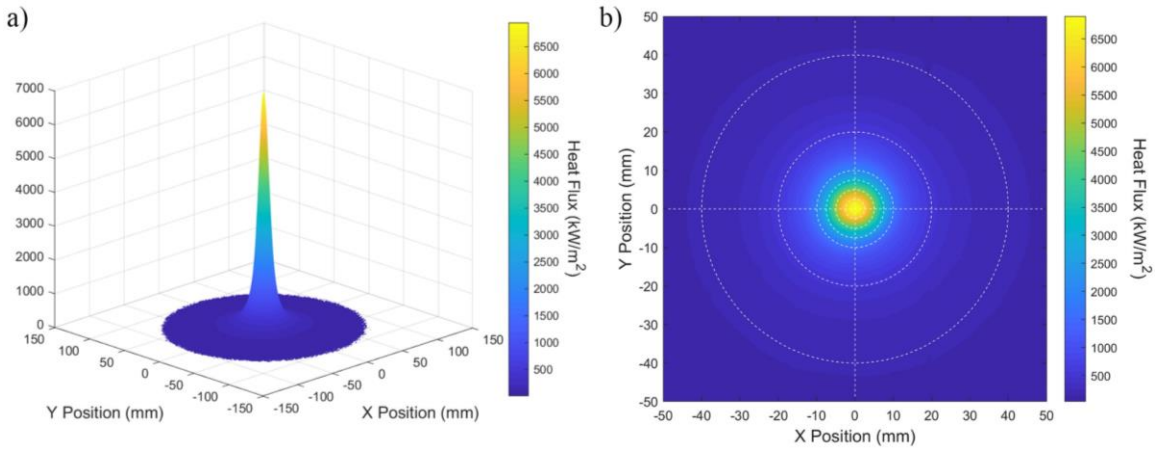

Figure 2-17: (a) Three-dimensional flux distribution on a 30 x 30 cm^2 target area obtained through merging of five flux maps, and at a HFSS input current of 200 A. (b) Two-dimensional view of the measured flux map on a 10 x 10 cm^2 target area obtained using the merging method, and at a HFSS input current of 200 A, where centered concentric circles are shown having radii of 0.25, 0.5, 0.75, 1, 2, and 4 cm.

Figure 2-18 depicts the flux density, both local and average, and the cumulative power of the merged flux map. The cumulative power at a radius of 5 cm equals to 3.55 kW which differs by approximately 0.24 kW from the values obtained with the regular heat flux mapping method (Figure 2-10). The total cumulative power for the obtained values within the radius of 10 cm was found to be 4.40 kW. Based on these results, it can be implied that the portion of significant incident radiative power at the focal plane falls within the circular area with 10 cm radius, and thus encompasses an area larger than the area of interest (approximately 5 cm in radius). In addition, the *merging method* seems to be a promising approach for the characterization of wider flux distributions, e.g. parabolic concentrators.

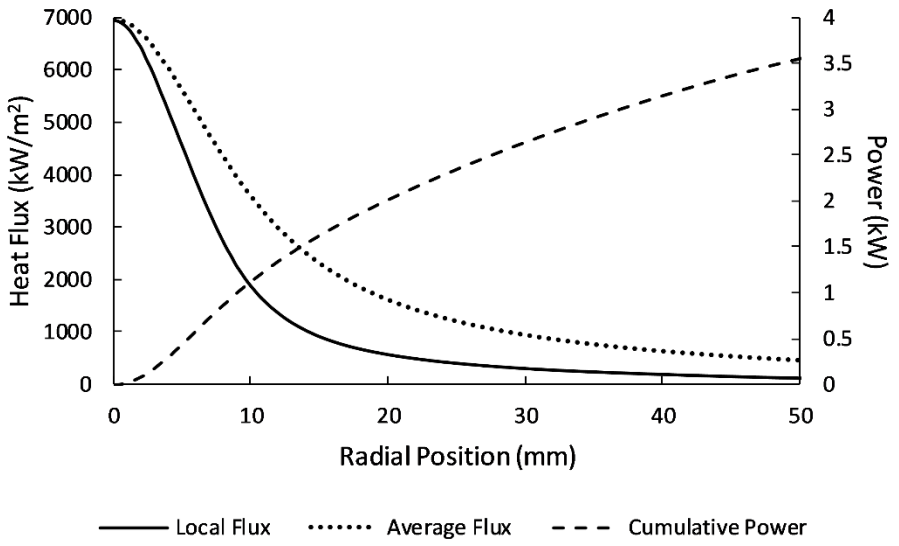

Figure 2-18: Local flux density, average flux density, and cumulative power as a function of radial distance from the target center at a HFSS input current of 200 A obtained using the merging method

2.5. Conclusions

In this chapter, an indirect heat flux mapping of a new 10 kW_e HFSS for solar thermal and thermochemical applications is presented. The method implemented for the characterization comprises the calibration of a CMOS camera with heat gauge data obtained, which classifies the method as an indirect one. Compared to most other methods, this method uses only one Lambertian target. This removes misalignment errors, which would otherwise occur when interchanging the targets or covering the HFG with a smaller Lambertian target to obtain the grayscale values at that location. Furthermore, this method would also save an additional cost and time. The heat flux maps obtained at maximum power provided a peak flux density of 6.99 MWm^{-2} with a total power of 3.49 kW incident on a 10 x 10 cm^2 target. Variation of the power supply current showed to have no effect on the overall heat flux distribution other than a linear and uniform increase or decrease of the flux. The results of a sensitivity analysis on the number of images captured by the CMOS camera concluded that the threshold for stable and repeatable data was 30 images. The new method, namely the *merging method*, presented would enable acquiring incident flux data on larger target sizes. Although the resolution of the raw grayscale images obtained through this method was significantly lower than the original method, the resulting peak flux density deviated just by 0.6% while the total power on the same target size of 10 x 10 cm^2 differed by 6.5%. The method was predicted to be favorable for wider flux distributions in the field of concentrated solar power.

Chapter 3[2,3]

Numerical Characterization of Solar Simulator

In Chapter 3, the numerical characterization of solar simulators is presented. Through the experimental mapping technique presented earlier in Chapter 2, or any of the other techniques implemented by other researchers as seen in literature, important directional information is lost. There are two methods that can be used to restore the lost directional information: a forward method based on the Monte Carlo Ray Tracing, which is the most commonly practiced approach in literature, and an inverse ray tracing method. Both of these methods are described and presented here in details. The experimental setup developed at HFGL is reviewed and experimental data relevant to this chapter is presented. The results obtained from both methods are then presented and compared, where Chapter 3 then ends with conclusions.

3.1. Introduction

HFSSs provide indoor experimental testing of solar thermal reactors and receivers for power, fuel, and commodity production. HFSSs are a stable and controllable source of high flux radiation, allowing for reproducible laboratory results and experimental testing under varying conditions. In the last decade, several HFSSs have been designed and built, most of which use xenon arc lamps as their radiative source [30], as covered previously in Chapter 2. With the use of any HFSS, it is vital to accurately map and characterize the radiative flux from the simulator at the focal plane and any other plane of interest. This is not just to determine the performance of the HFSS, but to also identify the input parameters for the energy balance equations and basis for efficiency calculations [51]. Through an accurate numerical model, receiver designs can be optimized in advance to ensure that the highest optical efficiency is achieved. Therefore, an accurate numerical characterization method of the HFSS is required for rigorous research results.

Through the flux characterization of a HFSS, all directional information of the flux distribution at the focal plane is lost. In the case of an indirect mapping method as that presented earlier in Chapter 2, this is due to the diffuse reflection characteristic of the Lambertian target. Therefore, the

[2] A small portion of this chapter contributed to paper by M. Abuseada, N. Ozalp, and C. Ophoff, titled “Numerical and experimental investigation of heat transfer in a solar receiver with a variable aperture”, published in Int. J. Heat Mass Transfer. 128 (2019) 125-135.

[3] A portion of this chapter was accepted for publication by the ASME as M. Abuseada, N. Ozalp, titled “Intensity distribution from a single-bulb solar simulator identification through inverse ray tracing”, to appear in the proceedings of the ASME 13th International Conference of Energy Sustainability, Paper No: ES2019-3860.

obtained flux maps at the focal plane or any other plane of reference can provide no estimation of the flux distribution on an arbitrary surface, such as a solar reactor. Hence, a method to restore the lost directional information should be developed.

The most common approaches in literature to numerically characterize HFSSs either use ray tracing in-house developed codes based on the Monte Carlo Ray Tracing (MCRT) method, as previously performed by the author in [64], or commercial software such as TracePro [65], VEGAS [66], or CUtrace [67]. These are used to simulate the intensity distribution based on the HFSS geometries and obtained flux maps. Despite their wide usage and popularity, these approaches rely on ideal geometries, and fail to predict intensity distributions due to non-ideal conditions such as surface imperfections. Therefore, an experimental approach is necessary to restore the directional information as first described in [68]. The methodology implements the use of flux maps at different optical planes to achieve the intensity distribution at the focal plane. By having the heat flux distribution known and the intensity unknown, this creates an inverse radiation problem.

In this chapter, the numerical characterization of the HFSS is presented and performed using the two aforementioned methods: the well-established forward MCRT, and the inverse ray tracing methods. The intensity distribution of the HFSS is determined at the focal plane. This is performed through the use of 13 experimentally obtained heat flux maps at the focal plane and optical planes further away from the HFSS. The forward MCRT method is implemented first by developing an in-house MCRT code to provide a reference solution to the inverse ray tracing methodology under investigation because it is a well-defined problem. A volumetric isotropic shape is proposed to accurately model the 10 kW_e xenon arc of the HFSS for use in this study and further ones. Then, the challenging inverse problem is attempted following the methodology described in [68] and [69] with few modifications and proposed changes. Several different solution strategies are examined to determine the most accurate method. To validate the solution method, the in-house MCRT code is used to model the xenon arc and provide heat flux maps at different optical planes similar to that obtained experimentally to provide a basis for the evaluation of performance of the different strategies. By comparing the obtained solutions to the reference solution from the MCRT code, the method of choice is determined based on relative percentage error values and then used to solve the inverse problem using the 13 experimentally obtained heat flux maps through the indirect flux mapping technique.

3.1.1. Forward Monte Carlo Ray Tracing

The Monte Carlo (MC) method is a classification for a broad and diverse group of methods that rely on appropriate statistical sampling techniques to solve mathematical problems of interest. Its use in radiation heat transfer has been common, where the method has been used in various problems such as nanoscale radiation, large-scale tomography, and surface radiation with or without participating media [70]. Due to the reason that only few analytical, closed-form solutions exist in radiation problems and that radiation heat transfer occurs through discrete energy bundles (photons) that travel along straight paths, the MC method becomes of great importance and is well suited for thermal radiation problems. Therefore, the MC method applied to thermal radiation involves tracing energy bundles from their emission to their absorption points, taking into account any intermediate interactions with surfaces or participating media [71]. Hence, the method is named MCRT.

Since the MCRT method relies heavily on statistical representations and approaches, random numbers and probability density functions play an important role. In a best case scenario, true random numbers can be obtained by acquiring noise through some sensor connected to the computer or by having a stored externally-determined set of real random numbers [72]. However, throughout a MCRT simulation, random numbers in the order of millions need to be generated or drawn quickly. This makes using a set of true random numbers being very impractical, which leads to the need of generating random numbers by the computer itself. These randomly generated numbers are referred to as pseudorandom numbers, and are predetermined values that seem to be random (meets all random numbers criteria), but are not truly random. Their use in the MCRT method is a valid and common alternative, given that care is taken in evaluating the randomness of these numbers based on the number generator of choice [73]. Throughout the scope of this thesis research, pseudorandom generator functions developed by MATLAB have been used.

The MCRT method functions by dividing a radiation source or surface into a large number of rays (energy bundles) that have equal powers, where rays are emerged in a stochastic manner through the use of random numbers. Each single ray is then traced from its point of emission to its final point, where reflections and interactions with intermediate surfaces of an enclosure are accounted for, and the loss of the ray from the system of interest is a possibility. Once the final destination of the ray has been determined, its history is terminated and a new ray is emerged and traced. Hence, the MCRT method provides the distribution of rays from the emitting surface to all surfaces within an enclosure, and so it incorporates the use of a so-called distribution (or exchange)

factor, D_{ij}. This factor represents the ratio of absorbed radiation by surface j to that emitted by surface i, due to direct radiation and all possible reflections [71]. A general review of the MC method and its implementation in radiative heat transfer can be found in [74], while a more recent review of the method's advancement and relevance to CSP application can be found in [75]. Further information and details are discussed later in the Methodology section.

3.1.2. Inverse Ray Tracing

A common engineering problem in heat transfer is that the result is given, whether it is a desired or an experimentally measured one, and the set of conditions that achieves this result needs to be obtained. These kind of problems are classified as inverse problems. Despite their significance and importance, inverse problems and their results are not covered extensively in literature as compared to forward or direct problems [76]. The need for an inverse solution strategy here and/or in many engineering applications in heat transfer is due to the fact that experimental observations of heat flux or temperature cannot be obtained at the desired physical location. The quantities of interest at the desired location need to be found using experimental measurements obtained at an accessible location instead. However, radiative inverse problems are usually complicated since the results are affected by all radiant sources in a given system. Therefore, special approaches and optimization techniques should be implemented to obtain useful results. Inverse design problems, solution approaches, and optimization techniques are reviewed in [76–78].

Unlike forward radiation problems that are well-posed and have unique solutions, inverse problems are usually ill-posed [79]. For an ill-conditioned inverse problem, multiple solutions can be obtained, where many are either physically unrealistic or significantly oscillate in space and/or time. Hence, they usually suffer from three main issues: no solutions may exactly match the data (solution existence), exact solutions may not be unique (solution uniqueness), and solution processes are unstable to small perturbations or noise (instability) [80]. These issues are much more prominent as the number of solution unknowns becomes larger relative to the number of measurements known, which represents the number of equations that describe the given problem. Therefore, there is a need to apply additional solution constraints and criteria that will provide both stable and unique solutions for inverse problems once discretized. Hence, changing the ill-conditioned system of equations (SoEs) or operations to well-conditioned, and creating a parameter estimation problem.

The process of changing an ill-conditioned to a well-conditioned SoEs is generally performed through the use of regularization techniques, irrelevant to the solution method of choice [78]. There

are two main solution methods for inverse problems: direct and iterative methods. Direct methods include the singular value decomposition (SVD), where regularization techniques can be implemented for the solution process, such as the truncated SVD (TSVD) and Tikhonov regularization of zeroth or higher orders. Iterative methods include Kaczmarz's algorithm, gradient descent method, and the conjugate gradient least squares (CGLS) method, where regularization techniques include Tikhonov regularization and a constraint on the number of iterations attempted by the solver. Iterative methods are preferred over direct ones for large problems, due to their ability to perform better with sparse matrices and not generate auxiliary matrices that are more dense than the original mapping operator in the SoEs [80].

3.2. Experimental Setup and Procedure

The HFSS consists of a lamp house that securely holds a 10 kW_e xenon arc, and is equipped with intake and exhaust fans to properly ventilate the interior of the lamp house. The xenon arc is placed at the first focal point of an ellipsoidal reflector with its two focal points (f_1 and f_2) at 7.5 and 90 cm from the vertex of the ellipsoid. The truncated reflector has starting and ending diameters of 9.1 and 39 cm that represent d_{tr1} and d_{tr2}. The HFSS is also equipped with a power supply that enables the control of its output power by varying the current supply within the range of 80-200 A.

The HFSS was characterized using an indirect heat flux mapping technique that incorporated the use of a HFG, water cooled Lambertian target, CMOS grayscale camera with optical filters, three-axis (XYZ) slider assembly with a dedicated motion controller, and cRIO system for data acquisition. The 35 x 35 cm^2 Lambertian target was used to diffusely reflect radiation incident from the HFSS at the focal plane and any other planes of interest. It also had a center opening to allow for mounting the HFG, for direct measurements, while protecting the setup and structure from the HFSS's high flux radiation. The XYZ slider was used to mount the Lambertian target and control its position within the three axes with a maximum linear displacement of 0.5 m to indirectly obtain the flux distribution at any plane of interest. The CMOS grayscale camera was used to capture raw images of the Lambertian target and correlate the captured grayscale values to heat flux measurements. The experimental setup used and its main components are shown in Figure 3-1, while further information on the HFSS or the experimental setup and equipment are covered previously in Chapter 2.

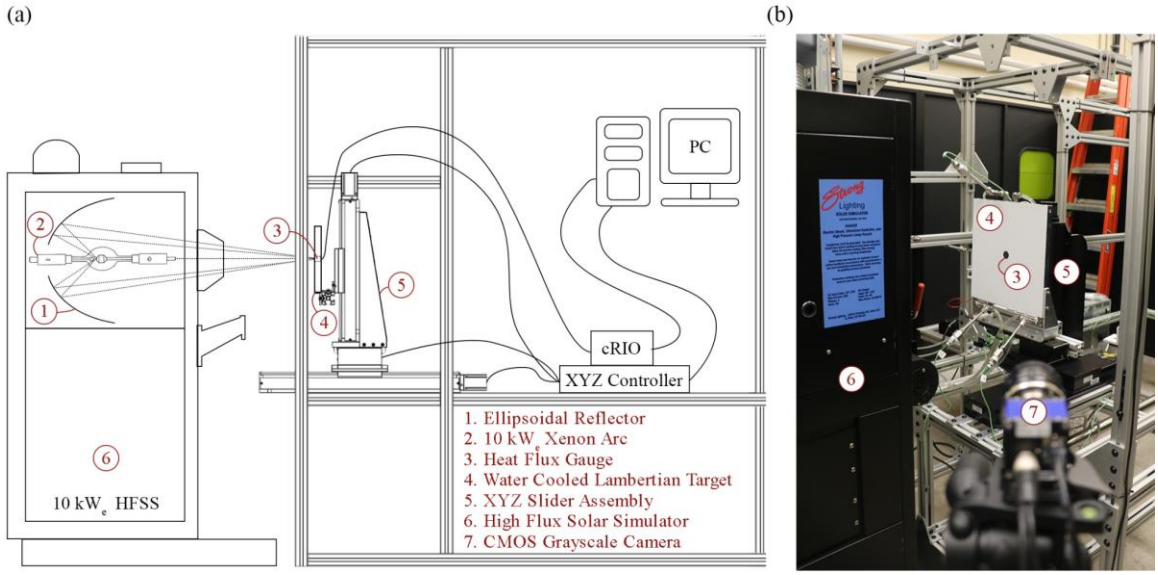

Figure 3-1: Experimental setup and components (a) schematic illustration, and (b) photo

To begin with indirectly characterizing the HFSS, the HFG was mounted at the center of the Lambertian target and used to directly map the range of flux density values at the focal plane through the use of the XYZ slider, while noting down their respective positions. The CMOS camera then captured grayscale images of the Lambertian target that was moved within the focal plane to get a continuous diffuse surface area of 16.6 x 16.6 cm^2. The grayscale values were then correlated to flux density values, which showed a linear relationship, as shown in Chapter 2. Once the calibration was complete, the CMOS camera was used to optically align the bulb for its optimum position. Then, the heat flux distribution was obtained at the focal plane as well as 12 other planes in the positive z-direction (away from the HFSS) at z-positions of 0-4.8 cm with increments of 0.4 cm. The experimentally measured flux maps obtained on a 10 x 10 cm^2 portion of the target and at the maximum supply current value at the focal plane as well as at z = 1.6 cm are shown in Figure 3-2. As can be seen, both flux maps show a symmetrical distribution around the center, which shows that the bulb was properly positioned at the reflector's first focal point. The peak flux density and total power values on the target at the focal plane was determined to be approximately 7000 kWm^{-2} and 3.49 kW, which dropped to approximately 5300 kWm^{-2} and 3.40 kW at z = 1.6 cm. In addition, Figure 3-3 shows the flux density distribution with respect to radial position from the center at seven different optical planes that span the range of experimental measurements. Further information on the characteristics of the HFSS and its heat flux distribution at the focal plane can be found in Chapter 2.

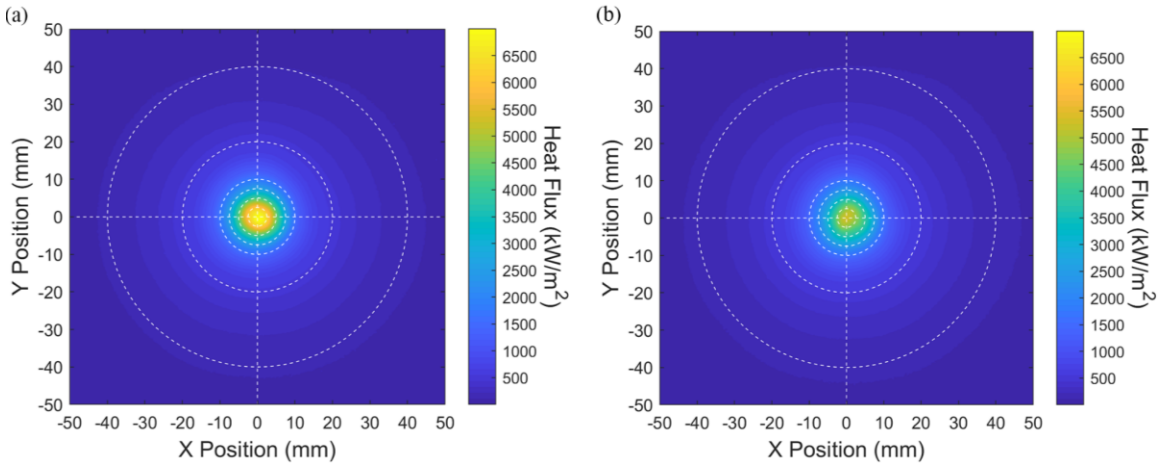

Figure 3-2: Experimentally measured heat flux distribution on a 10 x 10 cm^2 target area and a HFSS supply current of 200 A (a) at the focal plane, and (b) at z = 1.6 cm. Centered concentric circles are shown having radii of 0.25, 0.5, 0.75, 1, 2, and 4 cm.

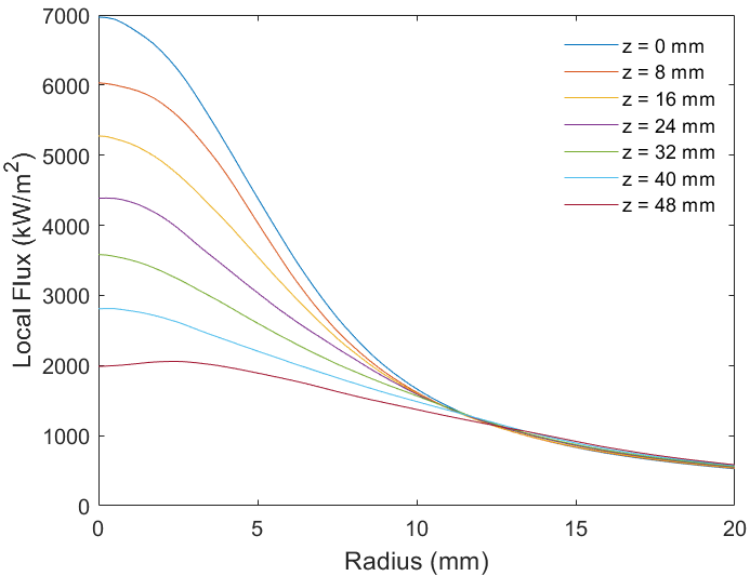

Figure 3-3: Heat flux distribution with respect to radial position at different optical planes

3.3. Methodology

As previously mentioned, the HFSS can be numerically characterized using two techniques. The first technique is based on the forward MCRT method and its implementation for the HFSS system, where an in-house code based on this method has been developed by the author and used. The in-house code has been previously tested on a 7 kW_e HFSS at KU Leuven, Belgium, in [64], where the developed code showed a great agreement with the obtained experimental results. The desired outcome of this method is to obtain the shape of the xenon arc that matches well with the experimental observations, abiding to any relevant physical laws and manufacturer specifications.

Once the shape of the arc is found, it can then be used in implementing the MCRT method in determining the heat flux on any arbitrary shape, as discussed later in Chapter 4. The second technique is to solve the ray tracing inverse problem as defined by the governing equations of the system. The outcome of this method is to determine the intensity distribution of the HFSS at the focal plane and restore the lost direction information from the experimental result. The obtained solution can then be easily used to determine the flux distribution on any shape of interest.

Through the MCRT in-house code, heat flux maps at several optical planes can be generated, where the code keeps track of the directions of all rays. This allows for calculating the intensity distribution at the focal plane to be used as a reference solution. Afterwards, the obtained flux maps can be used by the inverse ray tracing method for validation of the inverse methodology. Once validated, the algorithm can then be used on the experimental results to obtained the intensity distribution, which can also be used as a verification of both solutions. The methodology of both methods is discussed in further details in the upcoming sections of the thesis.

3.3.1. Forward Monte Carlo Ray Tracing

The MCRT method utilizes stochastic sampling to obtain and model independent variables based on statistical models that are derived from relevant physical laws. Therefore, the method depends heavily on probability density functions (PDFs) and the implementation of random numbers. These functions are used to stochastically determine properties of an emerged ray, such as points, directions, and wavelengths of emission, reemission, and/or reflection, in addition to results of events in participating media or when a surface intersection occurs. As aforementioned, the MCRT method uses the PDFs to stochastically emerge a ray from a surface or volumetric radiation source, tracking the history of the ray as it interacts with participating media and system surfaces. The final result of the method can either be the distribution factor D_{ij} or the resulting power distribution, depending on whether surface and other relevant properties are assumed to be constant or are functions of temperature.

Since the methodology of the MCRT method can significantly differ depending on the assumptions and treatments considered, it is vital to begin the methodology section by first describing the assumptions of the model. Then, only the relevant equations and formulations will be covered based on the assumptions followed. The general relations of the MCRT method for radiative heat transfer presented in this section were obtained from [70,71,73]. Further discussion on the methodology of the MCRT method is done in Chapter 4, where the MCRT model has a larger scope of action.

Assumptions. The objective of the MCRT model throughout the scope of this research is to determine the power distribution from the primary radiative source (HFSS) and any surfaces within the system (to be considered in Chapter 4). Therefore, any information about the phase of the light wave is not considered, where only the energy of the wave is tracked. Since the MCRT method depends on stochastic approaches, rays' events follow the Markov chain, where new events are completely independent of all prior ones. The reflection property of the ellipsoidal reflector is independent of temperature and radiation wavelength, and so can be considered to be a gray surface with a constant reflectivity. The surrounding air is treated as a non-participating medium since it is clean and free of any dust particles. Finally, the setup and surrounding surfaces are treated as non-participating, so their re-radiation effects (if any) are neglected. Based on the objective of the MCRT model and the significance of neglected parameters' effects, the above assumptions are valid for the scope of this research.

Fundamentals of MCRT. The variables governing the action of a ray, such as direction of emission, are independent of each other. For example, in a spherical coordinate system, the zenith and azimuth angles defining the direction of the ray are independent. Therefore, a PDF, p, can be formulated for a random variable, γ, based on a frequency function, F, that describes the distribution of the variable obtained from certain properties. The PDF is just a normalized version of F as shown in Eqn. (3-1).

$$p(\gamma) = \frac{F(\gamma)}{\int_{-\infty}^{\infty} F(\gamma)\, \mathrm{d}\gamma} \tag{3-1}$$

Based on Eqn. (3-1), a cumulative PDF, P, can then be constructed by integrating p up to a certain limit. The cumulative PDF then represents the probability that γ would occur within the range of integration. Since $P(\infty) = 1$ and $0 \leq P(\gamma) \leq 1$, the cumulative PDF can be equated to a random number, $\mathfrak{R}$, as shown in Eqn. (3-2).

$$P(\gamma) = \int_{-\infty}^{\gamma} p(\gamma)\, \mathrm{d}\gamma = \mathfrak{R}_{\gamma} \tag{3-2}$$

Through Eqn. (3-2), variables governing the motion of the ray can be determined, as will be presented later in the upcoming sections of the thesis.

Surface Descriptions and Ray Tracing. The surfaces considered in the current MCRT model are the ellipsoidal reflector and the target placed at the focal plane, which is where the global origin of the coordinate system is taken. A detailed schematic of the system is shown in Figure 3-4, where the Cartesian coordinate system is the primary coordinate system used.

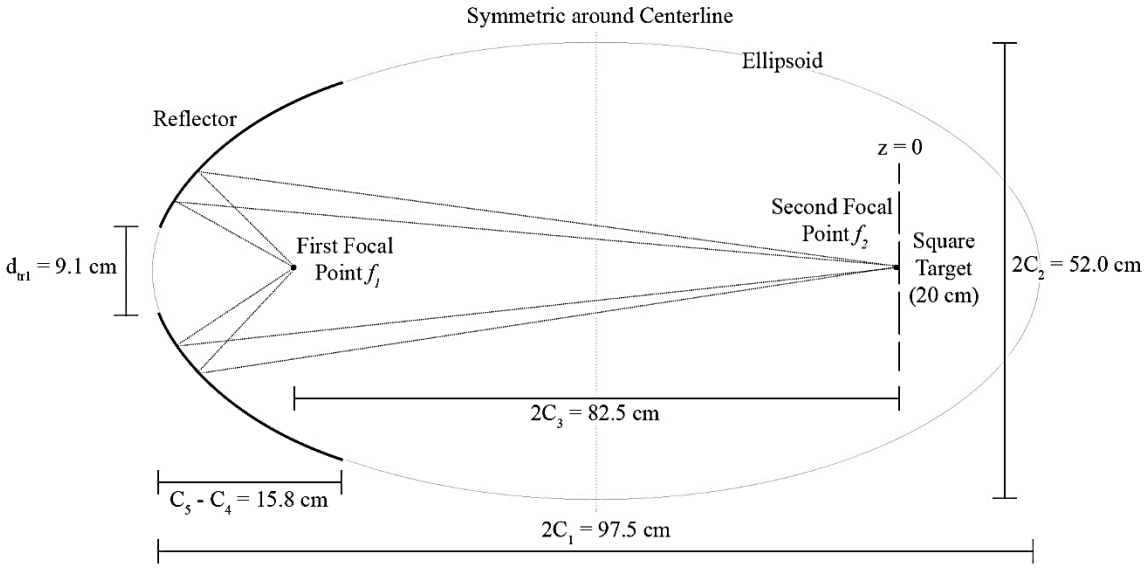

Figure 3-4: Schematic of MCRT system for characterizing the HFSS

As shown in Figure 3-4, both the ellipsoidal reflector and the target are placed centered around the z-axis. Hence, both surfaces can be assumed to be symmetric. Nevertheless, the model of the system cannot be treated to be two-dimensional, as the three-dimensional characteristic would be required for the full MCRT method coupling the heat transfer model as illustrated later in Chapter 4. With that being said, let's proceed by first defining the reflector surface based on the nomenclature defined in Figure 3-4. The surface of the reflector is described as in Eqn. (3-3).

$$\frac{(z+C_3)^2}{C_1^2}+\frac{y^2}{C_2^2}+\frac{x^2}{C_2^2}-1=0 \quad \text{for} \quad C_4 \le z \le C_5 \tag{3-3}$$

where the geometric constants $C_3=(f_2-f_1)/2$, $C_1=C_3+f_1$, $C_2=\sqrt{C_1^2-C_3^2}$, and $C_{4\,\text{or}\,5}=-C_3-\sqrt{C_1^2(1-d_{tr1\,\text{or}\,2}^2/4C_2^2)}$.

Next is the square target placed at the focal plane to intercept radiation from the HFSS and identify the obtained heat flux. The square target has the dimension of 20 cm, and its surface is described as in Eqn. (3-4).

$$z=0 \quad \text{for} \quad -0.1 \le x \le 0.1 \quad \text{and} \quad -0.1 \le y \le 0.1 \tag{3-4}$$

Having the surfaces of interest defined, several characteristics can then be presented, which allow for tracking the rays in the MCRT model. Despite the fact that the geometric configuration of the shapes in the current MCRT model are relatively simple, a systematic way of describing surfaces is much more powerful. Hence, description of surface characteristics in vector form is the most logical approach. The first characteristic that would be very useful is the surface normal. Let's

assume that any surface can be described through its geometric representation in Cartesian coordinates as a function, as shown in Eqn. (3-5).

$$S = S(x, y, z) = 0 \tag{3-5}$$

The unit normal vector, $\hat{\mathbf{n}}$, of surface S is then calculated using Eqn. (3-6).

$$\hat{\mathbf{n}} = \frac{\nabla S}{|\nabla S|} = \frac{\frac{\partial S}{\partial x}\hat{\imath} + \frac{\partial S}{\partial y}\hat{\jmath} + \frac{\partial S}{\partial z}\hat{k}}{\sqrt{\left(\frac{\partial S}{\partial x}\right)^2 + \left(\frac{\partial S}{\partial x}\right)^2 + \left(\frac{\partial S}{\partial x}\right)^2}} \tag{3-6}$$

Once the unit normal vector is defined, two additional unit tangential vectors describing the surface at any point need to be defined. A good approach to choosing the tangential vectors is by having them perpendicular to each other and to the normal vector, following the right-handed coordinate system. Therefore, the two tangential vectors, $\hat{\mathbf{t}}_\mathbf{1}$ and $\hat{\mathbf{t}}_\mathbf{2}$, are calculated using Eqn. (3-7).

$$\hat{\mathbf{t}}_\mathbf{1} \cdot \hat{\mathbf{n}} = 0 \quad \text{and} \quad \hat{\mathbf{t}}_\mathbf{2} = \hat{\mathbf{n}} \times \hat{\mathbf{t}}_\mathbf{1} \tag{3-7}$$

Having the normal and two tangential vectors defined, a unit vector representing the direction of a ray, being emitted or reflected, can be determined through the geometric directional angles. The direction unit vector, $\hat{\mathbf{u}}$, is calculated using Eqn. (3-8).

$$\hat{\mathbf{u}} = \cos\theta\,\hat{\mathbf{n}} + \sin\theta\cos\phi\,\hat{\mathbf{t}}_\mathbf{1} + \sin\theta\sin\phi\,\hat{\mathbf{t}}_\mathbf{2} = u_x\,\hat{\imath} + u_y\,\hat{\jmath} + u_z\,\hat{k} \tag{3-8}$$

Then, the vector representing the path, $\hat{\mathbf{P}}$, of the ray can be determined based on the direction unit vector and the starting position, $\widehat{\mathbf{OP}}$, as shown in Eqn. (3-9) and demonstrated in Figure 3-5.

$$\hat{\mathbf{P}} = \widehat{\mathbf{OP}} + s\hat{\mathbf{u}} = (OP_x + su_x)\,\hat{\imath} + (OP_y + su_y)\,\hat{\jmath} + (OP_y + su_y)\,\hat{k} \tag{3-9}$$

where s is an arbitrary length parameter that is greater than zero and represents the distance traveled, which is to be calculated in order to find the exact path of the ray. With this, all the necessary formulations for tracing a ray has been covered and the MCRT algorithm can be introduced.

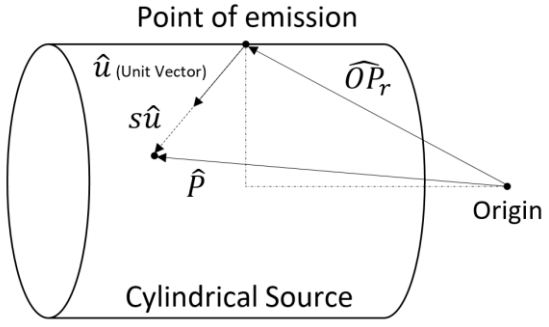

Figure 3-5: Schematic of a ray tracing for the MCRT model

The MCRT algorithm implemented to model the HFSS is illustrated in the form of a flowchart as shown in Figure 3-6. Explanation of the model is discussed in details, where the algorithm is divided into seven sections following the labeling indicated in Figure 3-6.

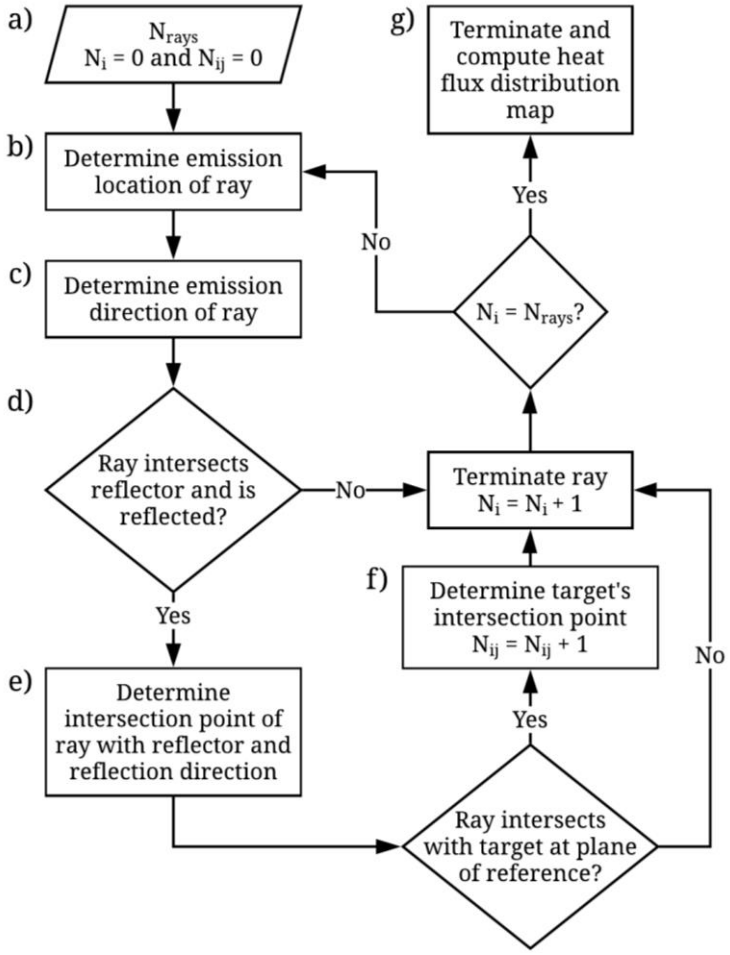

Figure 3-6: Flowchart illustrating the MCRT algorithm used to numerically characterize the HFSS

Initializing the Simulation - MCRT (a). The first step of the MCRT is to equally divide the emitting source into a large number of rays, N_{rays}, and to initialize the counters, N_i and N_{ij}, by equating them to zero. The aforementioned counters represent the current count of rays emitted by the source and that intersected the target's i'th and j'th element at the focal plane in the x and y directions. The total number of rays to be used depends on the computational time and accuracy required. A value of at least 10,000 multiplied by the number of surfaces in the analysis is generally recommended [71]. However, a convergence analysis should always be performed to ensure that the results converge to an acceptable accuracy. The value of N_{rays} will be presented later in the Results and Discussion section, with the corresponding convergence plot.

In addition to initializing the counters, system properties also need to be defined, including dimensions, electrical power of the xenon arc, electrical conversion efficiency of the HFSS, and surface properties such as reflectivity and imperfections. The electrical power of the bulb is 10 kW_e for an input current of 200 A, while its electrical efficiency was assumed to be 0.5, based on efficiency values normally used in literature for similar setups [52,68,69]. The reflectivity of the reflector and its surface imperfection were assumed in a similar manner, while ensuring that the assumed values provided results that are in an acceptable agreement with the obtained experimental results. The assumed values for these properties will be covered in the upcoming sections.

Determining Emission Location of Ray – MCRT (b). Determining the location of emission of a ray depends on the assumed shape of the xenon arc. The arc has been previously modeled in literature as a cylindrical volume, which is mainly based on manufacturer's specifications [52,81]. However, it was illustrated that the arc cannot be accurately defined and modeled by a single emitting shape, whether it is a sphere or a cylinder. A concentric multilayer model of the arc that incorporates both of the previously stated geometries is capable of capturing the complex characteristics of the arc [82]. Therefore, based on the results shown in [82], a combination of a hemisphere and a cylinder with different dimensions attached to each other was previously used by the author in [64] to model a 7 kW_e HFSS. The results obtained using this arrangement matched very well with the obtained experimental data, as was thoroughly validated in [64]. Therefore, the same arrangement was extended and used to model the current 10 kW_e HFSS, with the dimensions of the two shapes in addition to the power distributed among them being different.

In this study, the xenon arc is assumed to be a hemisphere that is centered at the first focal point and attached to a cylinder. The initial dimensions of the shape were based on the manufacturer's specifications for the dimension of the arc and its luminance intensity distribution. Then, the final dimensions were tuned while keeping the arc length relatively the same to properly fit the experimental heat flux distribution obtained across the focal plane as well as other optical planes captured. In addition, the power distribution across the two shapes was the major parameter to be modified in order to provide the best agreement with the experimental distribution and peak flux as well as the total power values. After tuning, the bulb is modeled as an isotropic volumetric source which consists of a hemisphere of 1 mm radius that is attached to a cylinder of 1 mm in radius and 10 mm in length with a power ratio between the two shapes of 0.23:0.77, respectively.

Since the xenon arc is assumed to be an isotropic volumetric shape, the ray would have an equal chance of being emitted from a location across the volume. Considering the cylindrical shape

of the arc first, the location of emission is best determined in cylindrical coordinates. This location is governed through Eqns. (3-10) – (3-12).

$$\Re_r = \frac{\int_0^{2\pi}\int_{z_{min}}^{z_{max}}\int_{r_{min}}^{r} \varepsilon\sigma T^4\, r\, \mathrm{d}r\, \mathrm{d}z\, \mathrm{d}\phi}{\int_0^{2\pi}\int_{z_{min}}^{z_{max}}\int_{r_{min}}^{r_{max}} \varepsilon\sigma T^4\, r\, \mathrm{d}r\, \mathrm{d}z\, \mathrm{d}\phi} = \frac{r^2 - r_{min}^2}{r_{max}^2 - r_{min}^2} \tag{3-10}$$

$$\Re_\phi = \frac{\int_{z_{min}}^{z_{max}}\int_{r_{min}}^{r_{max}}\int_0^{\phi} \varepsilon\sigma T^4\, \mathrm{d}\phi\, r\, \mathrm{d}r\, \mathrm{d}z}{\int_{z_{min}}^{z_{max}}\int_{r_{min}}^{r_{max}}\int_0^{2\pi} \varepsilon\sigma T^4\, \mathrm{d}\phi\, r\, \mathrm{d}r\, \mathrm{d}z} = \frac{\phi}{2\pi} \tag{3-11}$$

$$\Re_z = \frac{\int_0^{2\pi}\int_{r_{min}}^{r_{max}}\int_{z_{min}}^{z} \varepsilon\sigma T^4\, \mathrm{d}z\, r\, \mathrm{d}r\, \mathrm{d}\phi}{\int_0^{2\pi}\int_{r_{min}}^{r_{max}}\int_{z_{min}}^{z_{max}} \varepsilon\sigma T^4\, \mathrm{d}z\, r\, \mathrm{d}r\, \mathrm{d}\phi} = \frac{z - z_{min}}{z_{max} - z_{min}} \tag{3-12}$$

Where r_{min} is zero (but shown for completeness and future reference), r_{max} is the outer radius of the cylinder, and z_{max} and z_{min} represent the length of the cylinder. Eqns. (3-10) – (3-12) can then be rearranged to determine the location of emission in the three dimensional coordinate system (r, ϕ, z), where the corresponding position in Cartesian coordinates can then be obtained.

Now considering the spherical shape of the arc, the location of emission is best determined in spherical coordinates. This location is governed through Eqns. (3-13) – (3-15).

$$\Re_r = \frac{\int_0^{2\pi}\int_0^{\pi}\int_0^{r} \varepsilon\sigma T^4\, r^2\, \mathrm{d}r \sin\theta\, \mathrm{d}\theta\, \mathrm{d}\phi}{\int_0^{2\pi}\int_0^{\pi}\int_0^{r_{max}} \varepsilon\sigma T^4\, r^2\, \mathrm{d}r \sin\theta\, \mathrm{d}\theta\, \mathrm{d}\phi} = \frac{r^3}{r_{max}^3} \tag{3-13}$$

$$\Re_\theta = \frac{\int_0^{2\pi}\int_0^{r_{max}}\int_0^{\theta} \varepsilon\sigma T^4 \sin\theta\, \mathrm{d}\theta\, r^2\, \mathrm{d}r\, \mathrm{d}\phi}{\int_0^{2\pi}\int_0^{r_{max}}\int_0^{\pi} \varepsilon\sigma T^4 \sin\theta\, \mathrm{d}\theta\, r^2\, \mathrm{d}r\, \mathrm{d}\phi} = \frac{1 - \cos\theta}{2} \tag{3-14}$$

$$\Re_\phi = \frac{\int_0^{\pi}\int_0^{r_{max}}\int_0^{\phi} \varepsilon\sigma T^4\, \mathrm{d}\phi\, r^2\, \mathrm{d}r \sin\theta\, \mathrm{d}\theta}{\int_0^{\pi}\int_0^{r_{max}}\int_0^{2\pi} \varepsilon\sigma T^4\, \mathrm{d}\phi\, r^2\, \mathrm{d}r \sin\theta\, \mathrm{d}\theta} = \frac{\phi}{2\pi} \tag{3-15}$$

Where r_{min} is eliminated for clarity and r_{max} is the outer radius of the sphere. Eqns. (3-13) – (3-15) can then be used in a similar manner as presented for Eqns. (3-10) – (3-12).

Determining Emission Direction of Ray – MCRT (c). The direction of emission from a gray isotropic volume is best determined in spherical coordinates. This is performed using the previously obtained relationships presented in Eqns. (3-14) and (3-15), for the zenith and azimuth angles. Once the angles of emission are obtained, the direction unit vector in Cartesian coordinates can be easily found and the path of the ray is determined using Eqn. (3-9) along with the emission location determined in step (b). When evaluating θ, it is important to ensure that its value lies within the luminance intensity distribution provided by the manufacturer. For this, the rejection method was applied to θ to remain within the minimum and maximum values identified by the manufacturer,

which correspond to values of 40° and 160°. Any θ values that do not lie within this range are rejected.

Determining Intersection with and Reflection from Reflector – MCRT (d). The previously determined path of the ray will be used along with the equation of the ellipsoidal surface (or any surface of interest) to obtain an analytical expression of the length parameter s in Eqn. (3-9). This is done by substituting Eqn. (3-9) into the equation of the surface, Eqn. (3-3), to obtain Eqn. (3-16).

$$\frac{(OP_x + su_x)^2}{C_2^2} + \frac{\left(OP_y + su_y\right)^2}{C_2^2} + \frac{(OP_z + su_z + C_3)^2}{C_1^2} - 1 = 0 \tag{3-16}$$

Expanding Eqn. (3-16) and collecting the s terms together gives Eqn. (3-17), which is a quadratic equation to be solved in order to determine the distance parameter.

$$\begin{aligned} s^2\left(u_x^2/C_2^2 + u_y^2/C_2^2 + u_z^2/C_1^2\right) + s\left(2OP_x u_x/C_2^2 + 2OP_y u_y/C_2^2 + 2OP_z u_z/C_1^2 + 2u_z C_3/C_1^2\right) \\ + \left(OP_x^2/C_2^2 + OP_y^2/C_2^2 + OP_z^2/C_1^2 + 2OP_z C_3/C_1^2 + C_3^2/C_1^2 - 1\right) = 0 \end{aligned} \tag{3-17}$$

If a real positive value of s can be determined, then the ray intersects the ellipsoid. The determined s value will be substituted back in Eqn. (3-9) to obtain the exact location of intersection with the ellipsoid. If the z-coordinate of the intersection location lies within C_4 and C_5, then the ray intersects the reflector. If neither of the solutions of s are real positive values or the z-coordinate does not lie within the truncated range, then the ray does not intersect with the reflector and is deemed lost, where its history is terminated and the ray counter is incremented by one.

If the ray intersects the ellipsoidal reflector, it can either be reflected or absorbed. To determine if reflection occurs, a random number, $\Re_\varrho$, is generated and compared to the reflectivity of the surface, ϱ. The value of ϱ for the ellipsoidal reflector is assumed to be 0.9. If $\Re_\varrho \leq \varrho$, the ray is deemed to be reflected, and the analysis proceeds to step (e). Otherwise, the ray is lost, its history is terminated, and the ray counter is incremented by one.

Determining Reflection Direction from Reflector – MCRT (e). Determining the reflection direction from a reflector is different than determining the direction of emission of a ray or that reflected diffusely, as will be covered in Chapter 4. For the ellipsoidal reflector, the law of reflection is implemented. The reflected direction, $\hat{\mathbf{u}}_\mathbf{r}$, of an ideal surface is shown in Eqn. (3-18).

$$\hat{\mathbf{u}}_\mathbf{r} = \hat{\mathbf{u}}_\mathbf{in} - 2\hat{\mathbf{n}}(\hat{\mathbf{u}}_\mathbf{in} \cdot \hat{\mathbf{n}}) \tag{3-18}$$

Since the law of reflection assumes that surfaces are ideal, the law must be modified to accurately represent real surfaces. This is performed through the introduction of a specular error in the form of a deviating zenith angle, θ_{se} [52]. This angle is illustrated in Figure 3-7, where the real (modified) surface normal, $\hat{\mathbf{n}}'$, is calculated based on Eqn. (3-8). Since a deviating zenith angle is

introduced, an azimuth angle, ϕ_{se}, needs to accompany it to fully define the real normal as shown in Eqn. (3-19).

$$\hat{\mathbf{n}}' = \cos\theta_{se}\,\hat{\mathbf{n}} + \sin\theta_{se}\cos\phi_{se}\,\hat{\mathbf{t}}_{\mathbf{1}} + \sin\theta_{se}\sin\phi_{se}\,\hat{\mathbf{t}}_{\mathbf{2}} \tag{3-19}$$

where values of θ_{se} have a Gaussian distribution with a mean value of zero and a standard deviation of 5 mrad, while values of ϕ_{se} have a uniform distribution calculated using Eqn. (3-15). Once the real normal is obtained using Eqn. (3-19), the direction of the ray can be calculated by substituting the real normal back in Eqn. (3-18).

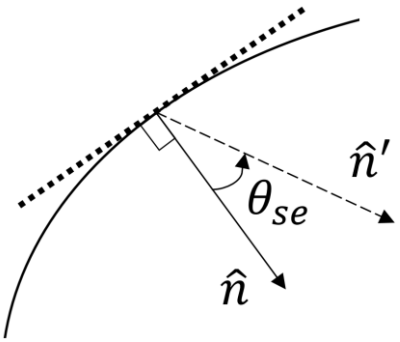

Figure 3-7: Illustrative diagram of specular error in real reflective surfaces

Determining Intersection with Target – MCRT (f). Determining the intersection with the target at the focal plane is performed in a similar manner as that described earlier for the ellipsoidal reflector. However, since the target has a much simpler geometry (is a vertical plane), the length parameter s can be easily determined by equating the z-component of Eqn. (3-9) with the z-position of the target (z = 0). Using s, the exact location of intersection is obtained and it is then determined if the ray intersects the range of the target, and at which discretized element it intersects. Since the target is really just an imaginary surface, it is assumed to be a blackbody. Therefore, if the ray intersects the target, it is always absorbed, the counters N_i and N_{ij} are incremented by one, and the history of the ray is terminated.

Looping and Terminating the Algorithm – MCRT (g). Once the history of a ray has been terminated and it has been deemed as absorbed or lost, the algorithm moves to the next ray. The algorithm shown in Figure 3-6 will terminate once the number of emitted rays reaches the desired number of rays to be emitted. Another approach is to terminate the algorithm once the maximum percentage change (tolerance) reaches a desired value. Both of these approaches are satisfactory when care is taken to evaluate the convergence of the power distribution along the target. Once the algorithm has been terminated, the heat flux distribution is obtained by multiplying N_{ij} by the power of each ray, $\dot{Q}_{ray}$, and then dividing by the area of each discrete element of the target.

It should finally be noted that the MCRT in-house code is capable of computing the intensity distribution at the focal plane. This is achieved by keeping track of θ and ϕ as a ray intersects a specific element on the target. The values of θ and ϕ can be recorded in their raw form, or divided up into further discrete elements in both angular directions and recorded through the use of counters. Since the number of rays emitted is in the order of millions, the second approach is followed for lower memory usage.

3.3.2. Inverse Ray Tracing

Inverse Problem Formulation. By having the heat flux distribution obtained at different optical planes, the flux maps can be used in an attempt to restore the lost directional information. The method investigated here follows the method that was first described in [68] for a general three-dimensional case. A schematic illustration of an incoming ray from the HFSS that passes through the focal plane at z_0 and other parallel planes in the z-direction is shown in Figure 3-8. Once a ray originates from the HFSS and passes through and beyond the focal plane, it travels through air that can be safely assumed to be a non-participating medium. Therefore, the intensity, I, remains constant in a straight path along any direction. With the intensity at the focal plane being I_0, which is constant along a straight path in a given θ and ϕ, the intensity at any plane can be projected and traced back to I_0. Following the coordinate notation illustrated in Figure 3-8, the intensity can be written as shown in Eqn. (3-20).

$$I(x, y, z, \theta, \phi) = I_0(x_0, y_0, \theta, \phi) = I_0(x + z\ \cos\phi \tan\theta\ , y + z\ \sin\phi \tan\theta\ , \theta, \phi) \tag{3-20}$$

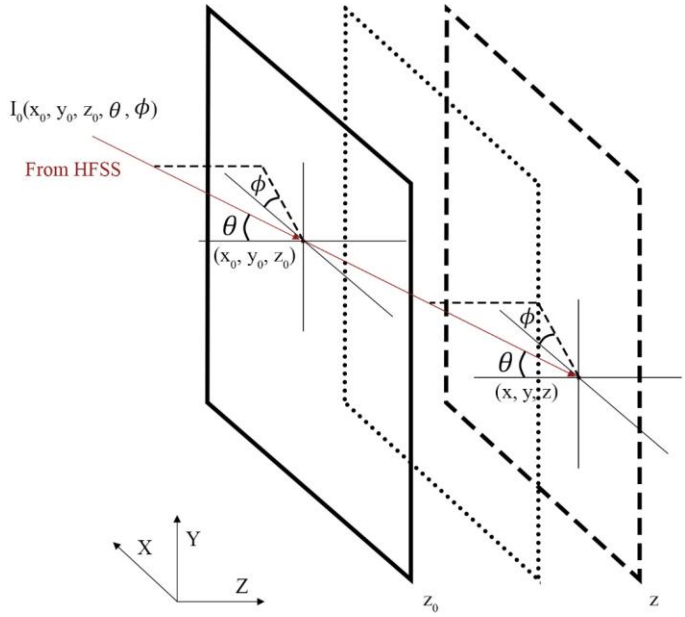

Figure 3-8: Schematic illustration of ray from HFSS passing through optical planes

The flux density, q'', at any position and plane can then be obtained by integrating the radiative intensity over the hemisphere, as shown in Eqn. (3-21).

$$q''(x,y,z) = \int_{\phi=0}^{2\pi} \int_{\theta=0}^{\pi/2} I(x,y,z,\theta,\phi) \cos\theta \sin\theta \, \mathrm{d}\theta \, \mathrm{d}\phi \tag{3-21}$$

By substituting the expression obtained in Eqn. (3-20) into Eqn. (3-21), the flux density expressed in terms of I_0 only can be written as Eqn. (3-22).

$$q''(x,y,z) = \int_{\phi=0}^{2\pi} \int_{\theta=0}^{\pi/2} I_0(x + z\ \cos\phi \tan\theta\ , y + \ z\ \sin\phi \tan\theta\ , \theta, \phi) \cos\theta \sin\theta \, \mathrm{d}\theta \, \mathrm{d}\phi \tag{3-22}$$

Eqn. (3-22) then needs to be solved by discretizing the system at hand. A square target at any given plane of side length of L will be discretized into N_x and N_y elements with Δx and Δy increments in the x and y planar directions (within a plane). The intensity and flux density will then be a function of these planar coordinates in addition to the optical position, which is discretized into N_z elements with Δz increment in the z direction (across captured planes). The intensity at any position is then further discretized into N_θ and N_ϕ elements with $\Delta\theta$ and $\Delta\phi$ increments in the zenith and azimuth directions. The radiative flux density at any location can then be represented as in Eqn. (3-23). The intensity can also be discretized in a similar manner in terms of i, j, k, m, and n, representing the position coordinates and the zenith and azimuth angles.

$$q''(x,y,z) = q''_{i,j,k} = q''\left(x_{ref} + i\,\Delta x, y_{ref} + j\,\Delta y, z_{ref} + k\,\Delta z\right) \tag{3-23}$$

Since the planar coordinates will now be regarded as discrete points ijk, tracing back the intensity in a given direction to the plane of reference (focal plane) will provide continuous coordinates x_0 and y_0 as defined in Eqn. (3-20). Therefore, an interpolation scheme will be required to obtain a value for $I_{i,j,k,m,n}$. The interpolation scheme can be of zeroth-order (rounding to the nearest position) or of first-order as previously used in [68] and [69], where the intensity value at the focal plane will be linearly interpolated from its four neighboring discrete points. In the case of a zeroth-order interpolation, Eqn. (3-22) will be discretized as shown in Eqns. (3-24) and (3-25), where $\hat{\imath}$ and $\hat{\jmath}$ represent the nearest point at z_0.

$$q''_{i,j,k} = \sum_{m,n=1}^{N_\theta, N_\phi} \left[I_{0,\hat{\imath},\hat{\jmath},m,n}\right] \cos\theta_m \sin\theta_m \, \Delta\theta \, \Delta\phi \tag{3-24}$$

and

$$\hat{\imath} = \mathrm{round}\left(\frac{x_0 - x_{ref}}{\Delta x}\right) \quad \text{and} \quad \hat{\jmath} = \mathrm{round}\left(\frac{y_0 - y_{ref}}{\Delta y}\right) \tag{3-25}$$

However, in the case of a linear interpolation, the four neighboring intensity values will be linearly distributed according to two weighing factors, W_x and W_y, in the x and y directions. This is shown in Eqns. (3-26)-(3-28), where $x_{\hat{\imath}} \le x_0 \le x_{\hat{\imath}+1}$ and $y_{\hat{\jmath}} \le y_0 \le y_{\hat{\jmath}+1}$.

$$q''_{i,j,k} = \sum_{m,n=1}^{N_\theta, N_\phi} \begin{bmatrix} W_x\, W_y\, I_{0,\hat{\imath}+1,\hat{\jmath}+1,m,n} + (1-W_x) W_y\, I_{0,\hat{\imath},\hat{\jmath}+1,m,n} \\ +W_x(1-W_y)\, I_{0,\hat{\imath}+1,\hat{\jmath},m,n} \\ +(1-W_x)(1-W_y)\, I_{0,\hat{\imath},\hat{\jmath},m,n} \end{bmatrix} \cos\theta_m \sin\theta_m\, \Delta\theta\, \Delta\phi \tag{3-26}$$

and

$$\hat{\imath} = \text{floor}\left(\frac{x_0 - x_{ref}}{\Delta x}\right) \quad \text{and} \quad \hat{\jmath} = \text{floor}\left(\frac{y_0 - y_{ref}}{\Delta y}\right) \tag{3-27}$$

and

$$W_x = \frac{x_0 - x_{\hat{\imath}}}{\Delta x} \quad \text{and} \quad W_y = \frac{y_0 - y_{\hat{\jmath}}}{\Delta y} \tag{3-28}$$

Depending on the interpolation scheme of choice, Eqn. (3-24) or (3-26) can be represented as a linear SoEs of the form $\mathbf{Q} = \mathbf{A}\,\mathbf{I_0}$, where $\mathbf{Q}$ represents the measured/known collection of radiative flux densities at the discrete planar positions, $\mathbf{A}$ represents the linear operator that maps $\mathbf{I_0}$ to $\mathbf{Q}$, and $\mathbf{I_0}$ represents the intensity at the focal plane. Thus, $\mathbf{Q}$ is a column vector of size $M = N_x\, N_y\, N_z$, $\mathbf{I_0}$ is a column vector of size $N = N_x\, N_y\, N_\theta\, N_\phi$, while $\mathbf{A}$ is of size $M \times N$.

Inverse Problem Solution Strategy. The linear SoEs formulated earlier is a discrete ill-posed type of problem. The challenge here rises due to the nature of the problem, where the problem is usually an underdetermined one, and the number of predictors is of equal or larger order of magnitude than the number of measured samples; it would be impractical to capture optical planes of a greater order of magnitude than that of solid angle combinations. For such problems, the SoEs need to be regularized to provide a useful solution rather than overfitting the measured samples. Regularization techniques include Tikhonov regularization, where the zeroth-order regularization is commonly implemented to decrease the norm of $\mathbf{I_0}$ to obtain a solution that has sufficient complexity to adequately fit the measurements, and with the least noise amplification [80]. The first or second order of Tikhonov regularization can also be implemented to obtain a solution with a bias towards a flat or smooth solution, respectively. Other solution methods implement solution constraints such as non-negative, equality, and inequality constraints. In the case of implementing one of the aforementioned constraints, regularizing the SoEs might not be of great importance, as was studied in [83].

The problem formulated in Eqns. (3-26)-(3-28) was previously studied and solved in [69] for three test cases and a case based on experimental measurements obtained from EPFL's HFSS introduced in Chapter 2, while implementing a zeroth-order Tikhonov regularization and different

unconstrained solvers. The test cases were with reference intensities of (a) uniform distribution, (b) Gaussian distribution, and (c) uniform angular distribution. The model performed satisfactory for the test cases but unsatisfactory for the experimental one. This can be attributed to two main reasons: the number of targets used for the test cases was much greater, and the gradient of the intensity distribution for the experimental case was larger. In addition, it was concluded that the center "black spot" in the intensity distribution due to the truncated reflector was not resolved in the inverse solution of the experimental case [69].

When regularizing a SoEs, a roughening matrix, **L**, and a regularization parameter α are used. The regularized SoEs is then formulated as in Eqn. (3-29).

$$\begin{bmatrix}\mathbf{Q}\\ \mathbf{0}\end{bmatrix} = \begin{bmatrix}\mathbf{A}\\ \alpha_{T\,p}\,\mathbf{L_{T\,p}}\end{bmatrix}\mathbf{I_0} \tag{3-29}$$

where the subscript T denotes the order of the Tikhonov regularization and p denotes the specific parameter that is to be regularized (x, y, θ, ϕ). In the case of implementing the zeroth-order regularization, the roughening matrix will be referred to as $\mathbf{L_0}$. The roughening matrix $\mathbf{L_0}$ is defined as an identity matrix, $\mathbf{L_{1\,p}}$ as a finite difference approximation of the first-order derivative, and $\mathbf{L_{2\,p}}$ as the second order derivative approximation of **A** in the parameter's direction. The linear SoEs can then be stated as a minimization problem as given by Eqn. (3-30), where $\| \|_2$ represents the Euclidean norm.

$$\min\left(\|\mathbf{A}\mathbf{I_0} - \mathbf{Q}\|_2^2 + \alpha_{T\,p}^2 \left\|\mathbf{L_{T\,p}}\mathbf{I_0}\right\|_2^2\right) \tag{3-30}$$

In the case of using a nonnegative least squares (NNLS) solver, such as that defined by Lawson and Hanson in [84], Eqn. (3-30) can then be restated as Eqn. (3-31).

$$\begin{gathered}\min\left(\|\mathbf{A}\mathbf{I_0} - \mathbf{Q}\|_2^2 + \alpha_{T\,p}^2 \left\|\mathbf{L_{T\,p}}\mathbf{I_0}\right\|_2^2\right)\\ \text{subject to } \mathbf{I_0} \geq \mathbf{0}\end{gathered} \tag{3-31}$$

When solving a discrete ill-posed problem even under regularization and a nonnegative inequality constraint, solutions may still arise that do not reflect the actual system at hand, especially when having a relatively low N_z value. Such solutions include intensity values at the solution plane and solid angles that do not trace back to the reflector, such as the "black spot" region previously discussed. In an attempt to eliminate these solutions and improve the accuracy of the obtained solution, the in-house code developed also traced back the points in the solution plane, depending on the discrete points and angles chosen, to determine whether they can be traced back to the ellipsoidal reflector. The reflector is defined as in Eqn. (3-3) previously introduced.

This inverse tracing portion of the code then generates matrix $\mathbf{A_{eq}}$ that is sparse and contains only ones at the locations corresponding to $I_{0,i,j,m,n}$ that do not trace back to the reflector. Then by implementing an equality constraint, the linear SoEs then become more well-defined, and Eqn. (3-31) can be restated as Eqn. (3-32).

$$\begin{gathered}\min\left(\|\mathbf{AI_0}-\mathbf{Q}\|_2^2+\alpha_{T\,p}^2\left\|\mathbf{L_{T\,p}I_0}\right\|_2^2\right)\\ \text{subject to } \mathbf{I_0}\geq\mathbf{0} \text{ and } \mathbf{A_{eq}I_0}=\mathbf{0}\end{gathered} \tag{3-32}$$

Due to the complexity of coding constrained least squares solvers with respect to other unconstrained ones, MATLAB's built-in function *lsqlin* was used to solve Eqns. (3-31) and (3-32). The solution algorithm used is "Interior-Point" algorithm since it supports sparse matrices. The algorithm is an iterative solver based on the interior-reflective Newton method described in [85]. It is important to note that the built-in function does not have a regularizing effect on its own as part of its solution strategy [86]. However, in the case of minimizing constrained objective functions, the solver implements the use of Lagrange multipliers in order to ensure that the local minima are within the set constraints. In an attempt to very this, the direct SVD method as described in [80] and used in [69] to solve an unconstrained SoEs was used here to solve the current unconstrained SoEs, where the results obtained were comparable to that obtained using *lsqlin*.

To obtain a solution for the intensity at the focal plane for validating the methodology, the in-house developed MCRT code was used to model the HFSS's distribution at different optical planes. The code was used to generate the heat flux distribution at the planes of interest, which represent the planes that were experimentally captured. In addition, the code also kept track of the direction of all the rays, as previously mentioned, which allows for calculating the intensity distribution at any position on the focal plane to be used as a reference solution to that of the experimental data and to provide a validation case for the solution methodology implemented.

3.4. Results and Discussion

3.4.1. Validation and Results: Forward Monte Carlo Ray Tracing

The first step of validating the model is to ensure that the number of rays emitted during the MCRT simulation is of a satisfactory magnitude and provides an acceptable accuracy. This initial step is of great importance in MCRT methods since convergence issues play a significant role. For this, the relative change of the heat flux value of each element is monitored to ensure that the maximum relative change in any of the flux values is less than 1%. A maximum value of 1% actually provides heat flux values at a relatively high accuracy and repeatability, since discrete

elements with high relative changes are those far away from the center of the target. Therefore, their heat flux values are relatively low, leading to 1% tolerances for these elements being very reasonable. A tolerance value less than 1% leads to a significant increase in the required computational time.

Throughout the entire simulation, the heat flux values were continuously calculated and updated after each iteration of the algorithm. Once the simulation ends, the normalized heat flux values are calculated based on the final flux values obtained. Therefore, illustrating the progression of the power distribution at each position, which ultimately should converge smoothly to unity. Figure 3-9 shows the normalized heat flux values w.r.t. the number of rays emitted from the xenon arc for the (a) spherical and (b) cylindrical volumetric sources. The value of N_{rays} used for the entire source is 1x10^9 rays, which is the total number of rays for both sources combined. The aforementioned N_{rays} value might seem significantly large, but it was required due to using a fine mesh on the target placed at the focal plane to obtain an accurate representation of the heat flux distribution and its high gradients. The discrete element size used was a square element with side lengths of 0.25 mm.

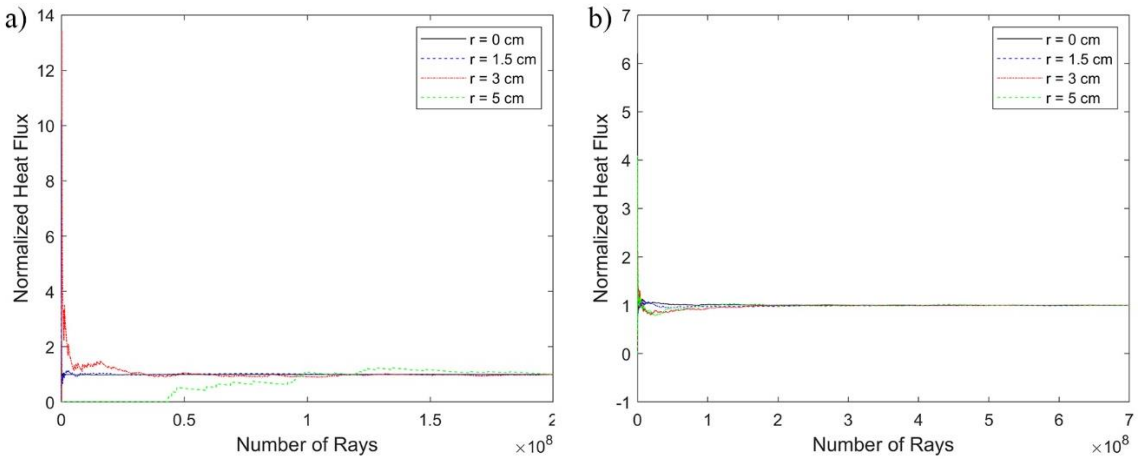

Figure 3-9: Convergence of normalized flux values on target's center from (a) Spherical, and (b) Cylindrical sources

Figure 3-9 shows the successful convergence of the heat flux values for four different elements on the target, having different radii of 0, 1.5, 3, and 5 cm from the center of the target. As can be seen in Figure 3-9, the elements closer to the center of the target (at 0 and 1.5 cm radius) converged much faster than those further away. As discussed previously, the closer elements have values with higher flux magnitudes, and so are the ones of most importance and effect on the accuracy of the simulation. With that being said, a value of 1x10^9 rays for N_{rays} has been deemed accurate enough for any MCRT simulation of the xenon arc at a target with discrete square element size of 0.25 mm.

The heat flux distribution obtained from the MCRT simulation at the focal plane and input current of 200 A is shown in Figure 3-10 (a). In addition, the peak flux and total power values on a 10 x 10 cm^2 target across the different experimentally obtained optical planes are shown in Figure 3-10 (b) and (c). As can be seen from Figure 3-10, the model of the xenon arc properly exhibits the same behavior as that experimentally measured in terms of heat flux distribution, power, density, and their rate of change across different optical positions. The major difference between the modeled and experimental flux distribution, shown earlier in Figure 3-2 (a), is that the modeled one is completely symmetric as opposed to the presence of slightly unsymmetrical behaviors in the experimental one, which is to be expected. This will be discussed further in the upcoming section of the thesis.

The modeled heat flux distribution at the focal plane can closely be described by a Lorentzian distribution, as was previously mentioned in Chapter 2. The modeled distribution at an input current of 200 A has a peak flux density of 6.985 MWm^{-2} and a total power on a 10 x 10 cm^2 target of 3.531 kW, as opposed to 6.99 MWm^{-2} and 3.49 kW for the experimentally obtained flux distribution. This leads to percentage errors of 0.07 and 1.17% for both the peak flux and total power values. In addition, the half width of the modeled distribution is 6.25 mm and its half power is 18.25 mm as opposed to the previously calculated experimental values of 6.25 and 18 mm. Readers are referred to Chapter 2 for more details on the experimental heat flux distribution and its characteristics.

Based on the aforementioned discussion of the flux's modeled and experimental characteristics in addition to the results shown in Figure 3-10, the source's proposed and used shape combination can be used to accurately model the xenon arc and its heat flux distribution at different optical planes. In addition, it will be used to obtain the intensity distribution as a reference solution to that obtained experimentally using the inverse ray tracing later in this section.

So far, the validation has been only performed for the maximum input power at the focal plane as well as the 12 other planes that were obtained experimentally. In order to compare the xenon arc model further, a two-dimensional heat flux distribution along the center of the target is plotted and shown in Figure 3-11. This is plotted for the maximum input current value of 200 A, an intermediate value of 160 A, and the minimum characterized value of 120 A. Since the heat flux distribution is taken along the center of the target, Figure 3-11 also shows a comparison of the maximum heat flux obtained from the model verses that experimentally measured.

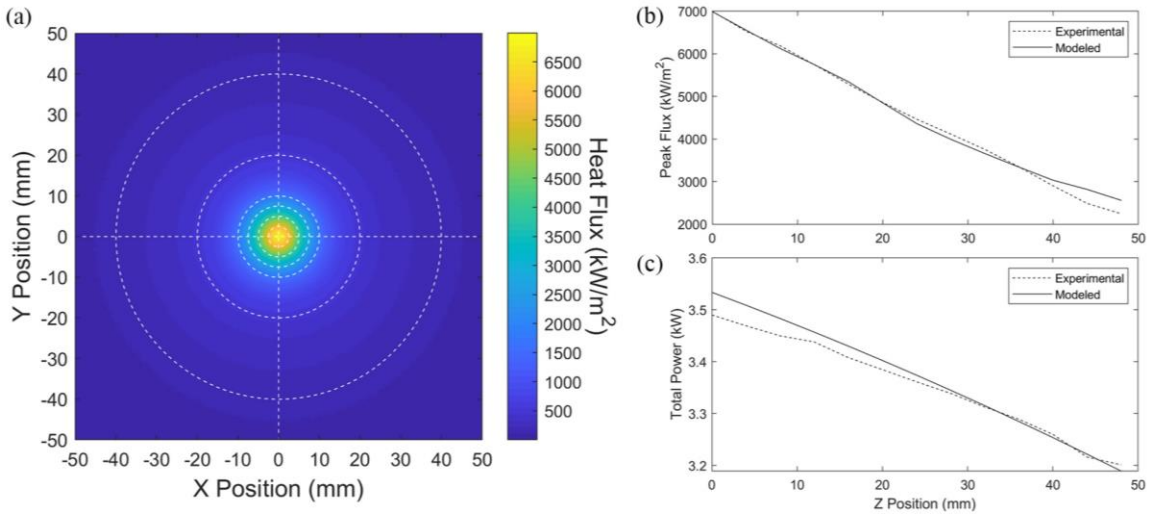

Figure 3-10: (a) Modeled heat flux map at focal plane, and comparison between experimentally measured and modeled maps for (b) peak flux and (c) total power on a 10 x 10 cm^2 target

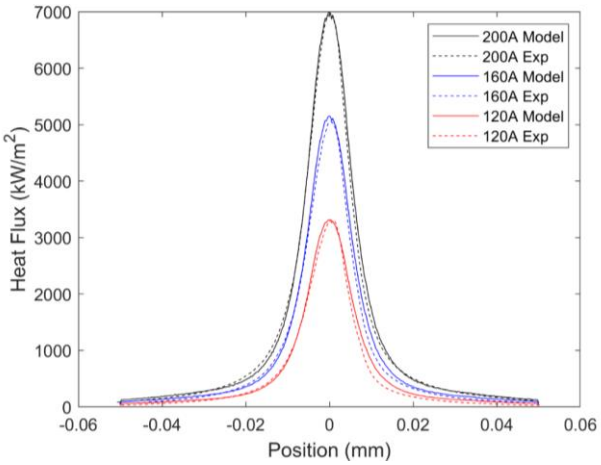

Figure 3-11: Two-dimensional heat flux distribution at focal plane and target center for 3 different current values

Comparing the experimental and modeled heat flux distributions in Figure 3-10 (a) and Figure 3-11, it can be noticed that the experimental distribution is not quite as symmetric as expected, or as the modeled distribution. The experimental contour is slightly distorted and deformed, which is a behavior often reported for the characterization of solar simulators in previous studies [35,42,82]. There are several potential reasons for this slightly distorted shape, which include: the angled position of the CMOS camera, minor alignment errors or shape distortions within the ellipsoidal reflector and solar simulator, and asymmetries in the arc.

In evaluating the total electrical power available at the xenon arc, and hence the power of each ray emitted by the MCRT simulation, the relationship obtained previously in Chapter 2 for the peak flux values w.r.t. the input current is used. The relationship of the peak flux values was used rather

than the total power since it provides higher accuracies. This is due to the fact that it does not incorporate the portion of the target with relatively low flux values, where the percentage uncertainty in these measurements is significantly higher than that of the peak flux due to the grayscale correlation and resolution of the CMOS camera. This gives Eqn. (3-33) that is to be used for determining the available electrical power at the xenon arc, $\dot{Q}_{arc}$, in Watts, with an input current of 200 A representing the rated power of 10 kW_e for the bulb.

$$\dot{Q}_{arc} = \frac{45.039\ Amp - 2128.1}{6879.7} \times 10^4 \tag{3-33}$$

From Figure 3-11, the maximum heat flux ranges from 6.985 to 3.315 MWm^{-2} for the model, while the total power intercepted at the focal plane ranges from 3.531 to 1.680 kW for an input current that ranges from 200 to 120 A. In comparison with the experimentally obtained values, these range from 6.99 to 3.31 MWm^{-2} and from 3.49 to 1.49 kW, respectively. The largest relative error is at the lowest input current value of 120 A, where the total power on a 10 x 10 cm^2 target is off by approximately 12%. This can be attributed to the significantly higher percentage uncertainties in the heat flux values, which are amplified when converted into power values. Therefore, the MCRT model can now be claimed to be validated and accurate for use, resulting in the radiation source being well-simulated.

3.4.2. Validation and Results: Inverse Ray Tracing

For the validation case of the inverse ray tracing method, 13 flux maps were obtained through the MCRT code at the same optical planes as those obtained experimentally. These maps were then used for solving the linear SoEs identified earlier in the Methodology section, and the solution for the intensity at the focal plane found was compared to that obtained from the MCRT code.

It was noticed that attempting to solve the SoEs presented by Eqn. (3-29) using 13 targets and unconstrained least squares in-house solvers with or without regularization did not provide useful results using both interpolation schemes. The intensity distribution obtained did not match the reference solution and in most cases had negative intensity values. This was mostly the case with using different kinds of roughening matrices and values of regularization parameters, where the solution obtained had at least one negative value. The only condition for which negative values were eliminated was by using relatively large values of $\alpha_{T\,p}$, where the solution suffered from great residual norms and errors. Roughening matrices used were of zeroth, first, and/or second order, in order to impose some system characteristics, such as symmetry or flatness ($\mathbf{L_{1\,p}}$), smoothness ($\mathbf{L_{2\,p}}$), or reduced magnitudes for more stable solutions ($\mathbf{L_0}$). The problem solved for is presented

in Eqn. (3-30), where the unconstrained solvers used included SVD and TSVD for direct methods, and gradient decent and CGLS for iterative methods. The algorithms followed are as explained in [80] and/or used in [69]. Hence, this created the motivation for moving to constrained least squares solvers, where they provided relatively better results.

Six different solution methods, based on constrained inequality and/or equality solvers were investigated. Information about the solvers and their performance are stated in Table 3-1, while Figure 3-12 shows the averaged intensity values in all ϕ directions (although they are not uniform) with respect to radial position on target placed at the focal plane for different θ values. The reference case represents the intensity obtained from the MCRT code, where a good solution is expected to match it.

Cases 1-6 represent the solution obtained for different solution methods using heat flux maps obtained from the MCRT code. For cases 1-3, linear first-order interpolation was used, where case 1 had no regularization applied and used a nonnegative solver, case 2 had regularization applied in the x, y, and ϕ to impose a bias towards a solution that is symmetric in nature (per expected from the centered reflector) and used a nonnegative solver, and case 3 had the same regularization as case 2 (with different parameter values) and used the equality and inequality solvers stated by the minimization problem in Eqn. (3-32). Cases 1-3 were duplicated for cases 4-6, but while using a zeroth-order interpolation scheme. The regularization parameters for each of the cases, when applicable, were determined using the discrepancy or the L-curve criteria. If the parameter values are of different magnitudes, the discrepancy criterion was favored over the L-curve, since it provided better relative error values and a distribution that better matched the reference case.

Table 3-1: Summary of solution methods, details, and calculated relative error values for the inverse ray tracing method

Solver No.	**Interpolation Scheme**	**Regularization** (Parameter values are x10^{-6})	$N_x \times N_y \times N_z \times N_\theta \times N_\phi$	$I_{0,\max}$ (MWm^{-2}/sr)	**Relative Error** (%)
Ref	-	-	11x11x( )x8x8	32.9	-
1	First	None	11x11x13x8x8	68.3	90.9
2	First	α_0 = 3, α_{1x}, α_{1y} = 60, $\alpha_{1\phi}$ = 40	11x11x13x8x8	30.7	69.3
3	First	α_0 = 1, α_{1x}, α_{1y} = 60, $\alpha_{1\phi}$ = 40	11x11x13x8x8	38.2	51.0
4	Zeroth	None	11x11x13x8x8	40.9	82.6
5	Zeroth	α_0 = 0.4, α_{1x}, α_{1y}, $\alpha_{1\phi}$ = 15	11x11x13x8x8	32.0	52.2
6	Zeroth	α_0 = 0.4, α_{1x}, α_{1y}, $\alpha_{1\phi}$ = 15	11x11x13x8x8	33.4	30.4
Exp	Zeroth	α_0 = 1.5, α_{1x}, α_{1y}, $\alpha_{1\phi}$ = 15	21x21x13x8x8	28.7	-

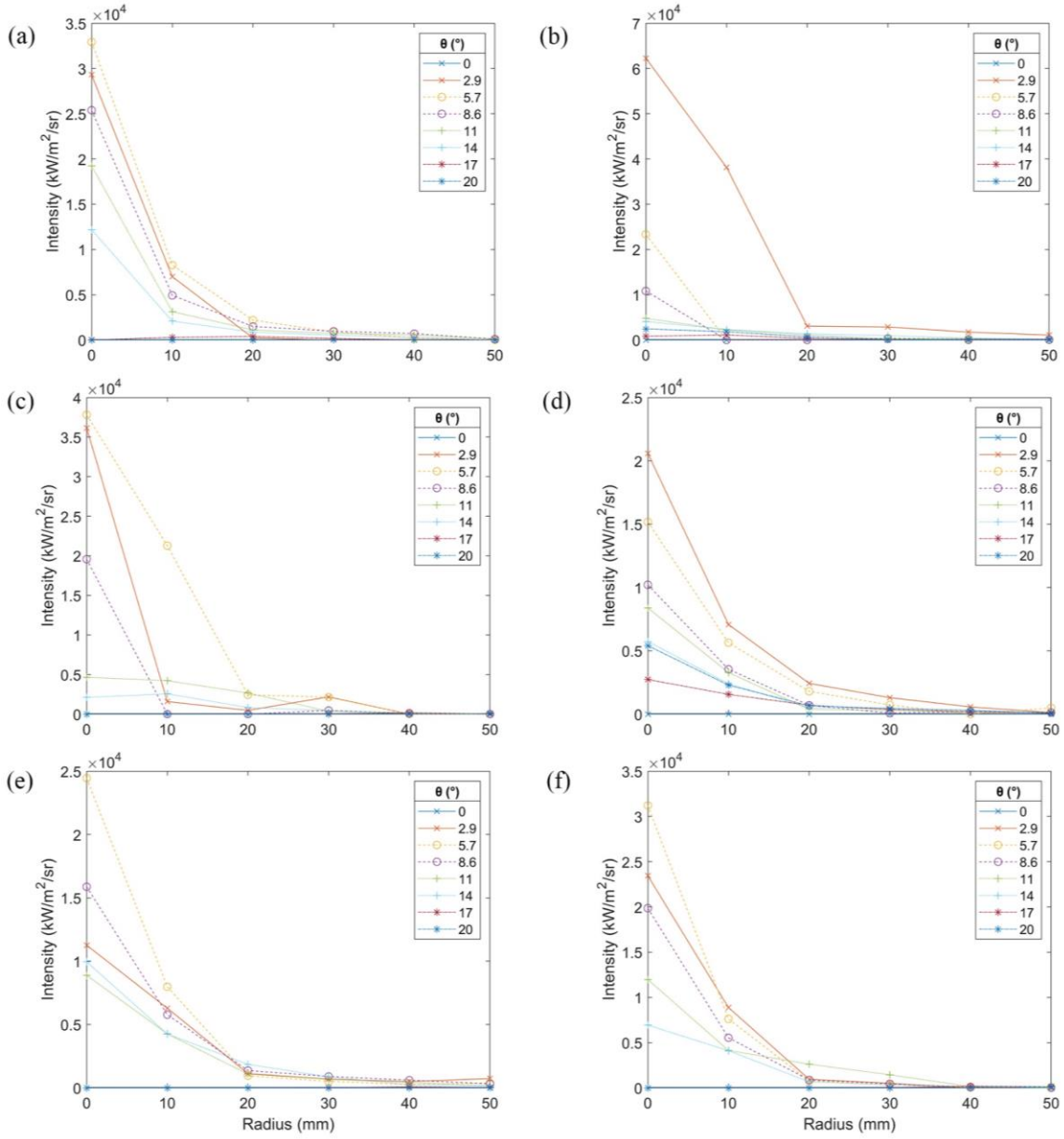

Figure 3-12: Average intensity values along the x and y directions and in all azimuth angular directions with respect to radius from the center of the target placed at the focal plane with $N_x = N_y = 11$ for (a) reference case, (b) case 1, (c) case 3, (d) case 4, (e) case 5, and (f) case 6.

By comparing cases 1 and 4, it can be noticed that there is a drop in the relative error value when changing from a first to zeroth-order interpolation scheme. The solution further shows much closer trends to that of the reference case. The first-order interpolation presented by Eqns. (3-26)-(3-28) seemed to cause an unnecessary complication to the SoEs and led to solutions that have higher error values. Also, a zeroth-order methodology was noticed to require much less

regularization, based on the regularizing parameter values, since it did not favor solutions that are unsymmetrical (in accordance with the coaxially placed bulb and reflector) or have relatively high intensity values as much as the first-order interpolation. Furthermore, a first-order interpolation solver required approximately five times more computational time in formulating and solving the linear SoEs. Using a Dell XPS 15 with an Intel core i7-7700 HQ CPU @ 2.80 GHz, 4 cores, 8 logical processors, and 8 GB of RAM, the computational times required to construct and solve cases 1-6 were 71, 121, 25, 11, 19, and 5 seconds, respectively.

Moving from case 1 to 2, there was a significant drop in $I_{0,\max}$ and the percentage error due to regularizing the SoEs. However, this came at the expense of having a greater residual norm, which is to be expected and fine since it is not desired to over fit the heat flux measurements. The average error of case 2 is 69.3%, which decreased even further to 51.0% after implementing the equality constraints based on Eqn. (3-32) as previously described. $\mathbf{A_{eq}}$ equated some of the intensity values in the SoEs to zero, and hence eliminated the need to solve for some of the predictors and better stabilized the solution. This is in addition to the lower computational time as previously mentioned. For cases 4-6, it can be noticed that changing to zeroth-order interpolation further improved the results. Moreover, by comparing Figure 3-12 (e) and (f), it can be clearly seen how the equality constraint based on $\mathbf{A_{eq}}$ helped in avoiding incorrect intensity solutions further away from the center of the target. For instance, the intensity at $\theta = 2.9°$ and $r = 5$ cm significantly dropped as a result, leading to a more accurate solution. Therefore, the solution method of choice is solver 6.

Once the solver of choice has been determined to be of an acceptable accuracy, it was used to solve for $\mathbf{I_0}$ using the experimentally obtained heat flux maps. The intensity solution is shown in Figure 3-13, while the parameters used for its solver are defined in Table 3-1. It should be noted that a relatively higher α_0 was used in the experimental case as a result of any noises within the obtained experimental flux maps. Therefore, further stabilizing the solution. Based on Figure 3-13, the obtained solution shows a similar trend to that of the test case's reference solution with the exception of $\theta = 2.9°$. Any differences can be attributed to noises within the experimental measurements in addition to differences between the modeled and real system.

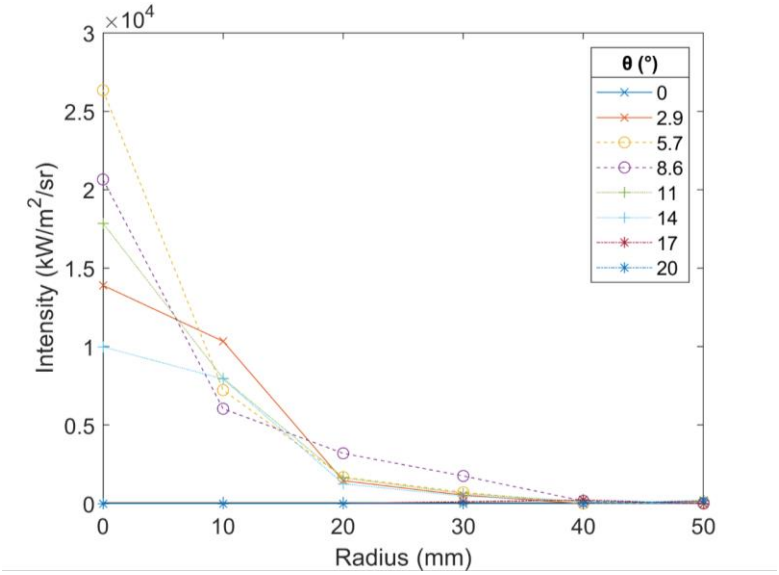

Figure 3-13: Solution of averaged intensity values with respect to radial position for the experimental case

3.5. Conclusions

In this chapter, the numerical characterization and modeling of a HFSS was presented using two different approaches. The first approach was based on the MCRT method, which is a well-established and well-defined forward analysis. Using an in-house developed MCRT code, the xenon arc was successfully modeled for its heat flux distribution at different optical planes and input powers to the HFSS. The results obtained from the model presented great agreement with the experimental ones, resulting in percentage errors of 0.07 and 1.17% for both the peak flux and total power values at the focal plane. As was shown previously in this chapter, all the relative errors between the experimental and modeled results remained within a very reasonable range, with the only exception being the total power at low current values due to the significant increase of percentage uncertainty within the experimental measurements. Based on the results presented in this chapter, the proposed shape to use for modeling a 10 kW_e xenon arc is a hemisphere with a radius of 1 mm centered at the focal plane that is attached to a cylinder of 1 mm in radius and 10 mm in length with a power ratio between the two shapes of 0.23:0.77. Therefore, this model of the xenon arc will be used in upcoming chapters or work to simulate the effect of the HFSS on any system of interest.

In addition, a second approach of experimentally determining the intensity distribution at the focal plane, or any other plane of interest, was presented. This was referred to as the inverse ray tracing method, where the formulation of the inverse problem was presented in details. This

approach is not a well-established one and it defines a highly ill-posed problem due to the nature of the system and high gradients in the intensity distribution from the HFSS. Two intensity interpolation schemes were examined, where it was shown that a first-order interpolation unnecessary complicates the problem, rather than providing a more accurate estimation of intensity values with respect to the zeroth-order interpolation. The percentage error reduced from 90.9% to 82.6% when changing the interpolation scheme from a first to zeroth-order. Based on the demonstrated superiority of results of the zeroth-order interpolation scheme and the significantly reduced computational time (five times reduction), it is thus recommended to use such scheme, which can further allow for larger resolution (higher N_x, N_y, N_θ, and N_ϕ values) for the solution at the plane of interest. Once the intensity solution is obtained, the first-order interpolation can be used to determine the heat flux distribution at any plane or shape of interest.

In addition, a new approach of constraining the formulated SoEs with an equality constraint that works by eliminating some of the intensity values that cannot be traced back to the ellipsoidal reflector is proposed. This equality constraint reduces the number of predictors to be solved for and eliminates the rise of unreasonable results. Therefore, it can be used as a technique to change the ill-conditioned problem to a well-conditioned one without depending heavily on Tikhonov regularization methods. The equality constrained linear SoEs using the new promising approach provided intensity values at the focal plane with a reduced percentage error based on the reference intensity obtained from the MCRT code. The percentage error reduced from 69.3% to 51.0% in the first-order interpolation scheme and from 52.2% to 30.4% for the zeroth-order, when implementing the equality constrained solver. Hence, the new approach seems to be a promising one for the reconstruction of lost directional information for HFSSs. It is finally worth noting that this method of eliminating the intensity values that cannot be traced back to the reflector does not necessarily have to be done using an equality constraint. A possible different approach is to eliminate these intensity values and their effects from the SoEs to avoid the use of an equality constraint.

Chapter 4[4]

Heat Transfer Analysis of Solar Receiver

In Chapter 4, the experimental setup at HFGL, which consists of a solar receiver in addition to other auxiliary components, will be introduced and the components' designs will be presented. The solar receiver, being the main component of the setup, is covered in details with further focus on any design progress and modifications. Following that, the heat transfer model of the solar receiver is presented. The in-house developed code of the model couples the previously introduced optical analysis performed through MCRT method (Chapter 3) with a two-dimensional heat transfer analysis based on the finite volume method. Experimental characterization of the solar receiver was performed, where its results are presented and used for the validation of the numerical model. Once the model is validated, it can be used to simulate different test scenarios, such as design alterations, scaling up of the solar energy source, and/or control strategies to regulate the temperature within the solar receiver (which will be the scope of Chapter 6).

4.1. Introduction

As previously mentioned in Chapter 1, central receivers are gaining great attention due to their good efficiencies at elevated temperatures, which allows for their implementation in processes in addition to direct electricity generation. These processes are referred to as solar thermochemical processes, and they usually work by producing storable solar fuels and chemicals that are traditionally obtained through the combustion of fossil fuels to provide the required high temperature process heat. These processes include the production of hydrogen, syngas, and/or carbon [10–13], zinc [16,17], and other products, such as lime [19]. Through the use of solar thermochemical processes, the carbon footprint is greatly reduced, where the solar alternatives involve relatively mild temperatures that have potential solar to fuel efficiencies exceeding 50% [20]. A common type of solar central receivers is a cavity-type receiver, which is a receiver with an aperture that aims for maximizing irradiation captured, while minimizing re-radiation lost within its cavity. Therefore, this type of receivers has an optimum aperture size that results from a compromise between the captured radiation energy from the solar source and the radiation emission lost from the receiver's cavity. Thus, the optimum aperture size depends on several factors, most

[4] A portion of this chapter contributed to publication by M. Abuseada, N. Ozalp, and C. Ophoff, titled "Numerical and experimental investigation of heat transfer in a solar receiver with a variable aperture", published in Int. J. Heat Mass Transfer. 128 (2019) 125-135.

importantly being the cavity's temperature, as was shown in [7], and the power distribution from the solar source.

There are several notable solar reactor designs in literature that are designed for different processes. The reactors can work through the direct irradiation and heating of the reactants, as is mostly the case, or through indirect heating as in [19,20]. The optimum aperture size of the reactor is pre-determined through analyses and simulations at the expected/nominal operating conditions, and the aperture is then remained fixed for all operating conditions. With all designs, whenever applicable, the reactor's cavity is sealed using a quartz window at the aperture to provide direct heating of the reactants inside the reactor. quartz is usually the material of choice due to its desirable optical characteristics in the solar irradiance's wavelength spectrum and its ability to withstand very high temperatures [87]. A comprehensive review of different solar reactors developed at PSI can be found in [19].

For a solar reactor system, the development of dynamic models of the system and their validation is necessary for several applications. First, the developed model can be used as a tool for designing solar reactors and optimizing their operating conditions, as in [88]. It can also be used to determine the optimum reactor's aperture for any given operating conditions, as previously mentioned and illustrated in [7]. Furthermore, the model can be used to assess the different forms of heat transfer and hence the overall process efficiency, as in [12,89]. Finally, the model can be used to simulate the transient and steady state responses and simulations of the system. This can be used for offline system identification and control applications to maintain semi-constant temperatures within the solar reactor, which include model predictive controllers and offline tuning of controllers, as in [90–92]. The use of an accurate validated model of the process can significantly save great time and costs associated with tuning controllers for solar reactors.

To be able to accurately model the solar reactor system, several analyses need to be coupled in order to obtain a full representation of the process's behavior. These include an optical analysis for the radiative heat transfer and input power from the HFSS, heat transfer analysis for the flow of energy within the reactor's walls and components, and a fluid dynamics analysis to monitor the feedstock's behavior and its effect on the convection heat transfer. In the case of reacting flows, additional equations and analyses are implemented to further govern the process at hand.

For the optical analysis within the solar receiver's cavity, two of the available approaches are the Radiosity Net Exchange (RNE) and the MCRT methods [70,71,73]. However, the MCRT is the most commonly used method to simulate thermal radiation in solar applications due to its capability

of incorporating probabilistic density functions and other surface properties that the RNE method cannot accommodate for [16,88,93]. In addition, it has been previously shown that the MCRT method is superior to the RNE method and provides more accurate representation of the temperature distribution, especially where two surfaces meet at perpendicular angles in a receiver [94]. Therefore, the use of MCRT technique has been extended beyond the scope of simulating the HFSS in Chapter 3 to model the heat transfer due to radiation emission from the receiver's cavity.

In this chapter, the complete experimental setup at HFGL will be presented. This includes the solar receiver, which is the main component of the setup, in addition to other auxiliary components and connections, such as an exhaust cleaning mechanism and a heat exchanger. The design of the solar receiver will be presented in details, while only brief details on its auxiliary components will be presented for completeness since they are out of the scope of this research work. Following that, the heat transfer model of the solar receiver will be presented, starting with the optical analysis performed using the MCRT method and its extension work to model the radiation emission as well as reflection within the receiver's cavity. The optical analysis is then coupled to a two-dimensional heat transfer analysis based on the finite volume method to effectively model the temperature distribution within the receiver. The finite volume method was the approach of choice over other approaches due to its capability of strictly abiding to all conservation laws [95]. These two analyses are usually coupled together when an in-depth study of radiative heat transfer is necessary [96]. For the validation of the model, an experimental characterization of the solar receiver was performed, presented, and used to validate the numerical model. Once the model is validated, it can then be used to simulate different test scenarios, such as design changes, scaling up of the solar energy source, and control strategies to maintain semi-constant temperatures within the solar receiver.

4.2. Experimental Setup and Procedure

4.2.1. Experimental Setup

Solar Receiver. The cavity-type solar receiver designed consists of five main components as follows: a cylindrical body, back plate, front flange, and two additional plates at the front. The two additional plates hold the quartz window, which ultimately seals the solar receiver. The front flange's purpose is to serve as a protection shield from any spilled irradiation (portion of radiation from the HFSS not falling within the fixed aperture's size) and as a mean of connection of other components, such as the quartz front and back plates, receiver's insulation outer shell, and a variable aperture (covered in Chapter 5). The five components come together to form the cavity of the receiver, which is made of stainless steel 316 and can safely withstand operating temperatures

up to approximately 1000 °C. An overview of the receiver being mounted in front of the HFSS is shown in Figure 4-1, while the dimensions and materials of its components are in Table 4-1.

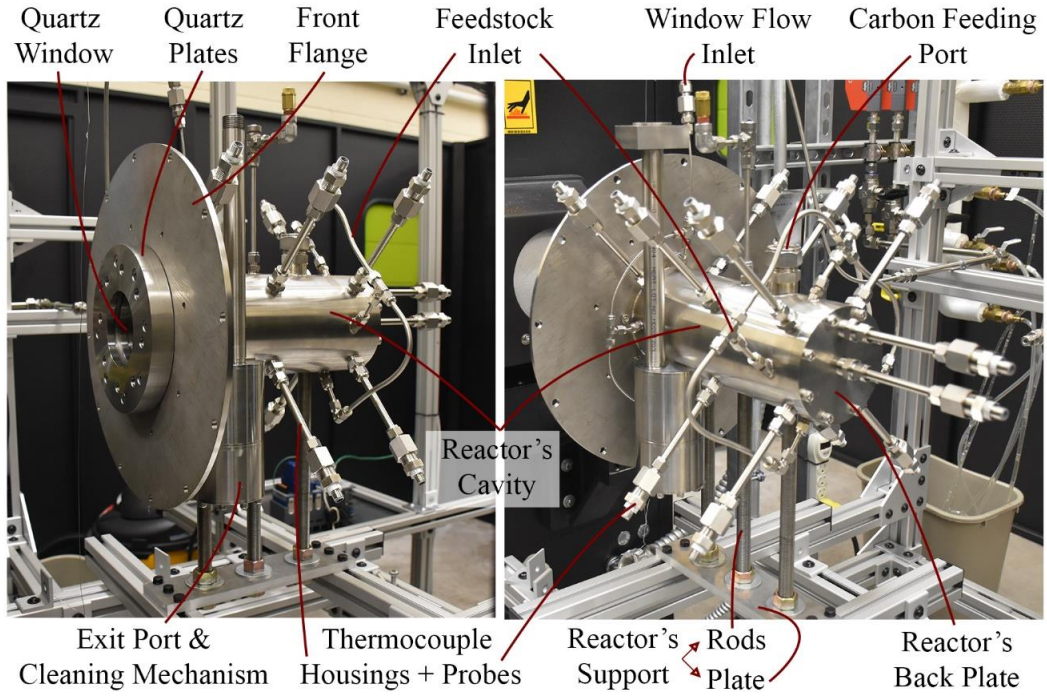

Figure 4-1:Illustration of solar receiver and connections before insulation

Table 4-1: Components of solar receiver, their materials, and dimensions

Component	Material	Dimensions (cm)
Main Cylinder	Stainless Steel 316	$d_{c,in}$ = 10.2, t_c = 1.52, L_c = 29.3
Back Plate	Stainless Steel 316	d_{bp} = 13.2, t_{bp} = 1.52
Front Flange	Stainless Steel 316	$d_{ff,in}$ = 10.2, $d_{ff,out}$ = 42.7, t_{ff} = 0.64
Quartz Plates	Stainless Steel 316	$d_{qp,in}$ = 8.89, $d_{qp,out}$ = 19.7, t_{qp} = 1.27
Window	Fused Quartz	d_w = 10.2, t_w = 0.74
Insulation	Calcium-Magnesium-Silicate Wool	$t_{ins} \approx$ 12.2
Shell Cover	Aluminum 6061	$d_{sc,in}$ = 37.6, t_{sc} = 0.25, L_{sc} = 42.3

The configuration of the solar receiver and dimensions of its components were partially based on the findings in [97] to improve the temperature uniformity within the receiver's cavity and improve its optical efficiency. Solar power distributions at the focal plane of cavity-type receivers are highly concentrated with steep gradients due to the parabolic or ellipsoidal reflectors. This creates "hotspots" within the cavity of the receiver, which are regions with significantly higher

temperatures. The presence of hotspots inside a solar receiver can severely affect its performance by reducing its overall performance and create a safety hazard due to thermal stresses and deformations [98]. Therefore, the solar receiver has been designed to reduce the temperature non-uniformity and any hotspots formation within its cavity. Reducing the temperature non-uniformity within the receiver has been approached by: (1) decreasing its aperture's diameter, (2) increasing the overall length of its cavity, and (3) reversing its fluid flow direction, so that the fluid flows in a similar manner to a counter flow heat exchanger rather than a parallel flow one. The overall design of the receiver will be covered in the upcoming sections of the thesis.

The solar receiver has four tangential inlet ports at the rear side for the entry of the main feedstock flow into the receiver with diameters of 0.48 cm. The tangential inlet ports are circumferentially distributed with equal angles of 90° in order to create a vortex-like flow and enhance convective heat transfer, similar to that implemented in [99] and studied in [100]. An illustration is shown in Figure 4-2, where the fluid flow is expected to follow a helical path as it progresses from the rear inlet to the front outlet. The exit port of the receiver (not visible in Figure 4-2) is located at the front side of the cavity and is equipped with an exhaust cleaning mechanism for experiments involving carbon particles flow (outside the scope of this research work), which is the reason for having the exit port being off-center. The receiver also has four additional inlet tangential ports at the front side with diameters of 0.23 cm, which are directed towards the quartz window. The purpose of these additional ports is to cool down the window and maintain it in a clean condition in experiments involving carbon particles flow. All the inlet ports are sealed through welding the connection fittings to the main cylindrical component of the solar receiver.

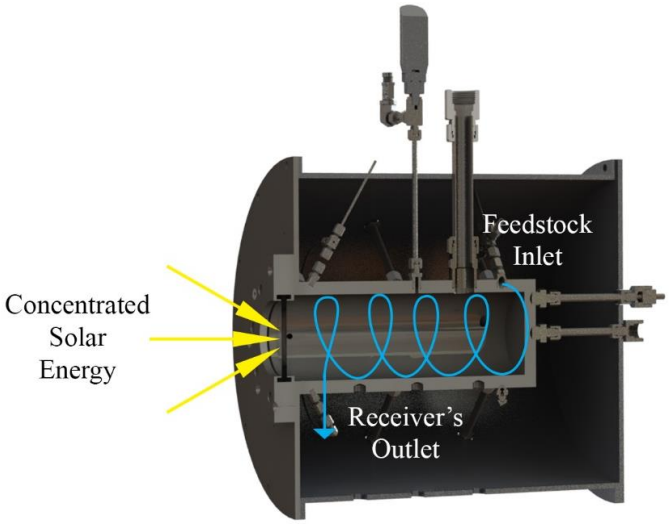

Figure 4-2: Cross-sectional view of the solar receiver illustrating the vortex flow

Furthermore, the receiver's cylinder and back plate are threaded to allow for the connection of 10 thermocouple probes around the cavity of the receiver and two additional probes at the back plate. The 10 thermocouple probes are located at the different locations within the cavity, which will be referred to as the front, middle, and back positions corresponding to their locations relative to the receiver's aperture. At the front, there are only two probes at the top side with an angular spacing of 90° due to the presence of the exhaust cleaning mechanism. At the middle and back positions, four thermocouple probes are equally distributed around the cavity with the same relative angular positions and an angular spacing of 90°. Measurements from these thermocouples provide a better estimate of the temperature distribution at each axial position in addition to providing a measure of temperature symmetry within the solar receiver. At the back plate, one thermocouple is located at the center of the plate, while the other is located vertically above the first thermocouple. This provides a better estimate of the power distribution from the HFSS at the back plate to better validate the numerical model. All thermocouple probes are shielded within stainless steel 316 tubes in order to extend their connections further away from the receiver's body for safe operation.

Moreover, the receiver has two additional through holes at the middle-top side of its cavity. These holes serve as means to connect a pressure gauge with a relief valve in addition to a carbon feeder for experiments that involve carbon particles injection. The receiver's cavity also has three threaded connections at the lower side to allow for the connection of support threaded rods as shown previously in Figure 4-1. The rods serve as a mean to connect the receiver to the main aluminum structure using a flat plate and a set of nuts. In this arrangement, the solar receiver can be easily aligned in the x-direction by moving the flat plate, in the y-direction by screwing or unscrewing the support nuts (above and below the flat plate), and in the z-direction by moving the aluminum extrude supports. Thus, allowing for an easy and accurate alignment of the solar receiver to coincide with the pre-determined focal point through experimental characterization. A color coded model of the solar receiver, its main components, and connections is shown in Figure 4-3.

In order to achieve high temperatures within the solar receiver, it has to be properly insulated with a relatively thick layer of insulating material. As shown in Figure 4-3, the receiver has an external aluminum 6061 shell that is bolted to the front flange. The external shell serves as a mean to house the insulating material, which is Calcium-Magnesium-Silicate wool (commercially known as Superwool plus blanket) that was obtained from Morgan Thermal Ceramics. The external shell is divided up into five parts: four sections around the cylindrical cavity of the receiver and a back plate as shown in Figure 4-4. The external shell was divided into parts to allow for the connections

that extend beyond the shell's radial distance, where all the parts then come together to elegantly enclose the insulating material. The dimensions of the external shell are previously presented in Table 4-1. Based on its dimensions, the insulation thickness is determined to be approximately 12.2 cm around the cavity and 11.5 cm around the back plate. Starting from the insulation blanket, pieces and parts had to be cut in the right sizes to fill in the void spaces between the receiver and external shell. The process of applying the insulating layer to the solar receiver and its progress is shown in Figure 4-4. With that, the experimental setup of the solar receiver is complete.

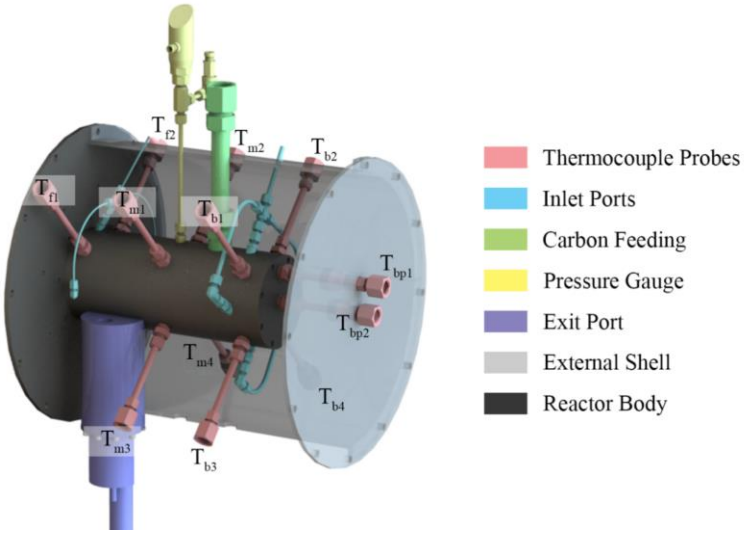

Figure 4-3: Color coded model of the solar receiver and its components

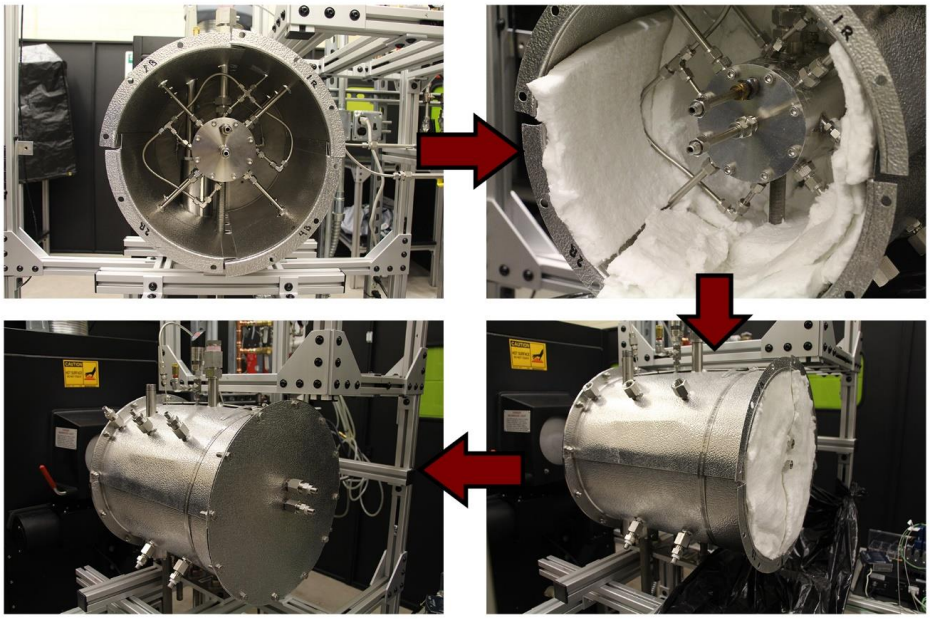

Figure 4-4:Progress of insulation layer around the solar receiver

Auxiliaries and Setup. Other components and auxiliaries of the complete setup include: a carbon feeder, exhaust cleaning mechanism, double-pipe counter flow heat exchanger with connections to a chiller, and a particle filter. All components are supported through an aluminum extrude structure as shown in Figure 4-5. The carbon feeder, exhaust cleaning mechanism, and particle filter are required for carbon particles injection experimentation. These auxiliaries are outside the scope of this research work, but are briefly mentioned for completeness. The carbon feeder is a volumetric feeder model 170-MI-5-AA/2 from Acrison Inc, and the exhaust cleaning mechanism involves a revolver of the exhaust tube and a scraper to clean any deposited carbon particles in the tube and ensure continuous and safe operation. The double-pipe heat exchanger has an outer diameter of approximately 5.1 cm, while an inner diameter of 2.5 cm. The heat exchanger is connected to an air-cooled recirculating chiller (ThermoFlex 900 from Thermo Scientific) in a counter flow arrangement with a cooling capacity up to 900 W. The heat exchanger ensures that the outlet gas temperature is within an acceptable limit of 50 °C under all operating conditions.

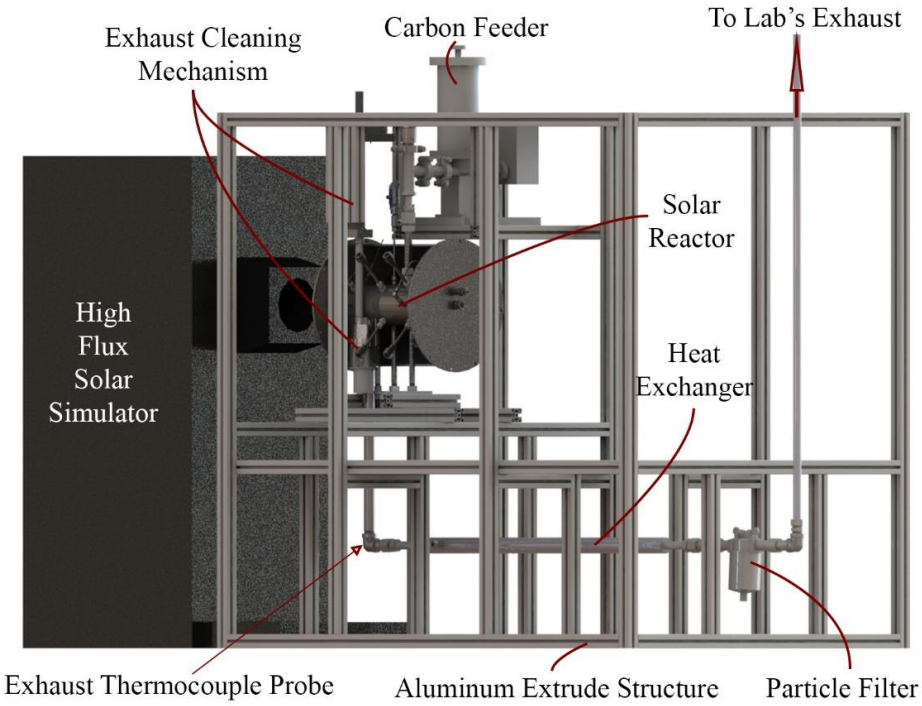

Figure 4-5: Overview of experimental setup and components at HFGL

Data Acquisition and Instrumentation. A data acquisition and control system using LabVIEW and hardware from NI was implemented to have real-time data collection and control. The system consisted of cRIO 9030 that can connect up to four modules, where all four slots were used. The first module, following Figure 4-6, is NI 9375, which is a digital input/output module

that has 16 channels for each. This module is used for motor control applications, such as controlling a variable aperture, which will be the focus of Chapter 5. The second and third modules are both NI 9214, which are temperature input modules that can allow connecting up to 16 thermocouples or sensors. The final module is NI 9215, which is a voltage input module with four channels to allow acquisition of additional measurements, such as those from a water flow meter. The data acquisition station is shown in Figure 4-6 with all the instrumentation and sensors being connected.

In addition, flow controllers are used to control the volumetric flow rates of both the feedstock and window line. The flow controllers are red-y smart series obtained from Voegtlin that can control the flow rate within the range of 0-30 LPM with an accuracy of 1% full scale. The connection to and from the flow controllers is established through a Modbus communication directly to the dedicated PC of the setup. Furthermore, type K thermocouple probes were used to monitor the temperature distribution within the solar receiver, as previously discussed and illustrated in Figure 4-3, in addition to an extra location at the exit pipe from the receiver (shown in Figure 4-5). These were obtained from Omega, model number M12KIN-1/8-U-6-B, and they are Inconel 600 type K thermocouple probes with 1/8" diameters and ½ NPT mounting threads that allow them to be easily connected to the setup. The thermocouple probes have a temperature range up to 1250 °C and tolerance of 2.2 °C or 0.75%, whichever is greater. Finally, type K bolt-on thermocouples were also used to monitor the temperature distribution around the shell of the reactor, as shown in Figure 4-7, to ensure that the insulation layer is performing satisfactory and for additional validation of the numerical model.

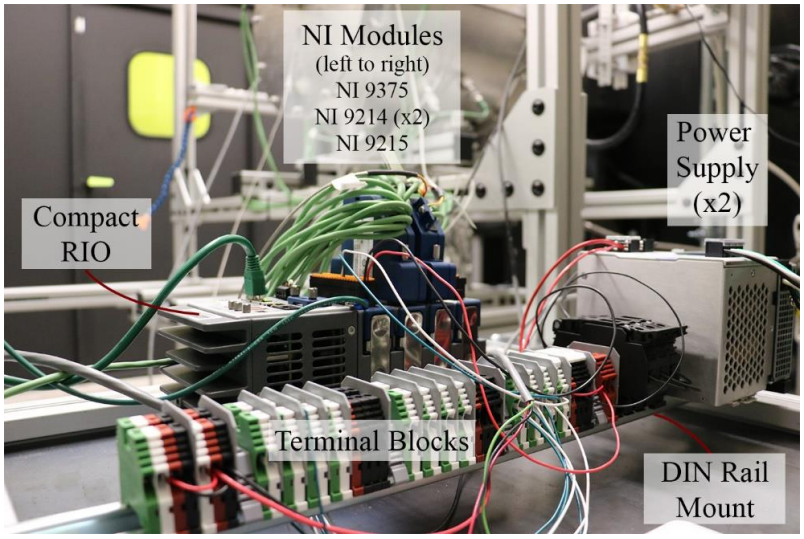

Figure 4-6: Data acquisition and control station

Complete Solar Receiver's Setup. The complete working setup of the solar receiver is shown in Figure 4-7. Flow connections were securely tightened and ensured to be leak free. Communication with all sensors was established and the data acquisition file was created in LabVIEW. The final step was to insulate the exhaust, including both the cleaning mechanism and outlet pipe, in order to minimize heat losses from the exhaust flow to the surrounding up to the point where the temperature measurement of the exit flow is taken. The insulation layer created around the exhaust is approximately 7 cm. Both the insulation layer and the variable aperture mount (further discussed in Chapter 5) are shown in Figure 4-7.

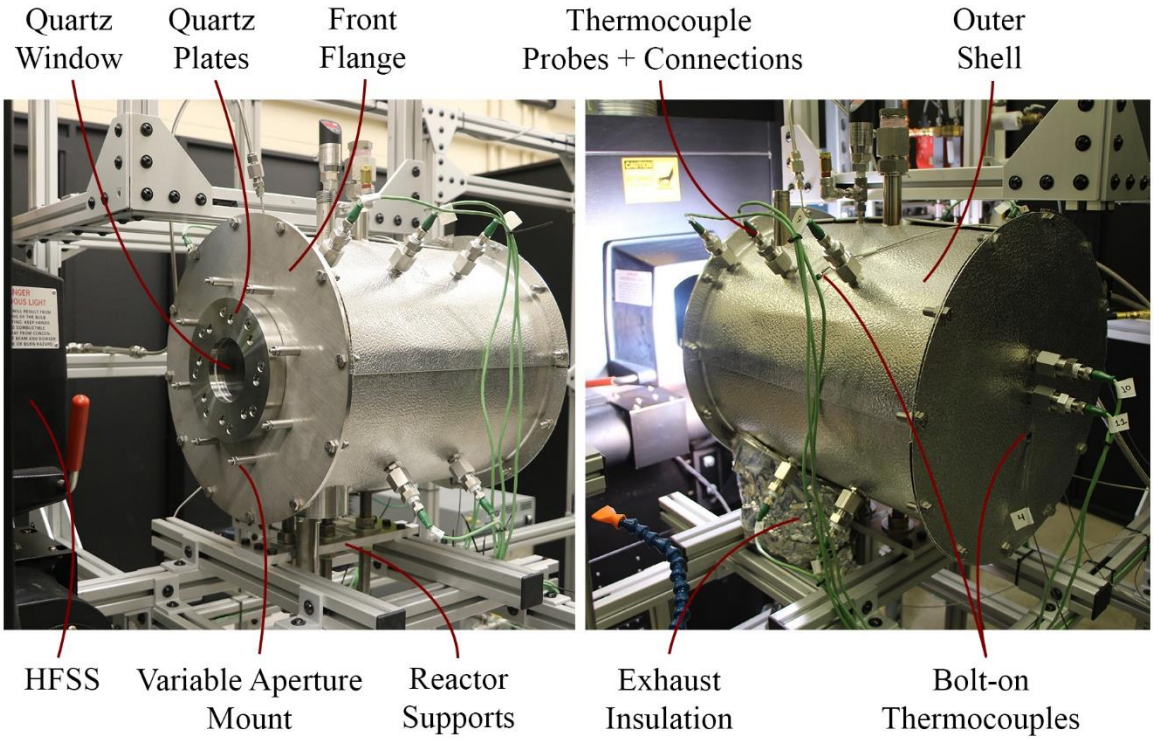

Figure 4-7: Complete working setup of the solar receiver

4.2.2. Experimental Procedure

The solar receiver is properly aligned at the second focal point of the HFSS's ellipsoidal reflector. The center of the receiver's front quartz plate coincides with the focal point so that the solar power into the receiver is maximized. To characterize the solar receiver, transient experiments under different operating conditions were performed to determine the transient and steady state responses of the temperature distribution within the receiver. As would be expected, it would take many hours for the temperatures within the receiver to stop increasing and ultimately reach a steady state. Therefore, the steady state from now on will be accepted as the point in time where the

temperature gradients' average value drops to approximately 0.05 °C/min. Therefore, remaining consistent throughout all experiments for different operating and/or starting conditions. The steady state requirement is achieved approximately after 6.5 hours when starting the experiment from room temperature.

Experiments on the solar receiver were performed to characterize its response to different power levels (input current to the HFSS) and feedstock flow rates. The feedstock fluid of choice was nitrogen in order to minimize deterioration of the receiver through the oxidation of its surfaces. Experiments were performed at three different current values starting with the maximum safe operating current. Per initial simulations and experimentation, this current value was determined to be 160 A, since it was the input current at which a maximum temperature of approximately 1000 °C was observed. Based on that, the three current values of choice were 160, 150, and 140 A since it is not desired to operate the HFSS for prolonged periods of time at any lower current values. For the feedstock's flow, experiments were done at four different flow rates of 2.5, 5, 7.5, and 10 LPM.

4.3. Numerical Modeling Methodology

4.3.1. Optical Analysis: MCRT method

The MCRT method has been previously covered in a great depth in Chapter 3 covering its fundamentals, ray tracing methodology, and the algorithm of the method to model the HFSS. Therefore, the information that will be presented here is only to complement those presented previously. In addition, two types of rays will be defined within the MCRT algorithm to distinguish between the sources contributing to radiation heat transfer, as commonly performed in literature. These are the primary rays, which represent the rays from the solar source (HFSS in this case), and the secondary rays, which represent the rays that are emitted by the receiver's cavity [16,65,99].

Assumptions. Since the optical analysis now involves a larger scope, it is best to start by extending the assumptions that the analysis considers. First, all the surfaces surrounding the solar receiver, such as the aluminum structure, are treated as non-participating. Hence, their re-radiation effects (if any) are neglected. Also, all surfaces are assumed to be diffuse gray (surface properties are independent of direction and wavelength), and have constant surface properties that are independent of temperature. Furthermore, the feedstock fluid flow, being nitrogen, is treated as a non-participating medium (completely transparent). Finally, the quartz window is assumed to have a refractive index of one, and hence, not affecting the direction of any incoming rays. While keeping these assumptions in mind, the description of the optical analysis shall proceed.

Surface Descriptions. The solar receiver consists of only two types of simple geometries: its different components can be described as a cylinder and/or a cylindrical flat plate. Therefore, the surface descriptions are relatively easy. The dimensions of each component where previously summarized in Table 4-1. In the case of the main cylinder of the receiver, quartz front and back plates, and front flange, the surfaces can be described as in Eqn. (4-1).

$$x^2 + y^2 - r_{in}^2 = 0 \quad \text{for} \quad z_{min} < z \leq z_{max} \tag{4-1}$$

where z_{min} and z_{max} represent the starting and ending positions. However, in the case of the quartz window, quartz front plate, front flange, and back plate, the surfaces can be described as in Eqn. (4-2).

$$r_{in} \leq \sqrt{x^2 + y^2} < r_{out} \quad \text{for} \quad z = \text{z position} \tag{4-2}$$

where $r_{in} = 0$ for the back plate and $z = 0$ for the quartz front plate.

MCRT Algorithm. The subscript i in N_{ij} can be dropped and substituted by "prim" for the primary rays, while the subscripts i and j now correspond to surface indices rather than x and y coordinates as in Chapter 3. The general MCRT algorithm for quantifying the primary and secondary rays is shown in Figure 4-8. The methodology for the primary rays approaching the solar receiver was extensively covered in Chapter 3. Here, the first step would be to determine if and where does intersection occur. For that, the surface equations will be used in a manner similar to that performed in Eqn. (3-17) to obtain equations that represent the distance travelled by a ray up until the intersection point. For intersection to occur, the determined value for the distance parameter, s, will need to be a positive real number. In the cases where multiple intersections are determined, the intersection with the lowest value of s is chosen. Then, whether a ray is absorbed or reflected by the solar receiver will depend on the surface properties, and will be determined probabilistically in a similar manner as in Chapter 3. In the case of an opaque surface (all surfaces except the quartz window), $\varrho = 1 - \alpha$, where $\alpha = \varepsilon$ as per Kirchoff's law for diffuse gray surfaces. If the ray is absorbed, the counter corresponding to the surface is incremented by one and the ray's history is terminated, where the algorithm moves to the next ray. If the ray is reflected, the reflection direction will have to be determined.

To determine the reflection direction from a receiver's surface, it is first assumed that reflection occurs in a diffusive manner, rather than a specular one as for the ellipsoidal reflector. For a diffuse reflection, Eqn. (4-3) is used to evaluate the direction of the ray.

$$(\theta, \phi) = \left(\sin^{-1}\sqrt{\Re_\theta}\,, 2\pi\Re_\phi\right) \tag{4-3}$$

Once the direction is obtained, the algorithm will proceed until the ray is determined to be absorbed by a surface, or lost from the solar receiver. The power distribution of the primary rays will be computed once N_{rays} rays have been emitted from the HFSS. With this, the section of the primary rays is complete, where the power at each surface element can then be easily obtained.

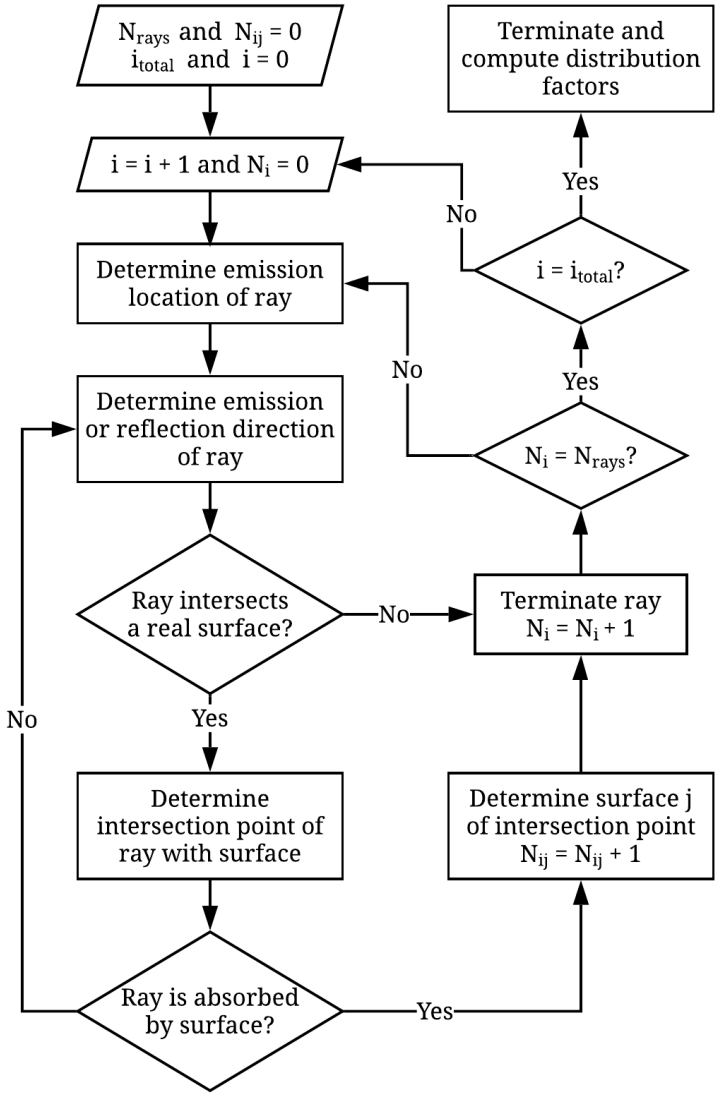

Figure 4-8: Flowchart illustration of the general MCRT algorithm used to model the solar receiver

For the secondary rays, a total number of i_{total} discrete surface elements are defined. For each element, a total number of N_{rays} rays are emitted to obtain the power distribution from surface i to surfaces j. The location of emission is determined similarly to that described in Chapter 3, by modifying Eqns. (3-10)-(3-12) to obtain Eqns. (4-4) and (4-5) for a cylindrical or flat plate section,

respectively. Then, the direction of surface emission is determined through Eqns. (4-3) and (3-8), and the algorithm proceeds as normal to emit all rays for all surfaces involved, while incrementing the corresponding counters.

$$(r, \phi, z) = \left(r_{in}, 2\pi\Re_{\phi}, (z_{max} - z_{min})\Re_z + z_{min}\right) \tag{4-4}$$

$$(r, \phi, z) = \left(\sqrt{\Re_r(r_{max}^2 - r_{min}^2) + r_{min}^2}, 2\pi\Re_{\phi}, z\right) \tag{4-5}$$

The last step would be to compute the distribution factor, D_{ij}, that represents the ratio of radiation emitted by surface i that is absorbed by j due to direct radiation and all possible reflections, where $i = j$ is a possibility. The distribution factor simply becomes $D_{ij} = N_{ij}/N_{rays}$ and the optical analysis is now concluded.

4.3.2. Heat Transfer Analysis

The heat transfer analysis of the solar receiver is performed using the finite volume method, which couples the MCRT method and its results. All system components under consideration are centered around the z-axis and have geometries and properties that are symmetric (except the exhaust and insulation layer). Therefore, the system can be treated as a two-dimensional one in the solid phase without sacrificing much of the accuracy of the model. This leads to the cylindrical coordinate system being the coordinate system of choice for the heat transfer analysis. Before proceeding any further, all assumptions of the model shall be covered.

First, the system will be assumed to be two-dimensional in the solid phase and one-dimensional in the fluid phase. Based on this, the system will be discretized in the form of annular elements throughout the solid phase having dimensions of Δz and Δr, and disk-shaped elements throughout the fluid phase. This form of discretization along with the coordinate system of choice are shown in Figure 4-9. In addition, it is assumed that the fluid enters from the feedstock inlet ports to the receiver right by the back plate, and then progresses throughout the cavity until the quartz window. Finally, the room temperature surrounding the solar receiver is assumed to remain constant at 25 °C. The room temperature is maintained through an air conditioner (not blowing around the solar receiver) and is constantly monitored through a bolt-on thermocouple right next to the receiver's shell, which never exceeds 32 °C within eight hours of operation. This makes the final assumption valid enough to be considered.

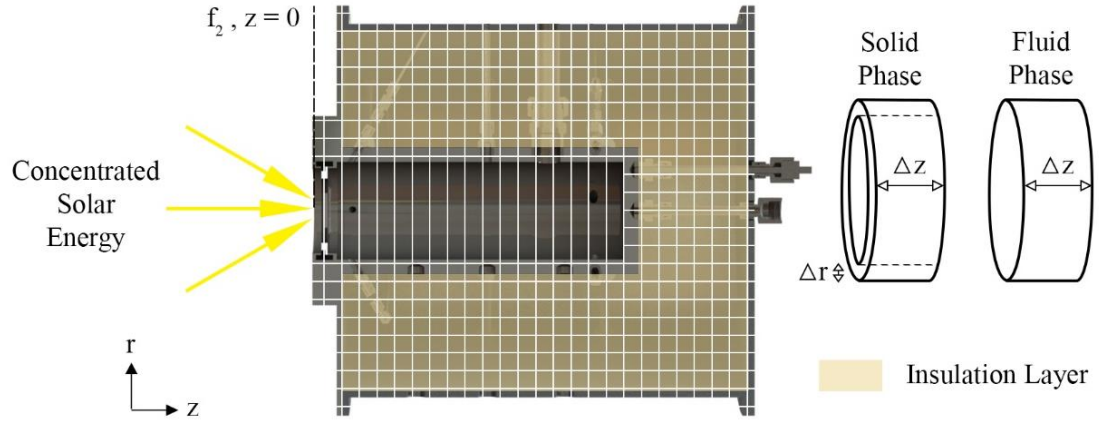

Figure 4-9:Mesh of the solar receiver system for the heat transfer analysis

For the solid phase, conservation of energy is used in order to determine the governing equation for each volumetric element, which describes the transient heat transfer of the entire model. Each group of elements has a different governing equation depending on its location within the receiver. The element's location will determine the direction and forms of heat transfer that the element undergoes. For example, the first layer within the cavity of the receiver will involve conduction, convection, and radiation heat transfer. Also, the power from the HFSS will be intercepted by this layer, and so it should be accounted for. On the other hand, interior (middle) elements only have conduction heat transfer, while exterior (outer) elements around the receiver have conduction, convection, and minor radiation heat transfer. The governing equation for the general case is shown in Eqn. (4-6), where heat transfer due to conduction and convection is assumed to be entering the control volume.

$$mc_p \frac{dT}{dt} = \dot{Q}_{in}^{cond} + \dot{Q}_{in}^{conv} + \dot{Q}^{rad,prim} + \dot{Q}^{rad,sec} - \dot{Q}^{rad,emit} \tag{4-6}$$

Each component shown in Eqn. (4-6) must be defined to accurately represent the heat transfer occurring. The term dT/dt is represented as $(T^{t+1} - T^t)/\Delta t$, where the superscripts represent the temperature at a specific discrete time period and Δt represents the time increment when solving for the temperature distribution's transient response. For the conduction heat transfer, the use of the harmonic mean for the thermal conductivity is implemented rather than the arithmetic mean, since it provides a better representation at an interface between two different materials [95]. When solving for the system's response and discretizing the governing equations further in the time domain, the fully implicit scheme is implemented due to its higher accuracy, as suggested in [95]. The fully implicit scheme assumes that temperature values are equal to their final values throughout the entire discrete time period.

The most critical location with the most heat transfer occurring is the first layer within the cavity walls. Therefore, the derivation analysis will only be shown for the group of elements that lie within the horizontal cylinder portion of the cavity. Starting from Eqn. (4-6), the different terms of the equation for the discrete volumetric elements within the cylindrical cavity portion are shown in Eqns. (4-7)-(4-11). The discrete elements are presented by i and j based on their relative location within the solar receiver. For clarity and to avoid confusion, the subscripts i and j for the MCRT optical analysis will be substituted by m and n. Indices in the optical analysis represent the corresponding surface element rather than its location. Hence, being different from the subscripts i and j used in the heat transfer analysis.

$$\dot{Q}_{in,i,j}^{cond} = \frac{(2k_{i-1,j}k_{i,j})(2\pi r_{m,j}\Delta r)}{(k_{i-1,j}+k_{i,j})\Delta z}(T_{i-1,j}-T_{i,j}) + \frac{(2k_{i+1,j}k_{i,j})(2\pi r_{m,j}\Delta r)}{(k_{i+1,j}+k_{i,j})\Delta z}(T_{i+1,j}-T_{i,j}) + \frac{(2k_{i,j+1}k_{i,j})(2\pi r_{j+1}\Delta z)}{(k_{i,j+1}+k_{i,j})\Delta r}(T_{i,j+1}-T_{i,j}) \tag{4-7}$$

$$\dot{Q}_{in,i,j}^{conv} = h(2\pi r_j \Delta z)(T_{i,j-1}-T_{i,j}) \tag{4-8}$$

$$\dot{Q}_{n}^{rad,prim} = N_{prim,n}\dot{Q}_{ray} = \frac{N_{prim,n}}{N_{rays}}\dot{Q}_{arc}\eta_{HFSS} \tag{4-9}$$

$$\dot{Q}_{n \text{ or } i,j}^{rad,emit} = \varepsilon_{i,j}(2\pi r_j \Delta z)\sigma T_{i,j}^4 \tag{4-10}$$

$$\dot{Q}_{n}^{rad,sec} = \sum_{m=1}^{m_{total}} D_{m,n}\dot{Q}_{m}^{rad,emit} \tag{4-11}$$

In Eqns. (4-7)-(4-11), $\dot{Q}_{arc}$ has been already defined in (3-33), η_{HFSS} represents the conversion efficiency of the HFSS, $r_j = r_{c,in}$, $r_m = r_{c,in} + \Delta r/2$, and $r_{j+1} = r_{c,in} + \Delta r$. With that being said, the mass term in Eqn. (4-6) becomes $m = \rho V = \rho(2\pi r_m \Delta r)\Delta z$. Just in a similar manner as presented earlier for the first horizontal layer within the cavity, several equations are obtained representing the heat transfer into different volumetric elements at the boundary surfaces of the receiver. At the outer boundary, the receiver system encounters heat losses in the form of convection and radiation losses, where the ambient temperature is maintained at 25 °C per assumptions stated earlier.

For the fluid phase, the mass conservation states that mass entering is the same as that leaving the control volume, which is equal to $\dot{m}$. Therefore, based on conservation of energy for an element in the fluid phase, energy due to fluid flowing in as well as that of convection heat transfer must equal to that of the fluid flowing out. With that mentioned and by applying the upwind scheme, the equation for the temperature at each location within the fluid phase is simplified and presented in

Eqn. (4-12), where $A = 2\pi r_{in}\Delta z$. By now, all equations representing the heat transfer are obtained and solved numerically to provide the temperature within the receiver for both the transient and steady states.

$$T_{i,j} = \frac{hA}{\dot{m}c_p + hA}T_{i,j+1} + \frac{\dot{m}c_p}{\dot{m}c_p + hA}T_{i+1,j} \tag{4-12}$$

4.4. Results and Discussion

4.4.1. Validation: Numerical Model

Optical Analysis Validation. The first step in validating the numerical model is to start by ensuring that the optical analysis once again converges successfully and provides results that are repetitive, just similar to that performed in Chapter 3. The number of rays required for convergence depends heavily on the size of the discretized elements; when the elements are larger in size, N_{rays} decreases significantly. Throughout this chapter, the solar receiver is discretized into a fine mesh with 462 x 213 elements in the axial and radial directions. The successful convergence of the optical analysis is demonstrated in Figure 4-10, where the (a) normalized power values of primary rays, and (b) normalized distribution factors of secondary rays are plotted w.r.t. the number of rays emitted from the (a) HFSS, and (b) each surface element.

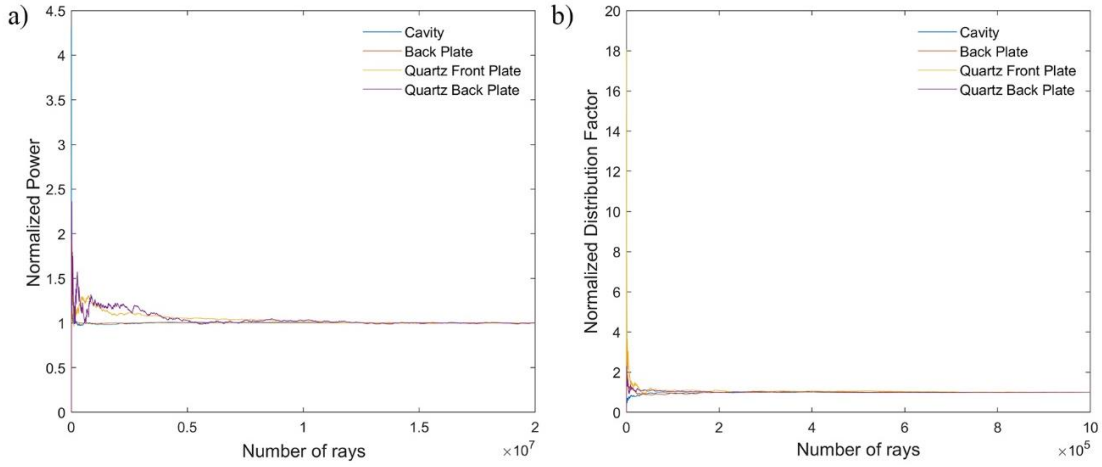

Figure 4-10: Convergence of MCRT analysis for different solar receiver's components for (a) normalized power values of primary rays, and (b) normalized distribution factor values of secondary rays

As shown, all values converge smoothly to unity, with the surface elements with lower power values (quartz plates) in Figure 4-10 (a) taking longer to converge. This behavior is per expectation, as previously discussed in Chapter 3, which results in the convergence of the quartz plates being less important than that of the cavity or back plate. In addition, Figure 4-10 shows the significant

decrease in the value of N_{rays} when moving from the simulation of primary rays to that of the secondary rays. The value of N_{rays} required for the primary rays is 20 times more than that of the secondary rays. This is can be attributed to the nature of the power distribution coming from the HFSS, which have relatively higher gradients and loses a significant portion of power outside the receiver's inner surfaces. With that being said, values of 2 x 10^7 and 1 x 10^6 for N_{rays} have been deemed accurate enough for primary and secondary rays simulations with the aforementioned discretization size.

HFSS Power Distribution. Once the successful convergence of the MCRT simulation is determined, the distribution of power inside the solar receiver can be inspected. Figure 4-11 demonstrates the input heat flux distribution along the surfaces of the solar receiver due to primary rays from the HFSS at an input current of 200 A. The MCRT simulation shows that the region with high flux inside the cavity is the back plate, as expected. This behavior is common in cavity-type solar receivers, where hotspots exist inside the cavity leading to non-uniform temperature distributions. With the results simulated in Figure 4-11, it can be expected that the back plate will be the hotspot region. However, inspecting the entire flux distribution, the region with the highest flux is the front quartz plate that is positioned at the focal plane, where the highest determined flux is approximately 160 kW/m^2. This value correlates very well with the experimental heat flux measured value at a radius of 4.45 cm in Figure 2-10, where the experimental value is 146 kW/m^2. The difference between the two values is due to additional input flux at the inner cylindrical portion of the corner element. Despite the fact that the front quartz plate has the highest flux region, it is not expected to have relatively high temperatures, due to its position within the system that subjects it to great thermal losses. The lowest heat flux region is also shown in Figure 4-11.

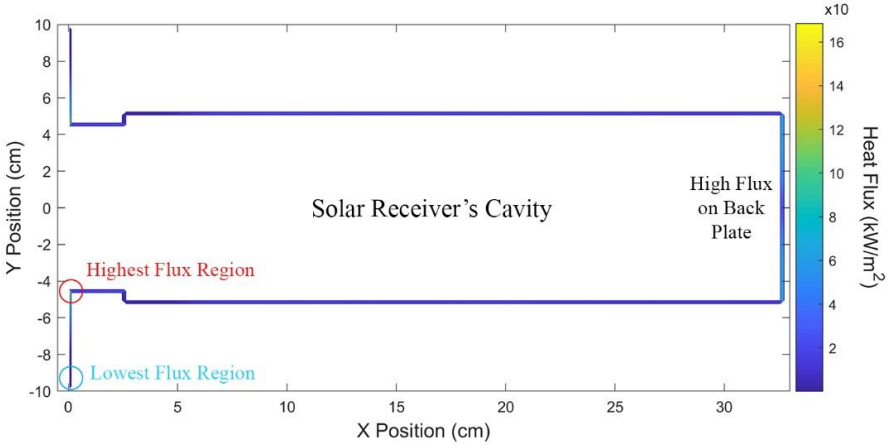

Figure 4-11: Primary rays' heat flux distribution on solar receiver

Material Properties. With the initial validation of the MCRT simulation portion of the numerical model, the heat transfer model will now be validated. As a starting point, the properties of all the materials of the receiver's setup need to be defined. The properties were initially evaluated from appropriate sources and then tweaked to better represent the response of the experimental results and hence the actual model. The material properties used in the numerical model, whether assumed to be constant or as a function of temperature in Kelvin, are summarized in Table 4-2. Properties were assumed to remain constant, unless sufficient data is available to determine the properties as a function of time and the changing properties have a significant impact on the response of the model.

Table 4-2: Material properties used in the numerical model. Temperature, T, is in Kelvin.

Material	$\boldsymbol{\rho}$ (kg/m^3)	$\boldsymbol{c_p}$ (J/kg.K)	$\boldsymbol{k}$ (W/m.K)	**Optical**	**Ref**
Stainless Steel	8238	$-1.78e^{-4}\,T^2 + 4.16e^{-1}\,T + 3.62$	$1.55e^{-2}\,T + 8.92$	$\varepsilon = 0.6$	[101]
Quartz	2203	700	1.3	$\tau = 0.95$, $\alpha = 2.7$ m^{-1}	[87]
Insulation	$160C_\rho$	1050	$(1.61e^{-7}\,T^2 - 4.56e^{-5}\,T + 2.65e^{-2}) + C_k$	-	[102]
Aluminum	2770	875	237	$\varepsilon = 0.8$	[101]
Nitrogen	1.056	1042	$2.75e^{-2}$	-	[101]

In the properties summarized in Table 4-2, only three were modified to closely resemble the overall response of the system. These were the stainless steel's emissivity, insulation's density, and insulation's conductivity. The emissivity of stainless steel can significantly vary depending on the surface condition, and so it was chosen as a parameter to be tweaked. Its value can have major effects on the overall temperature distribution inside the solar receiver. For instance, the highest temperature's value and location can change with different emissivity values. Therefore, the final value of choice, being $\varepsilon = 0.6$, was the closest in resembling the temperature distribution inside the receiver.

The two other tweaked parameters were the insulation's properties. This mainly arose due to the fact that the insulation shell is not completely filled with Superwool Plus blanket, affecting the overall thermal conductivity, and that the insulating material was significantly compressed inside the outer shell, affecting the overall density. Therefore, the insulation's thermal conductivity was modified by adding a constant C_k to the values provided by the manufacturer in order to obtain

temperatures at the outer shell layer that are close enough to that monitored experimentally. In addition, the insulation's density was modified by multiplying the density provided by the manufacturer by a constant C_ρ in order to obtain a transient response that closely resembles the transient response of the system. Hence, compensating for the actual system's setup discrepancies from that evaluated by the manufacturer. The final values of C_k and C_ρ were determine to be 0.3 W/m.K and 2.

Heat Transfer Analysis Validation. The heat transfer analysis discretizes the solar receiver into a fine mesh of 462 x 213 elements that span the entire system. Results from the numerical model were obtained for the transient temperature response of the system up to 6.5 hours, which is the point in time deemed as the steady state. Figure 4-12 shows the transient response of both the experimental and numerical results at five different locations and for four operating conditions. The five locations represent the average temperature values across the front, middle, and back sections of the receiver, in addition to the two positions at the back plate. The four operating conditions span the range of experimental measurements, where the feedstock flow rate and input current values were (a) 7.5 LPM and 160 A, (b) 7.5 LPM and 150 A, (c) 10 LPM and 160 A, and 10 LPM and 140 A.

As can be seen in Figure 4-12, the numerical model accurately represents the temperature distribution within the actual system. It exhibits the same non-uniform distribution across the back plate with the peak temperature being at its center. The average error value for the steady state temperatures shown in Figure 4-12 is 0.3% with a maximum relative error of 1.1%. However, the transient temperature errors at the beginning of the experimental runs are significantly large especially at the front and middle sections of the receiver's cavity. The maximum relative error recorded is approximately 65%, which occurs at the front section of the cavity.

The large initial errors between the experimental and numerical results can be attributed to three factors. The first one, which is believed to be the most dominant, is due to the transient nature of the HFSS, as illustrated and quantified earlier in Figure 2-11. The HFSS starts at approximately 75% of its steady state power and takes approximately 10 minutes to reach the 95% mark. It then reaches its optimal steady state within the first 20 minutes. This transient behavior has not been incorporated in the numerical model, since further identification of the transient behavior was not performed and it does not play a critical role in the system's overall response. However, based on the discrepancies between the numerical and experimental results, the transient behavior seems to be dominant in the directions and regions that intersect the front portion of the solar receiver. Hence,

leading to significantly higher modeled temperatures at the front regions. The second factor is due to the additional components attached to the front of the receiver that are not well modeled, such as the exhaust cleaning mechanism. These components can significantly affect the heat transfer occurring at the front region, which again was not modeled for. The third and final factor is due to the assumption of treating the fluid flow as one-dimensional. This assumption could have been a significant drive for the heat transfer from the backward sections of the receiver to the front ones, leading to higher transient temperature predictions.

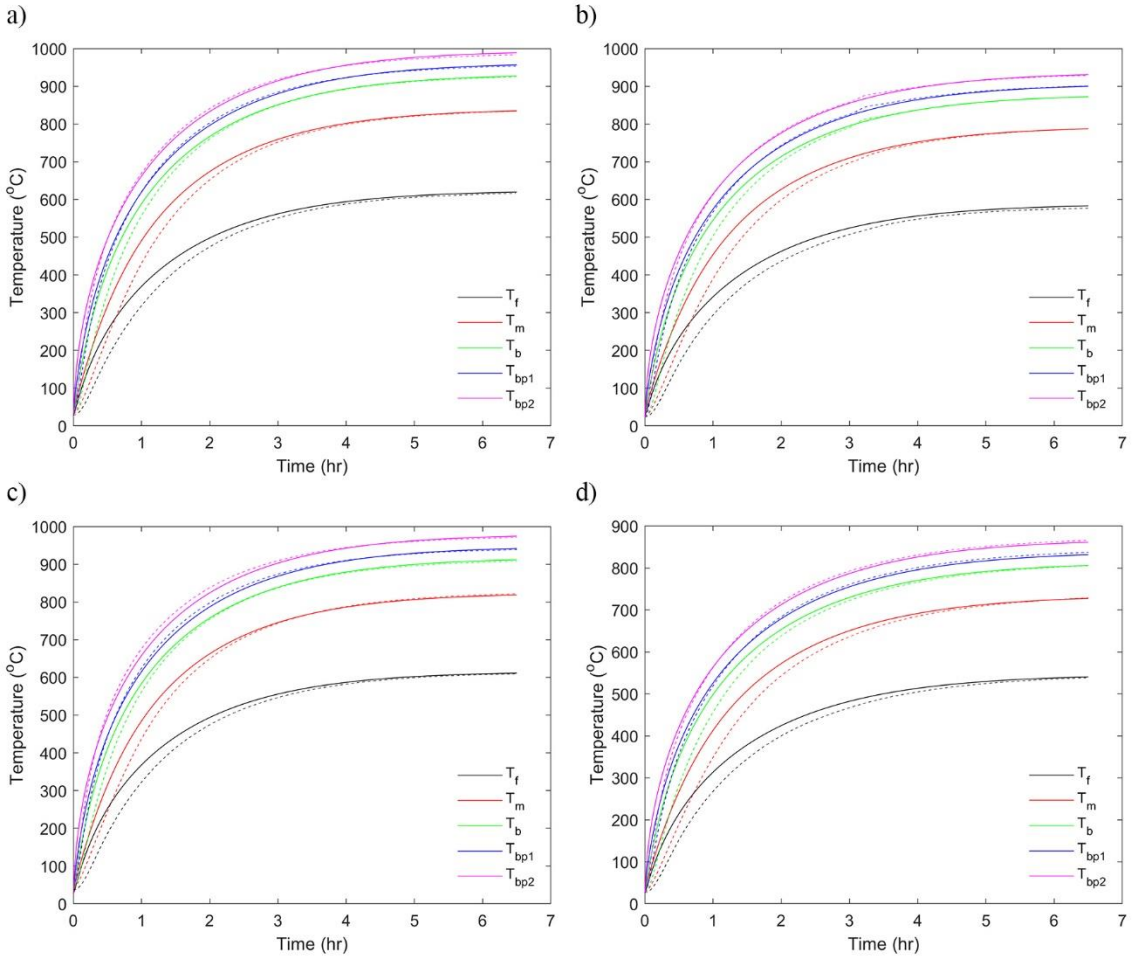

Figure 4-12: Solar receiver's temperature transient response of experimental and numerical results at five different locations and for different feedstock flow rate and input current operating conditions of (a) 7.5 LPM & 160 A, (b) 7.5 LPM & 150 A, (c) 10 LPM & 160 A, and (d) 10 LPM & 140 A.

4.4.2. Numerical Results

Heat Transfer and Power Losses. The heat transfer modes significantly change as the temperature within the solar receiver increases. To evaluate the accuracy of the model further and inspect different modes of heat transfer, the system's losses were evaluated at each time step. The

losses evaluated by the model are split into three modes: radiation losses inside and outside of the receiver's cavity ($\dot{Q}_{Rad}$), convection losses outside of the receiver's cavity to the surrounding ($\dot{Q}_{Conv}$), and convection heat transfer to the feedstock flow ($\dot{Q}_{Flow}$). These losses are evaluated based on the Eqn. (4-13), summation of $\dot{Q}_{out,i,j}^{conv}$ for the outer elements subject to T_{∞}, and $\dot{m}c_p\Delta T_{Flow}$, respectively, where ΔT_{Flow} represents the temperature difference between the feedstock inlet and outlet.

$$\dot{Q}_{Rad} = \sum_{n=1}^{n_{total}} \dot{Q}_n^{rad,emit} - \dot{Q}_n^{rad,sec} \tag{4-13}$$

The power input to the receiver, $\dot{Q}_{In}$, is just the summation over $\dot{Q}_n^{rad,prim}$ and the power consumed in bringing up the cavity to its temperature, $\dot{Q}_{System}$, is just the difference between $\dot{Q}_{In}$ and the sum of the three thermal loss modes, denoted as $\dot{Q}_{Loss}$. Figure 4-13 shows the simulation results of the (a) receiver's steady state temperature contour map, and (b) different modes of heat transfer through the transient response of the system operating under a feedstock flow rate and input current of 7.5 LPM and 160 A.

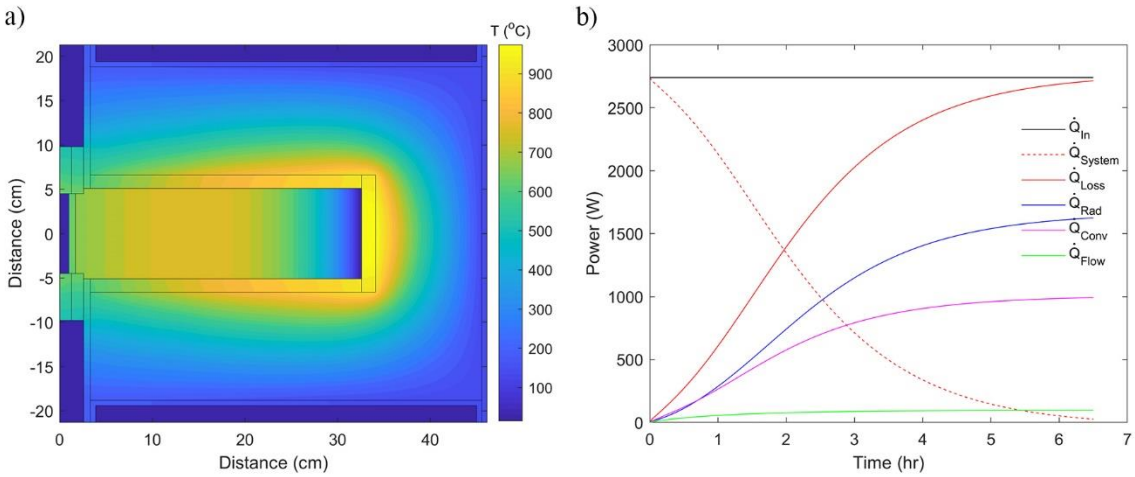

Figure 4-13: (a) Steady state temperature contour map, and (b) Modes of heat transfer though the transient response of the receiver to a feedstock flow rate of 7.5 LPM and input current of 160 A

From the results in Figure 4-13 (b), several observations can be made. First, the system reaches an approximate steady state after 6.5 hours of operation as previously assumed by the steady state criterion, since the value of $\dot{Q}_{System}$ drops from 2740 to 26 W. In addition, the numerical model is energy conservative, as $\dot{Q}_{Loss}$ approaches and never exceeds $\dot{Q}_{In}$ for any additional simulation time. Furthermore, it can be clearly seen that after approximately 2 hours of operation, where the system reaches an average temperature of approximately 700 °C, radiation losses start to dominate the

convection losses. At the approximate steady state, 60% of the input energy is lost through radiation, 36% is lost through convection, and only 4% is transferred to the feedstock flow. Therefore, attempts to increase the overall temperature inside the solar receiver should focus on reductions of the radiation losses.

In addition, the steady state temperature contour map of the solar receiver is shown in Figure 4-13 (a). It is clear from the contour map that there is a significant hotspot region around the back plate. The temperature non-uniformity within the receiver is approximately 37%, which represents the relative difference between the highest (T_{bp2}) and lowest ($\approx T_f$) temperatures with respect to the highest one in °C. Higher temperature non-uniformities within the cavity lead to lower receiver efficiencies since radiation losses are amplified at the hotspots, which results in higher overall radiation losses.

Grid Independence Test. The effect of the chosen mesh size on the results of the heat transfer model was investigated by conducting simulations for three different mesh sizes: (a) fine mesh with 462 x 213 elements, (b) medium mesh with 231 x 107 elements, and (c) coarse mesh with 154 x 71 elements, in the axial and radial directions, respectively. The steady state response of the system was compared amongst the three different mesh sizes to determine the appropriate mesh size to use based on the compromise between accuracy and computational time. Figure 4-14 shows the temperature distribution along the receiver's cylindrical cavity for an input current of 160 A and flow rate of 7.5 LPM for the three aforementioned mesh sizes.

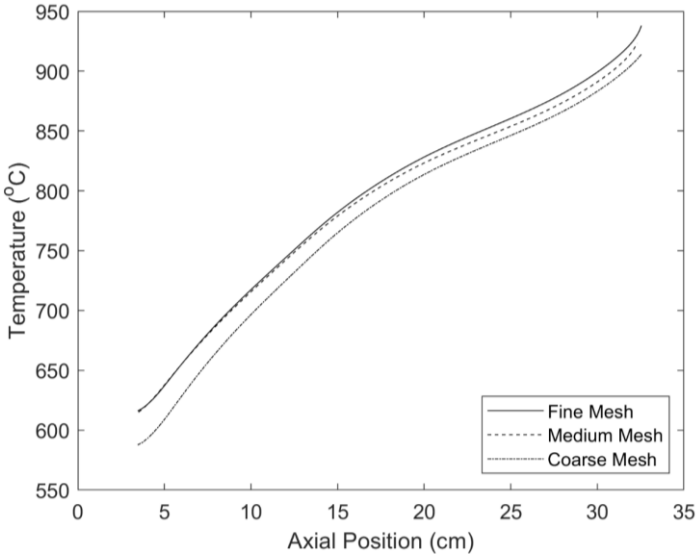

Figure 4-14:Temperature distribution along receiver's cylindrical cavity for an input current of 160 A and flow rate of 7.5 LPM, using three different mesh sizes of 462×213 elements (fine mesh), 231×107 elements (medium mesh), and 154×71 elements (course mesh)

Based on the temperature distribution results shown in Figure 4-14, it is clear that the course mesh had significantly different temperature values than that of the medium and fine meshes. However, it was still able to demonstrate the same trend in the temperature distribution, but with slightly lower temperature values by around 25 °C. The difference between the temperature distribution of the medium and fine meshes is very insignificant. It can be seen that towards to front region of the cavity that both mesh sizes provided identical results. They then start to diverge slightly at the rear end. Nevertheless, the difference can still be treated as insignificant. However, the fine mesh was the final chosen size for the heat transfer model, in an attempt to capture more of the heat transfer dynamics for different conditions in the upcoming sections and in Chapter 5.

Solar Receiver Characterization. In order to characterize the response of the solar receiver, its steady states were evaluated by varying the input current (HFSS's power level) and the feedstock's flow rate. The average temperature inside the receiver's cavity, T_{avg}, is then evaluated at each operating conditions. T_{avg} represents the average temperature value of the four different thermocouple locations: T_f, T_m, T_b, and average of T_{bp1} and T_{bp2}. The average temperature values w.r.t. different operating flow rate and power level conditions are shown in Figure 4-15 (a) as a contour map plot, while the corresponding steady state radiation losses as a percentage of the power input are shown in Figure 4-15 (b).

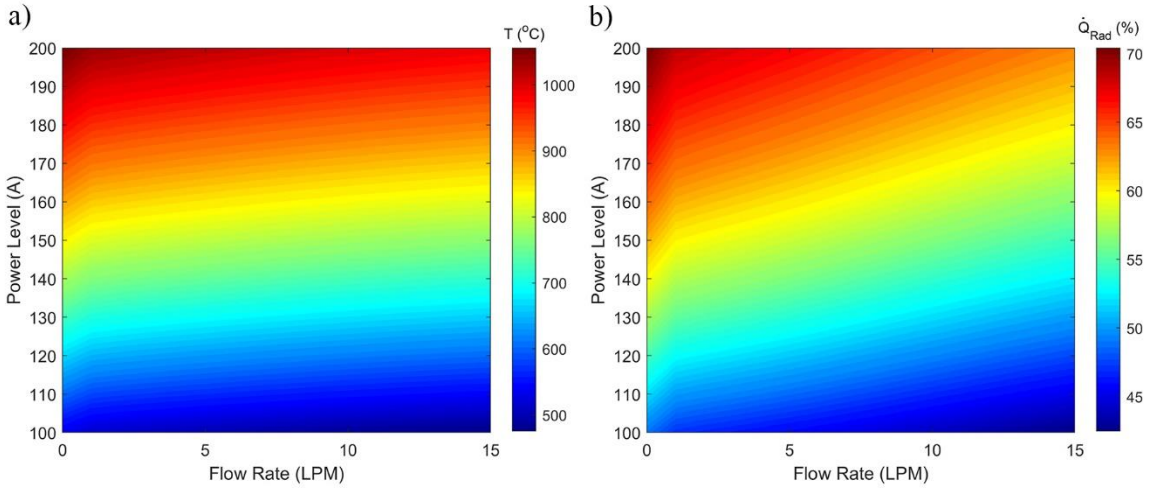

Figure 4-15:Numerical steady state (a) average temperatures and (b) radiation losses, for different operating flow rate and power level conditions

As can be seen in Figure 4-15, the average temperatures range between approximately 500 to 1100 °C, where their corresponding radiation losses range between 40 to 70%. The portion of radiation losses is more dependent on the feedstock's flow rate than the average temperature inside

the solar receiver based on the gradients demonstrated by the contour plots. With such characterization of the receiver, the approximate average temperature and portion of radiation losses can be determined at any point during the day, where the DNI and thus power level is varying. The data in Figure 4-15 can represent the conditions where radiation losses are too high, that it might be more effective to implement a variable aperture to help mitigate the radiation losses. Therefore, even reaching higher average temperature values.

To further validate the numerical model for the varying conditions and results shown in Figure 4-15, the average temperature values were compared to the experimentally obtained temperature values. The experimental runs had four flow rate and three power level values ranging from 2.5-10 LPM and 140-160 A. Both the experimental and numerical average temperature values are summarized in Table 4-3. In addition, Table 4-3 also summarizes the experimental temperature non-uniformity and numerical radiation losses for the different experimental operating conditions.

Table 4-3: Experimental and numerical steady state average temperatures, experimental temperature non-uniformity, and numerical radiation losses for different operating conditions

Flow Rate (LPM)	**Power Level** (A)	**Exp.** T_{avg} (°C)	**Model** T_{avg} (°C)	**Temperature Non-Uniformity** (%)	$\dot{Q}_{Rad}$ (%)
2.5	140, 150, 160	771, 808, 860	766, 808, 858	39.1, 37.4, 37.7	57.2, 59.3, 61.3
5	140, 150, 160	760, 795, 850	757, 799, 848	38.8, 37.1, 37.9	56.2, 58.3, 60.3
7.5	140, 150, 160	744, 788, 837	741, 789, 838	38.5, 37.9, 37.2	55.2, 57.3, 59.3
10	140, 150, 160	731, 767, 823	730, 778, 827	37.8, 36.3, 37.3	54.2, 56.3, 58.3

Based on the results summarized in Table 4-3, it can be clearly seen that the model describes the variation of T_{avg} well. The average error in the average temperature predictions is approximately 0.4%. The one-dimensional assumption for the fluid flow seems to be an acceptable one in terms of the effect of the flow on the receiver's wall temperature, since the numerical model provided values of acceptable accuracies and was representative of the system at different flow rate conditions. Any significant difference between the experimental and numerical results can be attributed to slight changes in the output power of the HFSS, such as a decrease in its output power over time or slight differences in the input current values. In addition, it can be seen in Table 4-3 that there is a small trend for decreasing the temperature non-uniformity due to increases in both the flow rate and power level conditions. Increasing the flow rate helps in reducing the temperature non-uniformity by transferring heat from the back side of the receiver to its front side, while

increasing the power level increases the temperature of the receiver, which increases the radiation heat transfer from the back side to the front side. Therefore, obtaining a slightly lower temperature non-uniformity within the receiver's cavity.

Optimum Aperture. A major parameter of design and performance optimization of the solar receiver is its fixed aperture. The size of aperture can have a significant effect on the temperature distribution inside the receiver's cavity in addition to its highest achievable temperature values. There will be a point where the radiation losses from within the cavity start dominating over the amounts of solar radiation entering the system, depending on the power level, where blocking some of the input energy saves relatively more of the radiation losses. The recovered radiation emission within the cavity will be referred to as $\dot{Q}_{Rec}$, and it can be easily quantified through evaluating the sum over Eqn. (4-11).

In an attempt to determine the optimum aperture size of this solar receiver's design, all its dimensions were kept constant with the exception of the quartz plates' inner diameter, defined earlier as $d_{qp,in}$. This will solely test the effect of the aperture on the temperature inside the cavity due to different aperture sizes, with no modifications to the receiver's cavity. For this, the value of $d_{qp,in}$ was varied between its highest possible value of $d_{c,in}$ to a value of 4 cm. An optimum aperture size lower than 4 cm in diameter is not expected to exist when using the HFSS. The primary rays and secondary rays were re-evaluated using the optical analysis, which is then coupled to the heat transfer analysis to re-evaluate the temperature distribution at each diameter value. As the initial investigation of the aperture's effect, the numerical model was used to simulate the temperature distribution at a flow rate of 7.5 LPM and power level of 160 A. Figure 4-16 shows the maximum temperature, average temperature, and radiation power recovered values for the solar receiver at different aperture diameters.

Based on the results shown in Figure 4-16, the average and maximum temperature values are predicted to reach their peak values at certain diameter sizes. Given the conditions of the simulation in Figure 4-16, the optimum aperture sizes were determined to be 8.2 and 7.6 cm for the maximum and average temperatures. These optimum aperture sizes did not coincide, since the temperature distribution within the receiver's cavity changes with different aperture sizes. Therefore, it is not a proportional change across the cavity, as is shown later in Figure 4-17. In addition, the obtained optimum aperture sizes do not coincide with the aperture size for the peak of $\dot{Q}_{Rad}$, with a value of 7.4 cm, since the aperture blocks some power as a result of its reduced size, which in turn does not compensate for the additional radiation recovered within the receiver's cavity at that lower aperture

size. Although the increase in the average temperature observed in Figure 4-16 is only 29 °C, which is not very significant, this effect can be much more significant in optimizing other receiver designs. To better observe the temperature distribution change within the cavity, the individual thermocouple temperatures at the five different positions with respect to the aperture's diameter are shown in Figure 4-17 (a), while the temperature non-uniformity relationship is shown in Figure 4-17 (b).

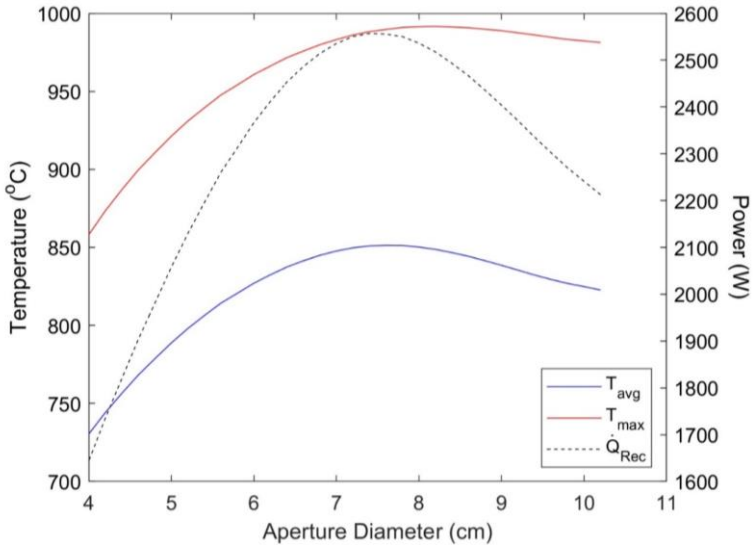

Figure 4-16: Average and maximum temperature values within the solar receiver for different aperture sizes at a flow rate of 7.5 LPM and power level of 160 A

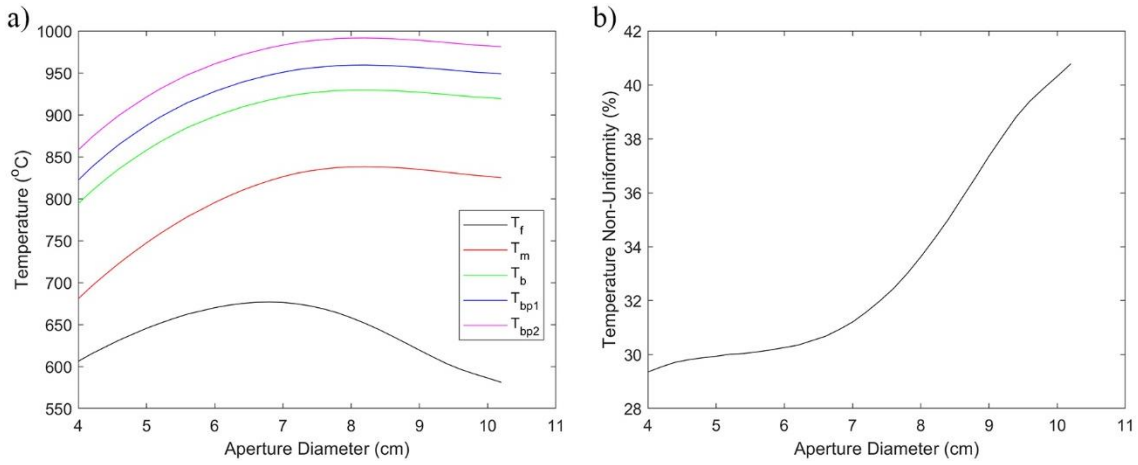

Figure 4-17: (a) Temperature values at different locations, and (b) temperature non-uniformity within the solar receiver for different aperture sizes at a flow rate of 7.5 LPM and power level of 160 A

As shown in Figure 4-17, the temperature distribution within the solar receiver changes as a result of the different aperture sizes investigated. Therefore, the temperature profile at each

individual thermocouple position might have its own unique aperture size at which it peaks. With the data shown in Figure 4-17 (a), T_b, T_{bp1}, and T_{bp2} peak at an aperture size of 8.2 cm, while T_m peaks at 8 cm and T_f peaks at 6.8 cm. Hence, depending on the objective of optimizing the aperture size (obtain highest maximum or average temperature), the optimum size is expected to be different. In addition, Figure 4-17 (b) shows the variation in the temperature non-uniformity based on having different aperture sizes. As a result of decreasing the aperture size from 10.2 to 4 cm, the non-uniformity dropped from 40.8 to 29.4%. However, it can be seen the at an aperture size of around 6.6 cm, the decrease in the non-uniformity starts to be insignificant. The non-uniformity values at the proposed optimum aperture sizes of 8.2 and 7.6 cm are 34.3 and 32.5%. Therefore, optimizing the aperture size does not just provide higher temperature values, but it also significantly improves the temperature distribution within the receiver's cavity.

As previously mentioned, the optimum aperture size is expected to vary with respect to the characteristics of the power source, such as its distribution and power, at any given time. This behavior is one of the reasons behind proposing a variable aperture, which will be introduced in Chapter 5. Therefore, in an attempt to quantify such a variation, the aperture size was varied w.r.t. different power levels from the HFSS, to once again predict the optimum aperture sizes at different operating conditions. Figure 4-18 shows the variation of the average and maximum temperature values within the solar receiver for different aperture sizes at a flow rate of 7.5 LPM and two power levels of (a) 200, and (b) 120 A.

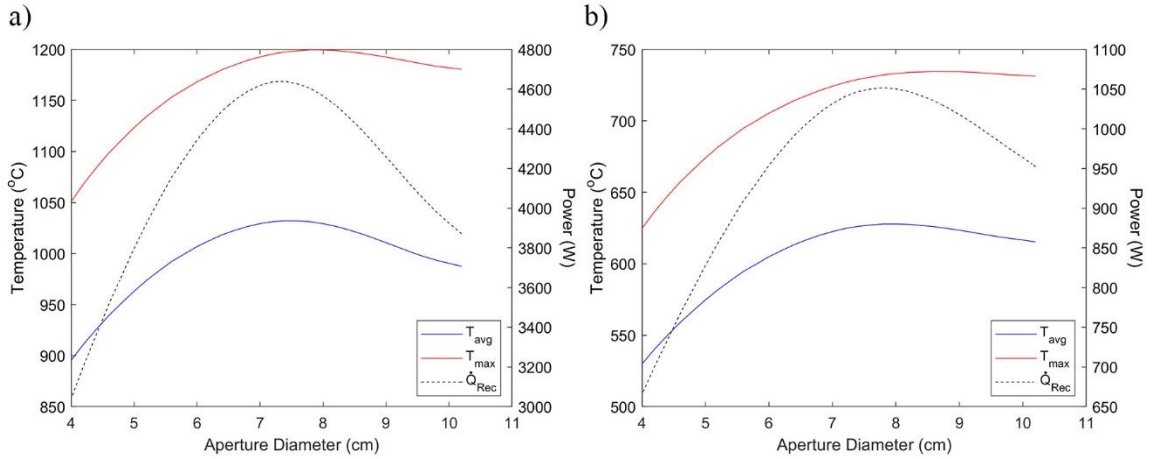

Figure 4-18: Average and maximum temperature values within the solar receiver for different aperture sizes at a flow rate of 7.5 LPM and power level of (a) 200 A, and (b) 120 A

As can be seen from Figure 4-18, the optimum aperture size is a function of the power level from the HFSS, which is representative to variation of the sun's DNI. At power values of 200 and

120 A, the optimum aperture sizes were 7.8 and 8.6 cm based on the maximum temperature, and were 7.2 and 8.0 cm based on the average temperature. The same simulations were replicated for 180 and 140 A, which showed optimum aperture sizes of 8.0 and 8.4, based on the maximum temperature, and 7.4 and 7.8 cm, based on the average temperature. As can be concluded, the optimum aperture sizes for both the maximum and average temperatures decrease as the power level from the HFSS increases. Therefore, with a varying DNI, the solar receiver can be continuously optimized at any given time, based on predictive models, by varying the aperture size of the receiver accordingly in order to obtain maximum process efficiencies.

4.5. Conclusions

In this chapter, the experimental setup at HFGL and its components' designs consisting of the solar receiver and its auxiliary components were presented. The optical analysis previously presented in Chapter 3 was extended to model the radiation power distribution within the solar receiver's components. Results showed a high flux region at the back plate of the receiver's cavity, which can lead to hotspot regions developing at the rear side of the receiver. The results obtained from the optical analysis, namely the primary and secondary rays, were then coupled to a heat transfer model to simulate the solar receiver's response to different operating conditions, such as input power levels and feedstock flow rates. Upon tuning few of the model's material properties, the average error value of the steady state temperatures within the receiver was 0.3%, with a maximum relative error of 1.1%. However, numerical transient temperature values were significantly higher than the experimental one, which was concluded to be due to the HFSS's output power transient behavior previously characterized in Chapter 2. It was then concluded that this transient behavior is significantly dominant at the directions that intersect the front and middle sections of the receiver's cavity.

Upon the validation of the numerical model, the different modes of heat transfer within the solar receiver were studied. It was shown that the majority of the input power is lost through radiation, where it comprised approximately 60% of the losses that occurred at a power level of 160 A. The solar receiver's steady states were then characterized for different flow rates and power levels within the range of 0 to 30 LPM and 100 to 200 A. The simulated average temperatures range between approximately 500 to 1100 °C, where their corresponding radiation losses range between 40 to 70%. Thus, showing the significant contribution of the radiation losses to the overall temperature state of the receiver. This led to the discussion on the optimum aperture size, where it was shown that the current receiver design can be further optimized by reducing its fixed aperture

size. The aperture diameter was varied from 4 cm to the maximum size of 10.2 cm without changing the size of the cavity itself. Through this, the maximum and average temperatures were plotted with respect to the different aperture sizes and for different condition, where the temperatures were seen to peak at a certain aperture size. For a feedstock flow rate of 7.5 LPM and power level of 160 A, the optimum aperture size was 8.2 and 7.6 cm based on maximizing the maximum and average temperatures. It was then finally shown that as the power level from the HFSS is increased (or decreased), the optimum aperture size becomes smaller (or larger). Therefore, leading to the proposal of being able to continuously optimize the performance of the solar receiver at varying sun's DNI. This might be possible to achieve using a variable aperture mechanism, which will be introduced in Chapter 5.

Chapter 5

Variable Aperture Coupled Solar Receiver

In Chapter 5, a variable aperture mechanism is introduced and its design is presented. The purpose of the variable aperture is to be coupled to the solar receiver, previously presented in Chapter 4, in order to control the amount of power entering the cavity or that leaving it through re-radiation losses. The solar energy from the sun cannot be controlled. Therefore, the variable aperture provides a mean of controlling the temperature of the receiver or possibly maximizing it through the behavior illustrated in Chapter 4. Further focus on control is the scope of Chapter 6. Since the variable aperture controls the temperature by blocking a portion of the incoming energy, it is designed with a heat exchanger in an attempt to recover that energy. In this chapter, the response of the system is characterized experimentally and numerically using the in-house developed numerical model. Experiments were performed to characterize the solar receiver's system with the variable aperture, while being air-cooled (natural convection) or water-cooled through the heat exchanger. The numerical model is extended by simulating the variable aperture's effect on the primary and secondary radiation rays, where the model is once again validated through the experimental results. By having a validated numerical model, different test scenarios can be simulated, such as design alterations, scaling up of the solar energy source, and/or control strategies to regulate the temperature within the solar receiver.

5.1. Introduction

Variable aperture concepts are being developed and implemented in a great number of fields for different purposes. Fields of applications include medicine, such as in radiotherapy [103] and radiosurgery [104], optics, such as in optical attenuation [105] and focus regulation [106] , and others, such as in irrigation [107]. For example, in [106], the diaphragm's aperture of a liquid lens is changed to change the shape of two immiscible liquids, which in turn results in tuning the focal length of the lens. However, in radiotherapy applications, a variable aperture is usually implemented to be able to focus and shape the radiation beam, such as that of a micro-CT scanner, to get high resolution images of small animals or deliver controllable therapeutic doses.

A variable aperture mechanism consists of a number of blades, normally not less than four, that move together in order to vary the opening of the mechanism in a desired manner. The motion of the blades can either be achieved through the rotation or translation of the blades. In general, there is no preference for a specific type of motion unless connections exist to or from the blades, such

as water cooling connections. In this case, translational motion is preferred since it is easier to accommodate for the blades' motion. In addition to their type of motion, the blades can either be aligned to move over one another (overlap), as in [106], or slide across one another, as in [108]. Mechanisms that have their blades overlap usually allow for more compact designs. The number and shape of the blades depends significantly on the desired shape of the varying aperture. In most applications, it is usually more desirable to have a circular aperture over a polygonal shaped one, which is more difficult to achieve.

For circular apertures, the edge of the blades need to be curved in order to provide the curvature required for a circular opening or at least to properly approximate one. The most convenient curved edge for blades would be an arc, which means that the mechanism will only allow for a perfect circular opening at the radius of the arc. The aperture then becomes less representative of a circle away from that radius. Furthermore, circular variable aperture mechanisms in literature tend to have a closer approximation of a circular aperture as the number of blades increases, as it would be expected and studied in [105]. Therefore, designing circular variable apertures becomes a challenging task since a perfect circle will only be achieved with a relatively large number of blades, which is not desirable. As the number of blades increases, the mechanism becomes larger in size and weight and more difficult to control and maintain. Hence, a compromise needs to be done between the level of circular approximation and the thickness or size requirements.

Theoretical studies and numerical investigations have shown that a cavity-type solar receiver has an optimum aperture size at which solar irradiance is maximized while re-radiation losses from its cavity are minimized. As previously mentioned in Chapter 4, this optimum aperture depends on many factors, most importantly being the operating temperature of the reactor and power distribution input at the receiver's aperture. Due to the transient nature of the sun's DNI, the optimum aperture is expected to vary throughout the day. Therefore, a variable aperture coupled solar receiver seems to be a promising approach to continuously optimize the aperture size. The aperture will need to be adjusted in a manner so that the additional recovered re-radiation losses from the cavity by closing the aperture to a certain size is in surplus of the incident power blocked. This will allow for higher efficiencies and operating temperatures to be achieved within the solar receiver. Previous variable aperture mechanisms coupled to solar receivers in different forms and control methods can be found in [109–111].

In addition to the variable aperture's application of maximizing the operating temperature within a solar receiver by changing to its optimum aperture size, the variable aperture mechanism

can be also used as a mean of controlling the temperature within a receiver. The type of application will depend on the chemical process involved and its efficiency's variation with respect to the receiver's temperature. In applications that require semi-constant operating conditions, the variable aperture mechanism can be used to directly affect the power distribution inside the receiver, and hence its operating temperature. This method of control can be superior to other methods currently being implemented, such as heliostats and Venetian-blind shutters control [109]. Further work on the subject of maintaining semi-constant temperatures through the variable aperture control will be the focus of Chapter 6.

In this chapter, the design of a variable aperture mechanism for a solar receiver is presented. The mechanism consists of eight blades that move in a translational type of motion to approximate a circular variable aperture. The solar receiver's setup with the variable aperture mechanism will also be presented. Since the mechanism will intercept a significant amount of power from the HFSS when fully opened or varying its aperture's size, the blades are designed with a heat exchanger in an attempt to transform the intercepted power into useful energy. Therefore, the mechanism has four primary water-cooled blades and four secondary air-cooled blades. Once the experimental setup and design has been presented, the response of the system is characterized experimentally. Experiments were performed to characterize the solar receiver's system with the variable aperture, while being entirely air-cooled and partially water-cooled through the heat exchanger in the four primary blades. For the water-cooled experiments, the amount of energy captured by the heat exchanger was quantified for different aperture sizes. The numerical model is then extended, beyond the scope of Chapter 4, by simulating the variable aperture's effect on the primary and secondary radiation rays, where the extended model is once again validated through the experimental results. Once the model has been validated, it is used to characterize the response of the receiver to different operating conditions and propose some design alterations.

5.2. Experimental Setup

5.2.1. Design of Variable Aperture

The variable aperture mechanism was designed to have several characteristics of interest in its application for cavity-type solar receivers. The overall design functional requirements to be met by the variable aperture are listed below. The mechanism needs to:

- closely resemble the iris of an eye by having a circular aperture. A circular aperture is preferred over a polygonal one, since the heat flux distribution incident on a solar receiver

from a parabolic/ellipsoidal reflector is circular in nature and has significantly high gradients. Therefore, a non-circular aperture will severely affect the power distribution inside the receiver, leading to a more non-uniform temperature distribution across its cavity. In addition, it will not be capable of resembling an optimum aperture size at different operating conditions, since the variable aperture will be blocking relatively higher solar power in some sections, while relatively lower in other sections as it changes its size.

- have a simple translational motion of the blades without any change to their orientation. This would allow for easy connections to be established from and to the blades, such as water connections, without any tangling or jamming issues.
- accommodate for a heat exchanger. This would allow for recovering a portion of the energy intercepted by the variable aperture mechanism in an attempt to increase the overall process efficiency of the solar reactor. The energy can be recovered as heat stored in a working fluid. In the case of the experimental work here, water will be used as the working fluid.
- be able to withstand significantly high thermal flux levels and thermal stresses, in addition to having a relatively good thermal conductivity. The variable aperture mechanism will be subjected to high thermal flux levels with high gradients and different operating conditions throughout a day. Therefore, it needs to be able to withstand these conditions for a prolonged period of operation. The mechanism's material also needs to be a good thermal conductor to be able to transmit energy efficiently to the working fluid in the heat exchanger.
- have a maximum aperture size similar to the fixed size of solar receiver. This would allow for a more flexible operation of the receiver, where the aperture can be changed up to the designed fixed aperture at the designed operating conditions.
- be compact in size and thickness. This would allow for easier integration with the solar receiver system and lower disturbance to the heat flux distribution at the aperture size of the receiver's fixed aperture.

With the overall design functional requirements defined earlier, the design of the variable aperture mechanism shall now be presented. The fabricated and fully assembled mechanism at the maximum aperture size is shown in Figure 5-1 for its front and rear views.

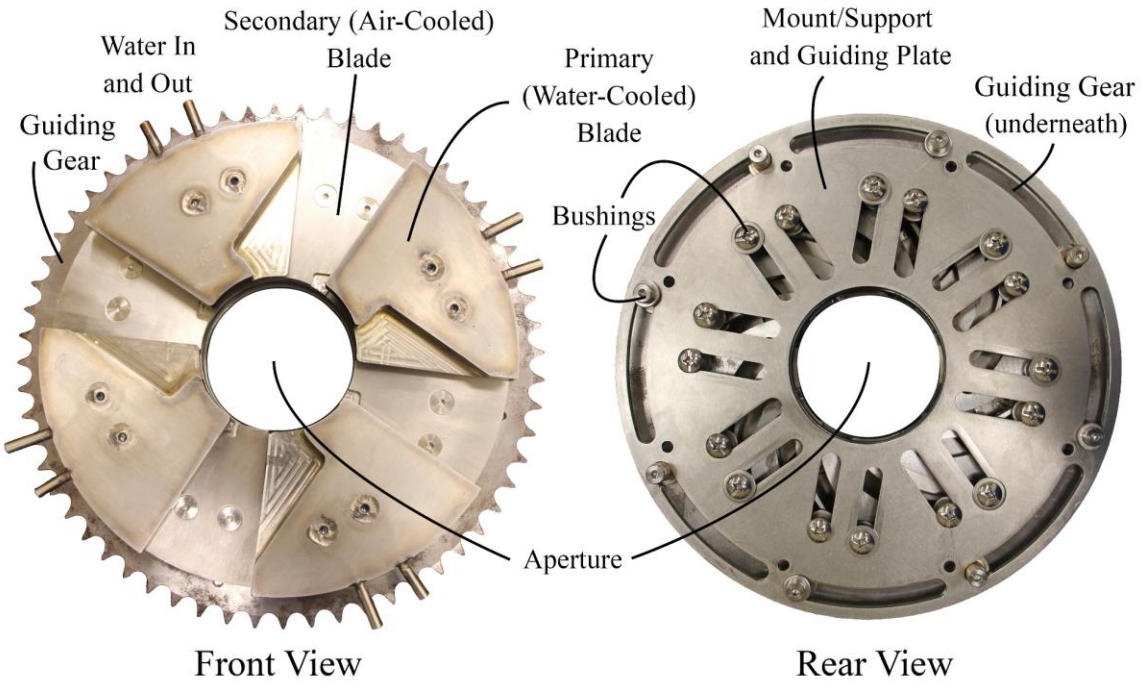

Figure 5-1: Illustration of the variable aperture, in real view, for a maximum opening size of 8.75 cm in diameter

As can be seen in Figure 5-1, the blades of the variable aperture mechanism have curved edges. Unlike some other mechanisms' blades that have straight edges, the blades presented here need to be curved in order to better approximate a circular aperture. With that being said, the blades are designed to provide a perfectly circular aperture when fully opened, by having their edges curved with arcs of that dimension. In addition, the variable aperture mechanism consists of eight blades in total. This number was based on a compromise between the level of circular aperture resemblance and the overall thickness of the mechanism. With eight blades in total, the mechanism's variable aperture can approximate a circular aperture well, without significantly increasing the mechanism's thickness. The overall thickness of the entire mechanism is approximately 4.0 cm.

As illustrated in Figure 5-1, the eight blades are divided into two groups: primary and secondary blades. The primary and secondary blades alternate, creating a fully circular aperture. The primary blades are coupled with a heat exchanger by designing channels that flow through them and cover most of their surface areas for a more efficient energy recovery system. The primary blades are split into two parts, lower and upper plates, that are clamped (bolted) together to form the primary blade and house the flow channels. The two parts of the primary blade and its water cooling channels are shown in Figure 5-2, where the support holes that connect the primary blade to the

mechanism are also shown. As for the secondary blades, they have much thinner diameters and do not have water cooling channels. Therefore, they are referred to as “air-cooled”. The secondary blades are not water-cooled, since coupling them to a heat exchanger would significantly increase the overall thickness of the mechanism. In addition, the secondary blades only cover up a relatively small surface area of the overall mechanism when fully opened, and are completely shadowed at smaller aperture sizes, as shown in Figure 5-3. Therefore, the energy intercepted by the secondary blades is not very significant. Finally, both the primary and secondary blades’ edges are designed like two-step stairs that allow the blades to overlap at smaller diameters for a more compact design (Figure 5-3). The total thickness of the primary blade is approximately 1.25 cm, while the secondary blade is just 0.45 cm in thickness.

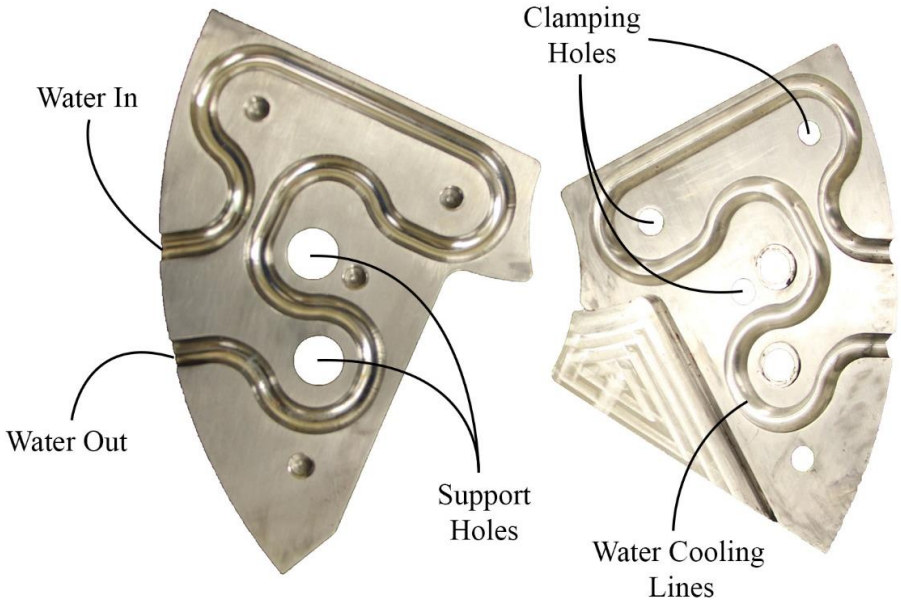

Figure 5-2: Cross-sectional view of the fabricated primary blade, showing the water cooling channel

5.2.2. Motion of Variable Aperture

The motion of the variable aperture mechanism’s blades was designed to be in a translational manner. This helps in avoiding any tangling or jamming issues between the water connections of the primary blades. The translational motion of the blades was achieved using mounting/guiding plate in addition to a guiding gear, as shown in Figure 5-1. The thickness values of these two components are 0.45 and 0.85 cm, respectively. The function of the mounting/guiding plate is to attach the mechanism to the solar receiver, while constraining the blades in a single axial motion. Moreover, it supports the bushings from the guiding gear, so that the gear rotates in a constrained circular motion as desired. It finally connects and supports all the blades (primary and secondary),

and keeps them within their desired levels and positions. Therefore, the mounting/guiding plate is not allowed to rotate. On the other hand, the guiding gear is the component that forces all the blades to translate in a synchronized motion. By rotating the guiding gear, through a driving chain, the arc paths within the gear, best shown in Figure 5-4, force the blades to follow the paths of the arcs, while still adhering to the constrained path set by the mounting/guiding plate. Hence, obtaining a translational motion that allows to control the aperture's size of the mechanism. Figure 5-3 shows the front and rear views of the fabricated variable aperture mechanism at three different opening diameters of 6, 4, and 2 cm. As can be seen, the variable aperture closely resembles a circular aperture at its different sizes. However, this resemblance decreases with decreasing diameters, as can be seen in Figure 5-3.

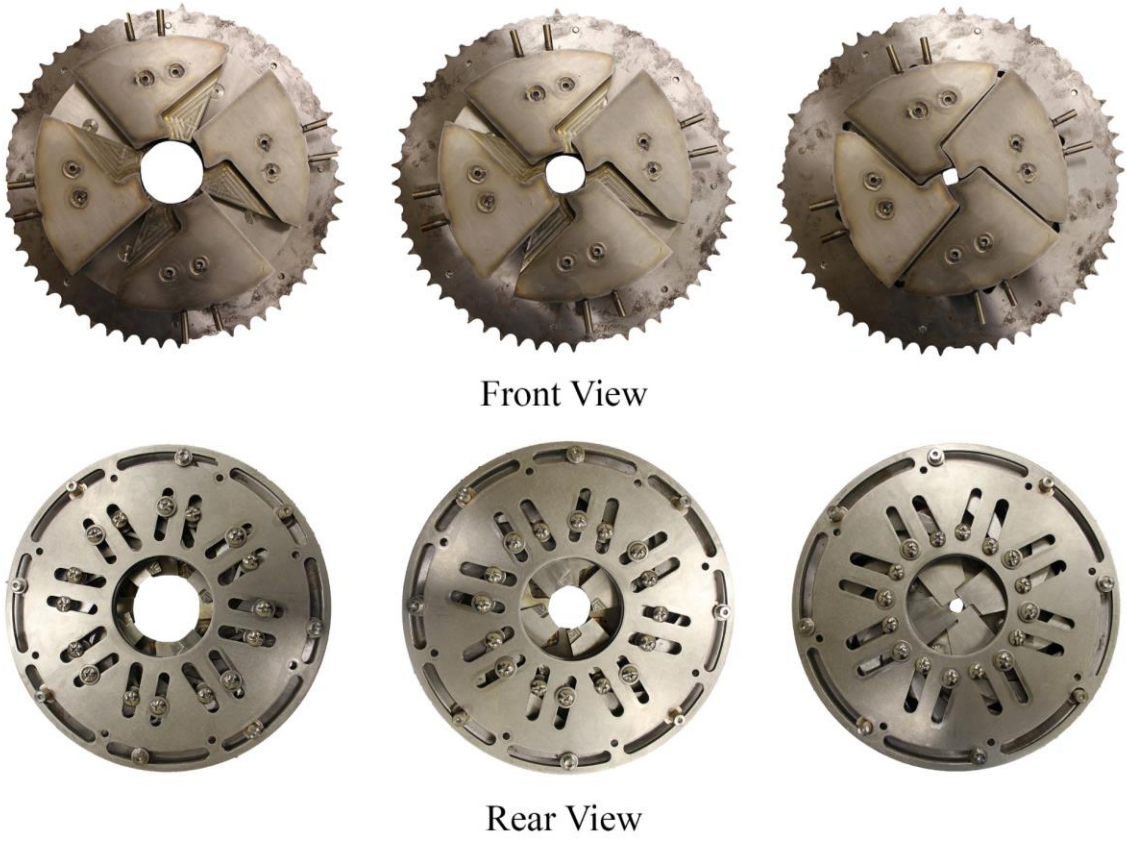

Figure 5-3: Front and rear views of fabricated variable aperture at opening diameters of 6, 4, and 2 cm

To be able to control the variable aperture's size, the governing relationship between the rotation of the guiding gear to the motion of the blades need to be obtained. This will in turn provide a relationship for the number of motor steps or rotation required to obtain any desired aperture size. The schematics of the guiding gear and mount/guiding plate of the variable aperture mechanism

are shown in Figure 5-4, where O represents the origin, c represents the center of the arc, and x_f represent a point with a fixed x-coordinate. From Figure 5-4, the variation of the radius or diameter of the variable aperture can be obtained analytically based on the equation of the paths that govern its motion.

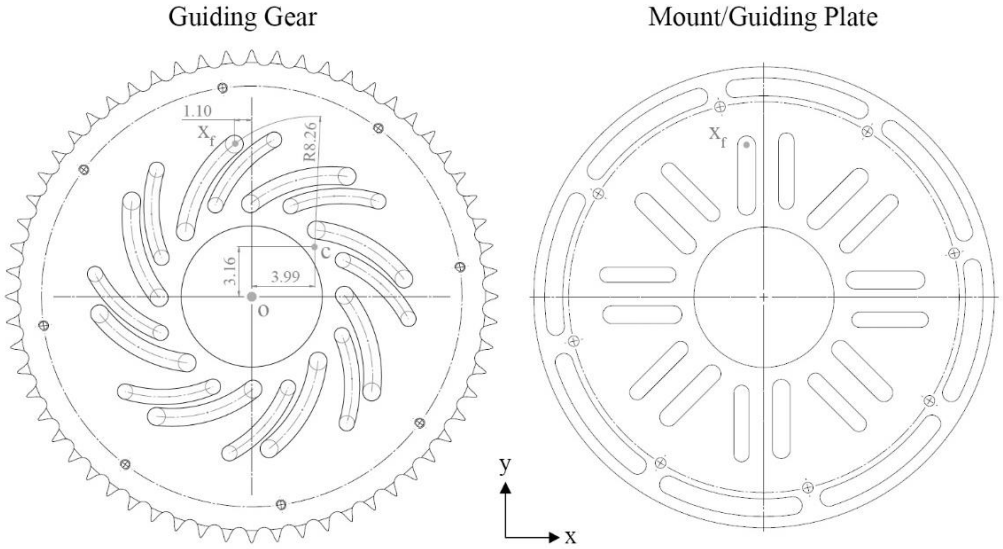

Figure 5-4: Schematics of the guiding gear and the mount/guiding plate of the variable aperture mechanism, where all measurements are in cm

Only one of the arc paths shown in Figure 5-4 will be considered, since the other paths have the same exact pattern. By considering the path within the guiding gear with its dimensions shown in Figure 5-4, the analytical position of the blade's support can be obtained by starting with the equation of a circle presented in Eqn. (5-1).

$$(x - x_c)^2 + (y - y_c)^2 = R_{circle}^2 \tag{5-1}$$

where R_{circle} = 8.26 cm, $x = x_f$ = –1.10 cm, and the initial values of x_c and y_c are 3.99 and 3.16 cm, as shown in Figure 5-4 and while taking the center of the aperture as the origin. In addition, y is the vertical position of the arc path, where it is related to the blade's curved edge through $y = r$ + 5.21, with r being the radius of the aperture. With the initial values of x_c and y_c, the initial polar angle β that the path creates with the x-axis when the aperture is fully opened is 38.3°. When the guiding gear rotates, the values of x_c and y_c change and are functions of the polar angle θ, as shown in Eqn. (5-2), where $R_c = \sqrt{3.99^2 + 3.16^2}$ = 5.09 cm.

$$x_c = R_c \cos(\theta + \beta) \quad and \quad y_c = R_c \sin(\theta + \beta) \tag{5-2}$$

Substituting Eqn. (5-2) into Eqn. (5-1) and solving for r gives Eqn. (5-3).

$$r = 5.09\sqrt{-0.43\cos(\beta_\theta) + \sin^2(\beta_\theta) + 1.58} + 5.09\sin(\beta_\theta) - 5.21 \tag{5-3}$$

where $\beta_\theta = (\pi\theta + 120.4)/\pi°$. Eqn. (5-3) then provides the relationship between the radius of the aperture when varying the angle of rotation of the guiding gear by $\theta°$, starting from the fully opened position. As can be seen in Figure 5-4, the guiding gear will need to rotate clockwise to start closing the aperture. Hence, θ will have negative values. By only considering the magnitude of angular rotation, its relationship w.r.t. the aperture's diameter can be plotted as shown in Figure 5-5.

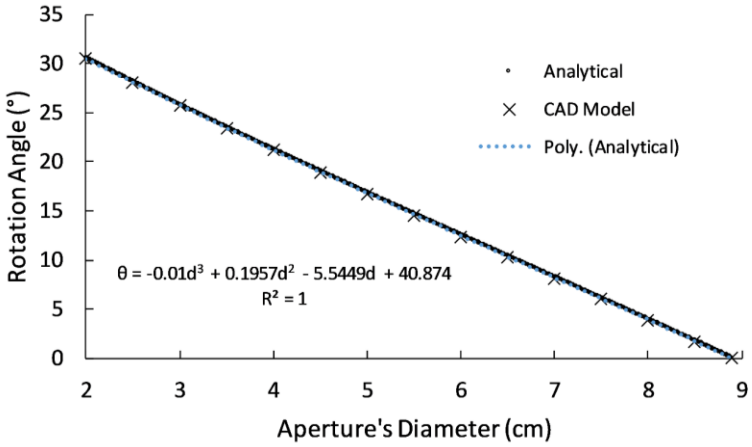

Figure 5-5: Relationship of variable aperture mechanism's opening diameter to the rotation angle of the guiding gear

In order to obtain a simpler expression to be implemented in the control algorithm of the variable aperture, the analytical relationship of the aperture's radius w.r.t. the angle of rotation is best-fitted with a third order polynomial equation. The best-fit polynomial plot and equation are shown in Figure 5-5 and Eqn. (5-4). This shows that there is no significant harm in treating the relationship as a third order polynomial. Therefore, Eqn. (5-4) will be used from now on to control the variable aperture, where θ and d are in degrees and cm. For a quick verification of the analytical solution, values of the angular rotation for different aperture sizes were also obtained from the CAD model of the mechanism. These values correlate well with the analytical solution provided by Eqn. (5-3), as shown in Figure 5-5.

$$\theta = -0.01d^3 + 0.1957d^2 - 5.5449d + 40.874 \quad (5\text{-}4)$$

5.2.3. Auxiliary Components

The auxiliary components of the variable aperture mechanism consist of a stepper motor, gearbox, motor mount, bearing, and gear. The complete setup is shown in Figure 5-6. The stepper motor, SureStep DC integrated stepper motor and drive (model number STP-MTRD-17038E), has a NEMA 17 frame size, maximum holding torque of 0.48 N·m, rotor inertia of 0.082 kg·cm^2, adjustable steps per revolution of 200 to 25,000 steps, and finally an external encoder. The stepper motor has been adjusted for 200 steps per revolution. In addition, the stepper motor has been

attached to a gear box, SureGear precision planetary gearbox (model number PGCN17-505M), that has a 50:1 gear ratio and allows for a nominal output torque of 16 N·m. The final component is the motor gear, that has a gear ratio of 3:1 with respect to the guiding gear of the variable aperture mechanism. With that being said, the stepper motor will need to perform 30,000 steps for a complete rotation (360°) of the guiding gear and approximately 2500 steps to move from a fully opened aperture to a fully closed aperture of 2 cm. Figure 5-6 also shows the motor's air cooling line, which is required for a safe continuous operation around the solar receiver's elevated temperatures.

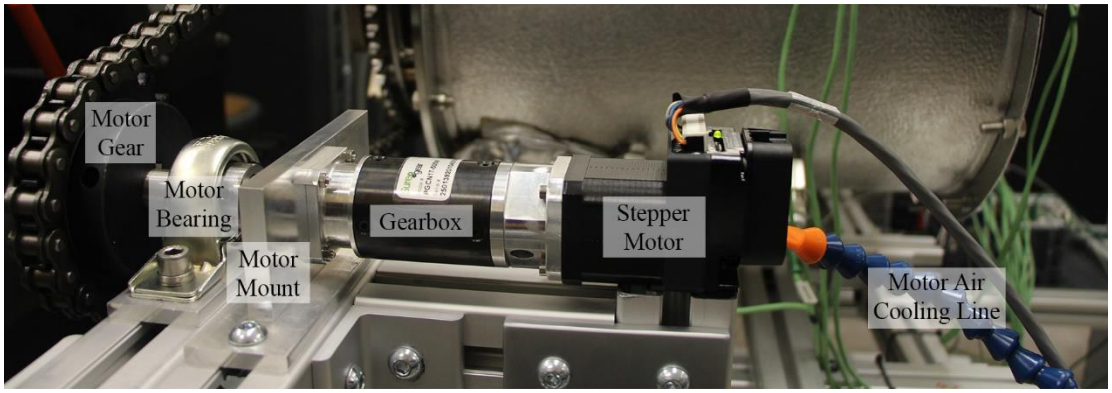

Figure 5-6: Auxiliary components for the variable aperture mechanism

5.2.4. Air-Cooled Variable Aperture Setup

The air-cooled variable aperture experimental setup is shown in Figure 5-7, demonstrating the different components and their assembly with respect to the solar receiver. Experiments without the use of the coupled heat exchanger were performed at different aperture sizes to test the effect of water-cooling the variable aperture on the temperature distribution within the receiver. Not having the blades water-cooled could potentially provide higher cavity re-radiation savings (shown in Figure 5-7a) and radiation emission into the receiver in addition to lower conduction losses. During the air-cooled experiments, all the cooling channels were completely free of water.

5.2.5. Water-Cooled Variable Aperture Setup

The air-cooled variable aperture setup was not allowed to run for more than few days in order to avoid the deterioration of the mechanism due to prolonged exposure to high thermal fluxes. Therefore, after characterizing the solar receiver's steady states with an air-cooled variable aperture, the rest of the experimental work was conducted using a water-cooled one. The experimental setup of the water-cooled variable aperture is shown in Figure 5-8. The primary blades are connected together and to the water supply inlet and outlet lines, through the use of stainless

steel flexible tubing, as shown in Figure 5-8. The stainless steel tubing is capable of withstanding the heat flux that it is exposed to at smaller aperture sizes.

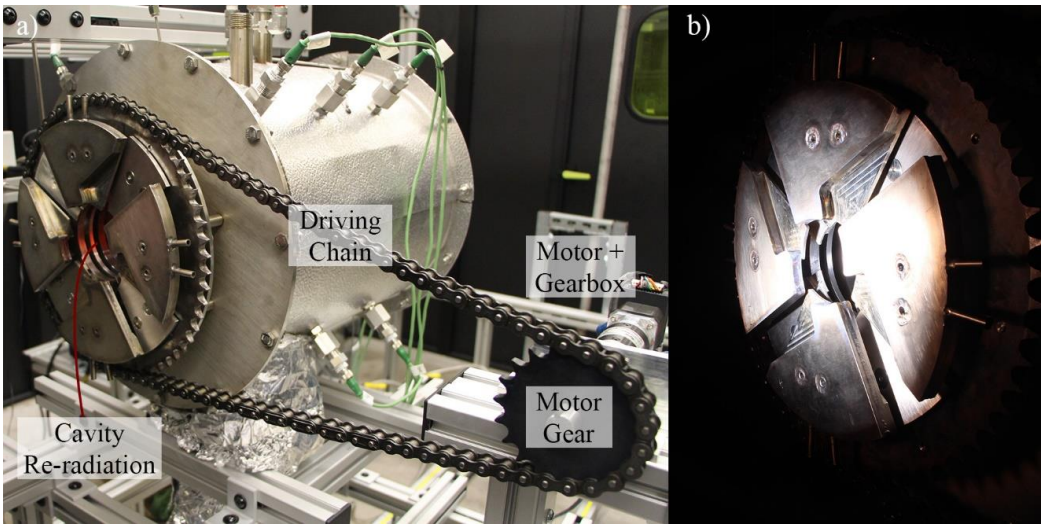

Figure 5-7: Air-cooled variable aperture experimental setup (a) after an experimental run, showing cavity re-radiation, and (b) during an experimental run

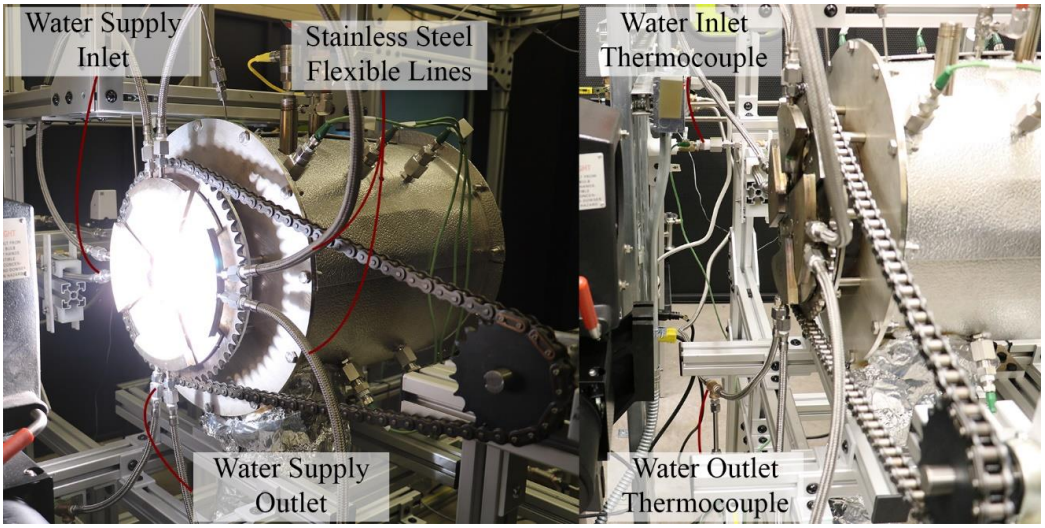

Figure 5-8: Water-cooled variable aperture experimental setup

In order to be able to quantify the amount of energy captured by the heat exchanger, type K thermocouple probes are connected to the water supply inlet and outlet lines as shown in Figure 5-8. The water flow rate is always kept below 1.0 L/min (usually around 0.4 L/min) to be able to measure a higher temperature difference, and hence decrease the uncertainty within the results due to the thermocouple probes. The water flow rate is being measured and monitored using a model S-111 flow meter provided by McMillan Company, which has a flow range from 0.1-1.0 L/min

with an accuracy of 1%. Connections are established between the cRIO and the flow meter to allow for continuous data acquisition.

5.3. Methodology and Procedure

The numerical model created earlier in Chapter 4 is modified in order to include the variable aperture mechanism. The variable aperture is assumed to be circular at all sizes and hence can be treated as a surface given by Eqn. (5-5), for different aperture radii of r_{ap}.

$$\sqrt{x^2 + y^2} < r_{ap} \quad \text{for} \quad z = -0.04 \text{ (front side) or } -0.02 \text{ (rear side)} \tag{5-5}$$

Eqn. (5-5) can then be used in the optical analysis to determine the variable aperture's effect on the primary and secondary rays of the solar receiver. This is the only mode at which the variable aperture is included in the model, since its temperature distribution is assumed to be insignificant and hence not included in the heat transfer model. Therefore, any radiation intercepted by the mechanism is assumed to be lost and the mechanism does not have any radiation emissions to the receiver.

In characterizing the effect of the variable aperture mechanism, steady state temperature values within the receiver are obtained in the same manner as in Chapter 4, keeping the same steady state criteria. The useful power captured/recovered from the mechanism can be easily obtained through Eqn. (5-6) for any moment in time during experiments.

$$\dot{Q}_{cap} = \dot{m} c_p \Delta T = \dot{V} c_p (T_{out} - T_{in})/60 \tag{5-6}$$

where $\dot{V}$ represents the water flow rate in L/min, T_{out} and T_{in} represent the thermocouple recorded temperatures, and c_p is assumed to be constant with a value of 4187 J/kg·K. The useful power captured can provide a basis for efficiency calculations w.r.t. the amount of power actually intercepted by the variable aperture mechanism. The power intercepted by the mechanism can be easily obtained from the primary rays' optical analysis (at z = –0.04) and can be verified by the experimental intercepted power at the focal plane using the results in Figure 2-9 and Figure 2-10. Once the intercepted power w.r.t. different aperture sizes has been obtained, a polynomial function can be fitted to the data to provide a mean of evaluating the power intercepted at any given period of time throughout an experiment. The relationship and fourth order best-fit polynomial equation are shown in Figure 5-9.

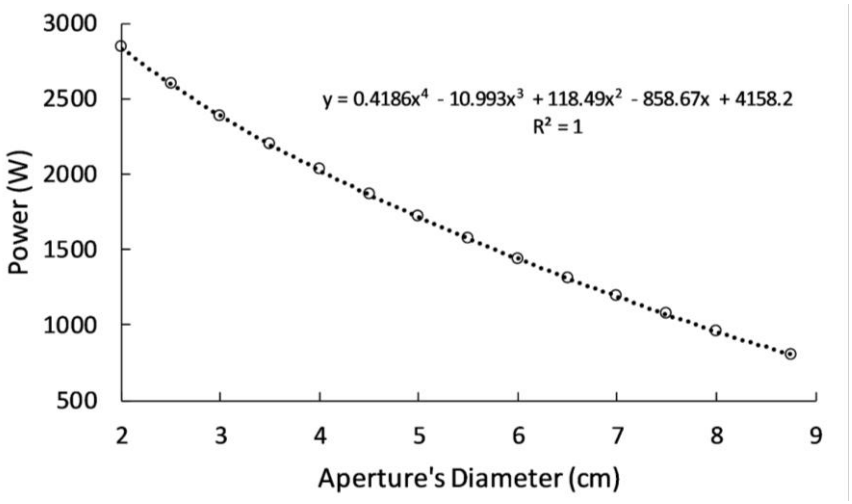

Figure 5-9: Relationship of power intercepted by variable aperture mechanism to its diameter

5.4. Results and Discussion

5.4.1. Air-Cooled vs. Water-Cooled Variable Aperture

The first part within the results section is to investigate the effect of water cooling the variable aperture and whether it has any effect on the temperature distribution inside the solar receiver. For this, the steady state temperature values across the receiver were obtained experimentally for different aperture sizes (ranging from 2 to 8.75 cm), while the variable aperture mechanism is air-cooled and water-cooled. The rest of the experimental conditions were kept relatively the same throughout, including the duration of experiment and starting temperatures, where the feedstock flow rate and power level were maintained at 7.5 LPM and 160 A. The experimental temperature values at different positions within the receiver are shown in Figure 5-10 w.r.t. the aperture's diameter for the two cooling methods. For the air-cooled experiments, the minimum aperture was only set to 4 cm in diameter to avoid the deterioration of the mechanism due to high radiation flux levels at lower sizes.

Based on the results shown in Figure 5-10, the steady state temperatures were not affected by water cooling the variable aperture mechanism. The two sets of temperatures at different positions and while air cooling or water cooling the mechanism were nearly identical at smaller aperture sizes and were slightly higher for the air-cooled experiments at larger aperture sizes. However, the maximum difference between the two sets of temperatures was approximately 4 °C or 0.45%. This difference is insignificant and can be attributed to changes in the uncontrolled variables, such as the decrease in xenon arc's output power over its operating hours.

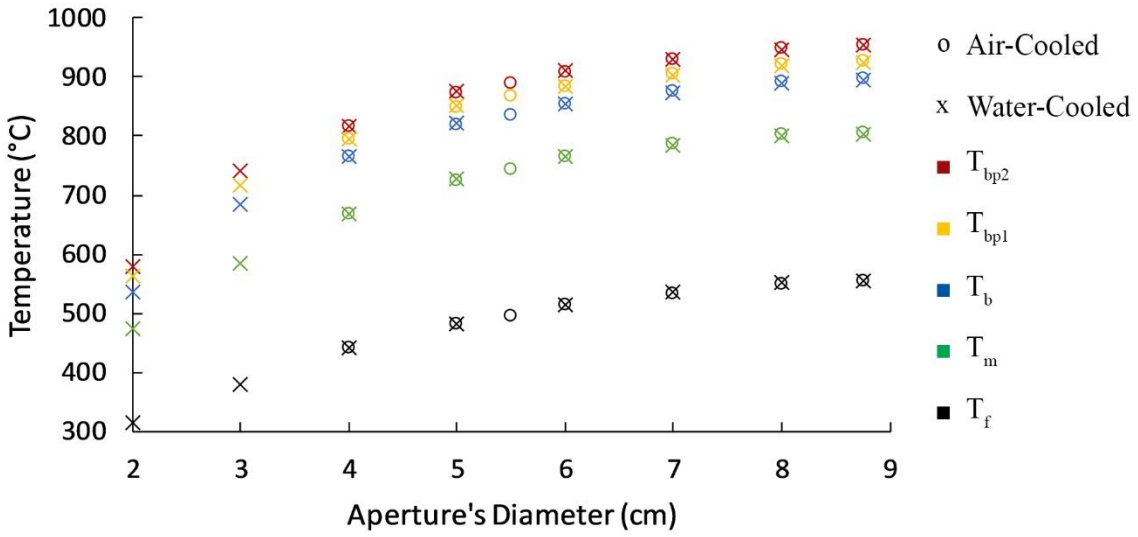

Figure 5-10: Steady state temperature distribution for air-cooled and water-cooled variable aperture at different diameters for a feedstock flow rate of 7.5 LPM and power level of 160 A

Furthermore, the addition of the variable aperture mechanism created a significant drop in temperatures within the solar receiver, with its front side having the most significant decrease. The steady state temperatures at T_{bp2}, T_{bp1}, T_b, T_m, and T_f for the experiment without the aperture mechanism and at a feedstock flow rate and power level of 7.5 LPM and 160 A (Figure 4-12a) were 984, 954, 926, 835, and 618 °C, while they were 956, 927, 898, 807, and 557 °C for experiments with the mechanism having a maximum aperture diameter size of 8.75 cm. This shows a drop of approximately 28 °C at all thermocouple positions, with the exception of the front thermocouple that had a drop of 61 °C, which is more than double. This is due to the reason that adding the variable aperture mechanism to the solar receiver intercepts the power from the HFSS that was previously intercepted by the front quartz plate and receiver's front section. Therefore, much lower powers are being absorbed by the front portion of the receiver, hence decreasing its temperature value the most. This behavior in addition to the thickness of the variable aperture, which intercepts slightly more power, results in a decrease in temperature values across the rest of the receiver. Such behaviors led to an increase of temperature non-uniformity, where it increased from 37.2% to 41.9% with the variable aperture fully opened at 8.75, and to 45.5% with the variable aperture fully closed at 2 cm. The general trend shows an increase in temperature non-uniformity as the variable aperture mechanism closes.

5.4.2. Numerical Model Validation

Based on the results discussed earlier, the power intercepted by the variable aperture mechanism seemed to not be transferred to the front side of the receiver. Therefore, the previously stated assumption of not including the mechanism in the heat transfer analysis, but rather only in the optical analysis, is now justified. With this assumption, the numerical model was updated using the new results from the optical analysis, where the steady state temperature values at different positions were obtained. Figure 5-11 shows a comparison between the experimental (water-cooled) and numerical steady state temperature values at different positions for aperture diameters ranging from 2 to 8.75 cm, while maintaining feedstock flow rate and power level at 7.5 LPM and 160 A.

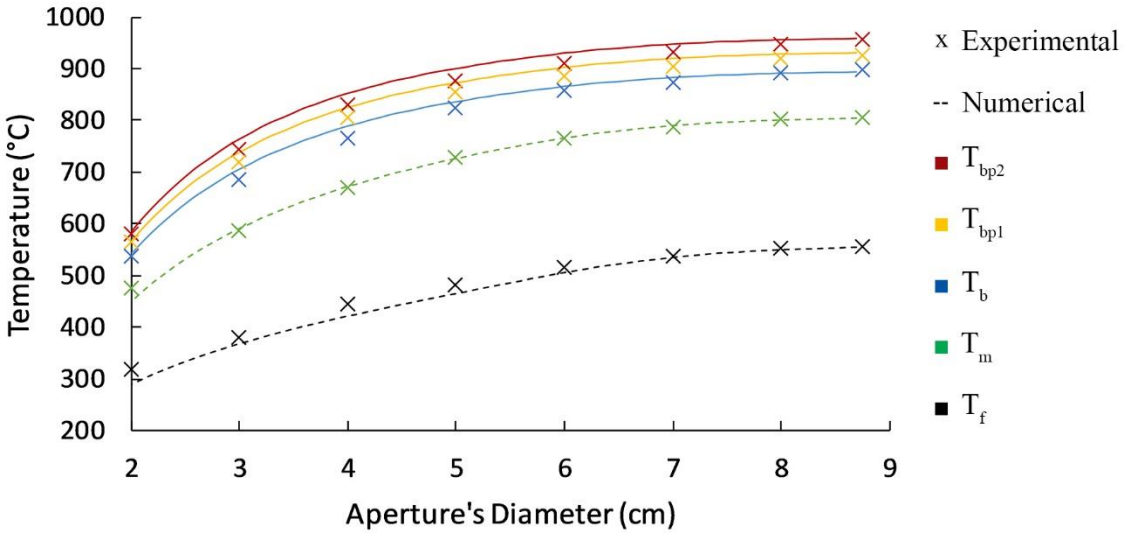

Figure 5-11: Temperature distribution comparison between numerical model and water-cooled experimental results with the variable aperture at different diameters for a feedstock flow rate of 7.5 LPM and power level of 160 A

As can be seen in Figure 5-11, the model comprising the variable aperture mechanism and its assumptions provides a satisfactory representation of the experimentally obtained results. The model simulates the system more accurately at larger aperture sizes, where lower temperature relative errors are observed between the numerical and experimental results. The model seems to diverge a little bit from the experimental results at the rear side of the receiver and for diameter sizes of 3 to 6 cm, where the model then seems to converge again for diameter sizes of 3 cm and below. This is due to the assumption of treating the variable aperture as a single surface at the higher location of the primary blades, whereas in reality, the secondary blades and second step of the primary blades are at a position further away from the HFSS. Thus, this creates the biggest errors in the region of 3 to 6 cm since the variable aperture's effect becomes much more significant

for aperture sizes of 6 cm and below. The errors then decrease in the region of 3 cm and below because the higher steps of the primary blades become the only visible portion of the mechanism, which coincides with the assumption implemented by the model. In addition, the model slightly overestimates some of the temperatures at all positions, with the exception of the front thermocouple position. This is due to the assumption already implemented, where the variable aperture was not considered in the heat transfer analysis. The model's maximum relative temperature error at the front position within the receiver is approximately 8.5%, which also represents the maximum error across all locations. The rest of the relative error values are approximately 4% and below. Therefore, this validates the numerical model of the variable aperture coupled solar receiver.

Based on both the experimental and numerical results shown in Figure 5-11, it is clear that the variable aperture mechanism did not provide a peak in temperature values due to variation of the mechanism's aperture size. The results previously shown in Figure 4-16 – Figure 4-18 illustrated that the temperatures within the solar receiver are expected to peak at a certain fixed aperture size that is different from the designed one. However, in the case shown in Figure 5-11, the power intercepted by the mechanism does not get transferred to the receiver and gets lost from the system. Hence, this no longer allows for a smaller aperture size to be an optimum one (within a variable aperture size range from 2 to 8.75 cm), since the additional cavity re-radiation losses saved by a smaller aperture size (which are partially lost from the system too) does not compensate for sacrificing nearly all of the additional intercepted radiation. Therefore, the designed variable aperture mechanism failed in depicting a similar behavior to that expected from a fixed aperture. Further investigation of the mechanism's design and improvements are covered later.

Finally, the results shown in Figure 5-11 demonstrates a non-linear relationship between the receiver's temperature and the variable aperture size, as expected due to the heat flux distribution from the HFSS. This creates a further challenge in controlling the variable aperture to regulate the temperature within the solar receiver or maintain it at a certain set point with the existence of disturbances due to the sun's transient variations. Further work on control is done in Chapter 6.

5.4.3. Power Captured by Variable Aperture Mechanism

With a heat exchanger coupled variable aperture mechanism, power intercepted by the mechanism can be captured and converted into useful power. In the case presented here, power captured is used to increase the temperature of water flowing through the heat exchanger, and so the water temperature difference between its inlet and outlet will be used as basis for efficiency

calculations. The captured power is calculated using Eqn. (5-6), as previously described, for different water flow rate values that range between 0.1 and 1.0 L/min at each different aperture size. The average captured power at each size is then calculated and the standard deviation of the experimental data was used to represent the uncertainty in the results. Figure 5-12 shows both the intercepted and average captured experimental power values, which were used to calculate the efficiency of the mechanism in capturing the intercepted power.

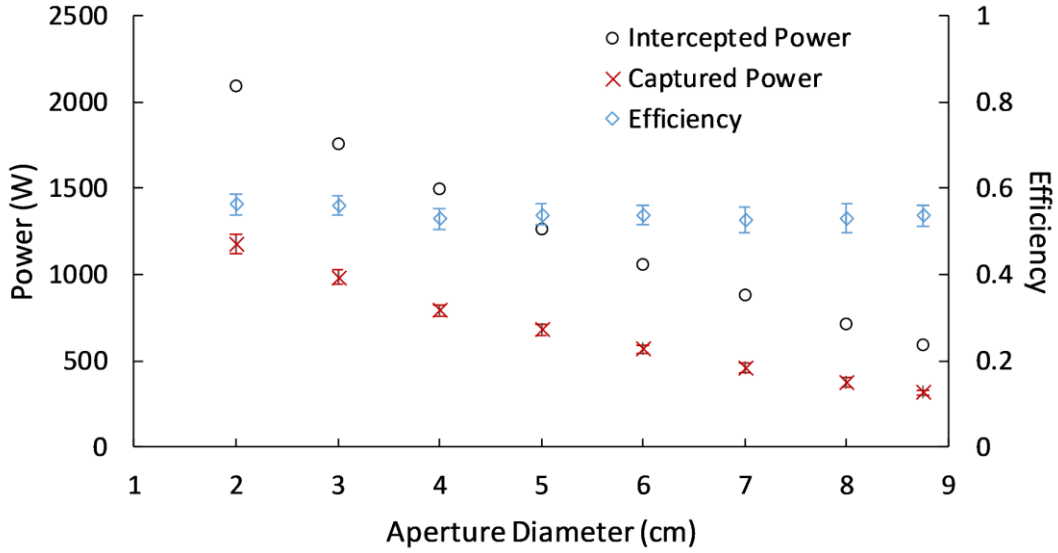

Figure 5-12: Intercepted and captured power by the variable aperture mechanism at a power level of 160 A for different aperture sizes, with error bars representing the standard deviation of results

As can be seen in Figure 5-12, the efficiency of the variable aperture mechanism remains relatively constant for different diameter sizes, with the uncertainty bars overlapping. Based on the uncertainty bars shown, it can be concluded that a flow rate within 0.1 and 1.0 L/min provides relatively the same efficiencies and captured powers. The efficiency of the mechanism was approximated to be 0.54, which is slightly less than the assumed emissivity value for stainless steel (Chapter 4). Therefore, an assumed value of 0.6-0.8 should be reasonable. At a power level value of 160 A, a fully opened aperture (8.75 cm) intercepts 594 W with an efficiency of 0.54, while a fully closed aperture (2 cm) intercepts 2093 W with an efficiency of 0.56.

5.4.4. Characterization of the Variable Aperture Coupled Solar Receiver

To further characterize the effect of the variable aperture mechanism, the model was used to simulate the variable aperture coupled solar receiver for different operating conditions. Figure 5-13 shows a contour map of the steady state (a) maximum temperature, and (b) average temperature values for varying power levels from the HFSS within the range of 100-200 A and for varying

aperture diameters within the range of 2-8.75 cm for a fixed feedstock flow rate of 7.5 LPM. As expected, the maximum temperature always occurs at T_{bp2}.

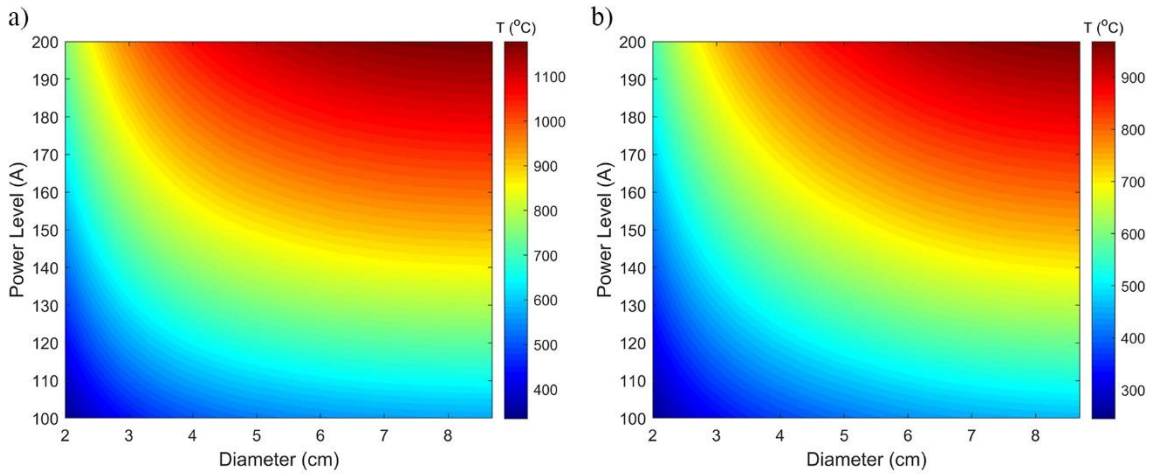

Figure 5-13: Steady state (a) maximum temperature, and (b) average temperature contours w.r.t. power level and variable aperture's diameter at flow rate of 7.5 LPM

Based on the results shown in Figure 5-13, several observations can be made. First, at a power level of 200 A, the maximum temperature ranged from 752 to 1180 °C, where the maximum temperature always increased as the aperture's diameter increased. Therefore, an optimum aperture size was still unobserved at the higher power levels and thus operating temperatures. This is once again due to the reason that the amount of additional cavity re-radiation losses saved and reflected back into the system by smaller aperture sizes does not yet compensate for the irradiance blocked and not transferred to the receiver. For the average temperature, it ranged from 563 to 970 °C at 200 A without observing any peak in its values as well. Furthermore, from Figure 5-13, it can be noticed that the gradient of decrease in temperature as the variable aperture closes is less for the maximum temperature than the average temperature. As the variable aperture closes, it starts blocking mostly the radiation intercepted by the front section of the receiver's cavity, causing a more significant drop in the front section than the rear one. This in turn further increases the temperature non-uniformity within the cavity, as was previously discussed. Finally, at a power level of 100 A, the maximum temperature ranged from 334 to 572 °C, while the average temperature ranged from 245 to 463 °C.

5.4.5. Future Design Recommendations and Improvements

Two design changes were investigated for the variable aperture, which are expected to improve its performance, to determine the amount of enhancement caused by each of the modifications. The

first change was in the emissivity of the variable aperture blades, where it has been changed from a value of 0.6 to a value of 0.2. Hence, having a higher reflectivity value and recovering more of the cavity re-radiation losses. This change could have been achieved on the experimental setup by having a finer surface finish on the aperture blades and not allowing the variable aperture to run dry (without water cooling) to minimize the oxidation and deterioration of the blades' surfaces. The second change was in the thickness of the variable aperture mechanism, where its thickness has been changed from a value of 4 to 2 cm. Hence, intercepting less of the solar power irradiated by the HFSS and allowing for higher temperatures to be achieved within the solar receiver. This could have been achieved on the actual design by decreasing the amount of clearance between the blades in addition to the wall thicknesses, which were slightly over-designed. These two design modifications should make the variable aperture mechanism exhibit a closer behavior to that obtained by varying the fixed aperture and possibly observe an optimum aperture size where the average temperature would peak, as that demonstrated in Chapter 4. Having said that, Figure 5-14 shows the average temperature within the solar receiver w.r.t the aperture's diameter for the current aperture mechanism in addition to two aperture mechanisms with the proposed modifications.

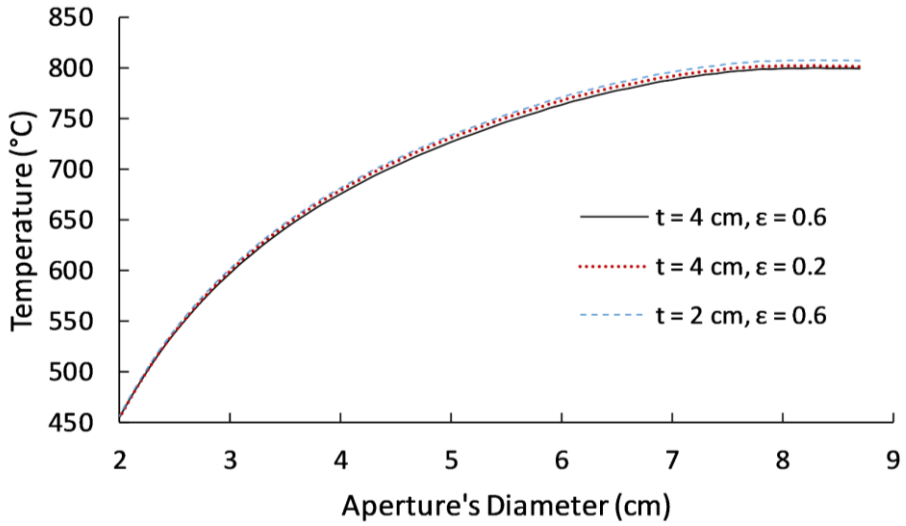

Figure 5-14: Receiver's average temperature w.r.t. aperture's diameter for different aperture mechanism modifications

Based on the results shown in Figure 5-14, it can be seen that the average temperature within the solar receiver slightly increased for each of the proposed modifications. However, this increase in temperature is insignificant, where the average temperature increased by a maximum of 3.8 °C upon decreasing the emissivity at an aperture diameter of 4.9 cm and increased by a maximum of 7.2 °C upon decreasing the mechanism's thickness at an aperture diameter of 8.75 cm. The average

temperature profile of both proposed improvements converges as the aperture's diameter decreases in size, since the change in emissivity has a more prominent effect as the aperture closes, but is also directly related to the temperature inside the receiver's cavity. Hence, the difference peaks at an aperture diameter of 4.9 cm, where a compromise between both effects is achieved. On the other hand, the temperature increase due to the reduction in thickness decreases directly with decreasing diameter, since the amount of power saved by this improvement decreases in magnitude.

Despite the fact that slight temperature peaks were observed in Figure 5-14 for both proposed improvements, the behavior exhibited by varying the fixed aperture size in Chapter 4 was not yet observed. The temperatures peak at 8 cm by 0.9 °C (relative to a fully opened aperture) for the reduced emissivity and at 8.3 cm by 0.6 °C for the reduced thickness, which is insignificant. The major issue that still remains is that the power intercepted by the variable aperture mechanism does not get transferred to the system, which is the assumption of the numerical model that provided an accurate representation of the experimental data. As long as this issue remains, the observation of temperature peaks at optimum aperture sizes will be difficult. Therefore, further work should be focused on integrating the variable aperture mechanism into the solar receiver's design more effectively, and thus allowing for the intercepted radiation to be transferred to the system more efficiently. If the objective of the variable aperture is to observe or achieve the highest possible temperature rather than controlling the temperature, this in turn means that the variable aperture mechanism shall not be water-cooled.

5.5. Conclusions

In this chapter, the variable aperture coupled solar receiver system was presented by describing the design and motion of the aperture mechanism in addition to the system auxiliaries and overall setup. The variable aperture introduced consists of eight blades that move in a translational type of motion to approximate a circular variable aperture, with the mechanism's total thickness being 4 cm. Four of these blades are water-cooled by coupling them to a heat exchanger, while the rest of the blades are just air-cooled. It has been shown that the relationship between the aperture's opening diameter and rotation of its guiding gear can be well represented through a third order polynomial, which is then used to regulate the variable aperture.

Then, the transient response of the system was characterized experimentally by running the aperture mechanism air-cooled and water-cooled, to obtain steady state temperatures within the receiver's cavity. The results showed that water cooling the variable aperture had no effect on the average temperatures at different aperture diameters, where the temperatures were nearly identical

at smaller aperture sizes and slightly higher for the air-cooled experiments at larger aperture sizes. However, the temperature differences between the two sets of experiments were insignificant, where the maximum difference was approximately 4 °C or 0.45%. Therefore, also leading to the conclusion that the intercepted radiation by the aperture mechanism is completely lost from the receiver's system. This was also the assumption implemented into the numerical model, which resulted in a good agreement with the experimental results by having relative temperature errors of approximately 4% and below. Hence, validating the numerical model of the new system. Since the intercepted power by the aperture mechanism was not transferred to the receiver's system, the behavior of obtaining peak temperatures by varying the aperture size was not observed by using the aperture mechanism. This is due to the reason that the additional cavity re-radiation losses saved by a smaller aperture size does not compensate for sacrificing nearly all of the additional intercepted radiation. Finally, the power captured by the variable aperture through its heat exchanger was experimentally measured at different aperture diameters based on the water flow rate and outlet-to-inlet temperature difference. The results showed that an average of 54% of the intercepted energy was captured by the heat exchanger.

The numerical model was finally used to simulate different test scenarios. First, it was used to characterize the full response of the variable aperture coupled solar receiver at different power levels and aperture diameters. Through this, it was demonstrated that an optimum aperture size, where the average temperature would peak, failed to exist even at higher power levels. In addition, it was shown that the relationship between the aperture's diameter and average temperature was a highly nonlinear one, which might cause additional challenges in effectively controlling the aperture for temperature regulation in Chapter 6. Additionally, the numerical model was used to simulate two proposed design changes that were expected to allow the aperture mechanism to exhibit a closer behavior to that obtained by varying the fixed aperture. These changes were to reduce the variable aperture's emissivity and thickness, where it was shown that both proposed changes led to a slight increase in the average temperature within the receiver. Despite the fact that slight temperature peaks were also observed for both of the proposed improvements, the behavior exhibited by varying the fixed aperture size was not yet observed. Therefore, if it is desired to maximize the temperature inside a receiver's cavity rather than just regulating it, further work should be focused on integrating the aperture mechanism more effectively into the solar receiver's design. Thus, allowing for the intercepted radiation to be transferred to the system more efficiently.

Chapter 6

Control of Transient Variations in Solar Receiver

In Chapter 6, the variable aperture mechanism, previously introduced in Chapter 5, is used to regulate the average temperature inside the solar receiver. The temperature inside the receiver can be controlled to follow a certain set point or to be maintained at a constant value with the existence of external uncontrolled disturbances or variations. To control the variable aperture mechanism, two different control methodologies were implemented. The first method is a simple PID controller, while the second is a model predictive controller that is based on the in-house developed model previously presented and validated in Chapter 5. Once the variable aperture control was tested, other control strategies, namely feedstock flow rate control and multi-input single-output (MISO)/hybrid control, were also investigated, where Chapter 6 then ends with some concluding remarks.

6.1. Introduction

The transient nature of the sun's DNI received by the Earth's surface creates a challenge for the operation of solar reactors. The fluctuation in the irradiance can cause major variations in the solar reactor's temperature, which in turn might significantly affect its performance. This would be more apparent in processes that require semi-constant temperatures within the reactor's cavity for maximized efficiency, or that have certain temperature limitations. In addition, care should be taken to avoid excessive thermal loads and gradients to avoid the reactor's deterioration. All solar reactors in literature are designed for a theoretical optimum aperture, based on the anticipated working conditions, which is then fixed in size for all operating conditions. The temperature regulation methods found in literature involve the control of (1) the reactants' flow rate(s) [91,112,113], (2) a shutter [114,115], (3) the heliostat field [6,116,117], or (4) an electric heater [118], to compensate for the fluctuating irradiance.

In solar power systems, unlike conventional power generation systems, the main energy source cannot be manipulated and used as the main control variable to regulate operating temperatures of solar receivers. Hence, the variation in the sun's DNI need to be compensated for to achieve optimum and steady operating conditions. In addition, solar processes have nonlinear dynamics that arise due to the fourth power temperature term and other nonlinear process behaviors, such as a shutter [114] or a variable aperture (as shown in Chapter 5). Therefore, temperature control within

solar receivers normally becomes a challenge, creating a high interest in developing more efficient methods and approaches to compensate for the intermittency of the sun's irradiation.

One of the most straightforward regulation methods is the reactants' flow rate(s) control. In [112], the inlet reactants' mass flow rate was controlled to regulate the temperature inside a solar reactor and obtain an exhaust with constant product composition for the steam gasification of petcoke and carbothermal reduction of steam. The regulation was achieved through a linear feedback controller using a linear quadratic Gaussian with loop transfer recovery. Based on their presented results, the controlled system exhibited a superior performance in comparison to the uncontrolled one for the reactor's conversion efficiency and product composition. Therefore, this illustrates the importance of controlling temperatures within solar reactors. In [91], a similar approach for control was implemented, where a model predictive controller (MPC) was used for regulating the temperature of a carbon steam gasification reactor. A MIMO control system was implemented by manipulating the reactants' flow rates to regulate the reactor's temperature and concentrations of CO and CO_2 in the exhaust lines. Their simulation results showed that a MPC system can respond to changes in solar irradiation in a better way than a conventional control strategy. The studies in [91] and [3] demonstrate the superiority of MPC systems over conventional fixed PID controllers that cannot handle the sun's intermittency very well. This is due to the reason that PID controllers normally tend to be detuned with low gains, giving them sluggish responses, in order to avoid high oscillations that may arise due to changes in the process or system dynamics [3]. Therefore, MPCs are usually the control systems of choice for solar energy applications.

Despite the promising simulation results of reactants' flow rate control methods, there are several applications where flow control methods should be avoided, such as water-splitting cycles. Varying the feedstock flow rate disturbs the flow pattern inside the reactor, which may lead to reduced heat transfer rates, and it also changes the production rate and residence time, which often cause severe losses in the conversion efficiencies. Such changes in the conversion efficiency provides low yields, which will require challenging separation and recirculation methods for any unreacted flow [6]. Hence, significantly decreasing the overall efficiency of the system. In addition, varying the reactants' flow rate generally has limited impact and control on the reactor's temperature under significant fluctuations in the solar irradiance. Therefore, control methods that have minimal effects on the fluid flow should be implemented, such as methods that regulate the solar power input to the reactor or that preheat the entering reactants.

There is some work in literature on regulating the solar flux density input either through the use of a shutter or by controlling the heliostat field. The shutter control is usually implemented for solar furnaces, which are mainly used for technology and design testing in addition to material treatment applications. In [115], a feedback linearization generalized predictive control (GPC) method was proposed to automate the control of the shutter for material treatment applications, while a MPC with integral action was proposed in [114] for the same main purpose. On the other hand, the automated control of the heliostat field has been extensively studied for a two-step cycling solar hydrogen production plant using a PI [6], PI and feedforward [117], and gain-scheduling [116] controllers. The plant consists of two reactors that run in parallel for a quasi-continuous production of hydrogen, where two temperature set points are required to be alternated and maintained. The water-splitting temperature maintained is 800 °C, while the regeneration temperature is 1200 °C. The regeneration temperature should be effectively monitored and controlled to not exceed 1250 °C, as the redox material will deactivate at higher temperatures. Although the results in [6,116,117] show promising outcomes, the method of heliostat control is a very challenging one since the controller has to determine the number and locations of heliostats to be focused or unfocused, which highly depends on the irradiance and time of the day [116]. Therefore, significant errors may arise throughout a day, leading to a substantial decrease in the controller's anticipated performance.

A different promising approach to regulating the temperature inside a solar receiver and compensating for the solar irradiance intermittency is the implementation of a variable aperture mechanism (as previously introduced in Chapter 5). The variable aperture mechanism will be capable of regulating the temperature within the solar receiver in applications where the feedstock flow rate control would fail in doing so. Just like the iris of a human eye, the mechanism would enlarge the aperture when the solar irradiance is low and reduce it when the irradiance is high. Therefore, compensating for the sun's intermittent behavior easily and without disturbing the flow pattern within the receiver. This type of control is much simpler and less costly than manipulating the entire field of heliostats. In the previous years, several variable aperture mechanisms were developed by the author and his team with different designs that aim at making this mechanism much more sustainable and effective [109,110,119].

In Chapter 6, two controllers were implemented and tested for the variable aperture mechanism to be able to effectively compensate for DNI fluctuations. The first one was a PID controller, where it has been tested and tuned numerically using the model of the system prior to its implementation. The second controller was a MPC system, where the solar receiver system was simplified and

treated as an ARX model. The parameters of the ARX model were identified using a recursive least square method with a forgetting factor applied to data obtained from the validated numerical model. Then, the MPC controller was tuned, once again through the use of the numerical model. The two controller types were extensively experimentally tested for tracking and maintaining set points in addition to rejecting disturbances through the simulation of actual sun's DNI data. Then, another variable aperture control consideration and two other control strategies were investigated, namely PID feedstock flow rate control and PID MISO control that can manipulate the variable aperture and feedstock flow rate.

6.2. Methodology

6.2.1. PID Controller

The first variable aperture control method investigated and implemented is a conventional PID controller, since it is simple to implement and is the most commonly used method of control in industry. Although the use of PID controllers are usually satisfactory, their implementation in the solar energy applications usually requires them to be slightly detuned to avoid high oscillations that may arise due to changing dynamics, as previously discussed. Therefore, the PID controller will only be used as a starting step and basis of comparison with a MPC system.

The discrete time form of the PID controller that is used to determine a control action is shown in Eqn. (6-1).

$$\Delta u(t_k) = \left(K_P + \frac{K_P \Delta t}{\tau_I} + \frac{K_P \tau_D}{\Delta t}\right) e(t_k) + \left(-K_P - \frac{2K_P \tau_D}{\Delta t}\right) e(t_{k-1}) + \frac{K_P \tau_D}{\Delta t} e(t_{k-2}) \quad (6\text{-}1)$$

where $\Delta u(t_k)$ is the control action, K_P, τ_I, and τ_D are the PID controller tuning parameters, Δt is the sampling time interval, and $e(t_k)$ is the error between the desired output and its set point at the sampling time k. The control action $\Delta u(t_k)$ is taken to be the change in the variable aperture in cm, while the desired output is taken as the average temperature within the receiver's cavity, as previously defined in Chapter 4. With that already defined, it is now time to discuss system and stability constraints which are shown in Eqn. (6-2).

$$u_{min} \leq u \leq u_{max} \quad \text{and} \quad |\Delta u| \geq |\Delta u_{min}| \quad (6\text{-}2)$$

where u_{min} and u_{max} represent the minimum and maximum possible aperture sizes of 2 and 8.75 cm, u represents the aperture size control signal in cm calculated through $u(t_k) = u(t_{k-1}) + \Delta u(t_k)$, and Δu_{min} is taken to be 0.1 cm. The additional constraint on the control action is implemented to obtain a less intensive aperture control, which should decrease the work load on the aperture mechanism and its auxiliaries in addition to allowing the system to reach a more stable

steady state of action. Having said that, the control action and then the control signal are externally adjusted to remain within the constraints in Eqn. (6-2). Therefore, Δu is neglected if its value is less than Δu_{min} and u is saturated to remain within the minimum and maximum limits.

The numerical model created and validated in Chapter 5 was used to tune the PID controller parameters and test the controller performance prior to its implementation in the solar receiver system. The parameters were tuned following the Ziegler-Nichols open loop approach, first described in [120], as this approach provides a quick response to load disturbances. However, the good disturbance rejection behavior comes at the expense of oscillatory transient responses to changes in the set point [121], which is not expected to be an issue here due to the already present transient response in the energy source (solar simulator or sun). The tuning method requires analyzing the step response of the system to calculate its static gain, process rate, and dead time. Since the system is highly nonlinear, the control tuning was performed for different aperture sizes ranging from 2 to 8.75 cm, and aperture steps ranging from 1 to 2 cm, where the final tuned parameters were averaged. In the tuning process, the power level input from the HFSS and feedstock flow rate were fixed at values of 160 A and 7.5 LPM. Having said that, the final obtained parameters for K_P, τ_I, and τ_D using the numerical model were 0.4 cm/°C, 200 s, and 50 s.

6.2.2. MPC Controller

MPC methods have several advantages over other control methods, such as: (1) their concepts are very intuitive, (2) they can be easily extended to MIMO systems and deal with difficult multivariable control problems, (3) they make use of system models to optimize controller performance and handle challenging dynamics, (4) they can compensate for dead times, and (5) they can explicitly incorporate system constraints in their control actions. These are some of the advantages that make MPC systems widely used in solar energy applications [3,122,123]. The general methodology for a GPC system was obtained from [124,125].

MPCs make use of system models to predict future outputs over a prediction horizon, N_p, by taking into account different control actions that change over a control horizon, N_u. After the sampling interval N_u, the control signal remains unchanged. The system model uses known (past) input (control signal) and output values in addition to future control signals to optimize the response of the controller by determining a set of future control signals that would keep the process output as close as desired to the reference trajectory. In determining the set of future control actions, system constraints can also be explicitly treated using an iterative optimization method. After that, only the first control action is sent to the process, while the rest of the $N_u - 1$ actions are rejected,

which is a property of MPCs referred to as a receding horizon approach. The procedure is then repeated at the next sampling time. Figure 6-1 shows a schematic representation of a MPC system. In this study, a GPC system has been designed and implemented.

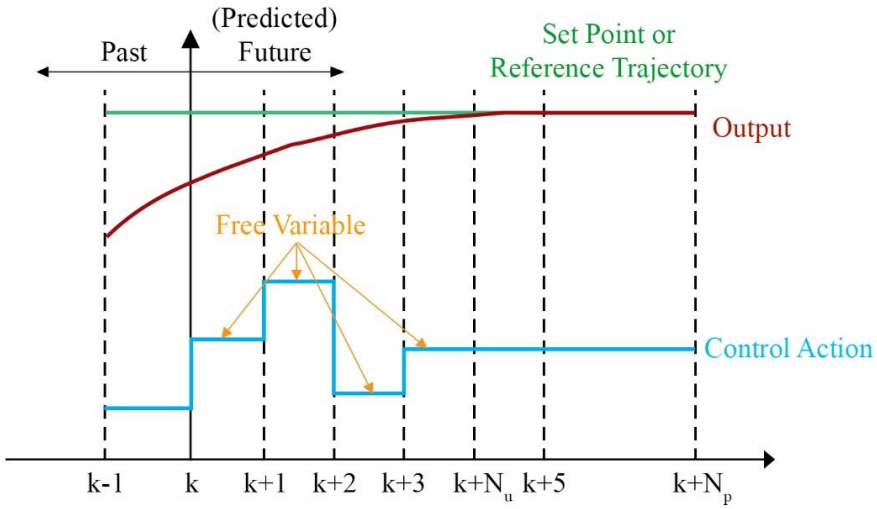

Figure 6-1:Schematic representation of a MPC system components and methodology

Since a MPC uses a model of the system to optimize the actions of a controller, an accurate model describing the system at hand is the key element in its algorithm. Therefore, substantial efforts should be focused on obtaining an accurate system model. A nonlinear plant, such as the solar receiver system, generally admits a locally-linearized model when its regulation is considered around a particular set point. The linearized model is described by a polynomial of the form shown in Eqn. (6-3), which is referred to as an autoregressive moving average with exogenous inputs (ARMAX) model.

$$A(q^{-1})\,y(k) = q^{-t_d}\,B(q^{-1})\,u(k-1) + C(q^{-1})\,\acute{e}(k) \tag{6-3}$$

where $u(k)$ and $y(k)$ represent the control/input (aperture diameter in cm) and output (average temperature in °C) series, q^{-1} is the backward shift operator, $\acute{e}(k)$ is a white noise representing the system disturbances, and t_d is the system dead time. For the solar receiver system presented here, the dead time is taken to be zero, and the C polynomial can be chosen to be one for simplicity, where the model of the noise becomes $1/A$ and is then coupled to the model dynamics. This simplifies Eqn. (6-3) to Eqn. (6-4), which is referred to as an ARX model.

$$A(q^{-1})\,y(k) = B(q^{-1})\,u(k-1) + \acute{e}(k) \tag{6-4}$$

where the polynomials A and B are presented in Eqns. (6-5) and (6-6).

$$A(q^{-1}) = 1 + a_1 q^{-1} + a_2 q^{-2} + \cdots + a_{na} q^{-na} \tag{6-5}$$

$$B(q^{-1}) = b_0 + b_1 q^{-1} + b_2 q^{-2} + \cdots + b_{nb} q^{-nb} \tag{6-6}$$

With the ARX model defined in Eqn. (6-4), the model parameters a_i and b_i need to be identified to represent the polynomials A and B that best describe the solar receiver system, given defined polynomial order values of na and nb. The system identification can be performed directly using experimental measurements. However, this will be an expensive and a time consuming process, where the system maybe be required to run for prolonged time periods to accurately identify the polynomial coefficients. Therefore, the numerical model created and validated for the solar receiver system was used to identify the coefficients offline in addition to testing and optimizing the performance of the MPC system. For this, the numerical model was used to simulate the response of the system to a pseudorandom generated aperture input signal that changes every hour for a total duration of 100 hours, where the power level from the HFSS and feedstock flow rate were maintained constant at 160 A and 7.5 LPM. The system identification then began to take place after approximately 4 hours of operation, to ensure that the system is being accurately defined after the initial heating up phase. Figure 6-2 shows the (a) pseudorandom generated control input signal, and (b) simulated output temperature of the solar receiver system.

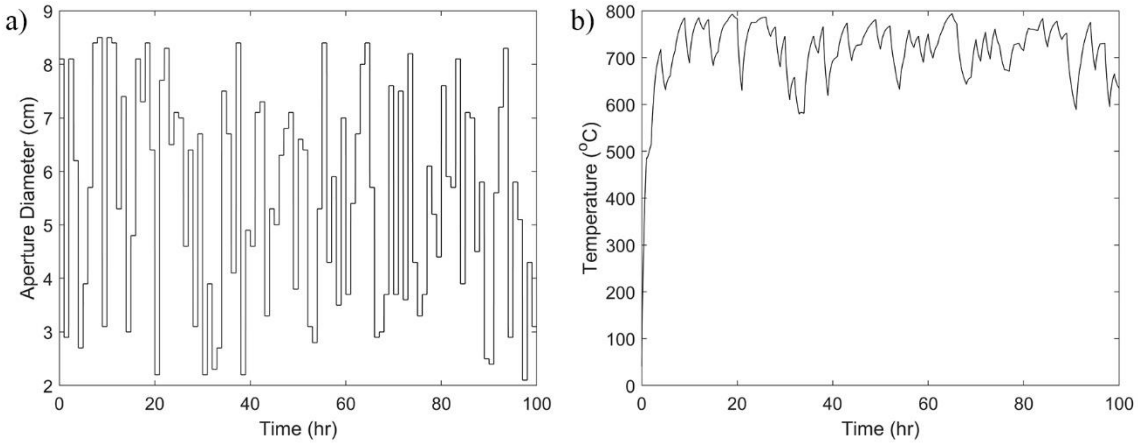

Figure 6-2: (a) Generated pseudorandom input signal, and (b) simulated output for solar receiver system identification

The system identification was performed using a recursive least square (RLS) method with a forgetting factor as illustrated and explained in [126]. By having the input $u(k)$ and output $y(k)$ of the ARX model already defined numerically, as shown in Figure 6-2, the identification shall now proceed. The order of the polynomials na and nb were taken to be 3, which seemed to provide a satisfactory fit of the numerical results. Having said that, the estimated output, $\hat{y}(k)$, of the ARX model is defined as in Eqn. (6-7).

$$\hat{y}(k) = \varphi^T(k)\hat{\theta}(k-1) \tag{6-7}$$

where φ represents the column vector of past (known) input and output values, as defined in Eqn. (6-8), and $\hat{\theta}$ represents the estimation of model parameters a_i and b_i, as defined in Eqn. (6-9) and calculated through Eqn. (6-10).

$$\varphi^T(k) = [y(k-1), y(k-2), y(k-3), u(k), u(k-1), u(k-2), u(k-3)] \tag{6-8}$$

$$\hat{\theta}^T(k) = [a_1, a_2, a_3, b_0, b_1, b_2, b_3] \tag{6-9}$$

$$\hat{\theta}(k) = \hat{\theta}(k-1) + \frac{P(k-1)\varphi(k)}{\lambda(k) + \varphi^T(k)P(k-1)\varphi(k)}\big(y(k) - \hat{y}(k)\big) \tag{6-10}$$

where P represents the covariance of estimation errors, as defined in Eqn. (6-11), and λ represents the forgetting factor, which is evaluated using Eqn. (6-12).

$$P(k) = \frac{1}{\lambda(k)}\left[P(k-1) - \frac{P(k-1)\varphi(k)\varphi^T(k)P(k-1)}{\lambda + \varphi^T(k)P(k-1)\varphi(k)}\right] \tag{6-11}$$

$$\lambda(k) = \max\left[\left(1 - \frac{y(k) - \hat{y}(k)}{1 + \big(y(k) - \hat{y}(k)\big)^2}\right), (\lambda_{min})\right] \tag{6-12}$$

where λ_{min} is set to 0.95. The forgetting factor determines the importance of older predictions in determining the model parameters. Therefore, the lower this factor is, the faster the older prediction errors will be neglected. A value of 0.95 for λ_{min} allows for some corrections to be made by the recursive identifier due to the receiver system still being in the heating up phase. The estimated model parameters along the 100 hours of simulation are shown in Figure 6-3 (a), while the model predicted output in comparison to the simulated output is shown in Figure 6-3 (b).

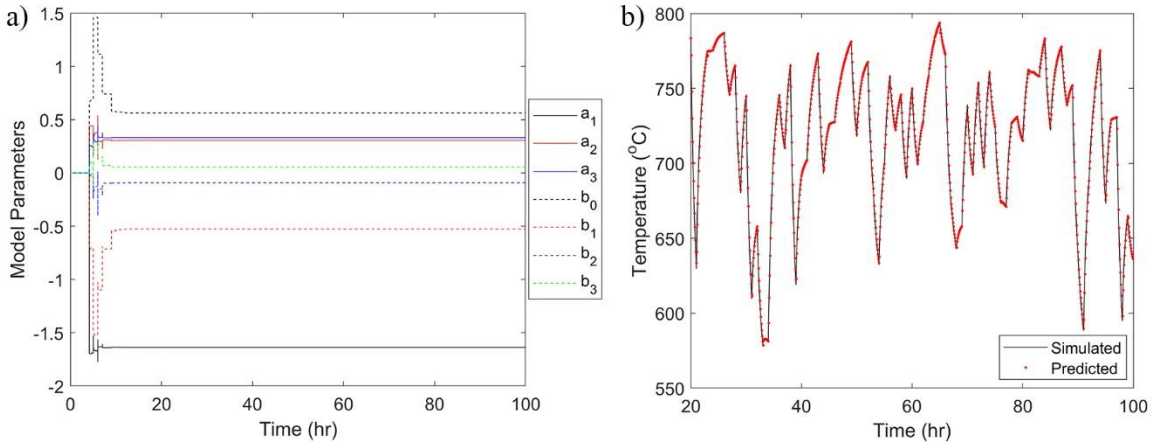

Figure 6-3: (a) ARX model's estimated parameters and (b) predicted output, based on the 10-step ahead prediction, in comparison with the simulated one

As shown in Figure 6-3 (a), the model parameters successfully converged to their final values not too long through the identification process. The obtained values for a_1 to a_3 were -1.6380, 0.3056, and 0.3325, while the obtained values for b_0 to b_3 were 0.5636, -0.5257, -0.0919, and

0.0556. Using these identified parameters, the ARX model predicts the output of the solar receiver system accurately, based on the 10-step ahead prediction shown in Figure 6-3 (b). It should also be noted that the final identified model parameters did not significantly change whether a forgetting factor was implemented or not (setting λ to 1.0).

Having the model of the system identified, it is then used to optimize the control action of the system by following the GPC algorithm, which aims at minimizing the multistage cost function J defined in Eqn. (6-13).

$$J(N_p, N_u) = \sum_{j=1}^{N_p} [\hat{y}(k+j \mid k) - w(k+j)]^2 + \sum_{j=1}^{N_u} \omega(j)[\Delta u(k+j-1 \mid k)]^2 \quad (6\text{-}13)$$

where $\hat{y}(k+j \mid k)$ is the j-step ahead system output prediction at time interval k, $w(k+j)$ is the future reference trajectory (or set point), and $\omega(j)$ is a weighing factor that controls the aggressiveness of the controller in following the reference trajectory, which is treated here as a constant. The weighing factor ω represents the penalty of the control action on the cost function, meaning that a lower weighing factor will provide a more aggressive controller that aims at keeping the exact output's set point. Hence, ω can be used as a design parameter. The system constraints already defined earlier in Eqn. (6-2) still remain for the MPC system, where they are enforced externally and separately from the cost function in a manner similar to that performed for the PID controller. With that being said and through implementing a linear time invariant ARX model, the optimization problem in Eqn. (6-13) can be easily and rapidly solved, reducing the computational load on the MPC.

In a manner similar to tuning the PID controller, the numerical model of the system was used to simulate the implementation of the GPC and obtain the best combination of N_p, N_u, and ω values. Since the rate of change of the system output is relatively slow, a relatively high value for N_p is not required. Therefore, the value of N_p was only taken to be 10 in order to reduce the level of mismatch between the predicted model and actual system outputs during experimentation. Following that, different combinations of N_u and ω were tested using the numerical model, where it was noticed that a value greater than 4 for N_u did not lead to a significant improvement in the GPC's performance. In addition, the lower the value for N_u, the less the amount of computation that needs to be performed by the optimizer. Therefore, the value of N_u was set to 4, where the corresponding optimal ω value was determined to be 15. The optimal ω value was obtained based on a compromise between the set point errors and amount of changes in the variable aperture size. As shown in [91], a MPC system can show instabilities when the ω value is relatively low and the

controller is away from its nominal operating region, showing oscillatory behaviors. This was avoided by tuning the MPC with a more conservative ω value, as was performed here, to obtain a more robust MPC system that can operate away from its nominal operating region.

6.2.3. Simulating Actual Sun's DNI Measurements

In addition to testing the two control approaches for set point tracking and system disturbances, it is vital to test their performance under a more realistic scenario that is based on actual sun's DNI measurements. For this, actual DNI measurements were obtained from the National Renewable Energy Laboratory (NREL) database, where data is available for any day year-round and is updated every ten minutes [22]. Once the data is obtained, the HFSS can be used to simulate the actual day by changing the supplied current through the use of a correlation equation. As previously discussed in Chapter 4, the relationship between the current supply and peak flux (obtained in Chapter 2) is used to regulate the power of the HFSS, since it provides a higher accuracy over the total power relationship. This relationship is shown in Eqn. (6-14).

$$q''_{peak} = 45.039\ Amp - 2128.1 \tag{6-14}$$

where q''_{peak} is the peak flux at the focal plane in kWm^{-2} and Amp is the supply current to the HFSS in A. Based on Eqn. (6-14), the maximum DNI expected (1050 Wm^{-2}) was correlated to the maximum peak flux of the HFSS (at supply current of 200 A), which was then implemented into Eqn. (6-14) to obtain Eqn. (6-15). The current value calculated through Eqn. (6-15) is then rounded to the nearest integer. This then provides an accurate way of simulating the actual obtained DNI in the laboratory for experimentation by changing the current supplied to the HFSS accordingly.

$$Amp = 0.1455\ DNI + 47.25 \tag{6-15}$$

6.3. Results and Discussion

6.3.1. Variable Aperture Control Simulation

Before implementing the two proposed controllers on the experimental setup, their performance was first tested using the in-house developed numerical model. The average temperature set point was changed within the range of 600 to 750 °C, in 50 or 100 °C increments, while maintaining the power level and feedstock flow rate at 160 A and 7.5 LPM, as shown in Figure 6-4 for the (a) PID, and (b) MPC controllers. This demonstrates the satisfactory performance of both control systems in tracking the desired set point temperatures with relatively fast response and high stability.

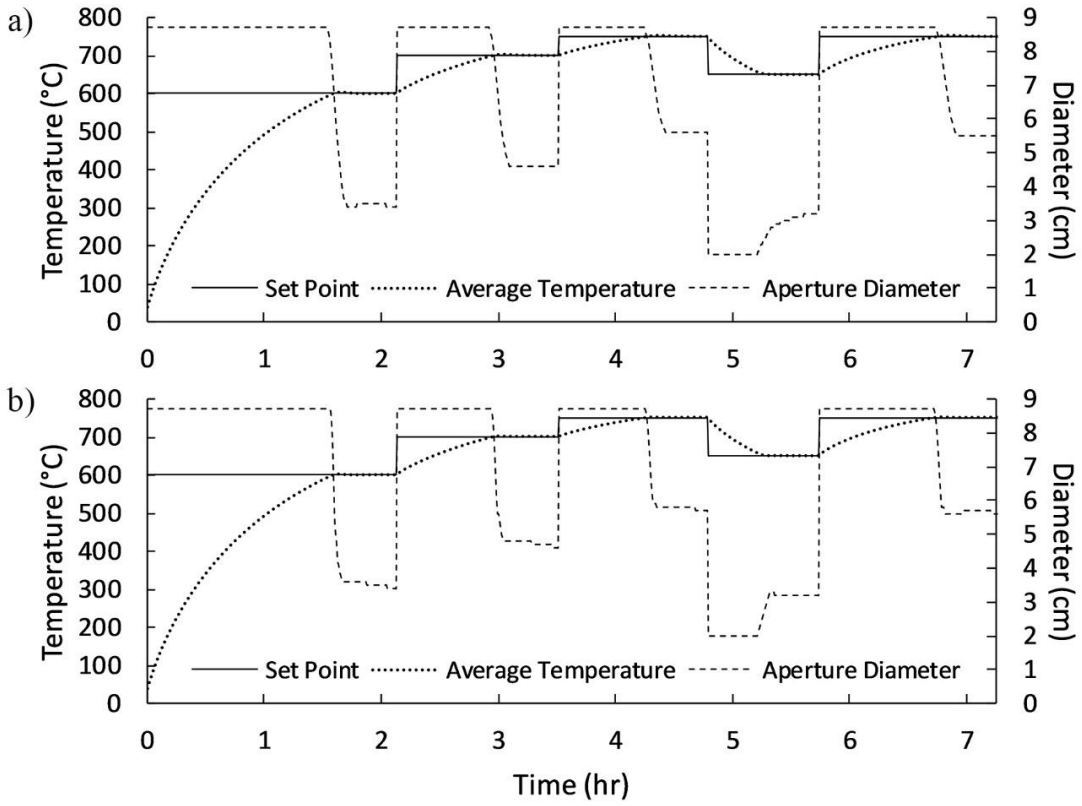

Figure 6-4: Control simulations for set point tracking at a power level of 160 A and flow rate of 7.5 LPM, showing set point and average temperatures with the variable aperture response using (a) PID, and (b) MPC controllers

Figure 6-4 shows that the PID and MPC controllers have similar responses to changes in the set point. The optimum aperture size for each set point temperature using both controllers is determined relatively fast, where then the aperture changes at a very slow rate to maintain the desired temperature. However, in the process of determining the optimum aperture size, the rate of aperture change using the MPC controller is higher than the one using the PID controller due to the highly nonlinear behavior of the average temperature w.r.t. the aperture size. The PID controller does not take into account that aperture changes within the range from 8 to 8.75 cm is very small (steady state temperature difference of 3.1 °C) and is small within the range from 7 to 8.75 cm (temperature difference of 14 °C). This behavior is accounted for better using the MPC system. Therefore, this leads to the PID controller having significantly larger overshoots when compared to the MPC system. This is more noticeable when tracking higher set points (heating up), where the variable aperture is controlled starting from the fully opened position. Having said that, the overshoots for the set point temperatures shown in Figure 6-4 are 3.8, 2.9, 2.3, -0.6, and 2.4 °C using the PID controller, while they are 1.7, 1.1, 0.9, -0.3, and 1.2 °C using the MPC system. This,

in addition to the similar stable aperture response of both controllers, clearly show the superior performance of the MPC system. Nevertheless, both control methods are now ready to be implemented in the experimental setup.

6.3.2. PID Experimental Variable Aperture Control

Tracking Set Point. The performance of the PID controller was experimentally tested for set point tracking, similar to that previously simulated in Figure 6-4 (a). The set point temperature was changed within the range of 600 to 750 °C, while maintaining the power level and feedstock flow rate at 160 A and 7.5 LPM. The responses of the system's temperature and variable aperture are shown in Figure 6-5 (a). In addition, during the experimental run, real-time data was obtained for the amount of power captured by the heat exchanger of the variable aperture mechanism, based on the water temperature difference and flow rate data, as was described in Chapter 5. Although the power captured by the cooling water is not being turned into useful energy here, the data of power captured can provide an estimate for the amount of power that can be made available for a secondary process or used to preheat the entering feedstock. Thus, trying to increase the overall efficiency of the solar system. The data of power intercepted and captured by the variable aperture mechanism is show in Figure 6-5 (b), where the power intercepted by the aperture is determined based on its size and the HFSS's power level, as described in Chapter 5. It should finally be noted that in all experiments performed in this chapter, the cooling water flow rate was maintained constant throughout each run within the range of 0.2 to 0.8 L/min.

As shown in Figure 6-5 (a), the PID controller was able to well-regulate the variable aperture to track the temperature set point within the range from 600 to 750 °C, under steady operating conditions. The overshoots for the set point temperatures shown in Figure 6-5 (a) are 5.2, 4.0, 3.0, -1.3, and 3.1 °C. When comparing these values to the previously obtained ones through simulations, it can be seen that the experimental overshoots are slightly higher, while still following the same trend as the numerically determined overshoots. The higher experimental overshoots have led the aperture response to experience some fluctuations prior to settling at the correct aperture sizes. The magnitude of these fluctuations seems to be greater when the system is heating up and when the set point is relatively low (directly related to the magnitude of overshoot), as shown in Figure 6-5 (a). This is due to the fact that when the regulation of the aperture starts, it is relatively further away from its optimum aperture size, in addition to the greater rate of change of the average temperature at lower set points. However, the PID controller performance is considered to be satisfactory, where the average temperature was maintained within ± 1.5 °C from its set point, with the exception of

the overshoots, and while maintaining a stable aperture control. Based on the results shown in Figure 6-5 (b), the variable aperture intercepted an average power of 926 W, out of which 500 W was captured by the heat exchanger throughout the time period of 7.25 hr. This gives an efficiency of approximately 54% for the heat exchanger.

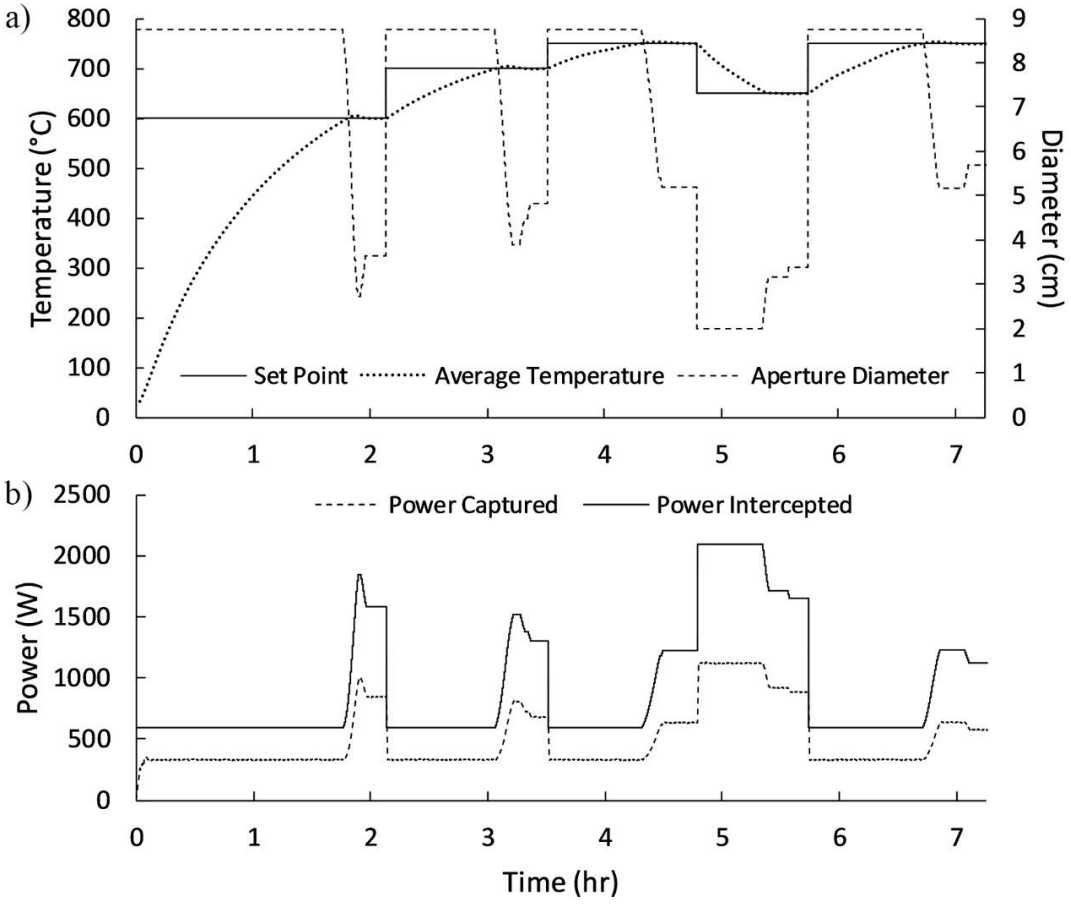

Figure 6-5: Experimental testing for set point tracking using PID controller at a power level of 160 A and feedstock flow rate of 7.5 LPM, showing (a) set point and average temperatures with the variable aperture response, and (b) power intercepted by the aperture and captured by its heat exchanger

Maintaining Set Point. To further evaluate the performance of the PID controller, the long-term response of the variable aperture in maintaining a set point was tested. This was performed at a different power level than that shown in Figure 6-5 to also observe the performance of the controller under a different operating condition. The results shown in Figure 6-6 demonstrate the response of the variable aperture to maintaining a set point temperature of 700 °C, while operating under a power level and feedstock flow rate of 170 A and 7.5 LPM. The results show an overshoot of 4.4 °C, which is greater in comparison to the overshoot of 4.0 °C shown in Figure 6-5 that was obtained at 700 °C. This is due to the higher temperature rate of change when operating at a power

level of 170 A. However, the variable aperture response demonstrated a more stable behavior, where the magnitude of the aperture fluctuation was significantly less than that shown in Figure 6-5 (a). In addition, following the overshoot in the average temperature, the PID controller was able to maintain the set point of 700 °C within ± 1.4 °C for a period of 1.12 hr, as demonstrated in Figure 6-6.

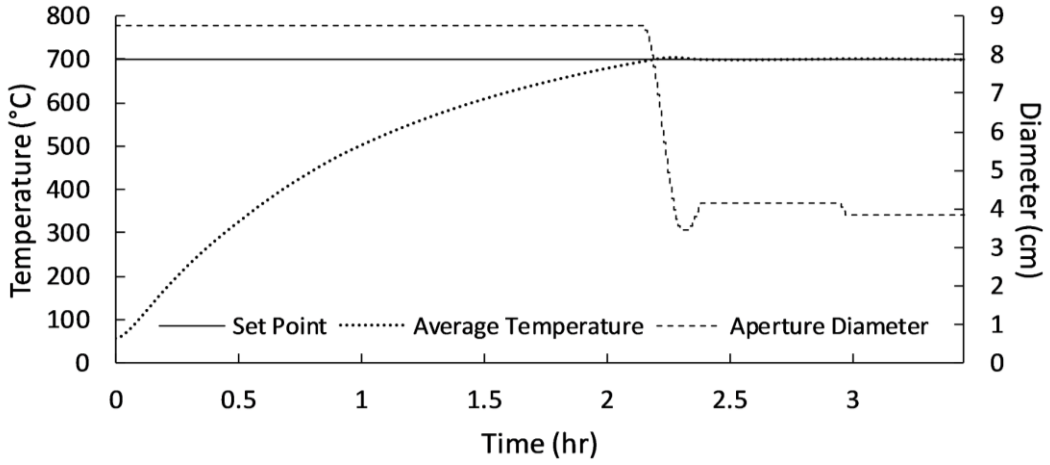

Figure 6-6: Experimental testing for maintaining set point using PID controller at a power level of 170 A and feedstock flow rate of 7.5 LPM, showing set point and average temperatures with the variable aperture response

Rejecting Disturbances. Once the PID controller demonstrated a good performance to tracking and maintaining desired set point temperatures, it was then necessary to test its performance under a more realistic scenario that is based on actual sun's DNI measurements. For this, actual DNI measurements were obtained from NREL [22], where the selected day was aimed to be in December or January to have a relatively short duration of sunshine and allow for mimicking the sun's DNI using the HFSS. The day chosen for experimentation was a relatively "*sunny day*", where passing clouds and sunshine disturbances were minimal. This corresponded to data gathered from the sun's DNI on December 15th, 2018. To be able to simulate that day using the HFSS, Eqn. (6-15) was used to correlate the DNI measurements to input current values, where then the current was allowed to change based on DNI increments of 50 or 100 W/m^2. With that being said, the actual and simulated DNI plots are shown in Figure 6-7 (a).

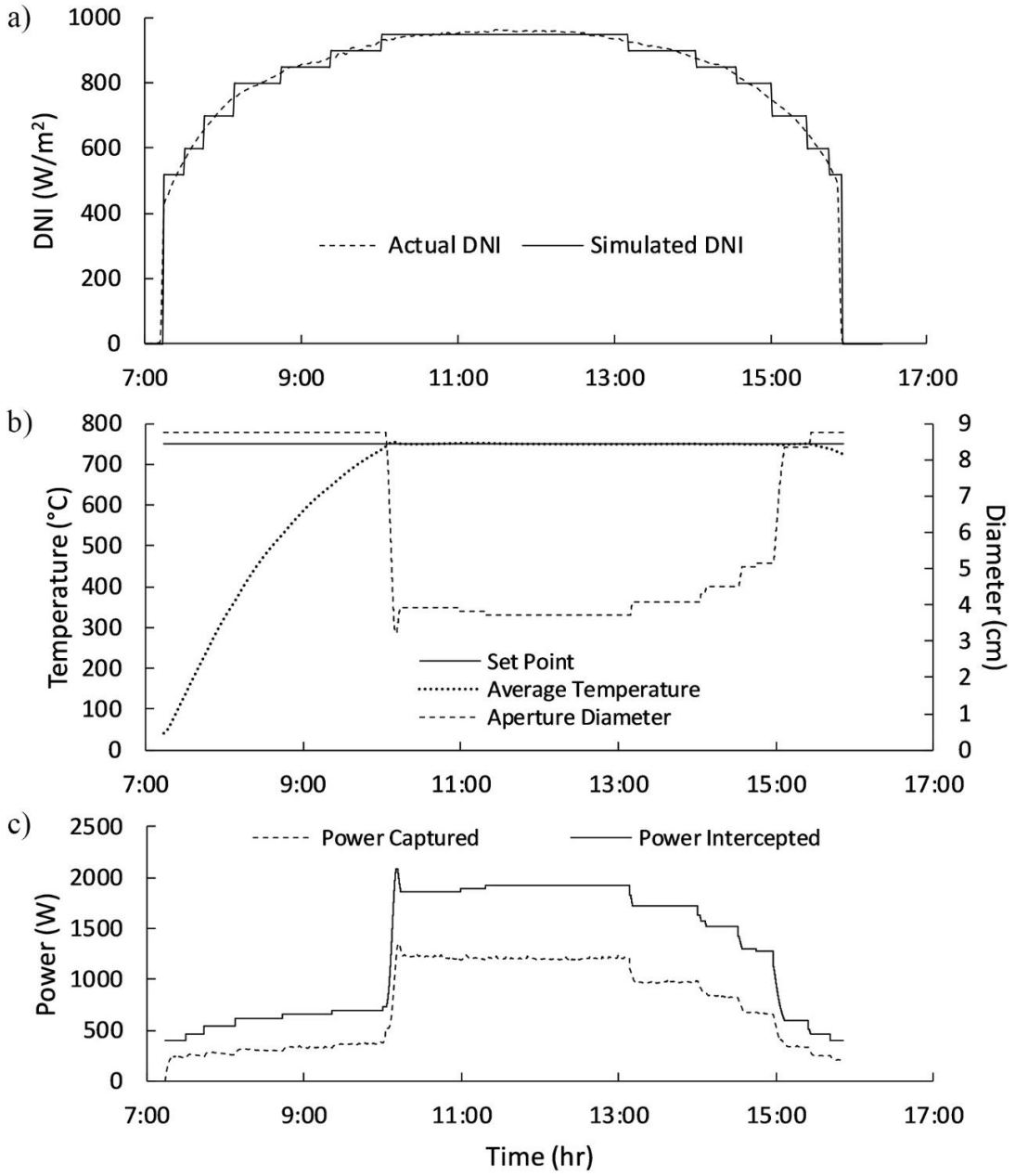

Figure 6-7: Experimental testing for disturbance rejection using PID controller for actual day simulation at a feedstock flow rate of 7.5 LPM, showing (a) actual and simulated DNI for December 15th, 2018, (b) set point and average temperatures with the variable aperture response, and (c) power intercepted and captured by the aperture

As can be observed in Figure 6-7 (b), the PID controller was able to maintain the set point temperature of 750 °C successfully throughout the entire day with changes in the DNI level, while the feedstock flow rate was maintained at 7.5 LPM. Thus, showing the ability of the PID controller in rejecting any disturbances caused throughout the day. Based on the results in Figure 6-7 (b), the first overshoot in temperature is 4.6 °C, after which the average temperature remained within ± 1.5

°C up until the point where the DNI level significantly dropped below 800 Wm^{-2}, where the set point errors increased to ± 3 °C. Following another decrease in the DNI level to 600 Wm^{-2}, the system was no longer able to achieve the desired set point temperature due to insufficient solar input provided by the HFSS. Throughout this period of time, the variable aperture response was very stable, where the mechanism was adapting to the optimum aperture size for each DNI level with no fluctuations. Finally, for a quick overview of the system's response, the average temperature of the system remained within ± 5 °C for 5.36 hr, within ± 2 °C for 5.13 hr, and within ± 1 °C for 4.92 hr. In addition, based on the results shown in Figure 6-7 (c), the variable aperture intercepted an average power of 1261 W throughout the day, out of which 720 W was captured by the heat exchanger. This gives an efficiency of approximately 57%.

6.3.3. MPC Experimental Variable Aperture Control

A MPC system instead of a PID controller was implemented on the experimental setup to further investigate a different control approach in tracking and maintaining a desired set point in addition to rejecting solar disturbances. Based on the numerical results shown in Figure 6-4, a MPC system illustrated a more superior response than a PID controller. For comparison purposes, almost the same set of experiments were duplicated using a MPC system as those performed using a PID controller.

Tracking Set Point. The performance of the MPC system was experimentally tested for set point tracking, similar to that performed in Figure 6-5 with the same temperature set points, power level, and feedstock flow rate. The responses of the system's temperature and variable aperture are shown in Figure 6-8 (a), while the data of powers intercepted and captured by the variable aperture mechanism is shown in Figure 6-8 (b). Based on the results shown, the MPC system was again able to control the average temperature of the receiver well, with a slightly more enhanced and stable response in comparison to that of the PID controller. The overshoots for the set point temperatures shown in Figure 6-8 (a) are 2.6, 2.0, 1.5, -0.5, and 1.6 °C, which are approximately half the overshoot values obtained using a PID controller, shown in Figure 6-5 (a). This difference in overshoots is due to the superior ability of the ARX model in accommodating for the non-linear behavior of the variable aperture and predicting the future response of the system.

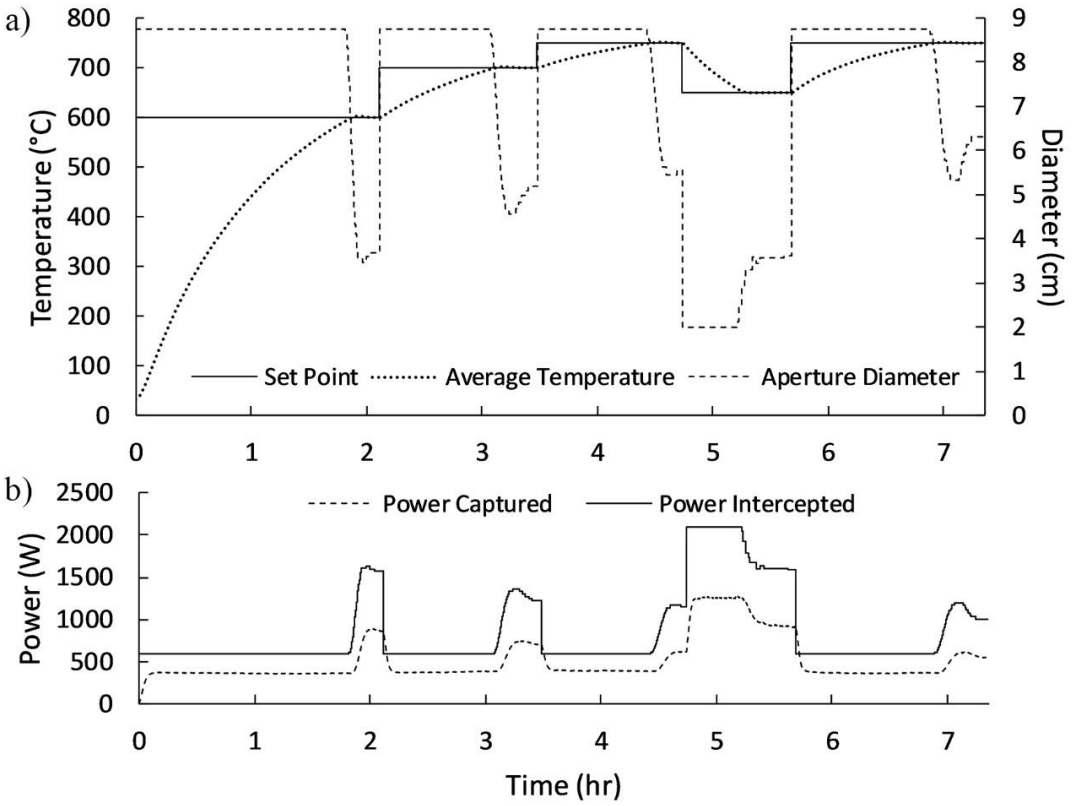

Figure 6-8: Experimental testing for set point tracking using MPC controller at a power level of 160 A and feedstock flow rate of 7.5 LPM, showing (a) set point and average temperatures with the variable aperture response, and (b) power intercepted by the aperture and captured by its heat exchanger

By comparing the response of the variable aperture for both control methods, it can be well-observed that the aperture's response is significantly more stable using a MPC system. The fluctuations previously present using a PID controller are eliminated or mitigated, with the exception of the last set point at 750 °C. In comparison to the PID controller, the average temperature was maintained within ± 0.6 °C (instead of ± 1.5 °C) from its set point, with the exception of the overshoots. However, the MPC aperture's response can sometimes be slightly less stable (or more aggressive) than that of the PID while the aperture size changes, as can be noticed by its response at 5.4 hr. At that time instant, the variable aperture seemed to have reached its optimum aperture size, but then decreased and increased in size back again around its optimum aperture size. Such a behavior was not observed using a PID controller. Finally, based on the results shown in Figure 6-8 (b), the variable aperture intercepted an average power of 870 W as opposed to 926 W. Definitely this significant difference can be partially attributed to uncontrolled/unmonitored experimental conditions. However, it again demonstrates the superior performance of the MPC system in making better use of the available energy and not blocking any

unnecessary solar energy. For completeness, the variable aperture captured an average of 510 W throughout the time period of 7.25 hr, which gives an efficiency of approximately 59% for the heat exchanger.

Maintaining Set Point. In evaluating the performance of the MPC system further, the system was allowed more time in maintaining two different set point temperatures of 650 °C and 675 °C, as shown in Figure 6-9. This was performed at a power level and feedstock flow rate of 160 A and 7.5 LPM. The results in Figure 6-9 show an overshoot of 2.4 °C at 650 °C and an overshoot of 1.3 °C at 675 °C. However, the result of the second overshoot does not quite follow the trend of the overshoot previously observed based on the results in Figure 6-8, since the overshoot experienced here at 675 °C is significantly lower than that experienced earlier at 700 or 750 °C. Nevertheless, the variable aperture response was relatively stable and reached its steady state while maintaining the set point closely. Following the overshoot in the average temperature, the MPC system was able to maintain the set point of 675 °C within ± 0.3 °C for a period of 0.41 hr, as demonstrated in Figure 6-9.

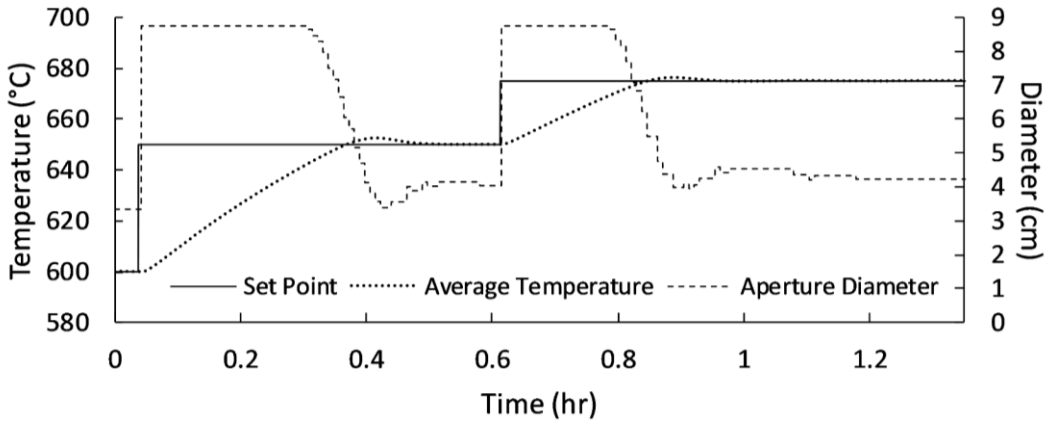

Figure 6-9: Experimental testing for maintaining set point using MPC controller at a power level of 160 A and feedstock flow rate of 7.5 LPM, showing set point and average temperatures with the variable aperture response

Rejecting Disturbances. Once the MPC system demonstrated a good performance in tracking and maintaining desired set point temperatures, it was then necessary to test its performance using actual sun's DNI measurements. For this, the same data used in Figure 6-7 and shown in Figure 6-10 (a), corresponding to data gathered from the sun's DNI on December 15th, 2018, was used to further test the response of the MPC system. This was performed while maintaining a feedstock flow rate of 7.5 LPM.

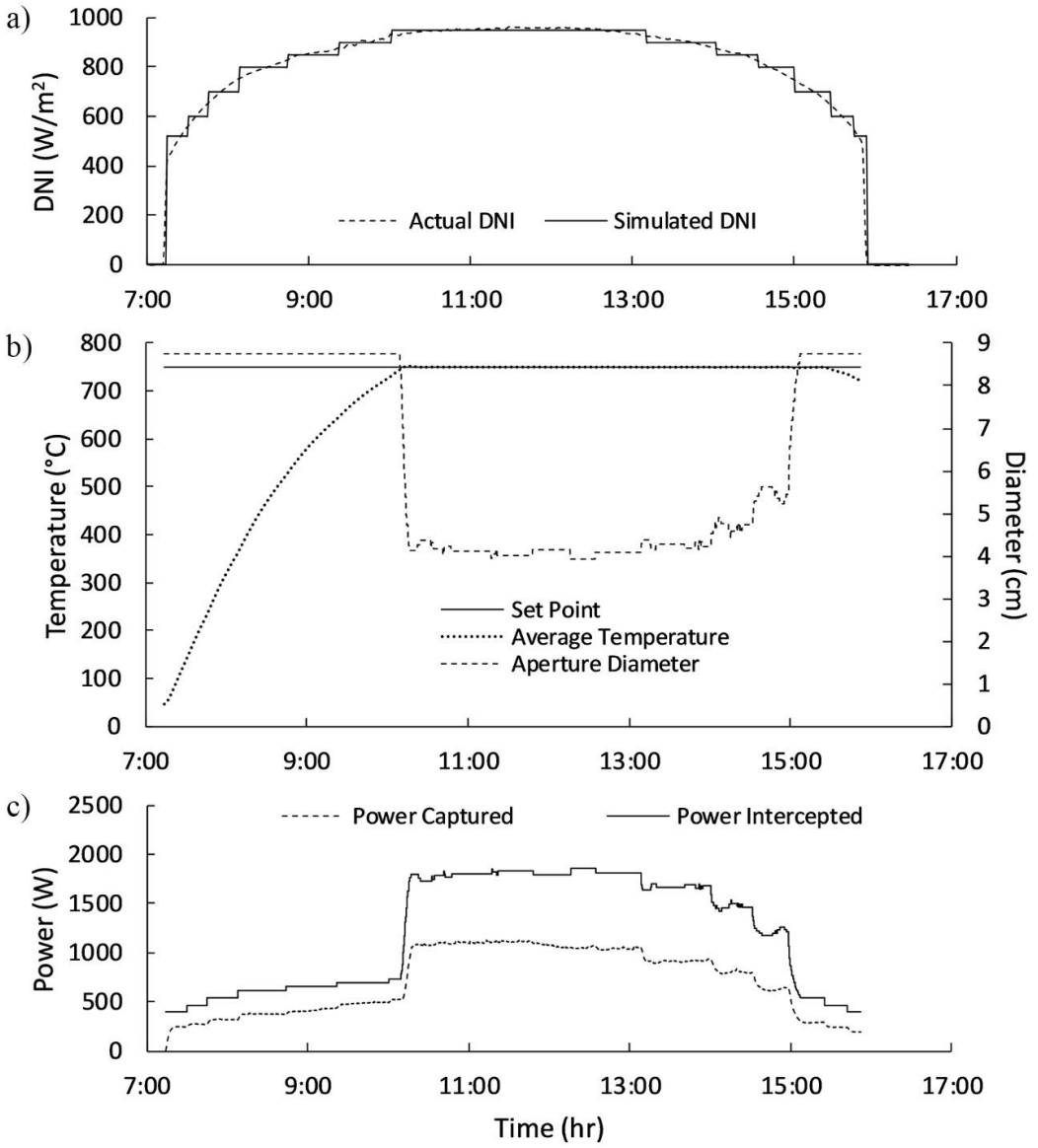

Figure 6-10: Experimental testing for disturbance rejection using MPC controller for actual day simulation at a feedstock flow rate of 7.5 LPM, showing (a) actual and simulated DNI for December 15th, 2018, (b) set point and average temperatures with the variable aperture response, and (c) power intercepted and captured by the aperture

Based on the results shown in Figure 6-10 (b), the MPC system was able to reject disturbances due to changes in the DNI level and maintain the desired temperature set point of 750 °C throughout the entire day with minimal variation. In comparison to the results obtained using a PID controller, the first overshoot in temperature is 2.2 °C (as opposed to 4.6 °C), after which the average temperature remained within ± 0.5 °C (as opposed to ± 1.5 °C) up until the point where the DNI level dropped below 800 Wm^{-2}. At a DNI level of 700 Wm^{-2}, the set point errors increased to ± 1.5 °C (as opposed to ± 3 °C). Following another decrease in the DNI level to 600 Wm^{-2}, the system

was no longer able to maintain the set point temperature, similar to the response of the PID controller. Although the MPC system was able to maintain the set point temperature in a superior manner, this came at the expense of having a less stable (more aggressive) variable aperture control. As can be seen in Figure 6-10 (b), the aperture response experienced some fluctuations as the DNI level was decreasing especially around 850 Wm^{-2}. However, the overall stability and robustness of the controller was still maintained. Finally, for a quick overview of the system's response, the average temperature of the system remained within ± 5 °C for 5.35 hr, within ± 2 °C for 5.28 hr, and within ± 1 °C for 5.10 hr. These values once again demonstrate the superior response of the MPC system, where the values obtained for maintaining the average temperature within 1 and 2 °C using the PID controller were significantly lower. For completeness, based on the results shown in Figure 6-10 (c), the variable aperture intercepted an average power of 1196 W, out of which 702 W was captured throughout the day. This gives an efficiency of approximately 59%.

6.3.4. Other Control Consideration

Passing clouds can severely affect the amount of sun's DNI that reaches the Earth's surface. In some cases, the DNI level can drop to an approximate value of zero, which can last for minutes or even hours based on the DNI data from NREL reviewed in [22]. In most of these cases, the DNI level throughout the day is already heavily disturbed and fluctuating. However, in other cases as that shown in Figure 6-11 for December 2nd, 2018, the sudden drop in DNI can occur during a *sunny day*. Through this sudden drop, all the temperature control techniques discussed previously will fail in rejecting this severe disturbance and continuing to maintain the set point temperature, with the exception of an electric heater control as in [118].

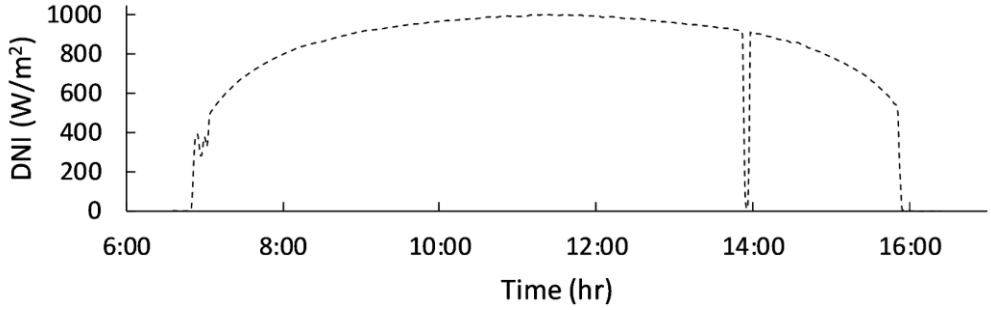

Figure 6-11:Actual sun's DNI obtained from NREL for December 2nd, 2018

Since radiation is the most dominant type of thermal loss during the sudden drop in Figure 6-11, the variable aperture can be used to mitigate these losses. This will have to be performed in a manner that contradicts the action of any of the previously implemented variable aperture controllers. During the sudden drop in the DNI level, the variable aperture will fully open as a result

of the control action calculated and sent from the MPC or PID controllers. However, this will increase the radiation losses experienced by the system and lead to a larger disturbance in the average temperature. Therefore, a better approach is to override the action sent from the controller in such severe cloud passing cases and fully close the aperture to reduce the amount of re-radiation losses experienced by the system. This approach will be referred to as the "*control override*" approach. The proposed approach was first tested numerically, where it has shown superior results to that obtained by simply letting the controllers determine the variable aperture action. Therefore, the *control override* approach was then tested experimentally to determine if such a superior behavior can still be observed. For this, the behavior in Figure 6-11 was simulated using the HFSS by turning it off for a period of 10 minutes (reducing the DNI to zero) and then turning it back on again. During this experimental testing, the power level and feedstock flow rate were maintained at 160 A and 7.5 LPM, while the initial and set point temperatures were fixed at approximately 750 °C. Figure 6-12 (a) shows the variation of the average temperature when the aperture is fully closed (*control override)* and when fully opened w.r.t. the power level, while Figure 6-12 (b) shows the power captured for both approaches w.r.t. the aperture diameter.

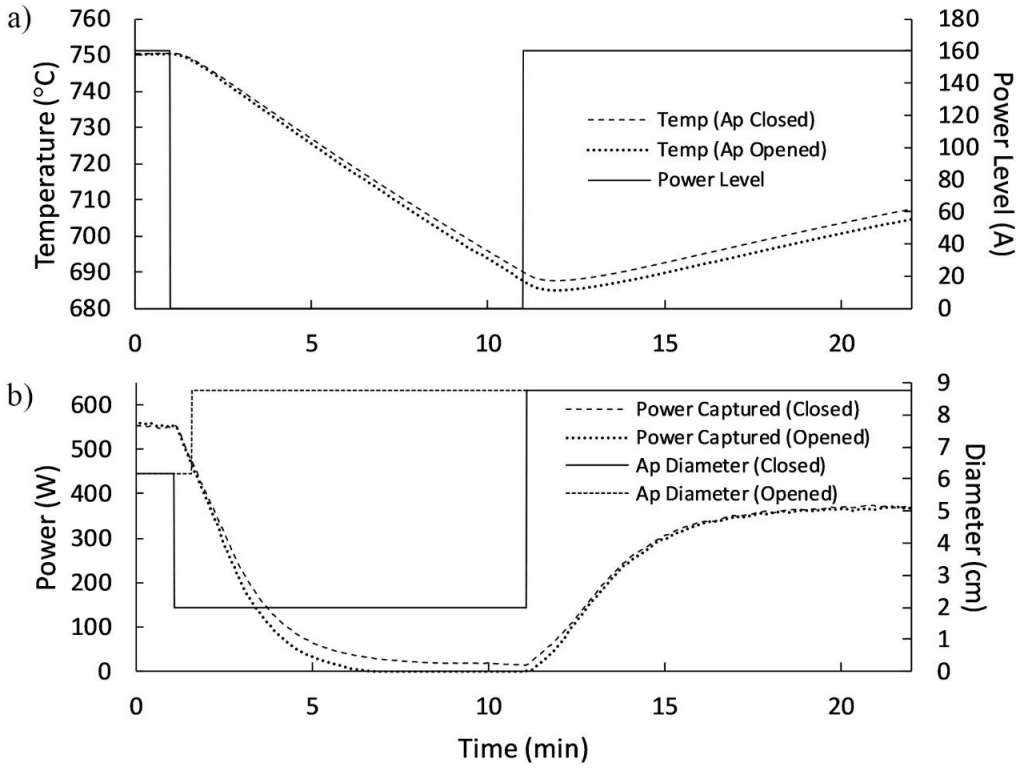

Figure 6-12: Experimental testing of the "control override" approach showing (a) average temperature variation w.r.t. power level, and (b) power captured w.r.t. aperture diameter

As shown in Figure 6-12 (a), the decrease in the average temperature over the span of 10 minutes is less when the *control override* approach is implemented and the variable aperture is fully closed. The difference in temperature between the opened and closed apertures is approximately 2.8 °C, which is not significant and may be attributed to sources of error. However, the data shown in Figure 6-12 (b) also support the behavior demonstrated in Figure 6-12 (a), where the aperture mechanism continues to recover a slightly higher amount of power by approximately 21 W throughout the period at which the power level is zero. Therefore, this illustrates the superior behavior of the *control override* approach in mitigating the disturbance caused by a severe drop in the DNI level by decreasing the re-radiation losses. Although the difference in the average temperatures is small (2.8 °C), this difference might eventually become significantly larger when the DNI drop extends to a longer duration or when the reactor's set point is higher than 750 °C. In addition, in applications where an electric heater is used to compensate for changes in the DNI, implementing a variable aperture and the *control override* approach should in turn result in lower power consumptions by the heater when operating under severe DNI drop conditions. Finally, as discussed in [112], the insulation of a reactor's aperture throughout night time, which can be easily achieved through the use of a variable aperture mechanism, may decrease the time required for heating up the reactor in the morning. Therefore, increasing the overall efficiency of the solar reactor system in all applications.

The *control override* approach illustrated above was simply implemented using an if statement that evaluates the DNI or power level with respect to a minimum constant (set as 10 A). If the power level drops below this minimum value, the control signal will immediately be overridden, where the variable aperture will be fully closed until the power level increases again, at which the variable aperture will fully open. The loop of the *control override* works at a much faster rate than the normal control loop, since there is no computational time required and the variable aperture needs to respond very quickly under these disturbances to make best use of its superior behavior illustrated above. This explains the slight delay in the aperture's response seen in Figure 6-12 (b) when the variable aperture was allowed to be fully opened. Having said that, the present way at which the system knows about the current power level is recorded manually into the DAQ and control LabVIEW VI. Using a more advanced method, the power level could have been recorded by the system using the HFG, after having it fixed in an illuminating position away from the solar receiver and calibrated. Thus, simulating a method that is more likely to be implemented in a real-

life application. However, testing this method in the laboratory will make it susceptible to errors as a result of the moving aperture or personnel due to the confined laboratory space.

6.3.5. Other Control Strategies

After the thorough investigation of using the variable aperture to compensate for transient variations in solar energy using a MPC and PID controllers, other control strategies will now be considered. Although the use of a variable aperture mechanism is mainly targeted for applications for which the flow rate cannot be manipulated (or manipulated at a minimal level), regulation of the receiver's average temperature will be investigated using two additional control strategies: regulating the average temperature using a PID feedstock flow rate controller in addition to a hybrid PID MISO controller that can manipulate both the feedstock flow rate and variable aperture. These two control strategies are investigated in the following sections.

PID Experimental Feedstock Flow Rate Control. A PID controller was developed to regulate the average temperature inside the solar receiver by manipulating the feedstock flow rate. Analogous to the aperture control, flow rate control signals are constrained within an operating range, which is between 2.5 LPM (lowest acceptable flow rate) and 30 LPM (highest possible flow rate from the flow controller). Control signals outside this range are treated as previously described for the PID aperture controller. However, there is no constraint on the control action Δu of the flow rate. The controller's parameters were identified using the numerical model in the same approach described previously for the variable aperture controller. Having said that, the final tuned controller parameters for K_P, τ_I, and τ_D were -5 LPM/°C, 250 s, and 62.5 s. Then, the PID flow controller was implemented on the experimental setup and its performance was tested for tracking different desired set point temperatures. For that, an experimental test was performed to examine the response of the system in tracking temperature set points in the range from 700 to 800 °C, while operating under a power level of 160 A. The system's response is shown in Figure 6-13. It is important to note that during feedstock flow rate control testing, the variable aperture remained attached to the solar receiver while being maintained at a fully opened position.

As can be seen in Figure 6-13, the average temperature within the solar receiver can only be regulated within the range from 700 to 800 °C. At 700 °C, the flow required to maintain the set point is around 29 LPM, which is very close to saturation, as can be concluded from the second set point of 700 °C. The first set point of 700 °C shows a significantly lower flow rate (approximately 23 LPM) since the solar receiver was still undergoing transient heating. If left for sufficient time, the flow rate would have gradually increased to coincide with that obtained at the second set point

of 700 °C. On the other hand, the flow required to maintain a set point of 800 °C is approximately 6 LPM, which is again close to the lower limit of the feedstock flow rate. This shows the limited ability of regulating the temperature within the solar receiver based on a non-participating gas flow, as expected. Nevertheless, feedstock flow rate control provided a more superior response in tracking a desired set point within its range of control, where the overshoots obtained for each of the set points shown in Figure 6-13 were 0.8, 0.6, 0.4, 0.2, 0.2, -0.3, -0.2, and 0.4 °C. These overshoots are significantly lower than that obtained using variable aperture control. As a final note, through comparison of the variable aperture and flow rate control responses, it can be seen that the variable aperture is able to track a change to a lower set point significantly faster, while the flow rate control is able to track a change to a higher set point significantly faster. This is due to the blocking ability of the variable aperture, where it can directly manipulate the solar power into the solar receiver to achieve a faster temperature drop in comparison to flow rate control.

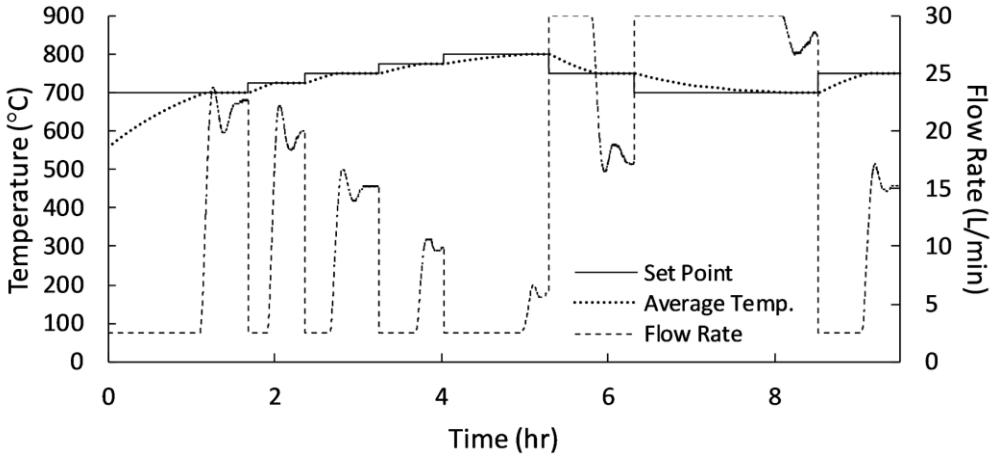

Figure 6-13: Experimental testing for tracking set point using PID feedstock flow rate controller at a power level of 160 A, showing set point and average temperatures with the flow rate response

PID Experimental MISO (Hybrid) Control of Aperture and Flow Rate. After the variable aperture and feedstock flow rate controllers demonstrated good responses, the implementation of a PID MISO (hybrid) controller was investigated. The PID MISO controller functions just as two separate independent PID controllers, where one manipulates the variable aperture while the other manipulates the feedstock flow rate. Although the two control methods could significantly affect the performance of one another, it has been tested numerically that the already tuned and tested PID parameters for the two control methods provide satisfactory results for the PID MISO controller under different operating conditions. The MISO controller then follows a set of rules to determine the appropriate PID controller to take action.

The rules followed by the PID MISO controller revolve around a single objective, which is to achieve the highest possible feedstock flow rate for a given set point temperature and power level. Therefore, the feedstock flow rate controller will always be considered as the controller of choice (primary controller) until it reaches its maximum limit and is no longer able to maintain a given set point, where the control action is switched to the variable aperture controller. Having said that, when the average temperature exceeds the set point by a certain value of $T_{tol,flow}$ ($e < -T_{tol,flow}$), the flow controller is deemed to be incapable of maintaining the set point, and the control action changes from flow rate to variable aperture controller. When this switch occurs, the feedstock flow rate is set to its maximum and the control action will stay reserved for the variable aperture, until it is deemed to be incapable of maintaining the set point or providing a faster set point tracking. This is determined to be the case when the average temperature drops below the set point in excess of $T_{tol,ap}$ ($e > T_{tol,ap}$), where the control action changes from variable aperture to flow rate controller. In a similar manner, the variable aperture is set to its maximum size and the control action will stay reserved for the feedstock flow rate, until it is once again deemed to be incapable of maintaining the set point. The above is achieved by implementing a simple if statement.

With the technique described above for determining the method of control action, the MISO controller can track a certain set point in a significantly faster manner than that previously achieved using any of the two individual PID controllers. When the system tries to reach significantly higher temperature values, the error value is positive which means that the flow rate controller is in action. This results in the system operating under a flow rate and aperture size of 2.5 LPM and 8.75 cm, which provides the fastest rate of temperature increase possible. On the other hand, when the system tries to reach significantly lower temperature values, the error value is negative, meaning that the variable aperture controller will be in action. This results in the system operating under a flow rate and aperture size of 30 LPM and 2 cm, which once again provides the fastest rate of temperature decrease possible. However, there is a drawback with such a control scheme. The system might remain trapped within the tolerance values of $T_{tol,flow}$ and $T_{tol,ap}$, where a certain PID controller is no longer able to reduce the set point error magnitude to zero but yet the MISO controller does not recognize its incapability to do so, leading to a set point offset error. In practice, the conditions under which a set point offset error can occur may not be observed, just as it did not occur through this experimental campaign. Nevertheless, it is important to keep this trapping region to minimum, without causing the MISO controller to falsely deem a PID controller as incapable and change the control action method. Therefore, and based on the overshoot values obtained earlier for the

variable aperture and flow rate PID controllers, the values of $T_{tol,flow}$ and $T_{tol,ap}$ were set to 1.0 and 2.5 °C, with the value of $T_{tol,ap}$ being more conservative to avoid an unnecessary abrupt change in the variable aperture under different operating conditions (like severe fluctuations in the power level).

Once the MISO controller was numerically tested under different operating conditions, it was then implemented on the experimental setup to further test its performance. The MISO controller was first tested for set point tracking, similar to that performed in Figure 6-5 and Figure 6-8, with the same temperature set points and power level. The responses of the system's temperature, variable aperture, and feedstock flow rate are shown in Figure 6-14. Based on the results shown, the MISO controller was able to well-regulate the average temperature within the receiver with stable responses for the variable aperture and flow rate. The overshoots for the set point temperatures shown in Figure 6-14 are 3.4, 0.8, 0.3, -1.6, and 0.4 °C. In comparison with the PID variable aperture controller in Figure 6-5, the first overshoot obtained here is significantly lower, even though there is a delayed response of the variable aperture as the MISO controller switches to aperture control. This is due to having a much higher feedstock flow rate that results in a slower rate of temperature increase. Similarly, the forth overshoot is greater in magnitude due to the resulting faster rate of temperature drop. The other three overshoots are significantly lower, since they are within the range regulated through the PID flow rate controller. Finally, it is worth noting that temperature tracking performed through the use of the MISO controller was much faster than that of the PID variable aperture controller shown in Figure 6-5.

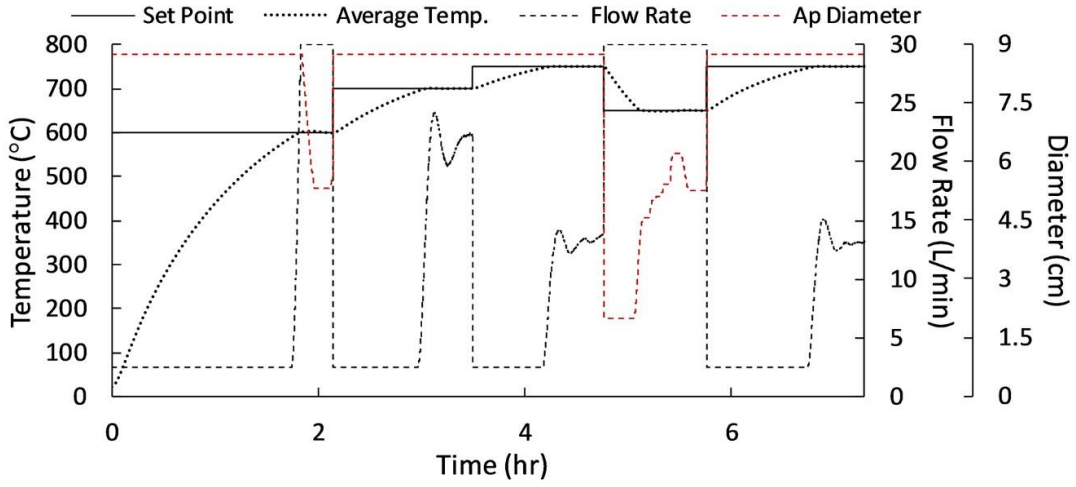

Figure 6-14: Experimental testing for tracking set point using PID MISO controller at a power level of 160 A, showing set point and average temperatures with the flow rate and variable aperture responses

With the results already demonstrated in Figure 6-14, the MISO controller can be deemed reliable in tracking a set point and hence accommodating for solar disturbances. In the upcoming sections, the focus will be on investigating the response of the system through the use of the MISO controller under severe fluctuations in the solar power supplied to the receiver. Through this, the response of the controller can be further examined, in addition to the variable aperture's capabilities in compensating for solar transient variations, which is the major focus of this research work.

As a way of simulating significant fluctuations in the DNI level experienced during a moderate cloudy day, the power level from the HFSS was varied within the range from 140 to 185 A, while the set point temperature was set to 700 °C. The changes in the power level investigated were of mild (5-15 A), moderate (16-25 A), or severe (26-40 A) forms. Figure 6-15 (a) shows the responses of the system's temperature, variable aperture, and flow rate, while Figure 6-15 (b) shows the power level in addition to the powers intercepted and captured by the variable aperture mechanism. As can be seen in Figure 6-15, the solar receiver system was able to maintain the average temperature at its set point despite all forms of power level changes. Throughout the entire experiment, the average temperature remained within ± 3 °C, with the exception of times when severe changes were applied to the power level. These occurred at power level changes from 150 to 180 A and 185 to 145 A, where the average temperature deviated a bit more from its set point, but still remained within ± 5 °C. Therefore, the tested MISO controller demonstrated a stable and effective approach to rejecting even severe changes in the DNI level. In addition to temperature control, the variable aperture mechanism intercepted an average of 874 W throughout the entire experiment, out of which 447 W was captured, based on the results shown in Figure 6-15 (b). This gives an efficiency of approximately 51%.

The final level of testing consisted of simulating the DNI level of a *cloudy day*, where passing clouds significantly affect sunshine, leading to major fluctuations in the amount of irradiance intercepted by the Earth's surface. The simulated day corresponded to data gathered by NREL for the sun's DNI on December 12th, 2018 [22]. Once again, the simulated day was chosen to be in December to have a relatively short period of sunshine. The DNI level was simulated in a manner similar to that performed for the *sunny day*, where the current was allowed to change based on DNI increments that were multiples of 50 W/m^2. With that being said, the actual and simulated DNI plots are shown in Figure 6-16 (a). In addition, the responses of the MISO system's temperature, variable aperture, and flow rate under fluctuations in DNI for a set point temperature of 650 °C are

shown in Figure 6-16 (b), while the intercepted and captured powers by the aperture mechanism are shown in Figure 6-16 (c).

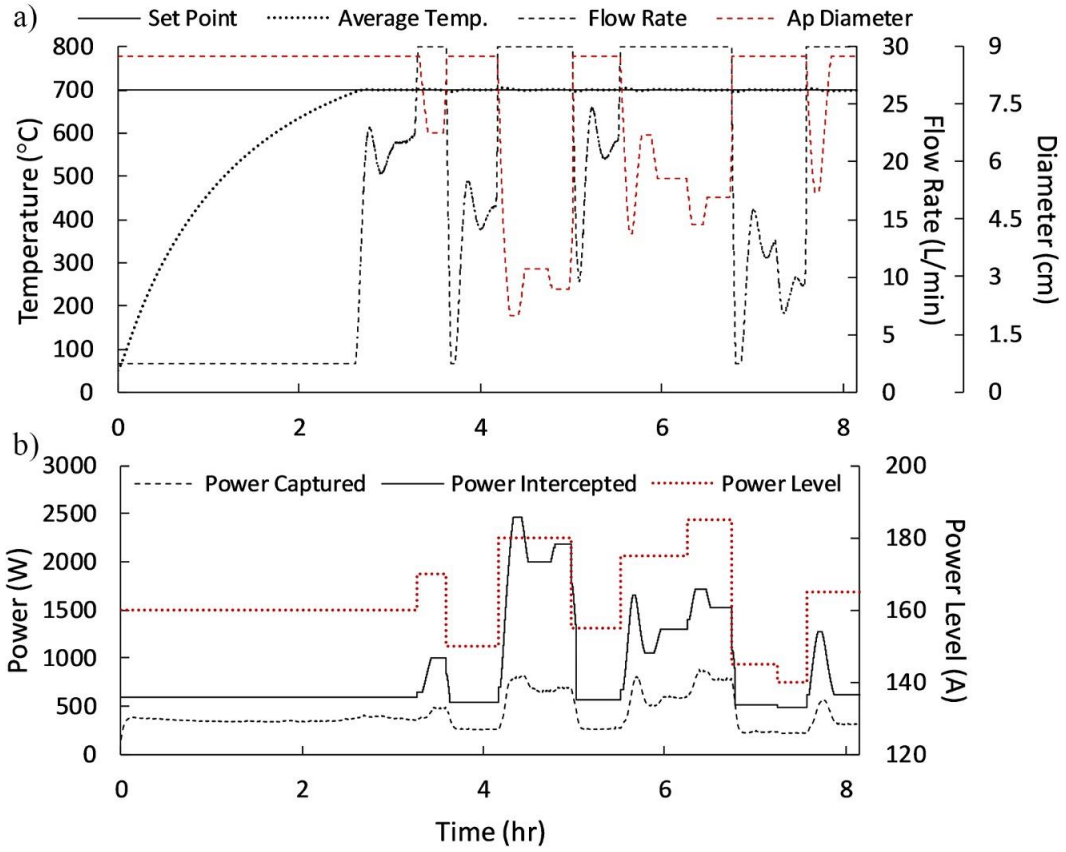

Figure 6-15: Experimental testing for maintaining set point using PID MISO controller at fluctuating power levels, showing (a) set point and average temperatures with the variable aperture and flow rate responses, and (b) power level in addition to power intercepted and captured by the aperture

Based on the results shown in Figure 6-16, the variable aperture coupled solar receiver was able to compensate for major fluctuations in DNI during a cloudy day and maintain the average temperature within a satisfactory margin of error. Average temperature values remained within ± 5 °C, except at time of 12:52, where the overshoot increased to 6.5 °C as a result of a severe sudden increase in the DNI level from 700 to 900 Wm^{-2}. With the exception of that overshoot, the MISO controller demonstrated a stable, smooth, and effective approach in determining the appropriate control action type and avoiding sharp changes in the variable aperture. For a quick numerical overview of the system's response, the average temperature was maintained within ± 5 °C for 6.38 hr, ± 3 °C for 5.90 hr, and ± 1 °C for 3.86 hr. For completeness, based on the results shown in Figure 6-16 (c), the variable aperture intercepted an average power of 954 W, out of which 495 W was captured throughout the day. This gives an efficiency of 52%.

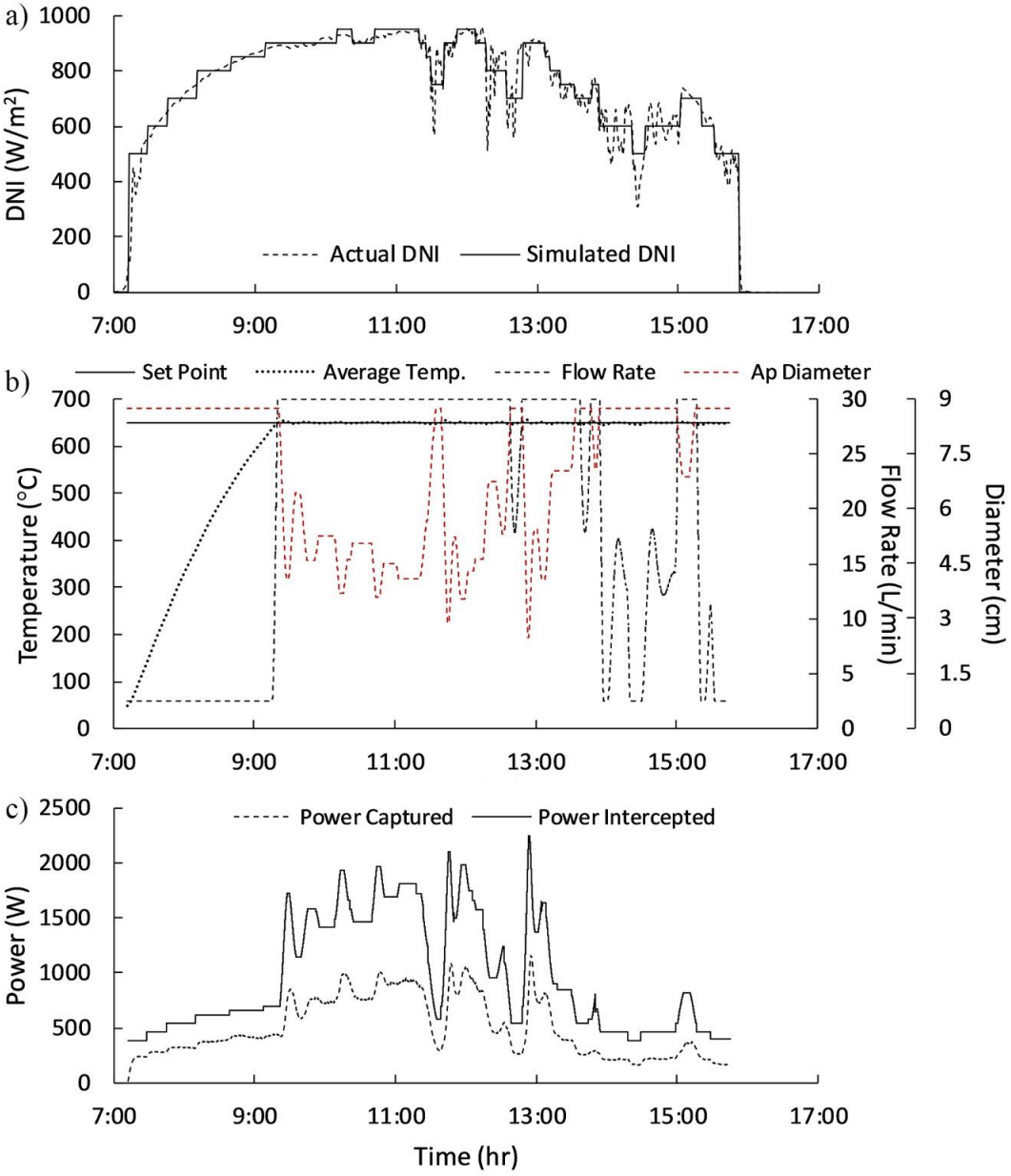

Figure 6-16: Experimental testing for disturbance rejection using PID MISO controller for actual day simulation, showing (a) actual and simulated DNI for December 12th, 2018, (b) set point and average temperatures with the variable aperture and flow rate responses, and (c) power intercepted and captured by the aperture

6.4. Conclusions

In this chapter, the variable aperture mechanism was used to regulate the average temperature within the solar receiver. Two different controllers were successfully implemented and tested on the experimental setup. The first control method was based on a simple PID controller, while the second was based on a MPC system. For the MPC, the receiver system was treated as an ARX

model, where a RLS method with a forgetting factor was used to identify the system using the numerical model. Upon numerically tuning and testing the two controllers, they were successfully implemented and tested on the experimental setup for tracking and maintaining different temperature set points that range from 600 to 750 °C. Additionally, sun's DNI measurements from a *sunny day* were used to experimentally test the performance of both controllers in maintaining a set point temperature within the solar receiver under mild variations in the DNI level. Based on the results shown, both controllers performed satisfactory, where their temperature overshoots and values remained within ± 3 °C from the set point. However, the MPC system's response was slightly superior than that of the PID, where its overshoots were significantly lower and its temperature values were maintained at a tighter tolerance within the set point. This was due to the superior ability of the ARX model in accommodating for the highly non-linear behavior of the variable aperture and predicting the future response of the system.

In addition to the high performance of the variable aperture in regulating the temperature within the solar receiver, two additional desirable characteristics were experimentally demonstrated. First, it was shown that the aperture mechanism was able to capture approximately 54% of the power it intercepts while it controls the receiver's temperature. This power can be made available to a secondary process coupled to the solar receiver or it can be used to preheat the feedstock in order to obtain better process efficiencies. Such behavior, in addition to the simpler dynamics and method of control, make a variable aperture mechanism much superior than its counterparts (heliostat field or shutter control). Additionally, it was shown that in severe passing cloud cases where the DNI level drops to an approximate zero, the aperture mechanism can help reduce the temperature drop in the system by fully closing its aperture (*control override*) and hence reducing the re-radiation losses from receiver's cavity. After 10 minutes of power absence and starting at a temperature of 750 °C, the system with the variable aperture closed was at an average temperature of 2.8 °C higher than that with the aperture fully opened. This difference is expected to be much more significant at higher operating temperatures. The second behavior discussed can be used to mitigate the effect of severe passing clouds or to decrease the heating up time required for a solar reactor in the following morning. Therefore, making the system more efficient.

Finally, two additional control strategies were implemented and experimentally tested as a mean of observing their performance. The first one was a PID feedstock flow rate controller, while the second one was a PID MISO controller that can manipulate both the feedstock flow rate and variable aperture based on their respective separate PID controllers. The MISO controller follows

a set of rules that allows it to determine the appropriate controller to take action to efficiently regulate the temperature within the solar receiver. The results of both control strategies were satisfactory. However, with the feedstock flow rate control, the range of average temperature within which the receiver can be regulated is slightly limited due to the presence of a non-participating flow. The PID flow rate controller can only regulate the average temperature between 700 to 825 °C, while the PID aperture and MISO controllers can regulate the temperature between 500 to 800 °C and 425 to 825 °C. The MISO controller also demonstrated a much faster set point tracking response when compared to each of the independent PID controllers. Finally, a *cloudy day* was tested for using the MISO controller, where the variable aperture once again demonstrated its superior capabilities in compensating for heavily fluctuating DNI levels and allowing the controller to maintain the average temperature within ± 5 °C of its set point throughout the entire day.

Chapter 7

Summary and Conclusions

One of the main challenges in CSP applications is to provide better control systems that are capable of absorbing changes and fluctuations in weather conditions. The operation and performance of a solar thermochemical receiver can be highly affected by changes in its operating temperature due to the intermittent behavior of the sun's DNI. These changes usually decrease the processes' efficiencies and create several complications in the operation of solar reactors, such as difficulties downstream of the reactor in the purification and separation processes. In addition, temperature regulation is also required to avoid deterioration of receivers due to excessive thermal stresses. Therefore, better and more reliable control systems and methods should be developed.

To perform experimental testing in a laboratory setup, a new 10 kW_e HFSS was presented and characterized in Chapter 2. This was performed using an indirect heat flux mapping technique that used a single Lambertian target, as opposed to the use of two targets in literature. This saves cost and time and eliminates misalignment errors that would otherwise occur. A slight misalignment of 4 mm, as an example, can decrease the peak flux density by around 6.8%. Upon characterizing the HFSS at the focal plane, the peak flux density and total power incident on a 10 x 10 cm^2 target were determined to be 6.99 MWm^{-2} and 3.49 kW for the maximum current supply of 200 A, while being 3.31 MWm^{-2} and 1.39 kW for the minimum current of 120 A. Hence, allowing for a great variation in power to mimic fluctuations in the sun's DNI. It was concluded that variation of the current supply had no effect on the overall flux distribution, but rather a linear increase or decrease in the flux values. Other characterized parameters for the HFSS include its transient time response, temporal instability, and radial non-uniformity. Finally, a new method, *merging method*, that is promising for wider flux distributions in the CSP field was presented to enable acquiring flux data on larger target sizes. Results of this method deviated by just 0.6% and 6.5% for the peak flux and total power, which was mainly due to the lower resolution as a result of the larger target size.

Then, the HFSS was numerically characterized and modeled in Chapter 3 using two different approaches, based on experimental data captured at the focal plane and 12 other planes. The first approach was the forward MCRT method, where the in-house developed model provided results that were in great agreement with the experimental ones, resulting in percentage errors of 0.07 and 1.17% for both the peak flux and total power at the focal plane. It was concluded that a composite shape of a hemisphere with a radius of 1 mm that is attached to a cylinder of 1 mm in radius and

10 mm in length with a power ratio between the two shapes of 0.23:0.77 can accurately model the 10 kW_e xenon arc. The second approach was an inverse ray tracing method, which is a highly ill-posed problem and is undergoing further research improvements. It was concluded that an intensity first-order interpolation scheme unnecessary complicated the problem, where a zeroth-order interpolation has been proposed. With a zeroth-order interpolation, the computational time and error values reduced significantly. Furthermore, a new approach of constraining the formulated SoEs with an equality constraint that eliminates intensity values that cannot be traced back to the reflector was proposed. This approach seems promising, as the error values and computational time further reduced significantly to a final error value of 30.4%. Although this value is still large, it is significantly lower than that obtained in literature for a HFSS using the inverse ray tracing method.

Following that, the setup of the cavity-type solar receiver was thoroughly presented in Chapter 4. Through the use of the validated MCRT model, a numerical model of the receiver was developed and validated based on experimental results, where the average error value of the steady state temperatures within the receiver was 0.3%. Based on differences between the modelled and experimental transient responses, it was concluded that the HFSS's transient time response was dominant at directions that intersected the front and middle cavity sections. Then, the numerical model was used to quantify system losses, where around 60% of the power at steady state was lost through radiation. This led to the discussion on the optimum aperture size at which the receiver's temperature would peak. It was numerically shown that this optimum size depends on the power level supplied by the HFSS, where the size decreases as the power increases. This led to the proposal of being able to continuously optimize the receiver at varying sun's DNI levels to obtain maximum temperatures if necessary, which might be possible to achieve using a variable aperture.

Then, the design and motion of the variable aperture mechanism was presented in Chapter 5, where it was then coupled to the solar receiver. The aperture mechanism consisted of eight blades that moved in a translational type of motion to approximate a circular variable aperture, with a total thickness of 4 cm. Four of these blades were water-cooled by coupling them to a heat exchanger, while the rest of the blades were just air-cooled. It was experimentally demonstrated that with this arrangement, an average of 54% of the intercepted energy can be captured by the heat exchanger. Then, the numerical model was extended by implementing the variable aperture, where once again the model was validated using experimental data. It was shown that water cooling the variable aperture had no effect on the average temperatures at different aperture diameters. Therefore, leading to the conclusion that intercepted radiation by the aperture mechanism was completely lost

from the receiver's system. Hence, the behavior of obtaining peak temperatures by varying the aperture size was not observed by using the aperture mechanism. Therefore, if it is desired to maximize the temperature inside a receiver's cavity rather than just regulate it, further work should be focused on integrating the aperture mechanism more effectively into the solar receiver's design.

Finally, the variable aperture mechanism was used to regulate the temperature within the solar receiver in Chapter 6. The aperture control was successfully implemented using a MPC and PID controllers, where both controllers performed satisfactory, keeping the average temperature overshoots and values within ± 3 °C of desired set points. However, the MPC system's response was slightly superior than that of the PID, where its temperature overshoots and values remained within a tighter tolerance. In addition, it was shown that the aperture mechanism was able to capture approximately 54% of intercepted power while controlling the receiver's temperature. Furthermore, it was shown that the variable aperture can mitigate the effect of severe passing clouds or decrease the heating up time by fully closing. Finally, two additional control strategies were implemented and experimentally tested as a mean of observing their performance. The first one was a PID feedstock flow rate controller, while the second one was a PID MISO controller that can manipulate both the feedstock flow rate and variable aperture. The limited performance of feedstock flow rate manipulation was shown, where it was only able to regulate the temperature between 700 to 825 °C as opposed to 425 to 825 °C using the MISO controller. Finally, a *cloudy day* was tested for using the MISO controller, where the variable aperture once again demonstrated its superior capabilities in compensating for heavily fluctuating DNI levels and maintaining the average temperature within ± 5 °C of its set point. To conclude, the conditions of the aperture mechanism before and after experimentation are shown in Figure 7-1.

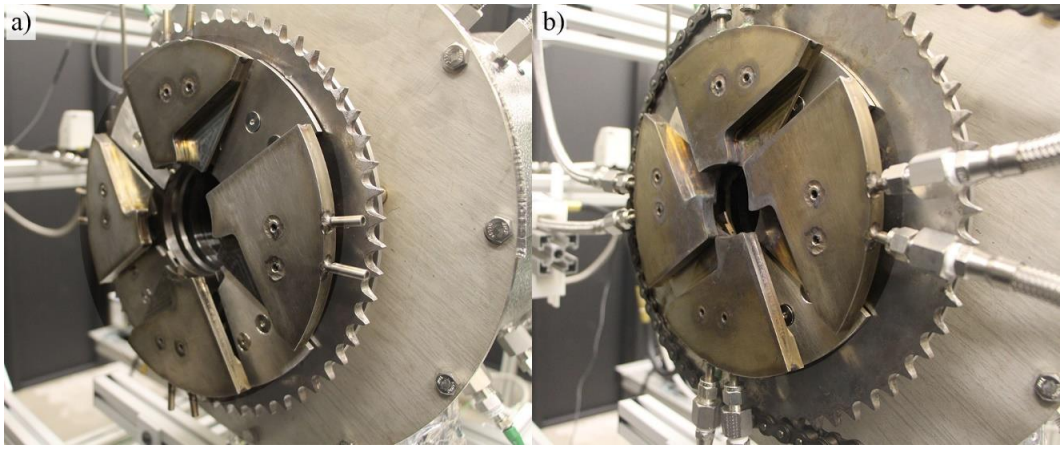

Figure 7-1: Photo of the variable aperture mechanism at the end of the experimental campaign

Based on the aforementioned information, the variable aperture meets the requirements of this research work, as described in Chapter 1. This is summarized in the following list, where the proposed control system, when compared to other control methods in literature, provides:

- Simpler method of control: The variable aperture, being relatively small in size, is regulated using a single motor and is directly attached to the solar receiver. This is much simpler than controlling a field of large heliostats or a gigantic shutter.
- Easier method of control: The dynamics presented by regulating the variable aperture are much less sophisticated than those presented by regulating the heliostat field.
- More accurate method of control: The average temperature of the solar receiver can be maintained within a tighter tolerance using the variable aperture when compared to results in literature.
- More energy efficient method of control: The variable aperture mechanism has a lower power consumption when compared to other control methods in literature. Additionally, the coupled heat exchanger is capable of capturing approximately 54% of the intercepted power, which can be made available to a secondary process.

In addition, the control system demonstrated its capability of withstanding relatively long times of operation and high thermal stresses. The variable aperture mechanism shown in Figure 7-1 (b) experienced hundreds of hours of operation, including some entirely air-cooled experiments. Nevertheless, the mechanism operated smoothly and with minimal maintenance.

Bibliography

[1] EIA, December 2017 Monthly Energy Review, Washington, D.C., 2017.

[2] Energy & Mining, World Bank. (2015). https://data.worldbank.org/topic/energy-and-mining?end=2018&start=1960 (accessed May 4, 2019).

[3] E.F. Camacho, M. Berenguel, Control of solar energy systems, in: 8th IFAC Symp. Adv. Control Chem. Process., The International Federation of Automatic Control, Singapore, 2012: pp. 848–855. doi:10.3182/20120710-4-SG-2026.00181.

[4] R. Palumbo, M. Keunecke, S. Moller, A. Steinfeld, Reflections on the design of solar thermal chemical reactors: thoughts in transformation, Energy. 29 (2004) 727–744. doi:10.1016/S0360-5442(03)00180-4.

[5] IEA, Technology Roadmap: Solar Thermal Electricity, Paris, 2014.

[6] J. Sack, M. Roeb, C. Sattler, R. Pitz-Paal, A. Heinzel, Development of a simulation-software for a hydrogen production process on a solar tower, Sol. Energy. 112 (2015) 205–217. doi:10.1016/j.solener.2014.11.026.

[7] A. Steinfeld, M. Schubnell, Optimum aperture size and operating temperature of a solar cavity-receiver, Sol. Energy. 50 (1993) 19–25. doi:10.1080/0020739840150306.

[8] T. Kodama, High-temperature solar chemistry for converting solar heat to chemical fuels, Prog. Energy Combust. Sci. 29 (2003) 567–597.

[9] A. Steinfeld, Solar thermochemical production of hydrogen — a review, Sol. Energy. 78 (2005) 603–615. doi:10.1016/j.solener.2003.12.012.

[10] N. Ozalp, V. Shilapuram, Step-by-step methodology of developing a solar reactor for emission-free generation of hydrogen, Int. J. Hydrogen Energy. 35 (2010) 4484–4495. doi:10.1016/j.ijhydene.2010.02.032.

[11] E. Baniasadi, Concurrent hydrogen and water production from brine water based on solar spectrum splitting: process design and thermoeconomic analysis, Renew. Energy. 102 (2017) 50–64. doi:10.1016/j.renene.2016.10.042.

[12] P. Furler, A. Steinfeld, Heat transfer and fluid flow analysis of a 4 kW solar thermochemical reactor for ceria redox cycling, Chem. Eng. Sci. 137 (2015) 373–383. doi:10.1016/j.ces.2015.05.056.

[13] S. Chuayboon, S. Abanades, S. Rodat, Syngas production via solar-driven chemical looping methane reforming from redox cycling of ceria porous foam in a volumetric solar reactor, Chem. Eng. J. 356 (2019) 756–770. doi:10.1016/j.cej.2018.09.072.

[14] O. Uyi, H. Dina, S. Abdullah, C.K. Cheng, Syngas production from methane dry reforming over SmCoO3 perovskite catalyst: Kinetics and mechanistic studies, Int. J. Hydrogen Energy. 42 (2017) 9707–9721. doi:10.1016/j.ijhydene.2017.03.061.

[15] J. Säck, S. Breuer, P. Cotelli, A. Houaijia, M. Lange, M. Wullenkord, C. Spenke, M. Roeb, C. Sattler, High temperature hydrogen production: design of a 750 KW demonstration plant for a two step thermochemical cycle, Sol. Energy. 135 (2016) 232–241. doi:10.1016/j.solener.2016.05.059.

[16] S. Kräupl, A. Steinfeld, Monte Carlo radiative transfer modeling of a solar chemical reactor for the co-production of zinc and syngas, J. Sol. Energy Eng. 127 (2005) 102. doi:10.1115/1.1824105.

[17] R. Muller, P. Haeberling, R.D. Palumbo, Further advances toward the development of a direct heating solar thermal chemical reactor for the thermal dissociation of ZnO (s), Sol. Energy. 80 (2006) 500–511. doi:10.1016/j.solener.2005.04.015.

[18] S. Kraupl, U. Frommherz, C. Wieckert, Solar carbothermic reduction of ZnO in a two-cavity reactor:

laboratory experiments for a reactor scale-up, J. Sol. Energy Eng. 128 (2005) 8–15. doi:10.1115/1.2147585.

[19] E. Koepf, I. Alxneit, C. Wieckert, A. Meier, A review of high temperature solar driven reactor technology: 25 years of experience in research and development at the Paul Scherrer Institute, Appl. Energy. 188 (2017) 620–651. doi:10.1016/j.apenergy.2016.11.088.

[20] B.J. Hathaway, J.H. Davidson, Demonstration of a prototype molten salt solar gasification reactor, Sol. Energy. 142 (2017) 224–230. doi:10.1016/j.solener.2016.12.032.

[21] H.I. Villafán-vidales, C.A. Arancibia-bulnes, D. Riveros-rosas, H. Romero-paredes, C.A. Estrada, An overview of the solar thermochemical processes for hydrogen and syngas production: reactors, and facilities, Renew. Sustain. Energy Rev. 75 (2017) 894–908. doi:10.1016/j.rser.2016.11.070.

[22] A. Andreas, T. Stoffel, NREL Report No. DA-5500-56509, Univ. Nevada Las Vegas, Nevada. (2006). http://dx.doi.org/10.5439/1052548 (accessed February 15, 2019).

[23] L. Zhu, Y. Lu, S. Shen, Solar fuel production at high temperatures using ceria as a dense membrane, Energy. 104 (2016) 53–63. doi:10.1016/j.energy.2016.03.108.

[24] J. Lapp, J.H. Davidson, W. Lipinski, Efficiency of two-step solar thermochemical non-stoichiometric redox cycles with heat recovery, Energy. 37 (2012) 591–600. doi:10.1016/j.energy.2011.10.045.

[25] R. Kumar, T. Geißler, A. Ab, A. Heinzel, K. Mehravaran, G. Mu, M. Plevan, C. Rubbia, D. Salmieri, L. Stoppel, S. Stu, A. Weisenburger, H. Wenninger, T. Wetzel, Development of methane decarbonisation based on liquid metal technology for CO2-free production of hydrogen, Int. J. Hydrogen Energy. 41 (2016) 8159–8167. doi:10.1016/j.ijhydene.2015.11.164.

[26] F. Lei, L. Freiberg, Y. Wang, I. Reddick, G. Jovanovic, A. Yokochi, N. Auyeung, Non-catalytic ethane cracking using concentrated solar energy, Chem. Eng. J. 355 (2019) 58–64. doi:10.1016/j.cej.2018.07.194.

[27] M. Roeb, J.P. Sack, P. Rietbrock, C. Prahl, H. Schreiber, M. Neises, L. de Oliveira, D. Graf, M. Ebert, W. Reinalter, M. Meyer-Grunefeldt, C. Sattler, A. Lopez, A. Vidal, A. Elsberg, P. Stobbe, D. Jones, A. Steele, S. Lorentzou, C. Pagkoura, A. Zygogianni, C. Agrafiotis, A.G. Konstandopoulos, Test operation of a 100 kW pilot plant for solar hydrogen production from water on a solar tower, Sol. Energy. 85 (2011) 634–644. doi:10.1016/j.solener.2010.04.014.

[28] B.M. Ekman, G. Brooks, M.A. Rhamdhani, Development of high flux solar simulators for solar thermal research, Energy Technol. 2015 Carbon Dioxide Manag. Other Technol. 141 (2016) 149–159. doi:10.1007/978-3-319-48220-0_17.

[29] G. Levêque, R. Bader, W. Lipiński, S. Haussener, High-flux optical systems for solar thermochemistry, Sol. Energy. 156 (2017) 133–148. doi:10.1016/j.solener.2017.07.046.

[30] A. Gallo, A. Marzo, E. Fuentealba, E. Alonso, High flux solar simulators for concentrated solar thermal research: A review, Renew. Sustain. Energy Rev. 77 (2017) 1385–1402. doi:10.1016/j.rser.2017.01.056.

[31] X. Dong, Z. Sun, G.J. Nathan, P.J. Ashman, D. Gu, Time-resolved spectra of solar simulators employing metal halide and xenon arc lamps, Sol. Energy. 115 (2015) 613–620. doi:10.1016/j.solener.2015.03.017.

[32] J. Petrasch, P. Coray, A. Meier, M. Brack, P. Haberling, D. Wuillemin, A. Steinfeld, A novel 50 kW 11,000 suns high-flux solar simulator based on an array of Xenon arc lamps, Sol. Energy Eng. 129 (2007) 405–411.

[33] N.P. Siegel, D. Drive, J.P. Roba, D. Drive, Design, modeling, and characterization of a 10 kW e metal halide high flux solar simulator, J. Sol. Energy Eng. 140 (2018) 1–7. doi:10.1115/1.4039658.

[34] W. Wang, L. Aichmayer, J. Garrido, B. Laumert, Development of a Fresnel lens based high-flux

solar simulator, Sol. Energy. 144 (2017) 436–444. doi:10.1016/j.solener.2017.01.050.

[35] R. Gill, E. Bush, P. Haueter, P. Loutzenhiser, Characterization of a 6 kW high-flux solar simulator with an array of xenon arc lamps capable of concentrations of nearly 5000 suns, Rev. Sci. Instrum. 86 (2015). doi:10.1063/1.4936976.

[36] G. Levêque, R. Bader, W. Lipiński, S. Haussener, Experimental and numerical characterization of a new 45 kWel multisource high-flux solar simulator, Opt. Express. 24 (2016) 1360–1373. doi:10.1364/OE.24.0A1360.

[37] L. Martínez-Manuel, M.I. Peña-Cruz, M. Villa-Medina, C. Ojeda-Bernal, M. Prado-Zermeño, I. Prado-Zermeño, C.A. Pineda-Arellano, J.G. Carrillo, I. Salgado-Tránsito, F. Martell-Chavez, A 17.5 kWel high flux solar simulator with controllable flux-spot capabilities: design and validation study, Sol. Energy. 170 (2018) 807–819. doi:10.1016/j.solener.2018.05.088.

[38] C. Ophoff, S. Korotunov, N. Ozalp, Optimization of design and process parameters for maximized and stable solar receiver efficiency, in: Proc. 2nd Therm. Fluid Eng. Conf., 2017: p. TFEC-IWHT2017-18225.

[39] P. Kuhn, A. Hunt, A new solar simulator to study high temperature solid-state reactions with highly concentrated radiation, Sol. Energy Mater. 24 (1991) 742–750.

[40] J. Li, J. Gonzalez-aguilar, C. Pérez-rábago, H. Zeaiter, Optical analysis of a hexagonal 42kWe high-flux solar simulator, Energy Procedia. 57 (2014) 590–596. doi:10.1016/j.egypro.2014.10.213.

[41] K. Wieghardt, K. Funken, G. Dibowski, B. Hoffschmidt, D. Laaber, P. Hilger, K. Wieghardt, K. Funken, G. Dibowski, B. Hoffschmidt, D. Laaber, P. Hilger, K. Eßer, SynLight – The world's largest artificial sun, in: AIP Conf. Proc., 2016: pp. 030038-1-030038–6. doi:10.1063/1.4949090.

[42] J. Sarwar, G. Georgakis, R. LaChance, N. Ozalp, Description and characterization of an adjustable flux solar simulator for solar thermal, thermochemical and photovoltaic applications, Sol. Energy. 100 (2014) 179–194. doi:10.1016/j.solener.2013.12.008.

[43] F. Gomez-Garcia, J. Gonzalez-aguilar, M. Romero, Experimental 3D flux distribution of a 7 kWe solar simulator, in: Proccedings SolarPACES Conf., Granada, Spain, 2011.

[44] E. Alonso, M. Romero, A directly irradiated solar reactor for kinetic analysis of non-volatile metal oxides reductions, Int. J. Energy Res. 39 (2015) 1217–1228. doi:10.1002/er.

[45] N. Gokon, S. Takahashi, H. Yamamoto, T. Kodama, Thermochemical two-step water-splitting reactor with internally circulating fluidized bed for thermal reduction of ferrite particles, Int. J. Hydrogen Energy. 33 (2008) 2189–2199. doi:10.1016/j.ijhydene.2008.02.044.

[46] K. Krueger, J.H. Davidson, W. Lipíñskí, Design of a new 45 high-flux solar simulator for high-temperature solar thermal and thermochemical research, J. Sol. Energy Eng. 133 (2011). doi:10.1115/1.4003298.

[47] B.M. Erickson, Characterization of the University of Florida solar simulator and an inverse solution for identifying intensity distributions from multiple flux maps in concentrating solar applicaitons, Master Thesis. (2012). doi:10.1017/CBO9781107415324.004.

[48] R.W. Moss, G.S.F. Shire, P.C. Eames, P. Henshall, T. Hyde, F. Arya, Design and commissioning of a virtual image solar simulator for testing thermal collectors, Sol. Energy. 159 (2018) 234–242. doi:10.1016/j.solener.2017.10.044.

[49] V. Esen, Ş. Sa, B. Oral, Light sources of solar simulators for photovoltaic devices: a review, Renew. Sustain. Energy Rev. 77 (2017) 1240–1250. doi:10.1016/j.rser.2017.03.062.

[50] K.R. Krueger, W. Lipiński, J.H. Davidson, Operational performance of the University of Minnesota 45 kWe high-flux solar simulator, J. Sol. Energy Eng. 135 (2013) 044501. doi:10.1115/1.4023595.

[51] A. Steinfeld, M. Brack, A. Meier, A. Weidenkaff, D. Wuillemin, A solar chemical reactor for co-

production of zinc and synthesis gas, Energy. 23 (1998) 803–814.

[52] K.R. Krueger, Design and characterization of a concentrating solar simulator, University of Minnesota, Minneapolis, MN, 2012. doi:10.1115/1.4036411.

[53] J. Xiao, H. Yang, X. Wei, Z. Li, A novel flux mapping system for high-flux solar simulators based on the indirect method, Sol. Energy. 179 (2019) 89–98. doi:10.1016/j.solener.2018.12.034.

[54] J. Ballestrín, S. Ulmer, A. Morales, A. Barnes, L.W. Langley, M. Rodríguez, Systematic error in the measurement of very high solar irradiance, Sol. Energy Mater. Sol. Cells. 80 (2003) 375–381. doi:10.1016/j.solmat.2003.08.014.

[55] ASTM-E927-05, Standard specification for solar simulators for photovoltaic testing, (2005).

[56] IEC-60904-9, International electrotechnical commission standard for solar simulator performance requirements, (2007).

[57] IREM SpA, Installation and Operational Manual: EX-200GM3, (2018).

[58] J. Ballestrin, C.A. Estrada, M. Rodríguez-Alonso, C. Pérez-Rábago, L.W. Langley, A. Barnes, Heat flux sensors: calorimeters or radiometers ?, Sol. Energy. 80 (2006) 1314–1320. doi:10.1016/j.solener.2006.03.005.

[59] E. Guillot, I. Alxneit, J. Ballestrin, J.L. Sans, C. Willsh, Comparison of 3 heat flux gauges and a water calorimeter for concentrated solar irradiance measurement, Energy Procedia. 49 (2014) 2090–2099. doi:10.1016/j.egypro.2014.03.221.

[60] B. Schwarz, G. Ritt, M. Koerber, B. Eberle, Laser-induced damage threshold of camera sensors and micro-optoelectromechanical systems, Opt. Eng. 56 (2017). doi:10.1117/1.OE.56.3.034108.

[61] S.C. Rowe, M.A. Wallace, A. Lewandowski, R.P. Fisher, W. Ray Cravey, D.E. Clough, I. Hischier, A.W. Weimer, Experimental evidence of an observer effect in high-flux solar simulators, Sol. Energy. 158 (2017) 889–897. doi:10.1016/j.solener.2017.09.040.

[62] S. Lighting, Xenon 10,000 Solar Simulator, (2017).

[63] ANSI/NCSL-Z540-2-1997, American national standard for expressing uncertainty - U.S. guide to the expression of uncertainty in measurement, (n.d.).

[64] M. Abuseada, N. Ozalp, C. Ophoff, Numerical and experimental investigation of heat transfer in a solar receiver with a variable aperture, Int. J. Heat Mass Transf. 128 (2019) 125–135. doi:10.1016/j.ijheatmasstransfer.2018.08.121.

[65] J. Sarwar, G. Georgakis, K. Kouloulias, K.E. Kakosimos, Experimental and numerical investigation of the aperture size effect on the efficient solar energy harvesting for solar thermochemical applications, Energy Convers. Manag. 92 (2015) 331–341. doi:10.1016/j.enconman.2014.12.065.

[66] J. Petrasch, A free and open source Monte Carlo ray tracing program for concentrating solar energy research, in: 4th Int. Conf. Energy Sustain., Phoenix, AZ, 2010: pp. 125–132.

[67] S.C. Rowe, D.E. Clough, B.A. Chubukov, A.J. Groehn, A.W. Palumbo, I. Hischier, A.W. Weimer, Worst-case losses from a cylindrical calorimeter for solar simulator calibration, Opt. Express. 23 (2015) A1309. doi:10.1364/oe.23.0a1309.

[68] B. Erickson, J. Petrasch, Inverse identification of intensity distributions from multiple flux maps in concentrating solar applications, J. Phys. Conf. Ser. 369 (2012) 012014. doi:10.1088/1742-6596/369/1/012014.

[69] C. Suter, A.T. Meouchi, G. Leveque, S. Haussener, Inverse analysis of radiative flux maps for the characterization of high flux sources, J. Sol. Energy Eng. 141 (2019) 1–13. doi:10.1115/1.4042227.

[70] M.F. Modest, Radiative Heat Transfer, third, Academic Press, 2013.

[71] J.R. Mahan, Radiation Heat Transfer: A Statistical Approach, Wiley, New York, 2002.

[72] W.L. Dunn, J.K. Shultis, Exploring Monte Carlo Methods, Elsevier Science, 2011. doi:10.1016/b978-0-444-51575-9.00020-8.

[73] J.R. Howell, R. Siegel, M.P. Mengüç, Thermal Radiation Heat Transfer, fifth, CRC Press, 2010.

[74] J.R. Howell, The Monte Carlo method in radiative heat transfer, ASME J. Heat Transf. 120 (1998) 547–560. doi:10.1115/1.2824310.

[75] J. Delatorre, G. Baud, J.J. Bézian, S. Blanco, C. Caliot, J.F. Cornet, C. Coustet, J. Dauchet, M. El Hafi, V. Eymet, R. Fournier, J. Gautrais, O. Gourmel, D. Joseph, N. Meilhac, A. Pajot, M. Paulin, P. Perez, B. Piaud, M. Roger, J. Rolland, F. Veynandt, S. Weitz, Monte Carlo advances and concentrated solar applications, Sol. Energy. 103 (2014) 653–681. doi:10.1016/j.solener.2013.02.035.

[76] Y. Jaluria, Solution of inverse problems in thermal systems, J. Therm. Sci. Eng. Appl. (2019). doi:10.1115/1.4042353.

[77] J.R. Howell, K. Daun, Inverse design in thermal radiation problems, in: Inverse Probl. Des. Optim. Symp., Rio de Janeiro, Brazil, 2004: pp. 1–12.

[78] M.J. Colaço, G.S. Dulikravich, Inverse and optimization problems in heat transfer, J. Braz. Soc. Mech. Sci. Eng. XXVIII (2006) 1–24.

[79] M. Vauhkonen, T. Tarvainen, T. Lähivaara, Inverse Problems, in: Math. Model., Springer, 2016: pp. 207–227.

[80] R.C. Aster, B. Borchers, C.H. Thurber, Parameter Estimation and Inverse Problems, 3rd Editio, Elsevier, 2018.

[81] P. von Zedtwitz, Hydrogen production by solar thermal steam gasification of coal, ETH Zurich, 2005. https://doi.org/10.3929/ethz-a-005066005.

[82] X. Dong, G.J. Nathan, Z. Sun, D. Gu, P.J. Ashman, Concentric multilayer model of the arc in high intensity discharge lamps for solar simulators with experimental validation, Sol. Energy. 122 (2015) 279–287. doi:10.1016/j.solener.2015.09.004.

[83] M. Slawski, M. Hein, Non-negative least squares for high-dimensional linear models: consistency and sparse recovery without regularization, Electron. J. Stat. 7 (2013) 3004–3056.

[84] C.L. Lawson, R.J. Hanson, Linear least squares with linear inequality constraints, in: Solving Least Squares Probl., Society for Industrial and Applied Mathematics, 1987: pp. 158–173.

[85] T.F. Coleman, Y. Li, A reflective Newton method for minimizing a quadratic function subject to bounds on some of the variables, SIAM J. Optim. 6 (1996) 1040–1058.

[86] MathWorks, Optimization Toolbox: User's Guide, (2019) 12-1-12–46. https://www.mathworks.com/help/pdf_doc/optim/optim_tb.pdf (accessed March 25, 2019).

[87] E.C. Beder, C.D. Bass, W.L. Shackleford, Transmissivity and absorption of fused quartz between 0.22 u and 3.5 u from room temperature to 1500, Appl. Opt. 10 (1971) 2263–2268.

[88] L. Li, C. Chen, A. Singh, N. Rahmatian, N. AuYeung, K. Randhir, R. Mei, J.F. Klausner, D.W. Hahn, J. Petrasch, A transient heat transfer model for high temperature solar thermochemical reactors, Int. J. Hydrogen Energy. 41 (2016) 2307–2325. doi:10.1016/j.ijhydene.2015.11.079.

[89] B. Guene Lougou, Y. Shuai, H. Xing, Y. Yuan, H. Tan, Thermal performance analysis of solar thermochemical reactor for syngas production, Int. J. Heat Mass Transf. 111 (2017) 410–418. doi:10.1016/j.ijheatmasstransfer.2017.04.007.

[90] A.J. Gallego, F. Fele, E.F. Camacho, L. Yebra, Observer-based model predictive control of a parabolic-trough field, Sol. Energy. 97 (2013) 426–435. doi:10.1016/j.solener.2013.09.002.

[91] E. Saade, D.E. Clough, A.W. Weimer, Model predictive control of a solar-thermal reactor, Sol. Energy. 102 (2014) 31–44. doi:10.1016/j.solener.2013.12.029.

[92] H. Abedini Najafabadi, N. Ozalp, Aperture size adjustment using model based adaptive control strategy to regulate temperature in a solar receiver, Sol. Energy. 159 (2018) 20–36. doi:10.1016/j.solener.2017.10.070.

[93] A.E. Kovtanyuk, N.D. Botkin, K.H. Hoffmann, Numerical simulations of a coupled radiative-conductive heat transfer model using a modified Monte Carlo method, Int. J. Heat Mass Transf. 55 (2012) 649–654. doi:10.1016/j.ijheatmasstransfer.2011.10.045.

[94] M. Abuseada, N. Ozalp, C. Ophoff, Two-dimensional transient heat transfer and optical analysis of a solar receiver, in: 16th Int. Heat Transf. Conf., Beijing, China, 2018: pp. 1–8.

[95] S. V. Patankar, Numerical Heat Transfer and Fluid Flow, McGraw-Hill, New York, 1980.

[96] D. Byun, C. Lee, S.W. Baek, Radiative heat transfer in discretely heated irregular geometry with an absorbing, emitting, and anisotropically scattering medium using combined Monte-Carlo and finite volume method, Int. J. Heat Mass Transf. 47 (2004) 4195–4203. doi:10.1016/j.ijheatmasstransfer.2004.05.008.

[97] H. Abedini, N. Ozalp, An advanced modeling and experimental study to improve temperature uniformity of a solar receiver, Energy. 165 (2018) 984–998. doi:10.1016/j.energy.2018.10.033.

[98] K. Wang, Y. He, P. Li, M. Li, W. Tao, Multi-objective optimization of the solar absorptivity distribution inside a cavity solar receiver for solar power towers, Sol. Energy. 158 (2017) 247–258. doi:10.1016/j.solener.2017.09.044.

[99] D. Hirsch, Hydrogen production by the solar thermal decomposition of natural gas using a vortex-flow solar reactor, ETH Zurich, 2003. https://doi.org/10.3929/ethz-a-004624776.

[100] M.-H. Chien, N. Ozalp, G. Morrison, Computational fluid dynamics and heat transfer analysis of vortex formation in a solar reactor, J. Therm. Sci. Eng. Appl. 7 (2015) 041007-1–8. doi:10.1115/1.4030697.

[101] Y.A. Cengel, A.J. Ghajar, Heat and Mass Transfer: Fundamentals & Applications, Fifth Edit, McGraw-Hill Education, New York, 2015.

[102] Superwool Blanket Data Sheet, Morgan Therm. Ceram. (2016). http://www.morganthermalceramics.com/media/1814/sw_blanket_data_sheet_english_1.pdf (accessed January 5, 2019).

[103] E.E. Graves, H. Zhou, R. Chatterjee, P.J. Keall, S.S. Gambhir, C.H. Contag, A.L. Boyer, Design and evaluation of a variable aperture collimator for conformal radiotherapy of small animals using a microCT scanner, Med. Phys. 34 (2007) 4359–4367.

[104] G.G. Echner, W. Kilby, M. Lee, E. Earnst, S. Sayeh, A. Schlaefer, B. Rhein, J.R. Dooley, C. Lang, O. Blanck, The design, physical properties and clinical utility of an iris collimator for robotic radiosurgery, Phys. Med. Biol. 54 (2009) 5359–5380.

[105] R.R.A. Syms, H. Zou, J. Stagg, H. Veladi, Sliding-blade MEMS iris and variable optical attenuator, J. Micromechanics Microengineering. 14 (2004) 1700–1710.

[106] L. Ren, S. Park, H. Ren, I.-S. Yoo, Adaptive liquid lens by changing aperture, J. Microelectromechanical Syst. 21 (2012) 953–958.

[107] L.R. Sobenko, A.P. De Camargo, T.A. Botrel, A. Frizzone, M.F. De Oliveira, J.V.L. Silva, An iris mechanism for variable rate sprinkler irrigation, Biosyst. Eng. 175 (2018) 115–123. doi:10.1016/j.biosystemseng.2018.09.009.

[108] E. Tanabe, M. Ito, X-Ray Collimator, U.S. Patent No. 8731142, 2014.

[109] C. Ophoff, N. Ozalp, A novel iris mechanism for solar thermal receivers, J. Sol. Energy Eng. 139 (2017) 061004. doi:10.1115/1.4037745.

[110] A. Rajan, M. Abouseada, P. Manghaipathy, N. Ozalp, F.A. Majid, A. Salem, A. Srinivasa, An experimental and analytical study on the feasibility of SMA spring driven actuation of an iris mechanism, Appl. Therm. Eng. 105 (2016) 849–861. doi:10.1016/j.applthermaleng.2016.04.033.

[111] C. Ophoff, H.A. Najafabadi, J. Bogaerts, N. Ozalp, D. Moens, An overview of variable aperture mechanisms in attempt to control temperature inside solar cavity receivers, in: 3rd Therm. Fluids Eng. Conf., ASTFE, Fort Lauderdale, Florida, 2018: pp. TFEC2018-22450.

[112] J. Petrasch, P. Osch, A. Steinfeld, Dynamics and control of solar thermochemical reactors, Chem. Eng. J. 145 (2009) 362–370. doi:10.1016/j.cej.2008.07.051.

[113] A. Muroyama, T. Shinn, R. Fales, P.G. Loutzenhiser, Modeling of a dynamically-controlled hybrid solar/autothermal steam gasification reactor, Energy Fuels. 28 (2014) 6520–6530. doi:10.1021/ef501535r.

[114] B.A. Costa, J.M. Lemos, E. Guillot, Control of a solar furnace using MPC with integral action, Int. Fed. Autom. Control. 49 (2016) 961–966. doi:10.1016/j.ifacol.2016.07.326.

[115] M. Beschi, M. Berenguel, A. Visioli, J.L. Guzmán, L.J. Yebra, Implementation of feedback linearization GPC control for a solar furnace, J. Process Control. 23 (2013) 1545–1554. doi:10.1016/j.jprocont.2013.02.002.

[116] L. Roca, A. De Calle, L.J. Yebra, Heliostat-field gain-scheduling control applied to a two-step solar hydrogen production plant, Appl. Energy. 103 (2013) 298–305. doi:10.1016/j.apenergy.2012.09.047.

[117] L. Roca, A. De Calle, J. Bonilla, A. Vidal, A control based on a knapsack problem for solar hydrogen production, Optim. Control Appl. Meth. 37 (2016) 496–507. doi:10.1002/oca.

[118] S.C. Rowe, I. Hischier, A.W. Palumbo, B.A. Chubukov, M.A. Wallace, R. Viger, A. Lewandowski, D.E. Clough, A.W. Weimer, Nowcasting, predictive control, and feedback control for temperature regulation in a novel hybrid solar-electric reactor for continuous solar- thermal chemical processing, Sol. Energy. 174 (2018) 474–488. doi:10.1016/j.solener.2018.09.005.

[119] A.K. Menon, A. Farid, N. Ozalp, A new solar reactor aperture mechanism coupled with heat exchanger, Chem. Eng. Trans. 35 (2013) 751–756. doi:10.3303/CET1335125.

[120] J.G. Ziegler, N.B. Nichols, Optimum setting for automatic controllers, Trans. ASME. 64 (1942) 759–768.

[121] A.S. Mccormack, K.R. Godfrey, Rule-based autotuning based on frequency domain identification, IEEE Trans. Control Syst. Technol. 6 (1998) 43–61.

[122] E.F. Camacho, A.J. Gallego, Model predictive control in solar trough plants: a review, Int. Fed. Autom. Control. 48 (2015) 278–285. doi:10.1016/j.ifacol.2015.11.296.

[123] B. Khoukhi, M. Tadjine, M.S. Boucherit, Nonlinear continuous-time generalized predictive control of solar power plant, Int. J. Simul. Multisci. Des. Optim. 6 (2015) 1–6.

[124] E.F. Camacho, C. Bordons, Model Predictive Control, Second Edi, Springer, 2007. doi:10.1007/978-0-85729-398-5.

[125] D.W. Clarke, C. Mohtadi, P.S. Tuffs, Generalized predictive control part I. the basic algorithm, Automatica. 23 (1987) 137–148.

[126] A. Padilla, Recursive identification of continuous-time systems with time-varying parameters, Université de Lorraine, 2017.